# New approaches to widely tunable semiconductor lasers

# New Approaches to Widely Tunable Semiconductor Lasers

## Proefschrift

ter verkrijging van de graad van doctor
aan de Technische Universiteit Eindhoven,
op gezag van de Rector Magnificus, prof.dr.ir. C.J. van Duijn,
voor een commissie aangewezen door het College voor Promoties
in het openbaar te verdedigen
op maandag 13 februari 2006 om 16.00 uur

door

**Hendrikus Gerardus Bukkems**

geboren te Veghel

Dit proefschrift is goedgekeurd door de promotoren:

prof.dr.ir. M.K. Smit
en
prof.dr.ir. R.G.F. Baets

Copromotor:
dr. E.A.J.M. Bente

This work was made possible by JDSU (JDS Uniphase corporation).

Front cover shows two SEM pictures of widely tunable laser die mounted on a carrier. The left side picture shows a Cascaded Sampled Grating laser. The right side picture shows a Tunable MMI laser.

CIP-DATA LIBRARY TECHNISCHE UNIVERSITEIT EINDHOVEN
Bukkems, Hendrikus G.
New approaches to widely tunable semiconductor lasers / by Hendrikus Gerardus Bukkems.
- Eindhoven : Technische Universiteit Eindhoven, 2006.
Proefschrift. - ISBN 90-386-1793-3
NUR 959
Trefw.: halfgeleiderlasers / gentegreerde optica / opto-elektronica.
Subject headings: semiconductor lasers / integrated optoelectronics / optoelectronic devices.

# Contents

# List of abbreviations

| Abbreviation | Explanation |
|---|---|
| AM | Amplitude Modulation |
| AR | Anti-Reflection |
| AWG | Arrayed Waveguide Grating |
| BPM | Beam Propagation Method |
| C-band | Wavelength range for optical communication (1527 - 1665 nm) |
| CSG | Cascaded Sampled Grating |
| DBR | Distributed Bragg Reflector |
| DFB | Distributed Feed-Back |
| ECL | External Cavity Laser |
| EIM | Effective Index Method |
| EML | Electro-absorption Modulator Laser |
| Epi-up | Epitaxial side up |
| FM | Frequency Modulation |
| FMM | Film-Mode Matching |
| FSR | Free Spectral Range |
| FWHM | Full-Width Half-Max |
| GCSR | Grating Coupler Sampled Reflector |
| L-band | Wavelength range for optical communication (1565 - 1610 nm) |
| MEMS | Micro-Electro-Mechanical System |
| MMI | Multi-Mode Interference |
| MSA | Multi-Source Agreement |
| O-E-O | Optical-Electrical-Optical |
| PL | Photo-Luminescence |
| QW | Quantum Well |
| RIE | Reactive Ion Etcher |
| RIN | Relative Intensity Noise |
| SE | Spontaneous Emission |
| SG-DBR | Sampled Grating Distributed Bragg Reflector |
| SiON | Silicon Oxy-Nitride |
| SIPBH | Semi-Insulating Planarly Buried Hetero |
| SMSR | Side-Mode Suppression Ratio |
| SSG-DBR | Super-structure Sampled Grating Distributed Bragg Reflector |
| TE | Transversal Electrical |
| TM | Transversal Magnetic |
| T-MMI | Tunable Multi-Mode Interference |
| TTG | Tunable Twin Guide |
| VCSEL | Vertical Cavity Surface Emitting Laser |
| WDM | Wavelength Division Multiplexing |

# List of symbols

| Constant | Description | Unit | Value |
|---|---|---|---|
| $\epsilon_0$ | Permittivity of vacuum | $F \cdot m^{-1}$ | $8.8542 \cdot 10^{-12}$ |
| $\gamma$ | Euler constant | | 0.57721566 |
| $c$ | Speed of light | $m/s$ | $2.99792458 \cdot 10^{8}$ |
| $e$ | Elementary charge | $C$ | $1.60217733 \cdot 10^{-19}$ |
| $h$ | Planck constant | $J \cdot s$ | $6.6260755 \cdot 10^{-34}$ |
| $\hbar$ | Reduced Planck constant | $J \cdot s$ | $1.05457266 \cdot 10^{-34}$ |
| $k_B$ | Boltzman constant | $J/K$ | $1.380658 \cdot 10^{-23}$ |
| $m_0$ | Electron rest mass | $kg$ | $9.1093897 \cdot 10^{-31}$ |

| Symbol | Parameter | Unit | First page |
|---|---|---|---|
| $\alpha(\lambda)$ | Material absorption coefficient | $m^{-1}$ | page 36 |
| $\alpha_{fc}$ | Free carrier absorption coefficient | $m^{-1}$ | page 28 |
| $\alpha_i$ | Internal loss coefficient | $m^{-1}$ | page 28 |
| $\alpha_m$ | Mirror loss coefficient | $m^{-1}$ | page 29 |
| $\beta_0$ | Bragg propagation constant | $m^{-1}$ | page 40 |
| $\beta_t$ | Propagation constant (for mode t) | $m^{-1}$ | page 40 |
| $\Delta E_g$ | Bandgap shrinkage energy | $eV$ | page 55 |
| $\delta\alpha_{fc}$ | Change in free carrier absorption | $m^{-1}$ | page 57 |
| $\delta\alpha_m$ | Difference in mirror loss | $m^{-1}$ | page 33 |
| $\Delta\beta(k)$ | Offset in propagation constant(for resonance k) | $m^{-1}$ | page 40 |
| $\delta\lambda$ | Spectral width of MMI transmission curve | $m$ | page 119 |
| $\Delta\lambda_{cav}$ | Cavity mode spacing | $m$ | page 156 |
| $\Delta\mu(E)$ | Refractive index change at energy E | $-$ | page 57 |
| $\Delta\mu_{contact}$ | Effective index change below MMI-contact | $-$ | page 165 |
| $\Delta\mu_{eff,k}$ | Change in effective index (mode k) | $-$ | page 40 |
| $\Delta\mu_{mat}$ | Change in material refractive index | $-$ | page 128 |
| $\Delta\nu$ | Linewidth enhancement | $Hz$ | page 35 |
| $\Delta\phi$ | Change in phase | $rad$ | page 156 |
| $\Delta_0$ | Split-off valence band energy | $eV$ | page 54 |
| $\delta g$ | Difference in gain | $m^{-1}$ | page 33 |
| $\epsilon_\infty$ | Background permittivity | $-$ | page 54 |
| $\epsilon_s$ | Static relative permittivity | $-$ | page 58 |
| $\eta_{i,e}$ | Injection/external efficiency | $W/A$ | page 31 |
| $\gamma$ | Effective grating strength | $m^{-1}$ | page 41 |
| $\gamma(k)$ | Effective grating strength (resonance k ) | $m^{-1}$ | page 41 |
| $\Gamma_k$ | Optical confinement (mode k) | $-$ | page 75 |
| $\kappa(k)$ | Grating strength (resonance k) | $m^{-1}$ | page 35 |

| Symbol | Parameter | Unit | First page |
|---|---|---|---|
| $\kappa_0$ | Grating coupling coefficient | $m^{-1}$ | page 40 |
| $\lambda$ | Wavelength | $m$ | page 35 |
| $\Lambda$ | Grating duty cycle | $m$ | page 40 |
| $\lambda_B$ | Bragg wavelength | $m$ | page 40 |
| $\mu(\lambda)$ | Refractive index | $-$ | page 36 |
| $\mu_{hh,lh}$ | Joint density of states | | page 56 |
| $\mu_{L,R}$ | Effective index at left and right side of buttjoint | $-$ | page 66 |
| $\mu_{mat,max}$ | Maximum achievable change in material index | $-$ | page 93 |
| $\mu_{ph2}$ | Effective index second phase section | $-$ | page 74 |
| $\mu_g$ | Group index | $-$ | page 30 |
| $\mu_r$ | Refractive index of slab | $-$ | page 118 |
| $\mu_r(y, E, T)$ | Refractive index | $-$ | page 54 |
| $\phi$ | Phase | $rad$ | page 165 |
| $\rho$ | Conductivity | $\Omega/m$ | page 63 |
| $\tau$ | Non-radiative recombination rate | $s^{-1}$ | page 28 |
| $a$ | Geometry factor for MMI | $-$ | page 119 |
| $A_F$ | Loss in front facet reflector | $-$ | page 31 |
| $B$ | Interband radiative recombination rate | $s^{-1}m^3$ | page 28 |
| $C$ | Interband Auger recombination rate | $s^{-1}m^6$ | page 28 |
| $C(y)$ | Absorption coefficient | $m^{-1}$ | page 55 |
| $C_{hh,lh}$ | Heavy/light hole absorption coefficient | $m^{-1}$ | page 55 |
| $D_{cladding}$ | Thickness of cladding layer | $m$ | page 62 |
| $d_0$ | Gaussian waist of input waveguides MMI | $m$ | page 119 |
| $dx$ | Slice thickness | $m$ | page 63 |
| $E$ | Energy | $eV$ | page 54 |
| $E_{ch,cl,vh,vl}$ | Interband energy transition energy | $eV$ | page 56 |
| $E_0$ | Bandgap tail | $eV$ | page 56 |
| $E_g$ | Bandgap energy | $eV$ | page 54 |
| $E_i(z), E_1(z)$ | Euler functions | $-$ | page 57 |
| $f$ | Fermi factor | $-$ | page 55 |
| $F$ | Quasi Fermi level | $eV$ | page 55 |
| $g$ | Gain coefficient | $m^{-1}$ | page 75 |
| $g_{max}$ | Maximum gain | $m^{-1}$ | page 59 |
| $g_{th}$ | Threshold gain | $m^{-1}$ | page 30 |
| $h\nu$ | Photon energy | $J$ | page 31 |
| $I$ | Injection current (subscript indicates section) | $A$ | page 28 |
| $I_{leakage}$ | Leakage current | $A$ | page 56 |
| $I_{N,s}$ | Current in MMI cross-section at node N | $A$ | page 63 |
| $I_{th}$ | Threshold current | $A$ | page 30 |

| Symbol | Parameter | Unit | First page |
|---|---|---|---|
| $J_{sat}$ | Diode saturation current | $A \cdot m^{-2}$ | page 63 |
| $k$ | Resonance number (for sampled grating) | – | page 41 |
| $L_{cav}$ | Cavity length | $m$ | page 29 |
| $L_{CSG}$ | Length (of CSG, SG1, SG2, phase, phase2) | $m$ | page 78 |
| $L_{b,p}$ | Burst/propagation section length | $m$ | page 41 |
| $m_{hh,lh,e}$ | Mass in units of $m_0$ (heavy/light hole, electron) | – | page 56 |
| $n$ | Carrier density | $m^{-3}$ | page 28 |
| $N$ | Slice-index | – | page 63 |
| $n$ | Ideality factor | – | page 63 |
| $n_{cr}$ | Critical carrier density for bandgap shrinkage | $m^{-3}$ | page 58 |
| $N_{SG1}$ | Number of periods in first sampled grating | – | page 41 |
| $n_{sp}$ | Spontaneous emission coefficient | $m^{-3}$ | page 29 |
| $n_{tr}$ | Transparency carrier density | $m^{-3}$ | page 59 |
| $N_c, N_v$ | Effective density of states | $m^{-3}$ | page 58 |
| $P_{absorption}$ | Absorbed power in optical component | $W$ | page 67 |
| $P_{OUT}$ | Power emitted from laser front facet | $W$ | page 31 |
| $P_{F,B}$ | Power incident on front/back facet reflector | $W$ | page 31 |
| $R(n)$ | Recombination rate | $s^{-1} \cdot m^{-3}$ | page 28 |
| $r_{11}^{SG1}$ | Reflection on sampled grating 1 | – | page 74 |
| $r_{CSG}$ | Amplitude based reflection coefficient (of CSG) | – | page 74 |
| $R_{CSG}$ | Power based reflection coefficient CSG | – | page 74 |
| $R_{p,s}$ | Resistance (parallel/series) | $\Omega$ | page 63 |
| $R_{sp}$ | Spontaneous emission rate | $s^{-1} \cdot m^{-3}$ | page 29 |
| $R_{F,B}(\lambda)$ | Front/back facet reflection | – | page 29 |
| $RIN$ | Relative Intensity Noise | $dB/Hz$ | page 34 |
| $s$ | Photon density | $m^{-3}$ | page 28 |
| $S_{xy}$ | S-matrix components | – | page 64 |
| $SMSR$ | Side Mode Suppression Ratio | $dB$ | page 32 |
| $T$ | Temperature | $K$ | page 36 |
| $t$ | Amplitude based transmission coefficient | – | page 74 |
| $T(\Delta\lambda)$ | Transmission of MMI | – | page 66 |
| $V_a$ | Active volume | $m^3$ | page 29 |
| $V_D$ | Diode voltage | $V$ | page 63 |
| $v_g$ | Group velocity | $m/s$ | page 28 |
| $V_N$ | Voltage in cross-section of MMI | $V$ | page 63 |
| $W_{contact}$ | Width of contact | $m$ | page 62 |
| $W_{MMI}$ | Width of MMI | $m$ | page 118 |
| $x, y$ | Arsenide/Phosphide-composition | – | page 53 |
| $Z(\alpha)$ | Parameter for MMI calculation | – | page 119 |

# Chapter 1

# Introduction

Tunable lasers have been a subject for development efforts, in industry and academia, since these devices offer great promise for telecom networks. In this chapter, as an introduction to this optical component, first the applications for tunable lasers are listed (section 1.1). After this, the demonstrated device concepts are introduced (section 1.2) and in section 1.3 the consensus requirements for widely tunable lasers are summarized. The chapter is concluded with an overview of the contents of this thesis and its contributions to the field of integrated widely tunable lasers (section 1.4).

## 1.1 Applications for tunable lasers

Tunable lasers have received attention since the middle of the 80's [63], driven by coherent optical detection techniques [64] and the emergence of Wavelength Division Multiplexing (WDM). The term 'tunable laser' refers to a single-mode laser, for which the lasing wavelength can be adjusted through an external stimulus. These devices are available for a wide range of frequencies (or wavelengths) and for several application fields (such as telecommunications, biomedical sensing [33], etc.). In this thesis, the focus is on widely tunable lasers for telecommunication applications, in the 1550 nm wavelength range. Here, widely tunable lasers are understood to have a tuning range that spans one of the main standardized communication-bands (i.e. C-band , 1529 to 1565 nm, or L-band, 1565 nm to 1610 nm).

The main application for tunable lasers is the replacement of fixed-wavelength lasers. Therefore their performance needs to be as good or better in areas such as output power, spectral purity, stability and reliability. Steady progress has been made over recent years, but since the performance of fixed wavelength sources also has improved, tunable lasers are still lagging, especially in output power and stability. Nevertheless, tunable lasers retain their promise for cost-saving and increased flexibility in telecommunication networks. In this section a diverse range of applications, and the benefit of tunable lasers to them, is discussed.

### 1.1.1 One-time provisioning

Wavelength Division Multiplexing (WDM) is a technique to transmit signals of multiple lasers, each at a different wavelength, over a single optical fiber. Using fixed-wavelength lasers, each signal needs to be generated by a unique laser (i.e. operating at a specific wavelength).

For device manufacturers, this means that each laser needs to be manufactured separately, increasing the complexity (and cost) of the production process. Secondly, these different products need to be placed in an inventory, until they are sold. This increases the inventory costs.

Similarly, for assembly of a module or a full system, tight manufacturing control is required to avoid mistakes (e.g. placing the wrong laser at the wrong position). Furthermore, it requires each laser to be in stock, increasing inventory costs, and each systems to be built to order, increasing lead-times.

The use of tunable lasers reduces these complications. A generic tunable laser can replace any fixed-wavelength laser. Since the laser wavelength can be selected just before shipment of the system, manufacturing is less complex and lead-time can be reduced. Both for system and device manufacturers the inventory costs are significantly reduced.

For the user of the system, a network provider, tunable laser systems also allow for a smaller inventory of laser-sources. This inventory is required to replace failing transmitters in a system. Again, the main benefit is cost-reduction, but there is also a significant simplification of the replacement operation: no specific knowledge about the devices is needed when replacing a transmitter, since all are the same. Even for legacy systems, with single wavelength transmitters, the option to replace a failing device with a tunable laser provides this advantage.

### 1.1.2 Dynamic reconfiguration

Tunability of the sources in a telecommunication system allows for the reconfiguration of the wavelengths on an optical link. This allows for the dynamic replacement of failing units and for the adaptation of a link to new traffic-patterns.

When devices fail in a telecommunication system, typically a service person needs to visit the system and manually replace the failed unit. Alternatively, if the failed device is backed-up by a second laser, this laser can be activated remotely to take over the function of the failed device. In a system with fixed-wavelength devices this however means that each laser needs to be backed up individually. As an alternative, a tunable laser can be a back-up for a number of lasers in a system. If one of these devices fails, the tunable laser is tuned to the wavelength of the failed device and its output is routed to the optical link. Such a configuration reduces the initial cost of the back-up system and enables remote reconfiguration, reducing the immediate need for an expensive manual replacement.

For some critical telecommunication systems a signal is not allowed to be interrupted for longer than 50 ms [103]. This is addressed by using a hot (i.e. operating) spare laser as a backup for each laser source. Again, tunable sources provide a cost-effective alternative, provided that the time to change the wavelength of the laser is in line with the required switching time.

A further opportunity, that the use of tunable lasers offers, is the reconfiguration of a telecommunication system. After the design and installation of a telecommunication link, the traffic patterns can change significantly over time. It is even possible, that the traffic patterns vary significantly over a day (consider the difference between day and night-time operation). The use of tunable lasers allows for reconfiguration of the wavelengths in a system to address these changes in load. This reconfiguration can be performed remotely. It is especially relevant for links with multiple access points and depends on the particular network configuration.

For the latter application to be possible, not only the lasers have to be tunable. Filters and (de)multiplexing elements have to support this tunability.

### 1.1.3 Optical node functionality

Tunable laser technology makes new network concepts, with more flexibility, better use of available bandwidth and lower cost, feasible. Especially, tunable lasers facilitate the migration from WDM point-to-point links towards WDM ring-networks, with multiple access-nodes and connections to other ring-networks.

At each access-point in a network one or more signals have to be dropped from and added to the optical link. In its most basic configuration such an add/drop component converts all the signals on the optical link into the electrical domain, processes the data and retransmits the data in the optical domain. This O-E-O conversion, however, takes time and requires a de-multiplexer, multiple detectors and multiple transmitters. In figure 1.1a an add/drop is shown that is more efficient, through the use of tunable laser technology. Instead of dropping all signals, only the desired signal/wavelength is dropped by a tunable filter and detected. A new signal is added to the link at the 'dropped' wavelength by a tunable laser. This concept dramatically reduces the component count in the add/drop multiplexer and it provides a less complex architecture. The network quality is improved by a shorter delay time for the unswitched signals. The number of signals that the node can add/drop is limited by the number of tunable lasers and filters.

A connection between two WDM rings, a cross-connect, needs to have the capability to transfer a signal at any wavelength on one ring to any wavelength on a second ring, while being transparent for signals that are not cross-connected. The non-tunable configuration would again be a full O-E-O conversion, which means that the non-cross-connected signals are detected and re-transmitted, leading to delay and possible error. Furthermore two multiplexers and de-multiplexers are required, as well as two detectors and lasers for each signal.

The tunable laser configuration allows for dropping only the signals that need cross-connection, by a tunable filter. These signals are then routed to the second ring, in the electrical domain, and added onto that ring, with a tunable laser at the desired wavelength. The cross-connect configuration is shown in figure 1.1b. Again, the number of signals that can be cross-connected is limited by the number of tunable lasers and filters in the cross-connect.

These add/drop and cross-connect configurations require not only the tunable laser technology, but also the availability of tunable filters.

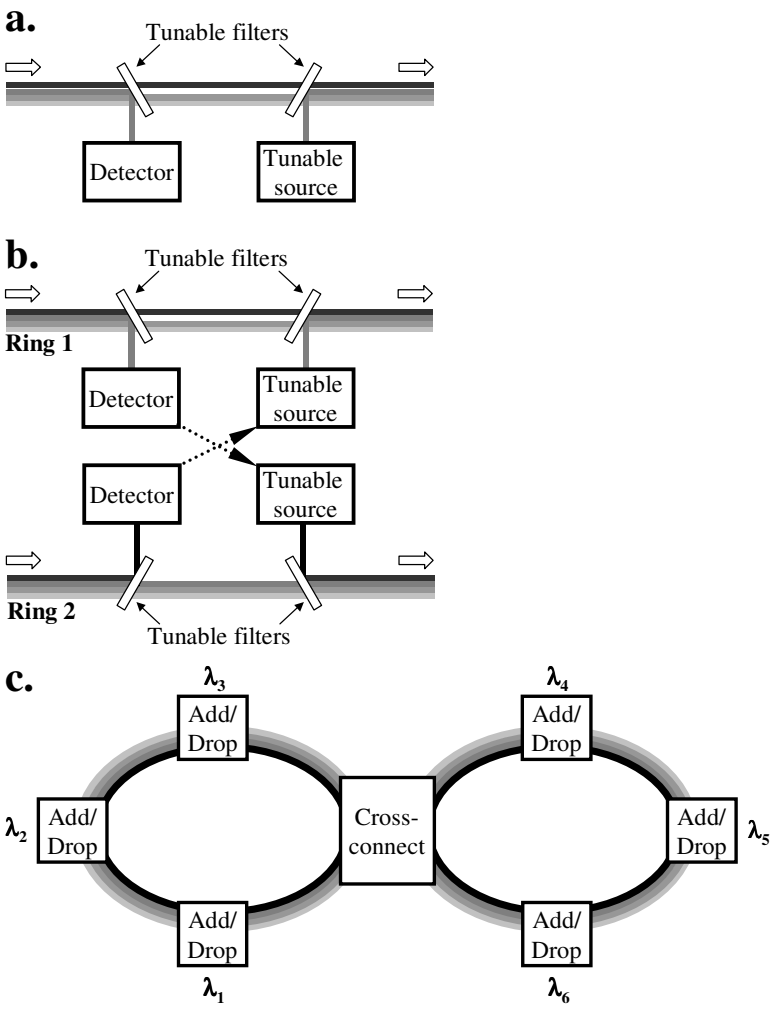


*Figure 1.1: Application of tunable lasers in an optical network; a) Add/drop node with tunable filters and laser. The first filter is set to drop one signal out of the incoming signals. This signal is detected. The tunable laser adds a new signal at the dropped wavelength, to be added to the unswitched signals; b) Optical cross-connect. The cross-connect consists out of two add-drop nodes. In each ring the dropped signal is detected and transferred in the electrical domain to the tunable transmitter on the other ring. There the signal is added to the unswitched signals; c) Dynamic allocation. To establish a network connection between two nodes, the transmitting node uses a tunable laser to transmit at the wavelength of the filter in the receiving node. All intermediate nodes are transparent for this wavelength. E.g. the left node (which can receive signals at $\lambda_2$) can transmit a signal at $\lambda_5$ and since all nodes are transparent to this wavelength it will be detected at the node on the right side.*

### 1.1.4 Network functionality

The use of WDM is important for increasing the capacity of fiber-links. However, significant system simplification is obtained by assigning a specific wavelength to each node in a network. Setting up a connection from one node to another is then done by selecting the appropriate tunable laser wavelength, as shown in figure 1.1c. Since all other nodes are transparent for this wavelength (through add/drops and cross-connects based on tunable laser technology), a minimum of processing delay is added, until the signal reaches the desired node. It simplifies the node architecture (basically an add/drop), since only detection of one signal and the transmission of a new signal is required. Nodes with a higher bandwidth requirement can be configured with more dedicated wavelengths (with additional detectors and transmitters). This provides bandwidth scalability at minimal additional cost.

As an extension to this dynamic allocation, which is used for slow variations in traffic patterns (with timeframes $> 1\ s$), a fully dynamic switching network can be envisioned. In this network configuration the wavelength allocation changes on a $\mu s$ timeframe. This allows packet-switching, where a signal for a specific destination is split into short packets. The transmitting node selects the wavelength consistent with the packet destination, transmits the packet, changes the wavelength for the next packet destination and transmits again.

## 1.2 Tunable laser concepts

The field of tunable lasers is diverse and a number of interesting device concepts have been proposed and demonstrated. No clear winner has emerged, yet, to address all device requirements and hence the search for better concepts continues. It is not clear if this will converge to a generic tunable laser design, which can address all applications, or that each application will require its own type of tunable laser.

Here, presently known concepts are ordered along five categories and the operation principles are discussed.

### 1.2.1 Integrated lasers with a small tuning range

Though outside the scope of this thesis, tunable lasers with a limited tuning range ($< 20$ nm) provide the basis for some of the widely tunable laser variants. Historically, these also were the first concepts to provide tunability.

**Tunable DFB** In figure 1.2a a DFB (Distributed Feed-Back) laser is drawn. Light is generated in the gain generating layer (either a bulk material or a multi-quantum well) along the length of the chip. A periodical variation in the layerstack, a grating, reflects the light within the laser cavity. Thanks to the periodicity of the grating, this feedback is maximum at one wavelength, forcing operation at that wavelength. A DFB laser is the most commonly used single-mode source laser for optical networks and provides excellent mode-selectivity and output power. A change in the temperature of the device changes the effective index of the material, resulting in a different operating wavelength. Typically, the wavelength shifts by

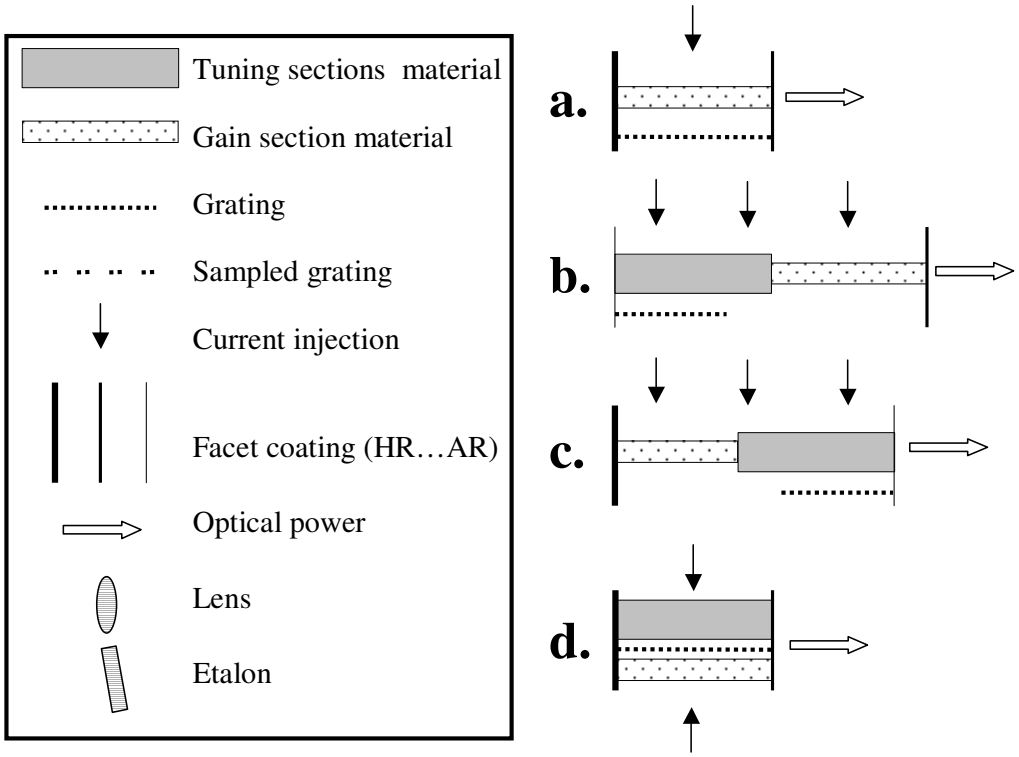


*Figure 1.2: Left hand side: legend for all the schematic drawings of laser concepts. Right hand side: schematic cross-section of integrated laser concepts with a small tuning range; a) Tunable DFB laser; Consists of a gain section between two facets. The pitch of the grating sets the lasing wavelength; b) Tunable DBR laser; Optical power is generated in the gain section and reflects upon the wavelength selective DBR section (to the left, with grating). A phase section between gain and DBR section fine-tunes the lasing wavelength; c) Alternative design for tunable DBR laser; The DBR section is placed between gain section and front-facet. A high reflection coating is applied on the back-facet. This design allows for integration of other semiconductor components between DBR laser and front-facet; d) TTG laser; The gain section and tuning section are vertically integrated, with a grating between the two layers. The pitch of the grating determines the lasing wavelength. With current injection in the tuning section the effective index of the optical mode decreases, lowering the lasing wavelength. This device does not require a phase section for alignment of the cavity mode.*

0.09-0.12 $nm/°C$ [2] [34] and a 30 $°C$ temperature tuning range is used to achieve more than 3 nm tuning range [65].

**Tunable DBR laser** In a DBR (Distributed Bragg Reflector) laser the grating is positioned between the gain generating region (the gain section) and the backfacet (figure 1.2b) [96]. The reflection spectrum of the DBR has a narrow resonance, which selects the wavelength for single mode operation. By injecting current into the DBR section the effective index of this section is lowered and the lasing wave-

length is shifted downward. Temperature tuning can be used to increase the selection wavelength by about 0.1 $nm/°C$. By combining these two tuning mechanisms a tuning range of up to 16 nm has been demonstrated [37]. To optimize single-mode operation and output power, the laser cavity modes need to be aligned with the DBR reflection peak. To achieve this at any wavelength a second tuning element (a phase section) is needed to change the optical length of the laser cavity and align the optical cavity modes with the DBR reflection spectrum. An alternative device configuration is shown in figure 1.2c. There, the gain section is located at the (high-reflection coated) back-facet and the optical power leaves the laser cavity through the DBR section. This allows for inclusion of additional functional elements (such as an optical amplifier or a modulator) between tunable laser output and front-facet [4].

**TTG** The TTG (Tunable Twin Guide) laser offers an alternative to the DBR laser, which needs 2 tuning sections. In the TTG the lasing wavelength is set by a fixed grating pitch and the effective index of the optical mode. Since the gain generating layer and the tuning layer are integrated in one stack (see figure 1.2d), the optical mode has a partial overlap with both. Current injection in the gain layer generates the optical power, while current injection in the tuning section lowers the effective index of the optical mode and tunes the wavelength to lower values. Again, temperature tuning can be used to increase the tuning range [13]. A tuning range of up to 5 nm has been demonstrated [92].

### 1.2.2 External Cavity Lasers (ECL's)

External Cavity Lasers (ECL's) consist of a laser chip, with an anti-reflection (AR) coating on one facet. The power from the AR-coated facet is coupled to an external cavity, which provides wavelength selective feedback. This provides single-mode operation and wavelength tuning.

**Littman-Metcalf cavity with rotating mirror** In figure 1.3a the device configuration is shown. Optical power from the gain chip is coupled to a collimated beam and launched onto a reflecting plate with periodical grooves (a free space grating). This plate reflects the light under an angle, which depends on the wavelength. The desired laser wavelength is selected by limiting the optical feedback of the external cavity to a narrow angular region, with a small mirror. By changing the selected angular region (e.g. by rotating and translating the small mirror around a pivot point [72]) the laser wavelength is tuned. In the figure the free space grating and the mirror, rotating around a pivot point, are shown. The fabrication and movement of the mirror varies between different device technologies [15] [35].

**Littman-Metcalf cavity with laser array** This concept uses the same ECL configuration as the previous concept, with regards to the position of the laser chip and the mirror. However, the single laser is replaced by an array of lasers. The optical field from each laser gets projected onto the free space grating under a different angle. As a result for each stripe in the array the wavelength range that is incident on the fixed (partial transmitting) mirror is different. This allows tuning of

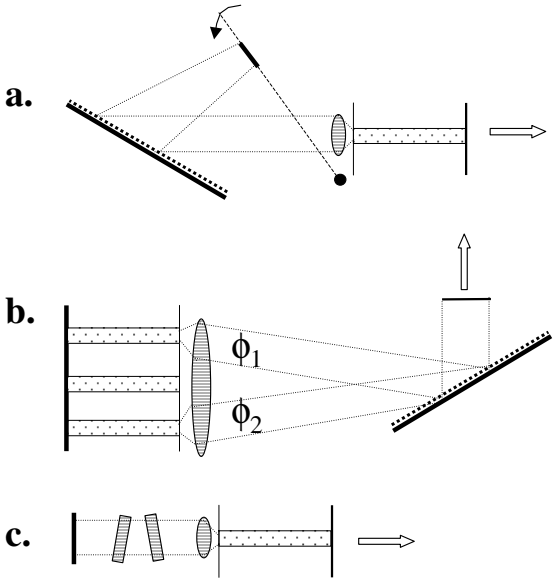


*Figure 1.3: Schematics of external cavity tunable lasers; a) Littman-Metcalf cavity with rotating mirror; The optical power is generated in the gain section. The light is coupled to a collimated beam and projected on a free space grating. A small mirror reflects a spectral portion of the reflected beam, forcing lasing at that particular wavelength. By rotating the mirror around the pivot point, a different wavelength is selected; b) Littman-Metcalf cavity with array selection; The optical power is generated in one of the lasers in the laser-array and reflected on the free space grating, before being incident on the partially transmitting mirror. By selecting another laser in the array, the feedback of the extended cavity is at a different wavelength. This concept uses no moving part and the wavelength is tuned by temperature; c) Temperature tuned etalons; A collimated beam is coupled from the gain section onto two etalons with different spacing between resonance wavelengths. The laser operates at the wavelength where both etalons are in resonance. The wavelength is tuned by changing the temperature of the etalons.*

the laser to discrete wavelengths without any mechanical motion. The principle is shown in figure 1.3b, where the light is collected through the partial transmitting mirror [58].

**Temperature tuned etalons** This concept (figure 1.3c) is based on the transmission of two silicon etalons, with a slightly different periodicity. The transmission spectrum of such an etalon has periodical resonances, of which the spacing depends on the etalon thickness. The transmission coefficient of the etalon at its resonance is dependent on the reflectivity of the surfaces. By combining two etalons with different spacing between the transmission peaks, only the wavelength, at which both etalons are resonant, is selected for laser operation. Temperature tuning of the etalons is used to shift their transmission spectrum and select a different lasing wavelength [35].

### 1.2.3 Vertical Cavity Surface Emitting Lasers (VCSEL's)

For some applications, surface-emitting lasers provide a low-cost alternative to edge-emitting lasers. The laser-cavity is formed by a gain layer between two mirrors. These two mirrors need to be close together to ensure single longitudinal mode operation. Furthermore, the device requires control over the distance between the two mirrors to provide wavelength tunability. The gain region is pumped either by electrical or optical means. Different concepts have been demonstrated that achieve this.

**Optically pumped VCSEL with dielectric top- and bottom mirror** Figure 1.4a [110] shows a laser cavity formed by a bottom dielectric mirror on a locally thinned substrate, and a curved top-mirror (to optimize the coupling of the reflected light back into the cavity) attached to a membrane. This membrane is supported at four points by a non-conductive material. By applying a voltage to this membrane the electro-static force between membrane and chip pulls the membrane towards the chip, reducing the cavity length and operating wavelength. A 1310 nm pump source is used to inject energy into the active region through the top-mirror. The output light is collected through the bottom mirror.

**Optically pumped VCSEL with wafer-fused mirrors** In contrast to the prior concept, the mirrors in the concept in figure 1.4b [99] are formed by an AlGaAs/GaAs DBR on a GaAs substrate. These mirrors are wafer-fused to the InP-based gain material. The advantage of this method is that a high mirror reflectivity is achieved with a semiconductor material that provides heat-sinking and electrical contact. After wafer-fusing a spacer layer is removed in the top-mirror to create a supported membrane, as in the prior concept. The distance between the top mirror and the active region is tuned by applying a voltage over the spacer layer. A 980 nm pump signal is applied through the bottom contact. The output light is collected through the top-contact.

**Electrically pumped VCSEL with epitaxial top and bottom mirror** Both previous concepts require an external laser to pump the gain layer. In figure 1.4c ([30]) an electrically pumped concept is schematically drawn. The bottom-mirror is formed by a semiconductor DBR-stack. Similarly, the top-mirror is formed by an epitaxial DBR stack. Between the active region and this top-DBR stack a sacrificial layer of semiconductor material is grown, that is removed at the end of the process. As a consequence the top-mirror is transformed into a cantilever, supported at only one edge. By applying a voltage over the cantilever the deflection of the top-mirror is controlled. In contrast to the prior concepts the energy is delivered to the active region by electrical pumping. This avoids the use of an extra pumping source, but results in a more severe device heating.

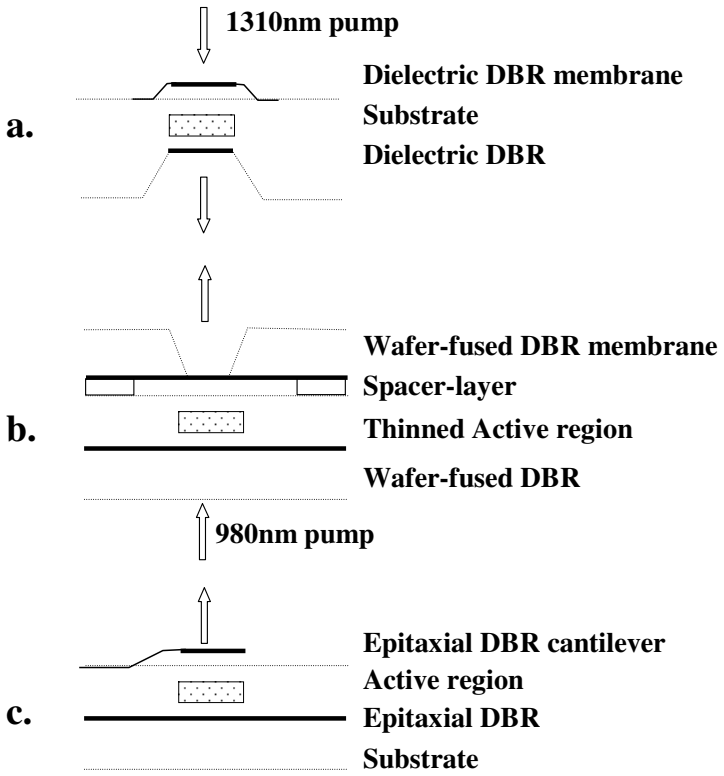


*Figure 1.4: Schematic cross-section of tunable VCSEL's; a) Optically pumped VCSEL with dielectric top- and bottom mirror; The light is generated in the gain section and reflects between the bottom dielectric mirror and the top mirror. By applying voltage on the top-mirror the position of the top mirror (and the lasing wavelength) is controlled. The power is generated in the gain section by pumping the material with a 1310 nm pump source; b) Optically pumped VCSEL with wafer-fused mirrors; Similar to the previous concept, but with wafer-fused DBR-mirrors and a 980 nm pump source; c) Electrically pumped VCSEL with epitaxial top- and bottom mirror; Both mirrors are formed by a semiconductor layerstack, and the top mirror is processed into a cantilever, displaced by applying a voltage. The gain section is electrically pumped.*

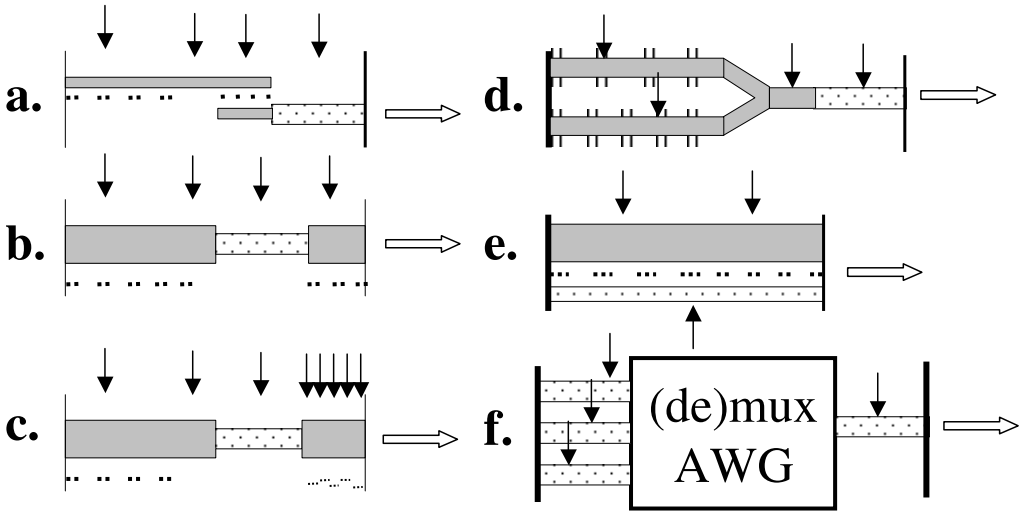


*Figure 1.5: Schematic cross-section of integrated Widely Tunable Lasers; a) Grating Coupler Sampled Grating laser; the laser consists out of a gain section, coupler section, phase section and sampled grating section (right-to-left); b) Sampled Grating DBR laser; the laser consist out of a first sampled grating section, gain section, phase section and a second sampled grating section (right-to-left); c) Digital-Supermode SG-DBR; the laser consists out of a number of short DBR sections (each to be controlled separately), gain section, phase section and a sampled grating section (right-to-left); d) Top-view of Modulated Grating Y-branch Laser; the laser consists out of a gain section, phase section and two parallel sampled grating sections (right to left); e) Sampled Grating Tunable Twin-Guide Laser; the laser consists of two vertically integrated sections with a continuous gain section and two separate sampled grating sections, with different resonance wavelength spacing; f) AWG digitally tunable laser; the laser consists of a number of gain sections at the inputs of the AWG, a (de)multiplexer and an output waveguide (with optionally an additional gain section). In an alternative configuration the output signal is collected inside the (de)multiplexer.*

### 1.2.4 Integrated widely tunable lasers

Widely tunable lasers that have all elements in one chip provide a compact, potentially cheap, solution for tunability.

**GCSR** The Grating Coupler Sampled Reflector laser is a 4-section device consisting of a gain section, a phase-tuning section, a grating assisted coupler section and a sampled grating section. In figure 1.5a the device configuration is shown. The laser cavity is formed between the front-facet and the sampled grating section. This sampled grating section has maximum reflection at its resonant wavelengths, which can be shifted by current injection. The grating assisted coupler has a high coupling efficiency for only one of these resonant wavelengths. In this section the optical mode is coupled from the lower waveguide to the upper waveguide, where it connects to the sampled grating section. For non-resonant wavelengths the optical power is absorbed in the lower waveguide of the sampled grating section. The

resonance wavelength of the coupler is determined by the pitch of the grating in this section and the injection current [44].

**SG-DBR** In figure 1.5b a Sampled-Grating DBR laser is shown. A laser-cavity is formed between the two sampled grating sections. The spacing between resonant wavelengths is different for both sections and only at the selected wavelength both are resonant. The lasing wavelength is shifted by tuning the resonance spectrum of both sampled grating sections (typically by current injection). The output power is collected at the front-facet, through the front-sampled-grating section [38]. Further improvement to this device have been made by chirping the sampled grating sections (Super-structure SG-DBR or SSG-DBR [52]).

**Digital Supermode SG-DBR** In this concept the tuning section between gain section and front-facet is formed by a number of short DBR sections. Each DBR section has a slightly different resonant wavelength, such that the combined reflectivity of these sections is uniform over the tuning range. By injecting current into one of the DBR sections, its resonance shifts to lower wavelength. When the reflection spectra of two short DBR sections overlap the combined reflectivity selects that wavelength. The power is collected through the front-facet, as indicated in figure 1.5c [88].

**Modulated Grating Y-branch Laser** This design is shown, in top-view, in figure 1.5d. Two sampled gratings with different spacing between resonant wavelengths are located at the back-facet. The light from the gain section is split and reflected by the two sampled gratings. The reflected signal is then re-combined. At the wavelength where the two sampled gratings are both resonant a laser mode is supported [115]. Again, the reflection spectrum of both sampled gratings is tuned by current injection.

**Sampled Grating Tunable Twin-Guide laser** Similar to the TTG, in section 1.2.1, the sampled grating TTG laser has its gain layer and tuning layer vertically integrated. A single optical mode overlaps with both layers. In figure 1.5e the cross-section of the device is shown. Instead of a continuous grating a sampled grating is used. In the two sections the periodicity is different and depending on the tuning current in both tuning layers any wavelength can be selected. The mechanism for alignment of cavity modes with the sampled grating feedback is similar as for a DFB laser. Using a $\lambda/4$ phase-shift between the sampled gratings ensures, theoretically, single mode operation [78].

**AWG digitally tunable laser** An AWG (Arrayed Waveguide Grating) is a component that splits multiple optical signals (at different wavelength) on one input channel to multiple channels (de-multiplexing), or vice-versa (multiplexing). A tunable laser based on a (de)mux is illustrated in figure 1.5f [41] [40]. At one input of the AWG an array of optical amplifiers is placed. By operating one of the amplifiers in the array a specific wavelength through the AWG is selected. The power is collected at the multiplexed output waveguide or is tapped from inside the AWG. Alternatively, an additional amplifier can be placed at the output to increase the laser power. Full wavelength access is achieved through temperature tuning.

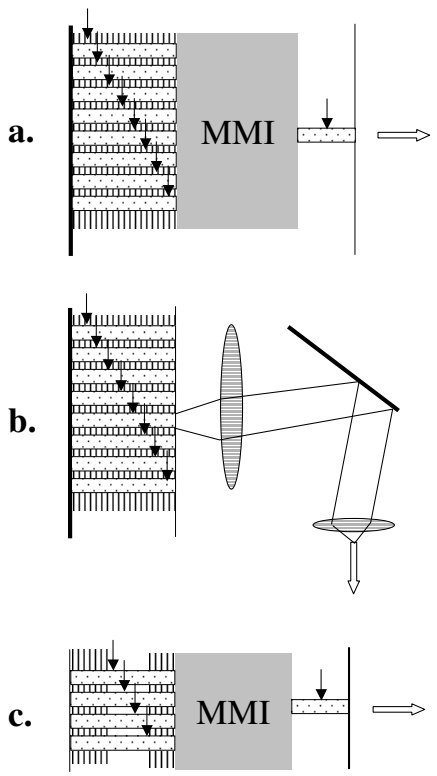


*Figure 1.6: Schematics of arrayed tunable lasers; a) DFB array combined with MMI; An array of DFB's is combined into one output channel, with an MMI. An optical amplifier is used to compensate for coupling loss; b) DFB array combined with MEMS; The output of any of the DFB lasers can be directly coupled to an output fiber by tilting the MEMS mirror; c) DBR array; An array of tunable DBR lasers is combined into one output channel and the signal is amplified.*

### 1.2.5 Array concepts

By combining a number of tunable lasers, with a limited tuning range, a device with a wide tuning range is obtained. The outputs of the different devices are combined into one single output, either by a passive or active coupling scheme.

**DFB array, combined by MMI** A single DFB laser can address a tuning range of about 3 nm by changing the device temperature over a 30 $^{\circ}C$ range. With several of these devices (typically 12-16 devices) on one chip, more than 36 nm tuning range is achievable. The output of these different devices is combined through a passive element, such as an MMI (Multi-Mode Interference) coupler. To overcome the loss of this combiner the light is amplified, on-chip, to generate sufficient output power. In figure 1.6a an illustration of this concept is provided [47] [81] [86].

**DFB array, combined by MEMS mirror** The optical loss in passive combining can be avoided by an active coupling technique. In figure 1.6b this is illustrated. A

MEMS-mirror (Micro-Electro-Mechanical System) is used to couple the output of any DFB in the DFB-array to an output fiber. By changing the tilt of the mirror a different DFB laser is coupled to the fiber [86].

**DBR array** A DBR laser has a wider tuning range than a DFB laser. No temperature tuning is required to achieve a tuning range of more than 10 nm. By combining 4 DBR lasers on one chip, with a passive MMI combiner and an optical amplifier, a tuning range larger than 36 nm is addressed. In figure 1.6c this device is illustrated ([43], also [39]).

## 1.3 Requirements for widely tunable lasers

The applications for widely tunable lasers vary from a simple replacement of fixed-wavelength source lasers to enabling novel network configurations. For all these applications the requirement is that the performance of the tunable laser is similar to, or better than, presently used source lasers. In addition, new applications tend to have higher requirements, particularly with regards to tuning time.

Several manufacturers for tunable lasers have agreed on a common specification for tunable laser modules. This MSA (Multi-Source Agreement) [51] is used here as the industry consensus for tunable lasers and as a reference for the design of the tunable lasers in this thesis. In table 1.1 the requirements are listed. These requirements must be fulfilled over the full wavelength tuning range of the laser.

| Parameter | Unit | Min. value | Max. value | Comment |
|---|---|---|---|---|
| Ex-facet power | mW | 30 | | 20 mW ex-fiber power |
| | mW | 15 | | 10 mW ex-fiber power |
| Side-mode suppression ratio | dB | 35 | | |
| Wavelength | nm | 1529 | 1565 | C-band |
| | nm | 1565 | 1610 | L-band |
| Tuning range | nm | 36 | | C-band |
| | nm | 45 | | L-band |
| Relative Intensity Noise | dB/Hz | | -135 | |
| Linewidth | MHz | | 20 | |
| Wavelength tuning time | | | $>$ s | dynamic reconfiguration |
| | | | 50 ms | protection switching |
| | | | 1 $\mu$s | packet switching |

*Table 1.1: Optical performance requirements for widely tunable lasers (from MSA [51])*

Output power from fixed-wavelength source lasers is typically 5, 10 or 20 mW (both lower and higher power devices are available on the market). To achieve a 20 mW coupled output power a chip output power of 30 mW is required (with 65% coupling efficiency). Tunable lasers with lower output power (e.g. 10 mW) can still be used to

replace lower-power source lasers. Over the tuning range the variation in drive current should be limited, to reduce the tuning complexity.

The spectral purity of the signal is required to be at least 35 dB (i.e. all side-modes are suppressed by at least this factor) to avoid cross-talk between different signals in a WDM system. The requirements on the noise properties (Relative Intensity Noise and linewidth) are set to ensure a high quality signal that can be transmitted over a long distance.

For operation in 1550 nm telecommunication applications, the wavelength of the laser has to be in the range where optical amplification is available and/or the fiber transmission loss is low. Several standard wavelength bands are defined, where optical amplification is available. The most used wavelength ranges are the C and L-bands (1529-1565 nm and 1565-1610 nm, respectively). Widely tunable lasers have to cover at least one of those bands.

Newer network applications require the chip to be able to switch from one wavelength to the other. Dependent on the application, the laser needs to stabilize within a certain timeframe. For network reconfiguration, which occurs occasionally, this can be several seconds. For packet-switching, which can occur multiple times per ms, the time allowed for switching is less than a $\mu s$. In addition, some applications require the output power of the device to be suppressed during switching. This is either achieved by additional components in the package (e.g. a shutter) or through integrated components on the chip, such as optical amplifiers/absorbers.

## 1.4 Position of this thesis

This first chapter describes a clear demand for (widely) tunable laser that can replace presently used single-wavelength source lasers and that provide extra flexibility in the optical network. The primary requirement is that these lasers perform as well as or better than their single-wavelength counterparts, as summarized in the requirements section. With the presently available designs this is not easily accomplished.

The search for new and improved widely tunable lasers continues and this thesis adds two novel widely tunable laser-types to this quest. These new designs are introduced and investigated, both theoretically and experimentally. In both designs the tuning sections are placed at the back-facet side of the laser. As will be demonstrated such a set-up allows, in principle, for higher output power from the laser, as well as a lower variation in power and SMSR over the tuning range.

The two wavelength selection elements in the first concept both have multiple sharp resonances, while in the second concept one of the selection elements has a single wide resonance peak. It will be shown that the latter configuration is more favorable in terms of reliability, controllability and noise.

In addition to the novel concepts this thesis emphasizes two aspects of widely tunable lasers that have been under-exposed in literature, thus far: the impact of design on the controllability of the tunable laser device and the effect of high power operation on the tunable laser performance.

The outline of this work is as follows:

Chapter 2 describes the theory of laser operation and, for tunable lasers, the sensitivity to the tuning section properties. An overview is provided of wavelength selection elements and tuning methods. The chapter finishes with a comparison of available widely tunable laser concepts.

Chapter 3 describes the simulation tools used in this thesis.

Chapter 4 describes the first new widely tunable laser concepts in this thesis: the Cascaded Sampled Grating (CSG) laser. The concept is explained, the design is extensively described and verification of operation is provided, both through simulation and experimental work.

Chapter 5 describes the second new widely tunable laser concept: the tunable MMI (T-MMI) laser. The design of this laser is described and both simulated and experimental data are presented.

Chapter 6 evaluates the results with the two new laser-types and provides a comparison with other widely tunable laser concepts. This chapter ends with a conclusion for the work in this thesis.

# Chapter 2

# Operation principles of tunable lasers

Tunable lasers differ from fixed wavelength lasers by the tunability of their feedback element(s). This requires the laser to have at least one additional control for the tuning element. To be applied in telecommunication systems, these devices are expected to perform comparably to single section lasers, but now over the complete tuning range. Therefore, understanding of the influence of the tuning element on the laser operation is required.

In section 2.1 the physical principles for operation of the gain and tuning sections are described. Special attention is paid to the interaction between the sections. In section 2.2 the available methods for wavelength selection and tuning are discussed. Finally, the different concepts, introduced in section 1.2, are compared in section 2.3, leading to the motivation for the work presented in this thesis.

## 2.1 Electro-optical interactions in semiconductors

Understanding of (integrated) tunable lasers starts with the interaction between semiconductor material properties, electronic carriers and photons. In this section these topics are introduced and applied to the gain and tuning sections.

#### Material-carrier interaction

Carriers in the valence band of a semiconductor material can absorb energy (either thermal, vibrational or optical) to get excited to a vacant state in the conduction band. Similarly, electronic carriers in the conduction band can absorb energy and get excited to higher energy states in this band, or emit energy to decay into a vacant state in the valence band. In this latter process energy is released, either as heat, phonon or photon. The probability of these absorption and recombination processes is determined by the number of carriers in the initial energy level, and the number of unoccupied states in the final energy level, as well as the lattice temperature.

To reach a significant density of electronic carriers in the conduction band, these carriers have to be confined within a specific region. For tunable lasers the tuning-layer, of lower bandgap material, is surrounded by higher bandgap material. Carriers can move freely within the tuning layer, but are confined electrically by the surrounding material. Injection of carriers into this layer (either through electrical current or photo-absorption) raises the carrier-density in the conduction band. This carrier-density changes the refractive index and absorption of the tuning layer.

With an increase in carrier-density, the probabilities of the different carrier excitation and recombination mechanisms change. At no injection current, most carriers are confined in the valence band and excitation of carriers to the conduction band dominates (i.e. absorption of energy). At higher injection current, the population in the conduction band increases and decay into the valence band (i.e. release of energy) becomes the dominant mechanism.

**Carrier-photon interaction**

An optical field interacts with the carrier-density in a semiconductor layer, either by exciting carriers to a higher energy-state, or by stimulating a carrier to decay to a lower energy state. Alternatively, a carrier can decay spontaneously. In the process of stimulated decay a photon is emitted that is coherent with the stimulating field. Spontaneous emitted photons have no phase or directional relationship with the present optical field.

In semiconductor structures where electronic carriers are confined, in both the lateral and transversal direction, a significant carrier-density $n$ can build up and interact with a photon density $s$, in an optical field that propagates in the longitudinal direction. The interaction between the carrier-density and the photon density in a semiconductor material is most conveniently described by rate-equations [11]. For the carrier-density this reads:

$$\frac{dn}{dt} = (\frac{I}{eV_a} + s \cdot v_g \cdot \alpha_i) - (s \cdot v_g \cdot g(n) + R(n) + s \cdot v_g \cdot \alpha_{fc}(n)) \tag{2.1}$$

Here it is stated that a change in carrier-density follows from an imbalance in the number of injected carriers (through current injection and photo-current) and lost carriers (through stimulated emission, spontaneous recombination and free carrier absorption). $\alpha_{fc}$ is the free carrier absorption coefficient, where it is assumed that all carriers excited by this absorption process escape from the electrical confinement. I is the current injected into the active volume $V_a$. $\alpha_i$ and $g$ are the internal loss and gain coefficient. $v_g$ is the group velocity of the optical mode and $R(n)$ is the spontaneous recombination rate, given by:

$$R(n) = \frac{1}{\tau} \cdot n + B \cdot n^2 + C \cdot n^3 \tag{2.2}$$

. This describes the interband non-radiative ($\frac{1}{\tau} \cdot n$), interband radiative ($B \cdot n^2$) and intraband Auger ($C \cdot n^3$) recombination process, respectively. In the above formula diffusion current is neglected. For the narrow, index-guided laser structures considered here, this is a correct assumption [7].

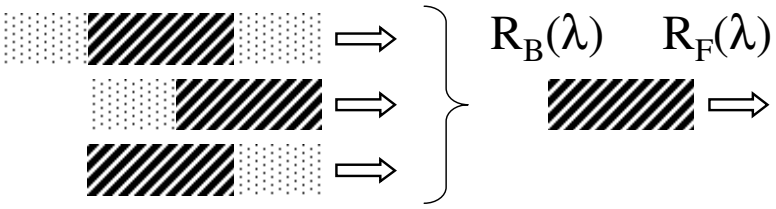


*Figure 2.1: Different multi-section tunable laser concepts (at the left side) can be described (at the right side) as a gain section (dark colored block) with a wavelength dependent mirror at both sides to describe the tuning sections (light colored block).*

Similarly, the photon density in the optical field is determined by the rate of added (stimulated radiation, spontaneous radiation and optical injection) and extracted photons (material absorption, optical emission and free carrier absorption):

$$\frac{ds}{dt} = (s \cdot v_g \cdot g + R_{sp}) - (s \cdot v_g \cdot \alpha_i + s \cdot v_g \cdot \alpha_{fc}) + \frac{ds}{dt}\Big|_{ext} \tag{2.3}$$

In this formula $\frac{ds}{dt}\big|_{ext}$ describes the change in photon density due to photons entering and leaving the active volume through the interfaces of the considered region. $R_{sp}$ is the spontaneous emission into the laser mode, expressed as $\frac{v_g \cdot g \cdot n_{sp}}{V_a}$ , with $n_{sp}$ the spontaneous emission coefficient [49].

**Relevance for device operation**

These rate equations are used to describe both gain and tuning section operation. The behavior of these sections is however distinctly different. Stimulated emission in the gain section efficiently converts electronic carriers into photons, which are emitted from the device. In contrast, without a significant photon density in the tuning section the carrier density increases with increased injection current. The associated change in material refractive index forms the basis for wavelength tuning. In the following two subsections the gain and tuning section are treated. Special attention is paid to how these sections interact.

Most widely tunable lasers can be understood conceptually as a gain generating medium and one or more tuning sections. Describing these tuning sections by their optical feedback ($R_F(\lambda)$, $R_B(\lambda)$ ) at both sides of the gain section (as is shown in figure 2.1), allows for describing different tunable laser concepts in similar terms, making comparison possible. Tunable lasers with feedback elements in the gain section (e.g. DFB lasers [10] and TTG [12]) do not fit this framework.

### 2.1.1 Gain section

A laser cavity is formed by a gain-generating section of length L with reflecting mirrors at both sides ($R_F$ and $R_B$). Light, incident on these mirrors, is partially reflected back into the cavity and the mirror-loss $\alpha_m$ is expressed as distributed over the device length: $\alpha_m = \frac{1}{2L} \cdot \ln(\frac{1}{R_F \cdot R_B})$.

At low injection current, internal loss and mirror-loss ($\alpha_i$ and $\alpha_m$) dominate and any photon is either absorbed or escapes the laser cavity. Hence the photon density is practically zero and the carrier-density is determined by $R(n)$.

At the transparency current the condition $g = \alpha_i$ is reached and light propagates with no attenuation in the cavity. However upon reflection at the mirrors photons escape the cavity and the $\alpha_m$ loss-term dominates.

At the threshold condition, $g_{th} = \alpha_i + \alpha_m$, both loss mechanisms are compensated for by the threshold gain ($g_{th}$). The optical field propagates within the cavity with a zero round-trip loss. However, only with a round-trip phase equal to a multiple of $2\pi$ constructive interference can occur. These two criteria are combined in the lasing condition ($\mu_g$ is the group index, to include the effect of refractive index dispersion at wavelength $\lambda$).

$$R_F \cdot R_B \cdot e^{2\cdot(g_{th}-\alpha_i)\cdot L} \cdot e^{i\cdot 2\pi \cdot \frac{2\cdot\mu_g \cdot L}{\lambda}} = 1 \tag{2.4}$$

For higher material gain ($g > \alpha_i + \alpha_m = g_{th}$), no steady-state situation exists. Therefore, with an increasing current injection the carrier-density is clamped to $g_{th}$ and excess carriers convert to photons to build up the photon density.

For high values of current injection, the photon density induces non-linear effects, such as spatial and spectral hole burning [95]. Furthermore, with increasing current, power dissipation in the chip raises the chip temperature and material properties change. These effects combine to increase the threshold gain until no lasing action is obtained anymore.

Formula 2.4 reveals the two basic mechanisms with which the lasing wavelength can be changed. Altering the round-trip phase allows for a shift of the lasing wavelength, limited to the cavity mode spacing. Tuning over a wider wavelength range is accomplished by changing the round-trip optical gain spectrum in favor of an optical mode at a different wavelength. The mechanisms with which this is achieved are discussed in the sections 2.1.2 and 2.2.

The interaction of the tuning section with the gain section is expressed through the feedback terms $R_F$ and $R_B$. As described in section 2.1.2, the reflection spectrum of tuning sections changes under current injection. This change can be a shift in wavelength of the spectrum or a change in reflectivity and phase. Consequently, the lasing condition 2.4 is affected. In the same manner the transmission of a tuning section (at the front facet) can change and alter the output power.

In this analysis it is assumed that the laser is operated at constant output power over the complete tuning range, through control of the gain section current. Furthermore, only current settings are considered in which all selection mechanisms are aligned to the selected cavity mode. The required fine-tuning of the wavelength is obtained by either a separate phase-section or by temperature tuning.

### Light output

At the threshold condition the gain equals both the internal loss plus mirror loss: $g_{th} = \alpha_i + \frac{1}{2L}\ln\frac{1}{R_F R_B}$. The threshold current ($I_{th}$) follows from the carrier-density rate equation (with s=0):

$$I_{th} = R(n\mid_{g_{th}}) \cdot e \cdot V_a \tag{2.5}$$

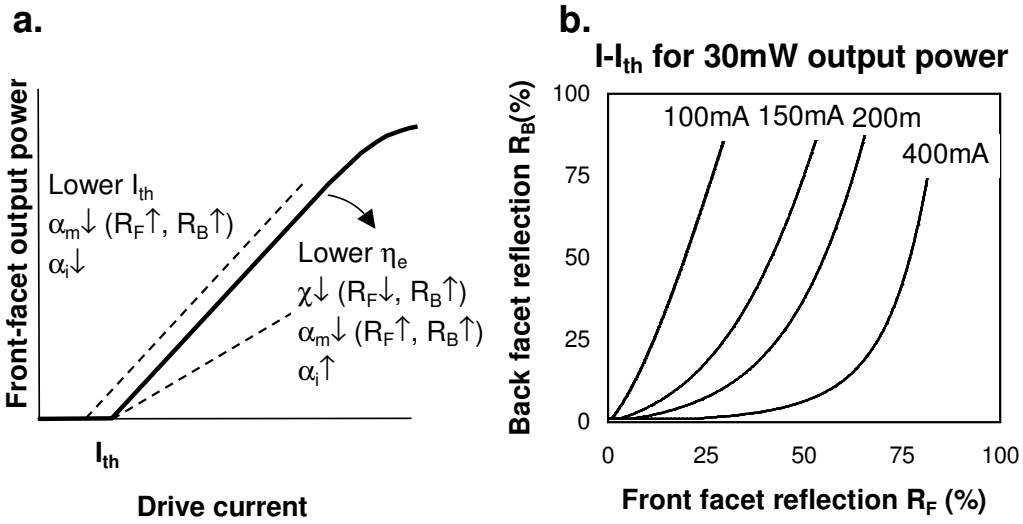


*Figure 2.2: a) Illustration of the dependence of light output on operating current (LI-curve). The figure illustrates the change in the key parameters, threshold current and external efficiency, with the properties of the laser cavity. b) Current above threshold for 30 mW operation, versus front- and backfacet reflectivity. For this calculation formula 2.6 is used. At low values of front- or back-facet reflection the laser threshold current is a significant part of the total operating current. For the calculation the following parameters were used: $\lambda$ =1550 nm, $n_{sp} = 2$, $P_{OUT}$ =30 mW, $A_F = 1$, $\eta_i = 80\%$ and $\alpha_i$ =12.5 $cm^{-1}$.*

Similarly, the output power at higher current is found as [11]:

$$P_{OUT} = (I - I_{th}) \cdot \eta_i \cdot \frac{h\nu}{e} \cdot \frac{\alpha_m}{\alpha_m + \alpha_i} \cdot A_F \cdot \frac{\chi}{\chi + 1} = (I - I_{th}) \cdot \eta_e \tag{2.6}$$

Here $\eta_e$ is the external slope efficiency of the laser, defined in this way, and $\chi$ is the front-back ratio, resulting from the imbalance in facet reflectivity:

$$\chi = \frac{P_F}{P_B} = \frac{\frac{P_{OUT}}{A_F}}{P_B} = \sqrt{\frac{R_B}{R_F}} \cdot \frac{1 - R_F}{1 - R_B} \tag{2.7}$$

In these two formulas a distinction is made between the optical power leaving the cavity through the front reflector $P_F$ and the back reflector $P_B$. $P_{OUT}$ is the power actually emitted through the laser front-facet. $P_{OUT}$ and $P_F$ are different if a tuning section is present between gain section and front facet with optical absorption (i.e. $P_{OUT} = A_F \cdot P_F$). Further, $\eta_i$ is the electrical injection efficiency into the semiconductor region and $h\nu$ is the photon energy.

In figure 2.2a the output power from a laser is plotted versus the injection current. Up to the threshold current $I_{th}$, the injected current builds up the carrier-density in the laser. At higher currents, the injected carriers are converted into photons and the laser emits optical power (the slope of this curve at threshold current is the external slope

efficiency $\eta_e$). Formula 2.6 is based on a threshold analysis and breaks down at higher injection currents, due to device heating and the sub-linear relationship between gain and carrier-density. These effects result in a decreasing slope with increasing injection current (known as roll-over).

In the figure it is indicated how threshold current and external efficiency are affected by the laser parameters. Lowering of internal loss is beneficial for both efficiency and threshold current. An increase in front- or back-facet reflectivity reduces the threshold current. The compound effect on the output power is dependent on the actual set-point of the laser.

In figure 2.2b the gain section current above threshold is plotted versus the reflectivity of both facets, for a front facet power of 30 mW (roll-over is neglected). To obtain the operating current, the threshold current needs to be added. Dependent on the internal loss, there is a combination of front- and back-facet reflectivity at which the operating current is minimized. For this purpose the back-facet reflectivity needs to be maximized, to collect as much light as possible at the front-facet. For the front-facet reflectivity an optimal reflection value needs to be found to reduce operating current above threshold. In addition, with a decrease in front-facet reflection the threshold current increases, potentially resulting in an increase in total operating current.

Together with the design requirements on the laser's spectral properties (see next section), the choice for front-facet reflection value is a trade-off, determined by the relative importance of the different device specification. Since the threshold current and operating current above threshold both decrease for an increase in back-facet reflectivity, it follows that the output power is more sensitive to variations in the back-facet reflectivity than in the front-facet reflectivity.

For a tunable laser the feedback of the tuning sections is not necessarily constant over the tuning range. For the laser to operate at constant output power, the gain section operating current has to be adjusted. This change in current is both due to a change in threshold current, resulting from a change in the threshold gain requirement, and to a change in external efficiency. For reduction of the complexity of device control, the variation of operating current over the tuning range is to be minimized.

### Spectral properties

The phase relationship in the lasing condition (formula 2.4) defines the spectral position of the cavity modes. Since the carrier-density is clamped above threshold (i.e. when one of the modes fulfills the lasing condition), only one of these cavity modes has a sufficient round-trip gain for lasing. Depending on the difference in round-trip gain with this main mode, other modes are able to build up a photon-density as well. As a consequence, the output spectrum of a laser shows, dependent on the round-trip gain distribution, one or multiple modes with significant intensity. Single mode operation requires, at least for laser cavities larger than about 5 $\mu m$, one or both mirrors to provide a wavelength selective feedback. The wavelength selection mechanisms, for tunable lasers in particular, are discussed in more detail in section 2.2.4.

The single mode nature of a laser is characterized by its Side Mode Suppression Ratio (SMSR), defined as the ratio of the power in the main mode and the next most dominant mode (illustrated in figure 2.3a). Following [11] an expression for SMSR is derived from

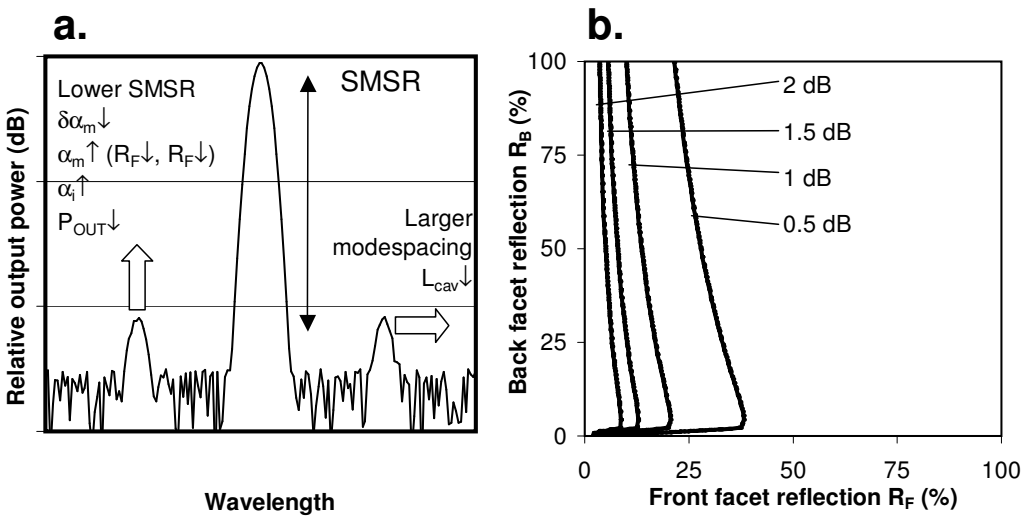


*Figure 2.3: a) Illustration of a single mode laser spectrum. The side-modes are suppressed by the SMSR. The figure illustrates how the SMSR and mode-spacing changes with a change in laser cavity properties. b) Minimum required round-trip gain difference $\delta\alpha_m \cdot L_{cav}$ for 40 dB SMSR, versus back- and front-facet reflectivity. The calculation is based on formula 2.8. For the calculation the following parameters were used: $\lambda$ =1550 nm, $n_{sp} = 2$, $P_{OUT}$ =30 mW, $A_F = 1$, $\eta_i = 80\%$ and $\alpha_i$ =12.5 $cm^{-1}$*

the rate-equations (under the assumption that the amount of spontaneous emission in competing modes is similar):

$$SMSR = \frac{\delta\alpha_m + \delta g}{h\nu \cdot v_g \cdot n_{sp} \cdot (\alpha_m + \alpha_i) \cdot \alpha_m} \cdot \frac{P_{OUT}}{A_F} \cdot \frac{1+\chi}{\chi} \tag{2.8}$$

In this formula $\delta\alpha_m$ and $\delta g$ (expressed per unit length) are the difference in mirror-loss and gain for the two most dominant cavity modes. Since the two competing modes are mostly closely spaced in wavelength the gain difference $\delta g$ is typically small. Selectivity is provided by the mirror-loss difference $\delta\alpha_m$.

From the formula, the SMSR increases with a decrease in optical loss in the cavity (i.e. a decrease in the front facet transmission $A_F$ or a decrease in mirror and/or internal loss, under constant output power operation). Since an increase in back-facet reflection is partly compensated for by an increase in front-to-back ratio the SMSR is less sensitive to changes in back-facet reflectivity than to changes in the front facet reflection. In absolute terms the impact of facet-reflectivity on SMSR is limited, since e.g. a 10 dB change in SMSR requires a factor of 10 change of the parameters in formula 2.8. For DBR lasers it is reported [118] that the SMSR decreases with an increase in tuning current. Following from the formula this decrease cannot be due to a reduced back-facet reflection, but should be attributed to a decrease in the tuning section selectivity (i.e. a decrease in $\delta\alpha_m$) or change in output power.

In figure 2.3a the spectrum of a single mode laser is illustrated. The dependence

of the SMSR on laser parameters is included in the figure. The spacing between the side-modes is determined by the length of the laser-cavity. A larger spacing between modes increases SMSR, in most laser concepts, since selectivity improves.

In order to ensure single-mode operation over the full wavelength range the selectivity $\delta\alpha_m$ has to be sufficiently high, as defined by formula 2.8. In figure 2.3b the required $\delta\alpha_m \cdot L_{cav}$ for 40 dB SMSR is plotted versus the front- and back-facet reflectivity (for 30 mW output power). As stated in equation 2.8, the SMSR depends mainly on the front-facet reflectivity. Therefore for reduction of the variation of SMSR over the tuning range a design with a stable front-facet reflection (i.e. without a tuning section at the front facet side) is preferred.

Minimizing the required gain difference between modes, and reducing the sensitivity of the SMSR to changes in reflectivity over the tuning range, requires a high value of front facet reflectivity. Since such a choice would reduce the output power, the choice for front facet reflectivity is a compromise between the output power and SMSR requirement.

It has to be realized that the used formula for SMSR is an approximation and an appropriate margin has to be taken in the design. In the design chapters a margin for SMSR of 5 dB (a factor 3) is taken.

### Noise properties

Laser properties described so far relate to steady state operation. Perturbations, both external and internal to the gain cavity, can push the laser out of this steady state. External feedback can be avoided by sufficient isolation (electrical and optical) of the laser from its surroundings. It is assumed that no external optical perturbations are present and that the laser operates in one single mode.

In addition to the noise in non-tunable lasers, tuning sections provide an extra source for noise. Typically, the noise contribution by the tuning sections makes tunable lasers noisier than single section lasers. In this section the impact of the tuning sections on the intensity noise (Relative Intensity Noise) and the wavelength noise (linewidth enhancement) is treated separately.

**RIN** On each round-trip through the gain cavity a number of photons is added and removed from the optical field. As a result the round-trip gain shows a statistical fluctuation over time. Fluctuations in the cavity round-trip gain result in Relative Intensity Noise (RIN) or amplitude modulated (AM) noise .

Fluctuations in the round-trip gain and photon density translate to noise in the output power. The interaction between carrier and photon density is frequency dependent and at the laser's relaxation oscillation frequency the coupling between carrier and photon density is maximal. RIN is defined as the noise power per frequency unit relative to the average output power. At the relaxation oscillation frequency (where the noise intensity is maximal over the frequency spectrum) it is expressed as on page 162 in [85].

That formula describes the AM fluctuations inherent to laser operation. Noise from tuning sections can add to this. However, in the high frequency range, RIN is dominated by the inherent laser noise, since current source perturbations at

these frequencies do not transfer well towards the device (unless the connection is specifically designed for RF coupling). The contribution of the tuning section to the RIN is therefore limited to instabilities in the feedback of the tuning section. With the lasing cavity mode aligned to the maximum in reflectivity of the tuning sections, the sensitivity of the laser output power to changes in feedback is low. Therefore, these noise terms do not significantly increase the RIN. In the low frequency regime extra noise can be introduced by mechanical instabilities. For most telecommunication applications this low-frequency noise is not relevant, since the low frequency component in telecommunication signals is removed.

**Linewidth** The other measure of laser noise is linewidth or frequency modulated (FM) noise. On each round-trip, along with stimulated emission of photons, spontaneous emission of photons adds to the optical field in the cavity. This spontaneous radiation has a random phase with respect to the present optical field and hence the round-trip phase fluctuates over time.

The fluctuations in round-trip phase result in a shift of the cavity mode positions and hence the lasing wavelength. Theoretically, over time the lasing wavelength shows a Lorentzian distribution. Linewidth is defined as the 3-dB width of this distribution. For the laser FM noise a formula is given in [50].

For most single section lasers this intrinsic linewidth is small ($< 1\ MHz$) and external perturbations play the most significant role (e.g. current source noise, mechanical vibrations, optical feedback, etc.)[50]. Additionally, for tunable lasers, the tuning sections add a noise-term. In general, only noise introduced by the tuning sections is a relevant concern for widely tunable lasers.

Noise terms in the tuning sections can be both electrical (current source noise) and optical (feedback noise) in nature. The feedback noise is caused by variations in the reflection phase of external tuning sections. Especially for tuning sections based on current injection this contribution can be large, since the carrier-density in the tuning sections is not stabilized (clamped), as in a laser. As a consequence, small variations in the injection current give relatively large variations in carrier-density and hence in material refractive index. The increase in linewidth due to this shot-noise process is given for a tunable DBR laser as [14]:

$$\Delta\nu = 4\pi \cdot \epsilon_0 \cdot \frac{c^2}{\lambda^2} \cdot ((\frac{\delta\Delta\lambda}{\delta I_p})^2 \cdot I_p + \kappa L(\frac{\delta\Delta\lambda}{\delta I_B})^2 \cdot I_B) \tag{2.9}$$

In this formula the derivative terms are the change in wavelength of the tunable laser with a change in phase-section or DBR-section current (the subscripts p and B, respectively). $\kappa$ is the grating strength of the feedback elements. The increase in linewidth is proportional to the variance of the round-trip phase due to the tuning section noise. Since the round-trip phase is proportional to the wavelength response of the tuning sections, the derivative of the wavelength is squared in this formula (page 69 in [11]). For different tunable laser concepts the exact formulation of the relation between tuning-section noise and linewidth is different (see chapter 6). However, the general trend remains that the increase in linewidth is largest for

low values of injection-current, where the change of refractive index with current ($\frac{\delta\mu}{dI} \sim \frac{\delta\lambda}{dI}$) is largest. Reducing the current noise and/or not using this low-tuning-current range can reduce the increase in linewidth reduced.

### 2.1.2 Tuning sections

In contrast to the gain section, the bandgap wavelength of the material in the tuning sections is lower than the laser wavelength. Therefore, both absorption and gain are low and, ideally, there is no interaction between photon and carrier-densities. The tuning is achieved through a change in material refractive index.

#### Physics

A change in refractive index $\Delta\mu(\lambda)$ of a semiconductor material is coupled to its change in absorption $\Delta\alpha(\lambda)$ by the Kramers-Krönig relationship [105]:

$$\Delta\mu(\lambda) = \frac{\lambda^2}{2\pi^2} \cdot P \int_{-\infty}^{\infty} \frac{\Delta\alpha(\lambda')}{\lambda^2 - \lambda'^2} d\lambda' \tag{2.10}$$

Here P denotes the Cauchy principal value [56]. This formula states that a change in refractive index is correlated to the material absorption over the complete spectrum. Hence, a change in refractive index can be induced by a change in absorption at any wavelength in the spectrum. The effect of a change in absorption is stronger close to the wavelength where the integral is evaluated.

For materials considered here, tuning is achieved by carrier injection into the tuning layer. This induces a change in the material absorption at the bandgap wavelength, resulting in a change of refractive index, at the evaluation wavelength.

The main physical effects are ([20], [114]):

**Bandfilling** Injected carriers occupy states in the conduction band, making these states unavailable for further interband absorption processes. The carriers occupy states close to the bottom of the conduction band; hence, especially the absorption at the bandgap energy decreases. For energies below the bandgap energy this results in a decrease in refractive index.

**Bandgap shrinkage** Free carriers in the conduction band repel one another, due to Coulomb interaction and the Pauli exclusion principle. The carriers are thus not completely free to move about in the tuning layer and have a reduced energy. Therefore, the bandgap energy decreases, with increasing injection current. For energies below the bandgap energy this results in an increase in refractive index.

**Free carrier effect** Carriers in the conduction band are available to absorb energy and get excited to a higher energy level within the conduction band, or to an energy level where the spatial confinement of the surrounding high bandgap material is lost. For energies below the bandgap energy this leads to an increase in absorption and a decrease in refractive index.

Bandfilling and bandgap shrinkage have no impact on the absorption below the bandgap energy. In contrast, the free carrier effect allows photons with a wide range of energies to excite a carrier to a higher state in the conduction band. This increase in material absorption is inherent to current injection. Along with a photon loss mechanism, this is also a carrier loss mechanism, since carriers in the tuning layer are excited to energies above the bandgap of the surrounding materials. At these energy levels the carriers are no longer electrically confined to the tuning layer.

In addition to the carrier-density, the temperature is a control parameter for the refractive index. With an increase in temperature the bandgap energy decreases and absorption states shift towards lower energies. Similar to the bandgap shrinkage this leads to an increase of the refractive index. In several tunable laser types this effect is used for wavelength tuning and tuning range enhancement (e.g. [37]). Power dissipation at high injection current increases the chip temperature and refractive index, counteracting the refractive index effects of current injection.

**Tuning characteristics**

Without the presence of an optical field, without current injection, the refractive index is given by the intrinsic material refractive index. The carrier-density with injection current is given by formula 2.1 ($s = 0$) and is mainly controlled by $R(n)$. It increases with $\tau \cdot I$ for low current and saturates as $\frac{1}{C} \cdot I^{\frac{1}{3}}$ (refer to formula 2.1 and 2.2). The change in material refractive index is related to this carrier-density, through the before mentioned physical effects.

The method used for effective index tuning determines the achievable tuning time. Methods that are fully or partially based on temperature tuning are inherently slow (ms range). In contrast, with current injection the tuning time is only limited by the carrier lifetime (ns range). Both tuning methods result in a continuous change in effective index during tuning [119]. As a result the tuning section is selective for intermediate wavelengths during switching and tuning is a continuous process. Furthermore, overshoot and damping phenomena can occur, before stabilization into the final state occurs.

**Interaction with an optical field**

The interaction between carrier-density and photon density in the tuning sections has been neglected, thus far. For a small tuning current and low optical power levels this is a reasonable assumption. However, the incident optical power on the tuning section generates photocurrent through material absorption. Furthermore, with an increase in carrier-density the absorption increases, due to free carrier absorption. The latter effect is largely composition independent (for the InGaAsP materials considered here), but the former effect depends on the difference between laser-wavelength and tuning material bandgap. The combined effect on the carrier-density is calculated by including the photocurrent terms in the formulas 2.1 and 2.3.

Additionally for distributed reflectors in tuning sections the power-density varies over the length of the element. The carrier-density follows this distribution even with a homogeneous injection current. As a result the reflection spectrum can be significantly altered.

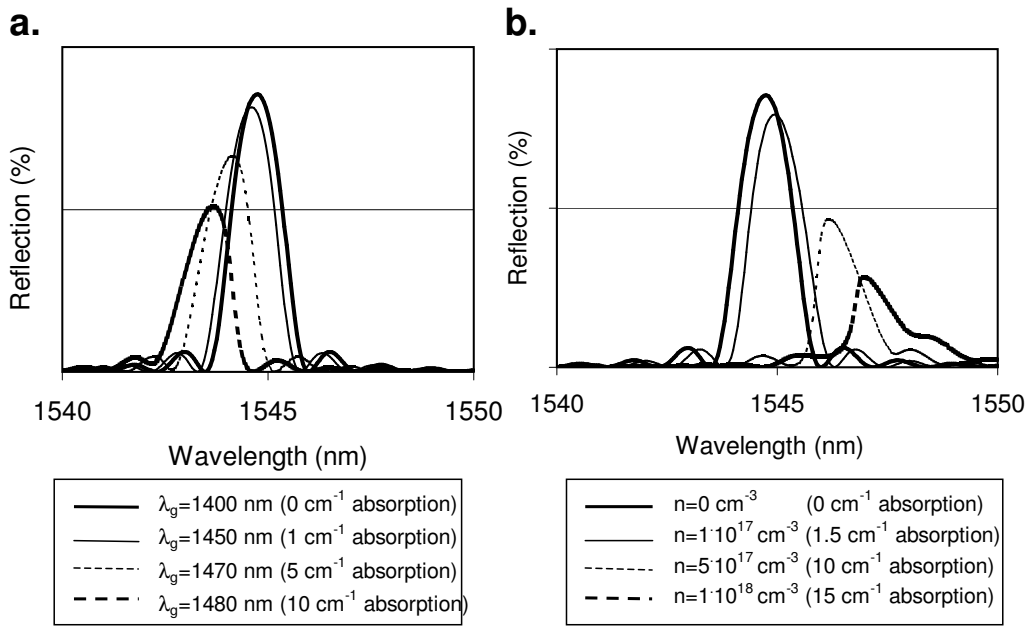


*Figure 2.4: a) The reflection spectrum of a DBR section for different bandgap wavelengths of the tuninglayer material, corresponding to different values of internal loss at he operating wavelength of 1550 nm. b) The reflection spectrum of a DBR section for different values of carrier-density in the tuning section, corresponding to different values of free carrier absorption.*

In figure 2.4a the response of a DBR (see section 2.2.1) with 15 mW incident power is shown for different values of tuning material bandgap and no injection current ($\alpha_{fc} = 0$). First, with a bandgap wavelength closer to the lasing wavelength, the material absorption increases. The photo-current increases the carrier-density in the tuning layer and the resonant wavelength shifts to a lower value. Secondly, the absorption reduces the effective length of the grating, widening the grating response. And thirdly, since the generated photocurrent is proportional to the power density, the carrier-density (and thus Bragg wavelength) is not uniform over the length of the grating. This effect further widens the resonance.

For this calculation the grating has been divided in short elements, which are assumed to be uniform and not inter-connected (i.e. no carrier diffusion between these elements). The simulation tool is described in section 3.4. It is also assumed that the reflectivity is probed by a single mode laser-source. If illuminated by a broadband source the results are different, since then the distribution of optical power over the grating is spatially more homogeneous.

In figure 2.4b the grating reflection is shown for different values of carrier-density or free carrier absorption (a low bandgap wavelength is assumed as to make $\alpha_i = 0$). The shift in resonance wavelength and spectrum is again observed, but the wavelength shifts in positive direction. This is due to the reduction of carriers in the conduction band by the free carrier absorption process.

An optimal choice of material bandgap wavelength can reduce the effects of the free carrier absorption. With a material that has gain at higher injection current the increase in absorption can be countered [96]. The drawback is however an increased interaction between photon and carrier-densities and a lower tuning range, since additional current is used for optical gain.

Figure 2.4 demonstrates that the choice of material composition is important. Tunability of the refractive index (linked to a change in absorption through formula 2.10) requires material with a bandgap wavelength in the vicinity of the lasing wavelength. Hence, the design requires a good trade-off between tuning range and material interaction with the optical field.

As a note, this effect is most pronounced for a front-facet tuning section since incident power, ideally, is highest at this facet.

A further consequence of the interaction between optical power and carrier-density is hysteresis in the tuning behaviour. This means that the laser wavelength at a given set point is dependent on the previous set point and the switching sequence towards that set point. For a given current setting, multiple stable set points might exist at different levels of incident power. As a result, any of these stable set points can be addressed by accessing the channel from specific initial conditions.

Thus, care has to be taken in the switching sequence and the starting point before switching. This complicates the device control.

The interaction between optical power and carrier-density is not the only source of hysteresis in semi-conductor devices. Also non-linear material properties can induce hysteresis, as well as thermal variations over a device.

## 2.2 Cavity mode selection and tuning

Thus far, the wavelength dependence of the reflection terms $R_B$ and $R_F$ was neglected. However, single mode operation of a laser requires a wavelength selective element and wavelength tuning requires the selection wavelength to be adjustable. In the analysis of tunable lasers here, only tuning schemes are considered that provide wavelength selectivity through tuning sections, external to the gain section. In the model, these show up as wavelength dependent mirror reflectivity, $R_B(\lambda)$ and $R_F(\lambda)$.

In this section first the two most common wavelength selective elements are introduced and discussed. Other elements are summarily treated. With this background information, a listing of selection and tuning schemes is presented.

It should be noted that the new wavelength selective elements, introduced in this thesis (CSG and T-MMI), are treated in detail in their respective chapters.

### 2.2.1 Grating

A basic wavelength selective element in integrated optics is the grating. With a periodic variation of the effective index, in the propagation direction of the optical mode, the distributed reflection adds coherently to create a wavelength dependent reflection spectrum.

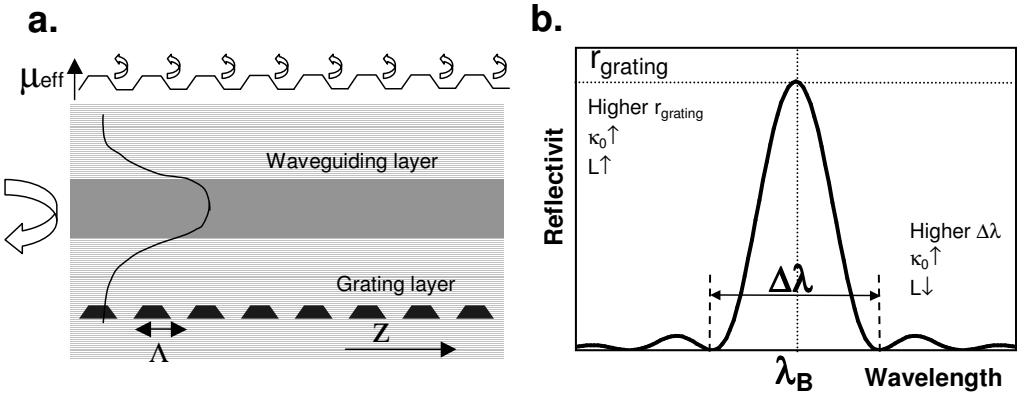


*Figure 2.5: a) Layer stack with a grating. Periodically, a layer in the stack is removed, resulting in a modulation of the effective index $\mu_{eff}(z)$. b) The spatial modulation of the effective index results in a reflection that is resonant at the Bragg wavelength $\lambda_B$, with a maximum reflectivity $r_{grating}$ and a spectral width $\Delta\lambda$. The dependence of the spectrum on device parameters is indicated in the figure.*

Figure 2.5 illustrates how this can be implemented by partial etching of a layer in the layerstack. The figure shows the longitudinal cross-section of the device and the reflection spectrum for an optical mode incident on the grating. At each grating-tooth the variation in effective index $\mu_{eff}(z)$ results in a small reflection-coefficient. The result is a reflection spectrum that is resonant at the Bragg wavelength, defined as $\lambda_B = 2 \cdot \overline{\mu_{eff}} \cdot \Lambda$. Here $\overline{\mu_{eff}}$ is the average effective index and $\Lambda$ is the grating pitch.

The overlap of the optical field with the grating layer determines the strength $\kappa_0$ of the grating, defined as the average reflection per unit length (e.g. for a symmetric stepwise effective index-variation $\Delta\mu_{eff}$ the grating strength is given by $\frac{2 \cdot r}{\Lambda}$ with $r = \frac{\Delta\mu_{eff}}{2 \cdot \overline{\mu_{eff}}}$). The exact grating strength depends on the geometry of the grating. For a sinusoidal variation of the effective index, the grating strength is given by $\frac{\pi \cdot \Delta\mu_{eff}}{2\lambda_B}$. For a different effective index variation, described by $\mu_{eff}(z) = \sum_i \alpha_i \cdot cos(2\pi \cdot i \cdot \frac{z}{\Lambda})$ the grating strength is derived from the first order Fourier component as $\alpha_1 \cdot \frac{\pi}{\lambda_B}$.

The reflection spectrum of a grating of length $L$ is described by [11]:

$$\begin{aligned} r_{grating} &= \frac{-i \cdot \frac{\kappa_0}{\gamma} \cdot \sinh(\gamma \cdot L)}{\cosh(\gamma \cdot L) + i \cdot \frac{\Delta\beta}{\gamma} \cdot \sinh(\gamma \cdot L)} \\ r_{grating}\,|_{\Delta\beta=0} &= -tanh(i \cdot \kappa_0 \cdot L) \\ \Delta\lambda &= \frac{\lambda_B^2}{2\pi \cdot \mu_g} \sqrt{(\frac{\pi}{L})^2 + \kappa_0^2} \end{aligned} \tag{2.11}$$

In this formula $\Delta\beta$ is the offset of the propagation constant $\beta$ from the Bragg propagation constant $\beta_0$ ($\Delta\beta = \beta - \beta_0 = \frac{2\pi \cdot \overline{\mu_{eff}}}{\lambda_B^2}(\lambda_B - \lambda)$). $\gamma^2$, the effective grating strength, is defined as $\kappa_0^2 - \Delta\beta^2$. The derived parameters in the second line are the reflectivity at resonance and the distance $\Delta\lambda$ between the first minima around the resonance. These expressions are correct for low values of $\kappa_0 \cdot L$.

The features in figure 2.5 are dependent on the grating strength and the length of the grating. An increase in either, increases the reflectivity. The width of the resonance increases for a higher grating strength and decrease with an increasing grating length. For a short grating the dependence on grating length is most pronounced.

### 2.2.2 Sampled grating

A sampled grating is created by alternating grating burst sections (of length $L_b$ ) with propagation sections without grating (of length $L_p$). At wavelengths where the reflection from the different burst-sections is in-phase (i.e. $\frac{2\cdot(L_p+L_b)\cdot\overline{\mu_{eff}}}{\lambda}$ = integer) the sampled grating is in resonance. This is illustrated in figure 2.6.

An analytical description for the sampled grating reflection spectrum is available from [54], where it is shown that, at each resonance k in the sampled grating spectrum (with the center resonance having index 0), the reflection-spectrum $r_{sg}(\lambda)$ is described similar to the grating formula 2.12 (with an effective grating strength $\kappa(k)$):

$$\begin{aligned}
r_{sg}(\lambda)\mid_{\text{near peak k}} &= \frac{-i\cdot\frac{k(k)}{\gamma}sinh(\gamma(k)\cdot L_{sg})}{-cosh(\gamma(k)\cdot L_{sg})+i\cdot\frac{\Delta\beta(k)}{\gamma(k)}\cdot sinh(\gamma(k)\cdot L_{sg})} \\
&\text{with} \\
\Delta\beta(k) &= \frac{2\pi\cdot\mu(\lambda)}{\lambda}-\frac{\pi}{\Lambda}-\frac{\pi\cdot k}{L_b+L_p} \\
\kappa(k) &= \kappa_0\cdot\frac{L_b}{L_b+L_p}\cdot\frac{sin(\pi\cdot k\cdot\frac{L_b}{L_b+L_p})}{\pi\cdot k\cdot\frac{L_b}{L_b+L_p}}e^{-i\cdot\pi\cdot k\cdot\frac{L_b}{L_b+L_p}} \\
\gamma(k)^2 &= \kappa(k)^2-\Delta\beta(k)^2 \\
L_{sg} &= \text{total length of grating} = (N_{sg}+1)\cdot L_b \\
\mu(\lambda) &= \text{effective index at the wavelength } \lambda \\
N_{sg} &= \text{number of propagation sections}
\end{aligned} \tag{2.12}$$

Similar to the grating, the reflection at resonance and the spectral distance between minima around resonance are calculated for the sampled grating:

$$r_{sg}(k)=-tanh(i\cdot\kappa(k)\cdot L_{sg}) \quad\text{and}\quad \Delta\lambda(k)=\frac{\lambda^2}{2\pi\cdot\mu_g}\sqrt{(\frac{\pi}{L_{sg}})^2+\mid\kappa(k)\mid^2} \tag{2.13}$$

Comparing this formula to the grating formula 2.12 shows that the central resonance ($k=0$), in the sampled grating spectrum is described by the grating formula, with $\kappa(0)=\kappa_0\cdot\frac{L_b}{L_b+L_p}$. For resonances off from the center resonance the effective grating strength decreases. These resonances thus have a lower reflectivity and are narrower than the center resonance (formula 2.13).

The features in figure 2.6 are dependent on the parameters grating strength, sampled grating length, burst section length and periodicity. The spacing between resonances is determined by the sampling period as $\frac{\lambda^2}{2\cdot\mu_g\cdot(L_b+L_p)}$. The reflectivity of the resonance at

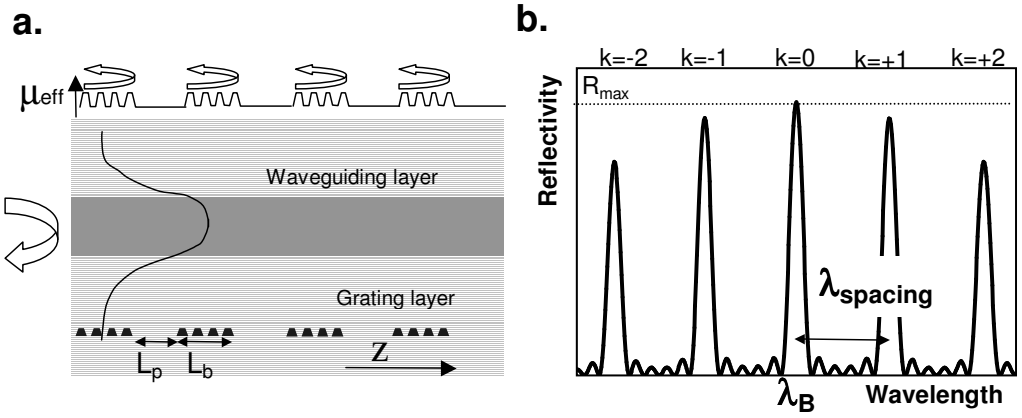


*Figure 2.6: a) Layer stack with a sampled grating. In addition to the periodical variation in effective index, the grating is periodically removed. B) This additional effective index modulation results in a spectrum with multiple resonances. At the Bragg wavelength $\lambda_B$ the fundamental resonance (k=0) is located. Higher order resonances are also shown. The spacing between peaks $\lambda_{spacing}$ is dependent on the periodicity of the grating.*

the Bragg wavelength is given by the effective length of the grating ($\frac{L_b}{L_b+L_p} \cdot L_{sg}$) and the grating strength. The reflectivity for higher order resonances depends on the effective grating strength. With more closely spaced resonances, the number of resonances within the tuning range increase and the variation in reflectivity over the tuning range is larger. Similarly, variation in reflectivity of the resonances over the tuning range is increased by a longer burst section length (with equal periodicity).

Equation 2.12 is based on the assumption that the grating pattern is applied continuously and is removed afterwards in the propagation sections. As a result the different grating burst sections are phase-coherent with one another at the Bragg wavelength. For a grating manufactured with a holographic projection this condition necessarily holds true, in contrast with gratings made by e.g. phase-shift masks or e-beam writing. The main consequence is that the center sampled grating resonance is at the Bragg wavelength.

Variants on the sampled grating have been demonstrated that allow for optimization of the reflection spectrum. These methods either vary (chirp) the pitch of the grating over a grating burst section or between grating burst sections [107] or introduce phase-shifts at specific positions in the tuning section [52]. The former method aims to reduce the wavelength dependence of the sampled grating reflectivity, while the latter alters the shape of the reflection spectrum.

### 2.2.3 Alternative selection elements

Though the (sampled) grating is the most commonly used selection element in integrated tunable lasers, other elements are available for wavelength selectivity:

**Grating enhanced Vertical Coupler Filter [24]** This element consists of two, ver-

tically integrated, coupled asymmetric waveguides. Thanks to close proximity, light in one waveguide couples to the other waveguide over the coupling-length, determined by the difference in effective index between the modes in both waveguides. This length is typically long, but by including a grating between the waveguides, of which the length equals the distance over which the two modes build up a $2\pi$ phase difference, the coupling-length is reduced significantly. This grating also adds a stronger wavelength selectivity to the transmission.

This element works in transmission mode and insertion loss is sensitive to the length of the structure. The transmission spectrum is too wide to provide good cavity mode selectivity. However, combined with an element that provides a multi-resonance reflection spectrum the vertical coupler filter is used for the selection of one of the resonances, leaving mode-selection to the other element. The combined structure can offer good resonance selectivity.

**Digital Supermode DBR [88]** This element is a sequence of short grating sections, all offset in Bragg wavelength from one another. With no injection current, the separate resonances from these sections combine into a mostly flat reflection spectrum. Current injection into one of the sections causes the resonance wavelength of that grating to shift towards lower wavelength and to shifts its spectrum to overlap with a spectrum of another section. The resultant spectrum has an increased reflectivity at that wavelength and allows for wavelength selection.

Each separate DBR section is short, resulting in a wide reflection spectrum and poor cavity mode selectivity, but as for the tunable laser with the vertical coupler filter, the Digital Supermode DBR is used to select a resonance from an element with a reflection spectrum with multiple resonances.

**Free space grating [83]** This free space optics element has an HR coated surface, with periodically etched grooves on the surface. A collimated beam, incident on such a plate, is reflected under an angle that depends on its wavelength. A broad incident spectrum is therefore angularly separated after reflection. Wavelength selection is achieved by providing optical feedback over only a small angular range. This is done by placing a small reflecting surface at a distance from the free space grating. Placed under the correct angle, this mirror reflects light back onto the free space grating, with a good overlap to the initial beam.

This element can provide excellent cavity mode selectivity by placing a small mirror at a sufficient large distance (order of mm's) from the free space grating.

**Fabry-Perot etalon [35]** This element is a medium between two parallel reflecting surfaces (typically coated air-glass or air-silicon interfaces). The transmission spectrum of this element has multiple resonances, spaced according to the distance between the reflectors. Transmission of light, incident perpendicular to the reflectors, can be close to unity. However, to avoid reflections within the laser cavity the etalon has to be placed under an angle, increasing the insertion loss. For highly selective resonances the two reflecting surfaces needs to have high reflectivity.

Using two of these elements with different periodicity between the resonances a wavelength is selected, where two resonances overlap. By tuning, either thermally

or mechanically, the spectrum of one of the etalons can be changed, as well as the wavelength of overlap between resonances. This element provides excellent wavelength selectivity [35].

**MEMS mirror[30]** In a short cavity (e.g. a VCSEL) only one cavity mode is available within the gain spectrum. Control over the wavelength is achieved through the optical length of the cavity. A MEMS (Micro-Electro-Mechanical System) moving mirror in the cavity provides this control. Displacement of the mirror is typically achieved through application of a voltage.

The short cavity of a VCSEL enables a large wavelength change through a small mirror-displacement. Because of the VCSEL's large cavity mode spacing the mirror does not need to provide mode selectivity, since within the gainpeak width only one cavity modes is available.

**Array selection [81] [86]** Instead of a complicated tuning scheme, different tunable lasers with a narrow tuning range can be combined to achieve a wide tuning range. The coupling of these lasers into one output channel can result in significant loss, which has to be compensated for by an optical amplifier (potentially integrated on the chip) [81]. Alternatively an active coupling scheme has been demonstrated, where the coupling of each separate laser to the output channel can be controlled by the tilt of a MEMS mirror [86]. Each laser in the array can be activated or deactivated separately.

Typically, the wavelength selectivity and properties of the widely tunable laser is defined by the worst quality laser in the array. However, since each device is optimized for one small wavelength range typically the mode-selectivity is excellent.

This description is by no means complete and other functional elements have been presented. The above list however, comprises the most used concepts for wavelength selection in widely tunable lasers.

### 2.2.4 Selection and tuning mechanisms

The basis for tunable laser operation is the ability to select one out of many cavity modes and to either tune this cavity mode or select any other cavity mode, within the tuning range. In the previous subsections, the elements for wavelength selection were introduced. Here, the use of these elements for wavelength tuning is described.

Wavelength selective elements, known so far in integrated lasers, show either limited wavelength selectivity over the tuning range or limited tuning range (typically less than 15 nm). Therefore, for integrated devices, one of the following three strategies (illustrated in figure 2.7) is used to create a widely tunable laser:

**Reduction of the number of cavity modes** Selection of one single cavity mode is achieved by reducing the cavity length. This increases the wavelength spacing between cavity modes up to the point that only one mode is present over the full spectral width of the gainpeak. Tuning is achieved by changing the (optical) cavity length. Since the mode spacing is larger than the available tuning range the change

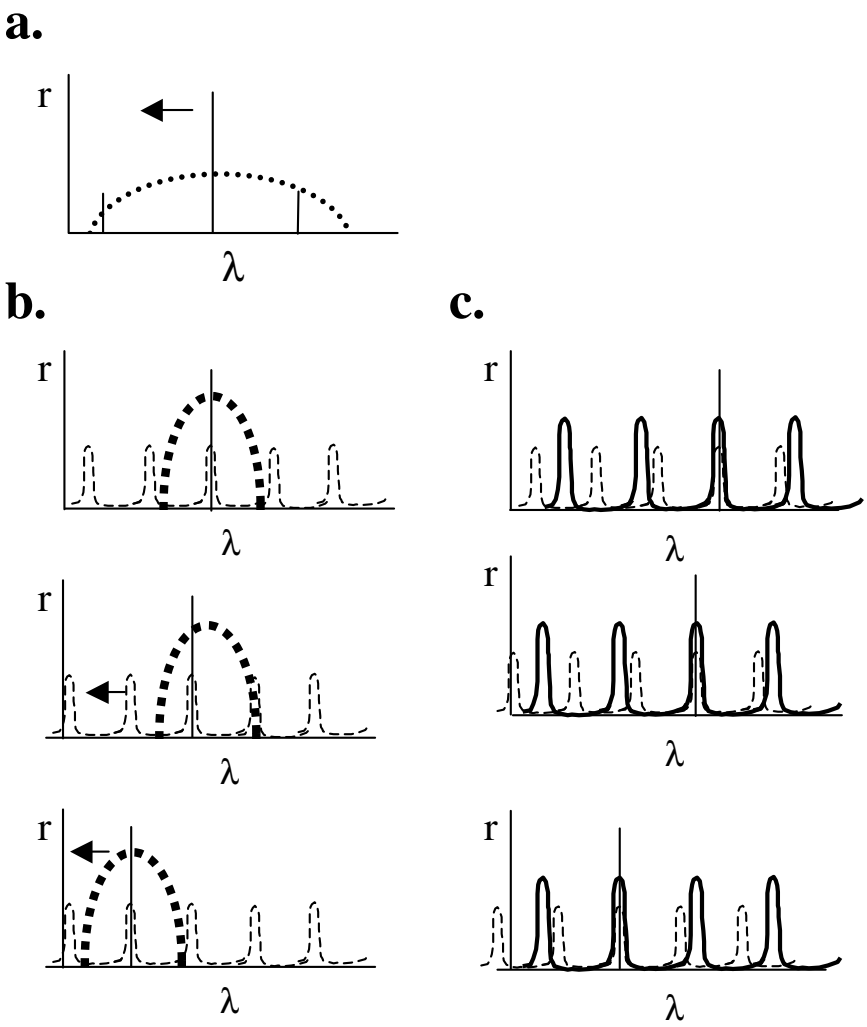


*Figure 2.7: The selection and tuning mechanism for integrated widely tunable lasers. In each graph a thin long vertical line indicates the lasing wavelength. a) Reduction of number of cavity modes. Within the gainpeak (dotted curve) only one cavity mode has sufficient gain. Tuning is achieved by shifting the selected cavity mode. b) Resonance selection by course filter. One of the resonances in the multi-resonance spectrum (thick dashed curve) is selected with the coarse filter. By shifting the multi-resonance spectrum (thin dashed curve) the wavelength is tuned over a small wavelength range. By shifting the filter wavelength, other resonances are selected. c) Resonance selection by Vernier effect. Two multi-resonance spectra (solid and dashed curve) with different spacing between resonances only have an overlap in resonance at one wavelength. By shifting both spectra simultaneously the selected wavelength is tuned over a small wavelength range. By shifting only one of the two spectra, two resonances at a different wavelength overlap.*

in cavity length required is less than half the operating wavelength (assuming the added cavity length is in air).

**Resonance selection by coarse filter** The combination of an element with several highly selective resonances, but with a limited tuning range, and a broad spectrum (with a wide tuning range), results in a tunable laser that can select a cavity mode and be tuned over the full tuning range. Essentially the resonance selection is provided by the broad spectrum, while the cavity mode selection is provided by the multi-resonance spectrum. Fine wavelength control within the broad spectrum is realized by tuning the multi-resonance spectrum, while tuning of the broad spectrum selects another resonance and provides the coarse tuning.

**Resonance selection by Vernier effect** Cavity mode selection is provided by two spectra with multiple narrow resonances. The spacing of these resonances is different for the two spectra. Overlap of two resonances at one wavelength implies that the other resonances do not overlap within the tuning range. Through the selectivity of the combined resonance, a mode at this wavelength is selected. Tuning of the selected resonance is achieved by tuning both spectra simultaneously. Overlap of the resonances in both spectra remains. Other resonances can be selected by tuning only one of the spectra. As a result the previously overlapping resonances misalign and a different combination of resonances overlap. This tuning mechanism is known as the Vernier effect.

## 2.3 Analysis of tunable laser concepts

With the background information provided in the preceding sections, the different concepts, in section 1.2, can be compared on performance in the most relevant areas for widely tunable laser operation:

A. optical output power
B. single mode operation
C. variation of power and SMSR over the tuning range
D. tuning complexity and stability
E. wavelength tuning time
F. device size
G. technological complexity

An analysis of these features for the key types of widely tunable lasers is given below. These types are Extended Cavity Lasers (ECL), Vertical Cavity Surface-Emitting Lasers (VCSEL), Array concepts (which combine several low tuning range lasers, either through passive or active coupling) and monolithically integrated single cavity concepts.

### A. Optical output power

**ECL** The amount of feedback from the extended cavity is determined by the coupling efficiency of the optical mode in the chip to a collimated beam. Since this collimated beam is projected back into the original mode the coupling loss is low, when alignment is well controlled.

For an ECL based on a free space grating, only the power incident on the mirror remains within the cavity. By design, near-unity reflection values are achievable ([83], chapter 9). The reflectivity of the small mirror limits the amount of light reflected back into the gain section.

For the ECL-concept based on tunable etalons, optical intensity is lost at each pass through an etalon, on account of the required tilted configuration. Careful alignment of the etalons is needed to both reduce this loss term and avoid reflection back into the laser chip.

With an optimized front-facet reflectivity ex-fiber output powers higher than 13 dBm over the complete tuning range have been demonstrated for both types of ECL's [15] [35].

**VCSEL** Feedback from the non-wavelength selective mirrors is high (typically higher than 90%). However, the short gain section and the required small aperture, for single mode operation, make the mirror loss comparable to the gain. Furthermore to prevent device heating, the injection current needs to be low.

Tunable VCSEL at 1550 nm have been demonstrated with output power higher than 0.5 mW [60] over a limited tuning range. To achieve significantly higher output power external amplification is required (either by a Semiconductor Optical Amplifier or a Erbium Doped Fiber Amplifier). Alternatively, to overcome the thermal limitations of current injection, optical pumping is used. Fiber-coupled output power of 10 mW over a 65 nm wavelength range, and 20 mW over a 27 nm wavelength range have been demonstrated with this approach [61].

**Array concepts** The output power for the separate lasers depends on their respective tuning mechanism. Given the low tuning range for each device, optimization of feedback is easier and 20 mW operation has been demonstrated for each of the used narrowly tunable devices [96] [37]. The passive combining of the signals of the separate devices into one output leads to optical loss. Hence, optical amplification (either integrated or hybrid) is required to reach 20 mW of output power. For laser-arrays where each laser is directly coupled to the output waveguide, by controlling the tilt of a mirror (active coupling), this loss term is prevented. The laser with lowest output power determines the output power of the widely tunable laser.

Both for actively and passively coupled tunable laser arrays output power higher than 20 mW over more than 35 nm has been demonstrated [81] [86].

**Integrated concepts** Efficient coupling between gain and tuning sections can easily be achieved in integrated lasers. Loss is typically a few percent. Based on the limited chip length (1-1.5 mm) and the available reflector types, the optimized feedback from a tuning section is typically calculated around 50% (e.g. [115] or [88]). The inherent free carrier absorption with current injection, however reduces the reflectivity over the tuning range.

So far the widely tunable laser concepts based on monolithic integration have had difficulty showing fiber coupled output powers of 20 mW over the full

tuning range. Loss, due to limited fabrication control or due to design trade-off, and variation over the tuning range, have yielded lasers with ex-facet output power of 25 mW over 25 nm, [44] and 5 mW over 40 nm, [38], for a GCSR and SG-DBR chip respectively. Higher output power can be achieved by integrating an SOA in the optical path. SG-DBR operation with 20 mW fiber-coupled power has been demonstrated with this concept [67]. Recently, the sampled grating Y-branch laser has demonstrated 20 mW ex-facet power over a 40 nm tuning range[116].

Inherently, a concept with a tuning section between front-facet and gain section (such as the SG-DBR) generates less output power than the concepts with the gain section directly at the front-facet (such as GCSR and sampled grating Y-branch laser). With no injection current the difference between these two variant is marginal, since front facet tuning section absorption is low and similar values of front-facet reflection can be realized. However, with current injection in the tuning section at the front-facet, the reflectivity is reduced (increasing the threshold current) as well as the tuning section transmission (reducing the output power). Therefore the maximum output power over the tuning range that can be generated with a tuning section between gain section and front-facet is low.

### B. Single mode operation

**ECL** The hybrid wavelength selective elements typically require the cavity to be several mm long. This results in a cavity-mode-spacing between 0.1 and 0.2 nm (cavity lengths of 6 - 12 mm). The separate selection element typically provides sufficient selectivity to select a single cavity mode. SMSR better than 40 dB is demonstrated over the full tuning range [15].

**VCSEL** Thanks to the short gain section length the mode spacing is typically wider than the gainpeak width. Since only one mode is present within this range, single mode selectivity is excellent. However, care has to be taken that a higher-order transversal mode does not start lasing under the influence of spatial hole burning or a too large aperture size. SMSR better than 40 dB is reported [62] [100] [71].

**Array concepts** Cavity mode spacing is given by the separate lasers and is typically in the range 0.3-0.5 nm. Since the separate lasers are optimized and based on well-known principles, SMSR better than 40 dB can typically be achieved (both with DFB and DBR type lasers).

**Integrated concepts** Since the chip is of limited length, the cavity mode spacing is in the range 0.3-0.5 nm. However, the limited size of the selection element makes optimization of the feedback selectivity a design trade-off with reflectivity. The selectivity of an ECL or a DFB laser is not matched. Routinely, SMSR better than 35 dB is achieved [15] [44]. For the sampled grating Y-branch laser recently 40 dB SMSR was achieved over the full 40 nm tuning range, at a 20 mW ex-facet output power [116].

### C. Variation of power and SMSR over the tuning range

**ECL** Thanks to the mechanical tuning scheme, without a wavelength dependent absorption and injection current induced absorption, the variation of the feedback over the tuning range is small. Therefore, the variation over the tuning range is mainly determined by the dependence of optical gain on wavelength.

**VCSEL** The mirror reflectivity in a VCSEL is typically wavelength independent. Combined with a short gain section, resulting in small gain variation, the device is expected to be wavelength independent over a wide tuning range. However the topside reflecting mirror is displaced during tuning and as a result the reflection back into the gain section is changed. Optical power variation over the tuning range of about 8 dB is reported [100].

**Array concepts** Since each separate laser performs differently the variation over the tuning range is given by the laser-to-laser variation and the inherent variation of the used tuning concept over the small tuning range. Since these lasers require significant temperature tuning the variation over the tuning range can be significant. Power-variation over a 16-DFB-array is reported as low as 0.5 dB, at a fixed temperature [81].

**Integrated concepts** Since free carrier absorption is an inherent part of the operation of integrated concepts the tuning section reflectivity can reduce significantly. Values up to 3 dB change in output power have been reported [38]. For devices with a front facet tuning section the variation is higher, since the impact of free carrier absorption is present at both facets. For the sampled grating Y-branch laser a value as low as 1.2 dB variation has been reported [116]. In a similar argument as for the output power, the variation over the tuning range in output power is expected to be larger for integrated concepts with a tuning section between front-facet and gain section.

**D. Tuning complexity and stability**

**ECL** The dependence of wavelength on the position of the mirror (for the device based on a free space grating) [72] or on the length of the etalons is well understood and straightforward. However, for the device based on the free space grating the control over the exact position and angle of the reflecting mirror is complex, demonstrated by the use of multiple actuators to control the position of the mirror. An active control-loop is used to stabilize the coupling efficiency. This might be considered an advantage since it can be used to compensate for shocks and vibration.

Device operation is highly simplified by the independent setting of wavelength (through the external cavity) and the output power (through the gain section current).

**VCSEL** Wavelength selection is through the movement of a mirror and is continuous. This device allows for straightforward control over device wavelength and a separate control for output power.

**Array concepts** Coarse wavelength selection is digital in nature, since one laser out of the array is activated. The complexity of the widely tunable laser is based on the complexity of the narrowly tunable laser. Typically, this

is relatively straightforward (either thermal tuning or through two separate tuning currents). For the actively coupled device the control over the mirror position is achieved by 4 actively controlled signals [108], complicating the control scheme considerably. As for ECL's, the use of an active feedback loop, to control the coupling to the output fiber, can be an advantage in compensating for shocks and vibration.

**Integrated concepts** The control over the wavelength and power of these devices is highly interdependent, due to the thermal and phase interaction between sections. Furthermore the tuning scheme either uses a course filter to select a resonance or uses Vernier tuning. Both control schemes require control over two tuning-elements and at least an additional phase control. Most devices need a wavelength locker to stabilize the wavelength.

**E. Wavelength tuning time**

**ECL** The tuning is either mechanical or thermal, resulting in tuning time in the ms range [15].

**VCSEL** The mechanical tuning, over short distance, results in tuning time in the order of 200 $\mu s$ or more [71].

**Array concepts** Coarse tuning of these devices entails the on/off switching of two devices and tuning to the correct wavelength. The tuning time is therefore limited to $\mu s$, with a ms time frame if temperature tuning is required.

**Integrated concepts** The tuning time of integrated concepts is in the order of ns, if based on carrier-density tuning (for most concepts) [106] [120]. Temperature tuning reduces the tuning time to the ms range, but is in these devices typically not used (for this very reason).

**F. Device size**

**ECL** The size of a gain section with an extended cavity is in the order of several tens of $mm^2$, due to the required coupling optics and for one concept the required angular selectivity of a reflecting mirror. For the concept based on etalons the size is determined by the dimensions of the etalons (typically several mm length per etalon to achieve a narrow cavity-mode-spacing).

**VCSEL** The size of the VCSEL itself is small (order of 0.05 $mm^2$), but since external amplification is required to generate sufficient output power the complete assembly is large (estimated at several $cm^2$).

**Array concepts** The size of the array is larger than separate tunable lasers, due to the size of the coupler and/or amplifier and the number of devices per chip. An estimate for chip size is 1500 x 500 $\mu m^2$ for passively coupled devices (which includes the devices, the coupling optics and the optical amplifier). For the actively coupled devices the size can be smaller (approx. 500 x 500 $\mu m^2$), but an external active coupling device is needed, which increases total size (order of 10s of $mm^2$).

**Integrated concepts** The size of these chips is typically small, of the order of 400 x 1500 $\mu m^2$.

**G. Technological complexity**

**ECL** The technology for chip fabrication is a relatively simple and high yielding process. The fabrication of the reflecting mirror with MEMS actuators is more novel, but builds upon experience with silicon technology. The real challenge of these concepts is in the low cost/high reliability assembly.

**VCSEL** The fabrication of VCSEL's at 1550 nm is difficult because of limited refractive index contrast in the material system that can generate optical gain at this wavelength. High reflectivity requires thick mirror stacks and the device is therefore difficult to fabricate. Alternatively, a mirror stack fabricated in a material with higher refractive index contrast, can be wafer-fused to the gain-material. The requirement of a moving mirror increases the complexity. Fiber coupling is however more straightforward for a VCSEL, if no other chips (optical amplifiers) are needed in the optical path (i.e. when the device is used for a low power application).

**Array concepts** The advantage of this concept is the use of well-established narrow-tuning concepts. The technological complication is in process control to ensure operation of each laser in an array. In the case of active coupling the accent is on process control as well as on optimization of the packaging scheme.

**Integrated concepts** The difficulty with these concepts is process control, since integration requires different layer-stacks and a large number of processing steps on a wafer. Packaging is similar to other lasers and therefore relatively straightforward.

The above analysis is condensed into table 2.1, with a plus, zero or minus sign to indicate the performance of each type of laser on a particular parameter. A generalized conclusion is that ECL type lasers are superior in performance to the other concepts. The cost in packaging and the associated concerns for stability and shock resistance, however, do not make this necessarily the best choice for network applications.

Whereas the low-power VCSEL can prove to be a short-range low-cost alternative for specific applications, the other concepts provide a direct alternative to the ECL in the metro and long-haul market. The main interest in these devices is the potential for low-cost manufacturing and a small package footprint. A concept that provides the lower cost and smaller footprint, at a sufficient performance level, is preferable to ECL-type widely tunable lasers. Furthermore specific applications require properties that are not achievable with an ECL, such as a short wavelength tuning time.

Array concepts don't have the promise of low cost, due to their complex processing scheme and/or their additional required components (either an integrated amplifier or an external MEMS mirror). Also, they do not possess the ability to reduce tuning complexity, since a large number of contacts are required to control the current injection in these arrays. Therefore, overall they are inferior to a good integrated concept.

In this section it was shown that for integrated widely tunable lasers the presence of a tuning section at the front-facet limits the available optical power from the device and increases the variation of power and SMSR over the tuning range, while not providing a clear performance advantage.

For these reasons it is worthwhile studying alternative integrated concepts that have the potential to provide the required performance level. In the chapters 4 and 5 alternative and improved concepts for integrated tunable lasers, without a tuning section at the front-facet, are analyzed and demonstrated.

| Type | Concept | Output power | Single-mode operation | Low variation over tuning-range | Low complexity/High stability | Fast tuning speed | Small device size | Simplicity of technology |
|---|---|---|---|---|---|---|---|---|
| ECL | | + | + | + | + | - | - | 0 |
| VCSEL | Electrical injection | - | + | - | + | 0 | - | - |
| | Optical injection | 0 | + | - | + | 0 | - | - |
| Array | DFB-array with MEMS active mirror | + | + | 0 | + | - | - | - |
| | DFB-array with MMI coupler | + | + | 0 | + | - | + | + |
| | DBR-array with MMI coupler | 0 | 0 | 0 | 0 | - | + | + |
| Integrated | SG-DBR | - | 0 | - | 0 | + | + | + |
| | GCSR | + | 0 | - | 0 | + | + | + |
| | Binary supermode DBR | 0 | 0 | 0 | 0 | + | + | + |
| | Modulated Grating Y-branch laser | + | 0 | 0 | 0 | + | + | + |

*Table 2.1: Comparison of tunable laser categories for most relevant areas of operation. A + sign indicates that the laser-type provides an advantage, in comparison to the other concepts, for the listed performance parameter. A - sign indicates a disadvantage and 0 means that this parameter is neither a positive or negative differentiator.*

# Chapter 3

# Simulation tools

Integrated photonic components often present a level of complexity that is not easily described by analytical formulas. Design optimization and explanation of experimental data require tools that are capable of capturing this complexity.

In this chapter the simulation tools, used in this thesis, are described. Modeling of material in the InP-InGaAs system is treated in section 3.1. In section 3.2 the commercial software that was used for optical simulations is introduced. In sections 3.3 a custom tool for electrical simulations is described and finally, in section 3.4, a tool for device simulation of tunable lasers is presented.

## 3.1 Material model

At the basis of a reliable simulation is a good description of the structure that is being simulated. Therefore, the description of optical and electrical properties of material in the InP-InGaAs system is crucial for this thesis. In this section, first the refractive index and absorption of material with no carrier injection is described. Later, the dependence of these parameters on carrier-density is added.

### 3.1.1 Intrinsic material properties

Material in the InP-InGaAs system is denoted as $In_{1-x}Ga_xAs_yP_{1-y}$, where the subscripts $x$ and $y$ are the atom ratio of Gallium (Ga) and Arsenide (As), compared to Indium (In) and Phosphide (P), respectively. Lattice matched quaternary material, which is used here solely, is alternatively notated by its bandgap wavelength (e.g. Q1.30 for quaternary material with a bandgap wavelength of 1.30 $\mu m$). For lattice matched material, the Ga and As content are related as $x(y) = \frac{0.4541}{1-0.029y}$ [57] and material parameters can be expressed as a function of only the As-fraction ($y$).

Tunable laser devices, discussed here, are mounted on a temperature controlled platform. Hence, the chip temperature is independent of the ambient temperature. However, energy dissipation in the chip, in combination with a finite thermal conductance to the

platform, makes the temperature of the, epi-up mounted, device dependent on the applied currents. Where available, the temperature dependence of material parameters is included in the model.

**Refractive index**

Both empirical and theoretical models are available to describe the refractive index of quaternary materials [109] [59] [26]. In general, good correspondence between these models is achieved, both in trend and value. Here, the choice is made to use empirical data to describe the refractive index, because of the proven validity and to simplify the calculations. The refractive index description used here is from a model by Adachi [5], fitted to measurements in [29] and [114]. This model for refractive index is appropriate for lattice matched material, at and around room-temperature, for photon energies below the direct bandgap energy $E_g$ down to 0.5 eV.

The refractive index $\mu$ of a quaternary material, with As-fraction $y$, at the photon-energy $E$ and temperature $T$ (in Kelvin), is expressed as:

$$\begin{aligned}
\mu^2(y,E,T) &= A(y)\cdot(f(z(y,E,T)) + \frac{1}{2}\cdot(\frac{E_g(y,E,T)}{E_g(y,E,T)+\Delta_0(y)})^{\frac{3}{2}}\cdot f(z_0(y,E,T))) \\
&\quad + B(y) + \frac{1}{\epsilon_0}\cdot\frac{d\epsilon_\infty(y,T)}{dT}\cdot(T-300) \\
f(z) &= \frac{2-\sqrt{1+z}-\sqrt{1+z}}{z^2} \\
z(y,E,T) &= \frac{E}{E_g(y,T)} \\
z_0(y,E,T) &= \frac{E}{E_g(y,T)+\Delta_0} \\
A(y) &= 8.616 - 3.886\cdot y \\
B(y) &= 6.621 + 3.461\cdot y
\end{aligned} \tag{3.1}$$

In this formula $E_g$ is the direct bandgap energy and $\Delta_0$ is the split-off valence band energy (the lowest energy level for holes in the valence band, beyond the light and heavy hole energy band). $\epsilon_0$ and $\epsilon_\infty$ are the permittivity of free space and the high-frequency permittivity, respectively.

The temperature and composition dependence of the bandgap energy is expressed as [57][7][5]:

$$\begin{aligned}
E_g(y,T) &= E_g(y,300K) + \frac{dE_g}{dT}\cdot(T-300) \\
&= (1.35 - 0.72\cdot y + 0.12\cdot y^2) - (3.18 - 0.41\cdot y + 0.61\cdot y^2)\cdot 10^{-4}\cdot(T-300)
\end{aligned} \tag{3.2}$$

For the remaining parameters in formula 3.1 the following expressions are used [84][5]:

$$\begin{aligned} \Delta_0 &= 0.118 + 0.225 \cdot y \\ \frac{\epsilon_\infty(y,T)}{\epsilon_o} &= 9.55 + 2.2 \cdot y + 5.16 \cdot 10^{-4} \cdot (T - 300) \end{aligned} \tag{3.3}$$

**Material absorption**

For the material absorption around the bandgap energy consistent descriptions are not abundantly available. A model for the absorption at photon energies above the bandgap energy is given in [20]. For the description of the absorption below the bandgap energy an empirical formula is available from [18].

The formulation for the Urbach tail ($\alpha(y,E,T)$ for $E < E_g + \Delta E_g$, with $\Delta E_g$ the bandgap shrinkage, due to carrier injection and $E$ the photon-energy) is derived from measurements on InP substrates [18]. It is assumed that the value of the slope (given by $E_0$) is equally valid for quaternary materials. Since the detuning of the operating wavelength from the tuning material bandgap is less than 100 meV, the Urbach tail dominates the below bandgap absorption and no correction for impurity absorption is required [18].

$$\begin{aligned} \alpha(y,E,T) &= \frac{C_{hh}(y)}{E} \cdot \sqrt{E - E_g(y,T) - \Delta E_g} \cdot (f_v(E_{vh}) - f_c(E_{ch})) \\ &\quad + \frac{C_{lh}(y)}{E} \cdot \sqrt{E - E_g(y,T) - \Delta E_g} \cdot (f_v(E_{vl}) - f_c(E_{cl})) \\ &\quad for \quad E > E_g + \Delta E_g \\ &= C(y) \cdot e^{\frac{E - E_g(y,T)}{E_0}} \\ &\quad for \quad E < E_g + \Delta E_g \\ With & \\ C(y) &= (1.004 - 1.318 \cdot y + 0.517 \cdot y^2) \cdot 10^5 \\ C_{hh,lh}(y) &= C(y) \cdot \frac{\mu_{hh,lh}^{\frac{3}{2}}}{\mu_{hh}^{\frac{3}{2}} + \mu_{lh}^{\frac{3}{2}}} \\ \mu_{hh,lh} &= (\frac{1}{m_e} + \frac{1}{m_{hh,lh}})^{-1} \\ E_{ch,cl} &= (E - E_g - \Delta E_g)(\frac{m_{hh,lh}}{m_{hh,lh} + m_e}) \\ E_{vh,vl} &= (E + E_g - \Delta E_g)(\frac{m_e}{m_{hh,lh} + m_e}) \\ f_{c,v}(E) &= (1 + e^{\frac{E - F_{c,v}}{k_B \cdot T}})^{-1} \\ E_0 &= 7.1 \ meV \end{aligned} \tag{3.4}$$

In this formula $C$, $C_{hh}$ and $C_{lh}$ are empirical absorption constants [114]. $f_c$ and $f_v$ are Fermi-factors and $F_c$ and $F_v$ are the quasi-Fermi energy levels. The subscripts v

and c denote the valence and conduction band, respectively. The factors $E_{ch,cl,vh,vl}$ are the energies associated with the interband transitions. The subscripts denote that the energies are relative to a zero at the conduction (c) or valence (v) band edge and that the transition is to a light (l) or heavy (h) hole state. $\mu_{hh,lh}$ is the joint density of states effective mass for light (lh) and heavy holes (hh). $E_0$ is the bandgap tail energy and $k_B$ is the Boltzman constant.

This description is not continuous around the bandgap energy. However, the interest here is for photon-energies at least 25 meV below the bandgap energy of the tuning layer. The expression for energies above the bandgap energy is only used in the Kramers-Krönig formula (where the change in below bandgap absorption is neglected), for calculating the dependence of the refractive index on carrier-density. Therefore, the discontinuity at the bandgap energy is of no concern for the simulations in this thesis.

The electron and hole mass for the quaternary system is given by [7][57][29] (with $m_0$ the free electron mass, and the subscripts denoting electron (e), light (lh) and heavy (hh) hole):

$$\begin{aligned} m_e &= (0.08 - 0.039 \cdot y) \cdot m_0 \\ m_{hh} &= (0.12 - 0.092 \cdot y + 0.024 \cdot y^2) \cdot m_0 \\ m_{lh} &= (0.12 - 0.092 \cdot y + 0.024 \cdot y^2) \cdot m_0 \end{aligned} \tag{3.5}$$

### 3.1.2 Impact of carrier-density

A layer, surrounded by material of higher bandgap energy, provides electrical confinement of carriers. Injection of carriers in that layer results in an increased carrier-density. This is the case for both the tuning layer in the tuning section and the quantum wells in the gain section. For this thesis it is assumed that these layers are not intentionally doped (i.e. $n = p$ with n and p the carrier-density for electrons and holes, respectively).

The material's refractive index and absorption are correlated through the Kramers-Krönig relationship [3] (formula 2.10). A change in material absorption affects the refractive index.

Three electro-optical effects cause a change in optical properties with carrier-density. These are free-carrier absorption, bandfilling and bandgap shrinkage. The free carrier absorption is described independently, but the latter two effects are linked. The description given here largely follows the work in [114].

#### Carrier-density

The carrier-density in a layer can be calculated by solving the steady-state rate-equation (formula 2.1):

$$\frac{dn}{dt} = 0 = \frac{I}{e \cdot V_a} + \frac{dn_{photon}}{dt} - \frac{I_{leakage}}{e \cdot V_a} - R(n) \tag{3.6}$$

This equation states that the steady-state carrier-density is a function of electrically injected carriers $\frac{I}{e}$, optical injected carriers $\frac{dn_{photon}}{dt}$, carrier escape $\frac{I_{leakage}}{e \cdot V_a}$ from the layer and the spontaneous decay processes $R(n)$ (defined in equation 2.2). $V_a$ is the volume

of the layer. For the calculation of $R(n)$, the following parameters are used [114]:

$$\begin{aligned} \tau &= 5 \cdot 10^{-9} \ s^{-1} \\ B &= 1 \cdot 10^{-16} \ \frac{m^3}{s} \\ C &= 7.5 \cdot 10^{-41} \ \frac{m^6}{s} \end{aligned} \tag{3.7}$$

The leakage of carriers out of the confined layer is set to zero, as it usually is only significant at high carrier-density.

**Free-carrier effect**

A carrier in the conduction band can be excited to a higher energy-level within this band by the absorption of a photon. The more carriers there are available in the conduction band, the stronger this absorption mechanism is. Given that the bandgap discontinuity in a layerstack is mostly lower than the photon energy, the excited carrier is free to escape the electrical confinement of the high bandgap material around the layer. The free carrier absorption, for photons at energy E, is expressed by [114] [20] [27]

$$\Delta\alpha_{fc}(E) = 3.1 \cdot 10^{-22} \cdot n + 4.252 \cdot 10^{-20} \cdot e^{-3.657 \cdot E \cdot p} \tag{3.8}$$

Through the Kramers-Krönig relationship the change in refractive index is calculated [105]:

$$\begin{aligned} \Delta\mu(E) &= -\frac{\hbar^2 \cdot e^2 \cdot n}{2 \cdot \epsilon_0 \cdot \mu_r \cdot m_e \cdot E^2} - \frac{\hbar c}{\pi e} \cdot \frac{\alpha_0}{2E} \cdot (e^{-b \cdot E} \cdot E_i(b \cdot E) + e^{b \cdot E} \cdot E_1(b \cdot E)) \cdot p \\ \alpha_0 &= 4.252 \cdot 10^{-20} \ m^2 \\ b &= 3.657 \ eV^{-1} \\ E_i(z) &= \gamma + ln(z) + \sum_{n=1}^{\infty} \frac{z^n}{n!n} \\ E_1(z) &= -\gamma - ln(z) - \sum_{n=1}^{\infty} \frac{(-1)^n \cdot z^n}{n!n} \\ \gamma &= 0.577215664 \qquad (Euler \ \ constant) \end{aligned} \tag{3.9}$$

In these formulas $E_i(z)$ and $E_1(z)$ are the Euler functions. $E$ is again the photon-energy at which the free-carrier absorption is evaluated.

**Bandfilling and bandgap shrinkage**

Carriers in the conduction band occupy states that were available for photon absorption. Additionally, at sufficient density these carriers repel one another, due to the Pauli exclusion principle and overlap in their wave-functions [20]. The induced screening potential, that lowers a carrier's energy, reduces the material's bandgap energy. Both these processes act simultaneously and are treated here as such.

The bandgap energy shrinkage due to the screening potential, is expressed as [117]:

$$\begin{aligned} \Delta E_g(n) &= -\frac{0.13}{\epsilon_s} \cdot (\frac{n}{n_{cr}} - 1)^{\frac{1}{3}} \qquad for \qquad n > n_{cr} \\ n_{cr} &= 1.6 \cdot 10^{30} \cdot (\frac{m_c}{1.4 \cdot \epsilon_s \cdot m_0})^3 \\ \epsilon_s &= (12.4 + 1.5 \cdot y) \cdot \epsilon_0 \end{aligned} \tag{3.10}$$

With $n_{cr}$ the critical carrier-density for bandgap shrinkage and $\epsilon_s$ the static dielectric function.

In formula 3.4 the term for bandgap shrinkage ($\Delta E_g$) was included.

The effect of bandfilling is calculated by solving the Fermi level energy and inserting this in formula 3.4:

$$\begin{aligned} F_c &= k_B T(ln(\frac{n}{N_c}) + \frac{n}{N_c} \cdot (64 + 0.05524 \cdot \frac{n}{N_c} \cdot (64 + \sqrt{\frac{n}{N_c}}))^{-\frac{1}{4}}) \\ F_v &= -k_B T(ln(\frac{p}{N_v}) + \frac{p}{N_v} \cdot (64 + 0.05524 \cdot \frac{p}{N_v} \cdot (64 + \sqrt{\frac{p}{N_v}}))^{-\frac{1}{4}} + E_g) \\ N_c &= 2 \cdot (\frac{m_c \cdot k_B T}{2 \cdot \pi \cdot \hbar^2})^{\frac{3}{2}} \\ N_v &= 2 \cdot (m_{lh}^{\frac{3}{2}} + m_{hh}^{\frac{3}{2}})(\frac{k_B T}{2 \cdot \pi \cdot \hbar^2})^{\frac{3}{2}} \end{aligned} \tag{3.11}$$

Here $N_c$ and $N_v$ are the effective density of states in the conduction and valence band, respectively. $F_c$ and $F_v$ are the carrier dependent quasi-Fermi levels, given by the Nilsson approximation [79]. Remember that the tuning layer is assumed non-doped (i.e. $n = p$).

The change in refractive index for a given value of carrier-density is calculated through the material absorption at zero carrier-density and at a given carrier-density. The Kramers-Krönig integration is then performed. Since the evaluation wavelength is always below the material bandgap, this function can be evaluated without discontinuity. However, no analytical formula is available, which makes numerical evaluation necessary.

In the evaluation of the Kramers-Krönig relationship, with respect to bandgap filling and bandgap shrinkage, absorption changes at energies below the bandgap energy are neglected. The magnitude of the change below the bandgap is small, since absorption drops exponentially towards lower energy, and negligible compared to the change in free-carrier absorption.

### Material gain

Finally, gain in the gain section material (as a function of carrier-density) is expressed

as [34] [36].

$$
\begin{aligned}
g(\lambda) &= g_{max} \cdot (1 - (\lambda - \lambda_{max})^2) \\
g_{max}(n) &= (n - n_{tr}) \cdot \frac{dg}{dn} \\
\frac{dg}{dn} &= 2.7 \cdot 10^{-20} \ m^2 \\
\alpha_i &= 12.5 \ cm^{-1} \qquad (3.12) \\
n_{tr} &= 1.4 \cdot 10^{18} \ cm^{-3} \qquad (3.13)
\end{aligned}
$$

Here the transparency carrier-density is given as $n_{tr}$. The value for $\frac{dg}{dn}$ is valid for low carrier-density. The value decreases with

This is a simplification, since spectral and spatial hole burning effects are not taken into account. Also, non-linearity in the gain versus carrier-density curve is neglected. At higher values of carrier-density this results in significant errors. Non-linear effects in the gain section, as well as the shift in wavelength $\lambda_{max}$ with carrier-density, are neglected.

**Impact of optical power**

Different optical absorption processes impact the carrier-density in a specific manner. Interband absorption excites carriers from valence band into the conduction band. Intraband absorption, such as free carrier absorption, excites an electron out of the tuning layer's electrical confinement. Finally, the optical gain in a section allows carriers to recombine, from conduction band to valence band, while emitting a photon. The combined impact of these three processes is expressed as:

$$\frac{dn_{photon}}{dt} = \frac{dn_{interband}}{dt} - \frac{dn_{intraband}}{dt} - \frac{dn_{gain}}{dt} \qquad (3.14)$$

The interaction between the optical field and the carrier-density enables instability and/or hysteresis for tunable lasers. Steady-state device operation becomes possible at multiple optical power levels. Hysteresis results from stable set-points, which can be accessed through different switching trajectories, e.g. with increasing current a switching point occurs at a different current setting than for decreasing the same current. Device instability arises when, for a given device setting, two or more operating power levels are possible, with low selectivity between them. A device can be switched between these multiple equilibrium positions by a small change (i.e. noise), resulting in oscillating behaviour.

## 3.2 Optical modeling

Optical simulation tools are used to calculate the profile of the optical mode in the cross-section of a device and the propagation of this optical mode through a device structure.

### 3.2.1 Optical mode-solver

Light propagates through guided structures in optical modes. In this thesis, the properties of such modes are calculated by the commercial package FIMMWAVE by 'Photon Design'. It makes uses of the Film Mode Matching (FMM) technique [97] [98]. This technique is more versatile than the Effective Index Method [69] and, for structures with a limited number of layers, it is faster than Finite Element Methods [87].

The calculation is performed in the plane of the mode, perpendicular to the direction of propagation. In this plane, the device cross-section is divided into vertical layerstacks. For each of these stacks a number of 1D-eigenmodes (also known as slab modes) are found, and at each interface between the stacks the overlap between these slab modes is calculated. Matching the slab modes at each interface forms 2D optical modes, such that the Maxwell-equations [53] are fulfilled over the complete calculation window. A trial value of the field amplitude is chosen at the boundary of the structure. This field is propagated to the opposite boundary by solving the Maxwell equations. From the opposite boundary the field is propagated back to the starting boundary and compared to the initial field. This process iterates until a self-consistent solution is found[73].

The method finds a vectorial solution for the Maxwell equations. Information on both the TE and TM component of the field is obtained. For a multi-quantum well laser structure addressed here, only modes with mainly a TE-component are amplified. This is because of strain in typical quantum well lasers [10].

The FMM-method assumes a calculation window with reflecting boundaries. Hence, the power remains within the calculation window and the position of the boundaries can have an impact on the simulation result. In the simulations it is verified that the distance of the side-walls has no impact on the simulation result.

This method is an effective tool for the calculation of optical modes in a device cross-section. Important optical parameters are found such as effective modal index, optical confinement in a specific part of the layerstack and the near and far field.

### 3.2.2 Optical field propagation

The propagation of an optical field through an optical component is simulated in this thesis with two commercial packages. These packages are a Beam Propagation Method (BPM), for which Olympios by 'C2V' is used, and an eigenmode expansion algorithm, for which FIMMPROP-3D by 'Photon Design' is used. A BPM tool is mostly applicable for structures with a high number of distinct cross-sections and for structures with gradual transitions. The eigenmode expansion algorithm is suitable for components with abrupt changes in cross-section structure and for long multi-component structures.

#### Beam Propagation Method

A BPM-tool calculates the propagation of an arbitrary optical input-field through an optical component, with a defined refractive index profile. It is most useful for components with a changing cross-sectional refractive index profile and it performs best for optical fields with low divergence (paraxial approximation). For divergent fields, the

BPM-approximation introduces errors and for devices without z-dependent refractive index profile faster methods are available.

The BPM tool is based on an approximation for the Helmholtz equation [91], where the rapid phase-variation in the propagation direction z is taken out of the equation. This introduces the assumption that the wave moves primarily along the z-direction. Therefore for fields that expand into the x and y direction a phase-error is introduced upon propagation. To address this, more accurate and calculation intensive, solutions are available for the Helmholtz equation, know as Padé approximations [45].

The simulation is performed by dividing the optical component into a grid. At each grid-point the refractive index is defined. The input optical field is defined as well. Using the approximation to the Helmholtz equations, the field is propagated a distance along the length of the device to the next grid-point. At this cross-section the new field is calculated. This field is propagated further to the next grid-point, until the end of the simulation window is reached. The result of the calculation is the output-field of the optical component and the distribution of optical power in the component.

For the boundaries of the simulation window it is assumed that light can escape out of the simulation window (transparent boundaries as defined in [46]). For all BPM calculations presented in this thesis a 2D method is used.

#### Eigenmode expansion algorithm

The limitations of the BPM method in handling large angles requires an alternative method for calculating non-paraxial waves.

The eigenmode expansion algorithm is based on the modes found through a modesolver (section 3.2.1) and their propagation through an optical component. The structure is divided into regions with the same cross-section. For each cross-section the optical modes are calculated and at each interface the overlap between all the modes is determined. By multiplying these overlap-factors appropriately and by including the phase effect of each region, a transfer-function between any mode at the input to any mode at the output is calculated. After decomposing the input field into the cross-section eigenmodes, for each mode the appropriate output modes are found and the output field is constructed by adding these modes.

Since this method is based on propagation of modes, the method becomes calculation-intensive for structures with a large number of modes (both transversal and lateral). Also, structures with a large number of distinctive cross-sections, such as tapers, are more appropriately modeled with a BPM (Beam Propagation Method) . Lastly the exact calculation of the propagation of an optical field through a non-guided structure is not possible with this method.

The package, used here, makes use of the eigenmodes found in the mode-solver FIMMWAVE. Since this mode-solver assumes reflecting boundaries, power radiated from the optical component can be reflected back into the waveguide.

## 3.3 Electrical modeling

The core of one of the tunable laser concept described in this thesis is a tunable MMI

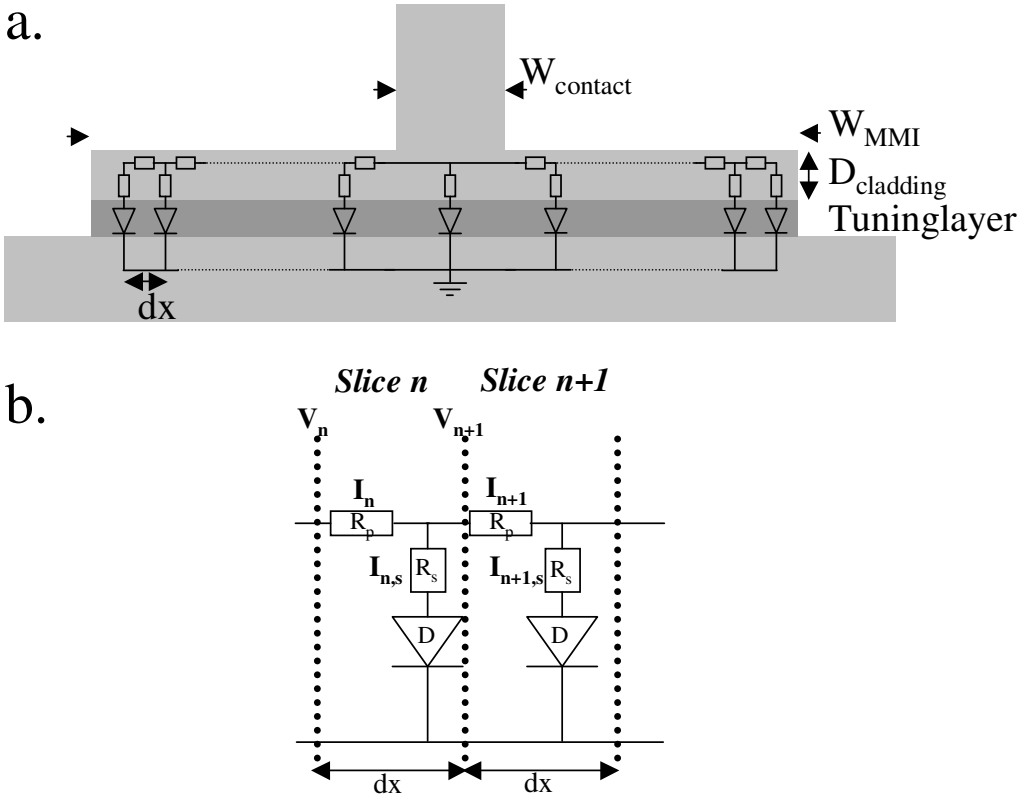


*Figure 3.1: Cross-section of a tunable MMI layerstack; a) The layerstack consists of an InP substrate with a quaternary tuning layer and an InP cladding and contact layer. The MMI is etched into the tuning layer and a contact is defined in the contact layer. The resistive diode model, used for current-spreading simulations, is super-imposed on the layerstack. Current is injected through the contact layer and spreads through the underlying layers that are described by resistors and pin junctions. For simulation purposes the cross-section is subdivided into slices of width dx; b) Definition of the components, voltages and currents in each slice.*

(Multi-Mode Interference) coupler. Operation of this component requires localized injection of carriers into a wide waveguiding region. In this section, the model is introduced to calculate current spreading in such a structure.

### 3.3.1 Resistive Diode model

In figure 3.1a the cross-section of a tunable MMI is shown. From bottom to top, the vertical structure consists of an InP substrate, a quaternary tuning layer, a $D_{cladding}$ thick InP cladding layer and an InP toplayer. A pin-junction is formed by the intrinsically doped tuning layer between an n-doped substrate and p-doped cladding layer. Horizontally, a wide waveguiding structure with width $W_{MMI}$ is defined in the tuning and cladding layer. A narrow current injection contact of $W_{contact}$ is defined in the toplayer.

To simulate current distribution in this cross-section, a distributed resistor-diode model, super-imposed on the figure, is used. This 2D-model assumes homogeneous current-injection through the toplayer, current distribution through an Ohmic cladding layer and a diode-type behaviour in the pin-junction.

The region outside of the contact area is horizontally divided into N slices of thickness dx (the numbering convention places slice N at the outer edge of the MMI). Each slab is described by a parallel resistor $R_p$, a series resistor $R_s$ and a diode D. Voltages and current are defined as in the inset in figure 3.1b.

$$\begin{aligned} V_N &= I_{N,s} \cdot R_s + V_D(I_{N,s}) \\ I_n &= I_{n+1} + I_{n,s} \\ V_n &= V_{n+1} + I_n \cdot R_p \\ R_s &= \frac{\rho \cdot D_{cladding}}{dx} \\ R_p &= \frac{\rho \cdot dx}{D_{cladding}} \\ V_D(I) &= \frac{kT}{n} ln(\frac{I/dx}{J_{sat}}) \\ \rho &= 0.02\ \Omega cm \\ J_{sat} &= 0.02\ \frac{A}{m^2} \\ n &= 1.5 \end{aligned} \tag{3.15}$$

The first equation describes the boundary condition at the edge of the MMI, while the other equations allow for the further calculation from this boundary condition.

The value for the resistors is based on the conductivity $\rho$ of InP at a doping level of $6 \cdot 10^{23}\ m^{-3}$ [76]. The pin-junction is modeled as a diode with $J_D(V) = J_{sat} \cdot e^{\frac{n \cdot V}{k \cdot T}}$. The parameters used are derived from measurements on tunable DBR devices (with the same layerstack, but different manufacturing process).

### 3.3.2 Simulation procedure

For simulation purposes only half of the structure is calculated, making use of the structure symmetry.

Current distribution within this model is calculated by choosing an arbitrary current through the outer slice N. Making use of the formulas in 3.15, the voltage and current of an adjacent slice is calculated. This is repeated, until slice 1 is reached. For simplification it is assumed that the voltage under the contact is homogeneous and equal to $V_1$. From this the total current is found as: $2 \cdot I_1 + J_{sat} \cdot e^{\frac{V_1 \cdot n}{kT}} \cdot W_{contact}$. By varying the current through slice N, at the edge of the MMI, the full current-voltage characteristic is calculated, as well as the currents in every slice of the device.

The model neglects electron diffusion currents in the tuning layer. Carriers injected in the tuning layer are confined vertically by the surrounding high-bandgap materials, but are free to move within the plane of the tuning layer. Along with the injection

current, this carrier-density is position dependent. Given the injection current in a slice, the carrier-density is calculated using formula 3.6. The parameters in formula 3.7 are used. For the electron diffusion constant the value 120 $\frac{cm^2}{s}$ is used [93].

After a device simulation, the electron diffusion current is calculated from the carrier-density along the width of the MMI. The calculated diffusion current is compared to the injection current. For all calculations presented in this thesis the fraction of diffusion current into or out of a slab of $dx$ width is negligible (less than 0.5%), compared to the total current injected into that slab. Note that the diffusion current is over-estimated in this way, since holes are less mobile than electrons by a factor 30 [93] and they create a screening potential for electron diffusion.

## 3.4 Device modeling

First demonstration of a new tunable laser concept is most practically preceded by device simulation. The effort in design of a process, the processing itself and the testing of crucial parameters can initially be avoided. Furthermore, the level of control over device and process parameters does not influence results. A transfer matrix tool has been developed that is used for demonstration of concept feasibility and for investigation of design dependencies.

In the basic simulation procedure the device structure is defined and the round-trip loss and phase for the optical field within the laser-cavity is calculated over a wavelength range wider than the device tuning range (assuming zero gain in the gain section). From this spectrum the cavity mode for which the lasing condition is satisfied, with lowest gain in the gain section is selected. For this wavelength the gain, operating current and threshold current are calculated, through the formulas in chapter 2. After finding the cavity mode with the next-lowest round-trip loss, the SMSR is calculated.

### 3.4.1 S-matrix concept

The simulation tool presented here is based on an S-matrix description of optical components [17]. The S-matrix method relates the optical field leaving an optical component to the ingoing optical fields. In figure 3.2a the basic formulation for an S-matrix is given. $S_{21}$ is the amplitude transfer-function for the incoming field from the left side (=1) to the outgoing field at the right side (=2). It can be seen that $S_{11}$ and $S_{22}$ are reflection coefficients and $S_{12}$ and $S_{21}$ are the transmission coefficients of the optical component.

Two cascaded optical components, which both are described by a separate S-matrix, can be described by a single new S-matrix, which describes the combined response. In figure 3.2b this is illustrated and the formula for the new S-matrix is given.

### 3.4.2 S-matrix description of devices

A full device is described by dividing it in components, which all can be described by an S-matrix. By applying the formula in figure 3.2b these S-matrices can be combined into one resultant S-matrix to describe the complete device response.

**a.**

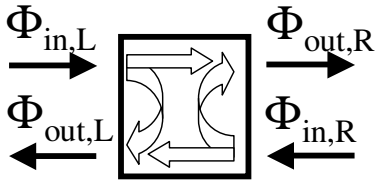


$$\begin{bmatrix} \Phi_{out,L} \\ \Phi_{out,R} \end{bmatrix} = \begin{bmatrix} S_{11} & S_{12} \\ S_{21} & S_{22} \end{bmatrix} \cdot \begin{bmatrix} \Phi_{in,L} \\ \Phi_{in,R} \end{bmatrix}$$

**b.**

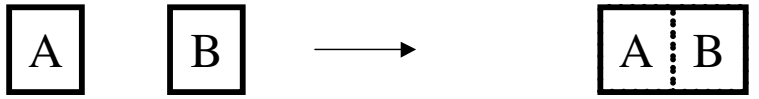


$$\begin{bmatrix} S_{11}^A & S_{12}^A \\ S_{21}^A & S_{22}^A \end{bmatrix} \begin{bmatrix} S_{11}^B & S_{12}^B \\ S_{21}^B & S_{22}^B \end{bmatrix} \longrightarrow \begin{bmatrix} S_{11}^A + \frac{S_{12}^A \cdot S_{11}^B \cdot S_{21}^A}{1 - S_{11}^B \cdot S_{22}^A} & \frac{S_{12}^A \cdot S_{12}^B}{1 - S_{11}^B \cdot S_{22}^A} \\ \frac{S_{21}^B \cdot S_{21}^A}{1 - S_{11}^B \cdot S_{22}^A} & S_{22}^B + \frac{S_{21}^B \cdot S_{22}^A \cdot S_{12}^B}{1 - S_{11}^B \cdot S_{22}^A} \end{bmatrix}$$

*Figure 3.2: S-matrix method; a) An optical component is described by the relation between ingoing fields and outgoing fields at both sides. The relation between these fields is described by an S-matrix; b) The description of two cascaded optical components, both described by an S-matrix, can be reduced to a single S-matrix, using the formula given here.*

Using this methodology, a laser cavity is described (figure 3.3) as consisting out of several cascaded components, such as coating, gain section, butt-joint interface, MMI, propagation section and grating-burst sections. To calculate the loss a photon experiences upon a round-trip within the laser cavity (the round-trip loss), the begin of the tuning section is chosen as reference point within the cavity. The S-matrices for components to the left and right of this point, $S^L$ and $S^R$, are calculated and the amplitude based roundtrip loss or gain for the optical component is found as $S_{22}^L(\lambda) \cdot S_{11}^R(\lambda)$. After calculation of the wavelength dependence of this round-trip loss and finding the cavity modes, important device parameters are calculated. These parameters include lasing wavelength, cavity mode spacing, optical gain in the gain section and gain-difference between modes.

The S-matrix description for the several optical components used in this thesis is:

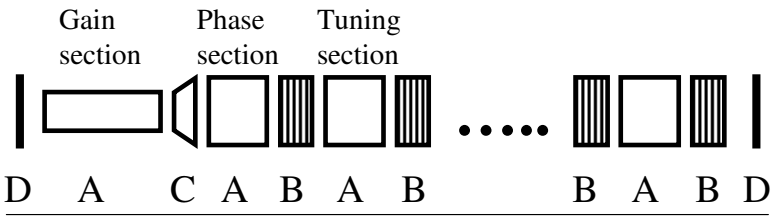


S-matrix description (see formula 3.16)

*Figure 3.3: An optical device is described as a cascade of optical components, all of which can be described by an S-matrix. One single S-matrix for the optical component is constructed from these. The letters here correspond to the S-matrices on page 66. Note that the gain section is described as a waveguide element.*

$$
\begin{aligned}
A \quad & Waveguide \quad \begin{pmatrix} 0 & e^{-i\cdot 2\pi\cdot\frac{\mu\cdot L}{\lambda}} \\ e^{-i\cdot 2\pi\cdot\frac{\mu\cdot L}{\lambda}} & 0 \end{pmatrix} \\
B \quad & Grating \quad \begin{pmatrix} S_{11} & S_{12} \\ S_{21} & S_{22} \end{pmatrix} \\
& S_{11} = \quad \frac{-i\cdot\frac{\kappa}{\gamma}\cdot sinh(\gamma L)}{cosh(\gamma L)+i\cdot\frac{\Delta\beta}{\gamma}\cdot sinh(\gamma L)}\cdot e^{i\cdot\beta_0\cdot 2\cdot x_0} \\
& S_{12} = \quad (cosh(\gamma L)-\frac{i\Delta\beta}{\gamma}\cdot sinh(\gamma L)-\frac{\frac{\kappa^2}{\gamma^2}\cdot sinh^2(\gamma L)}{cosh(\gamma L)+\frac{i\Delta\beta}{\gamma}\cdot sinh(\gamma L)})\cdot e^{-i\cdot\beta_0\cdot 2\cdot x_0} \\
& S_{21} = \quad (cosh(\gamma L)-\frac{i\Delta\beta}{\gamma}\cdot sinh(\gamma L)-\frac{\frac{\kappa^2}{\gamma^2}\cdot sinh^2(\gamma L)}{cosh(\gamma L)+\frac{i\Delta\beta}{\gamma}\cdot sinh(\gamma L)})\cdot e^{-i\cdot\beta_0\cdot 2\cdot x_0} \\
& S_{22} = \quad \frac{-i\cdot\frac{\kappa}{\gamma}\cdot sinh(\gamma L)}{cosh(\gamma L)+i\cdot\frac{\Delta\beta}{\gamma}\cdot sinh(\gamma L)}\cdot e^{-i\cdot\beta_0\cdot 2\cdot(x_0+L)} \\
C \quad & Buttjoint \quad \begin{pmatrix} \frac{\mu_L-\mu_R}{\mu_L+\mu_R} & \frac{2\cdot\mu_R}{\mu_L+\mu_R} \\ \frac{2\cdot\mu_R}{\mu_L+\mu_R} & -\frac{\mu_R-\mu_L}{\mu_L+\mu_R} \end{pmatrix} \\
D \quad & Coating \quad \begin{pmatrix} r & \sqrt{1-r^2} \\ \sqrt{1-r^2} & r \end{pmatrix} \\
E \quad & MMI \quad \begin{pmatrix} 0 & e^{i\cdot 2\pi\cdot\frac{\mu\cdot L}{\lambda}}\cdot T(\Delta\lambda) \\ e^{i\cdot 2\pi\cdot\frac{\mu\cdot L}{\lambda}}\cdot T(\Delta\lambda) & 0 \end{pmatrix}
\end{aligned}
\tag{3.16}
$$

In these formulas the symbols are as defined before. The symbols $\mu_R$ and $\mu_L$ are the effective index at both sides of the buttjoint. $r$ is the amplitude-based reflection of a coating and $T(\Delta\lambda)$ is the transmission of an MMI at a spectral distance $\Delta\lambda$ from its wavelength of maximum transmission.

The description of the buttjoint in this manner assumes an abrupt transition from one cross-section to another one. Gradual transitions can be modeled as a sequence of short waveguide sections connected by a buttjoint, with a gradual change in the effective index. Barring the formation of an interface layer that creates a short Fabry-Perot cavity at the buttjoint (preventable in a good epitaxial growth process), the given description is sufficiently accurate.

Absorption is introduced to above formulas by replacing $\mu$ by $\mu - i \cdot k$ (with $k$ the extinction coefficient $k = \alpha\frac{4\pi}{\lambda}$). The consideration of absorption in the tuning sections leads to a complication in the calculation. Associated with photon absorption is the excitation of electronic carriers. Hence the carrier-density becomes not only a function of the electrically injected currents, but also of the optically injected carriers. This latter term is proportional to the absorption in the tuning section and the optical power incident on the tuning section.

The consequence of photo-current is that the distribution of optical power and carrier-density in the tuning sections is dependent on the level of incident power. This means that, for a given value of operating current in the gain section, multiple stable state situations can be calculated, all with a different optical power and tuning section reflectivity at the laser wavelength (this is one of the causes of hysteresis).

Within the S-matrix model the absorbed optical power in component B is expressed for a tuning section by describing it as three cascaded components A, B and C. Here component A is the combination of all components of the tuning section before component B. Component C is all components of the tuning section behind component B. The light is incident onto the left component A and has to be transmitted through this component to be absorbed in component B. The transmitted light through component B can be reflected by component C to make another pass through component B, and so forth. This approach takes these multiple reflections into account. The absorbed power, in each pass through component B, is found by subtracting the power incident on component B by the power leaving component B (through reflection or transmission). In this manner the nature of the physical absorption process within the component can be ignored.

$$P^B_{absorbed} = P_{in} \cdot (S^A_{12})^2 \cdot \frac{1}{1 - (S^B_{12} \cdot S^C_{11} \cdot S^B_{21} \cdot S^A_{22})^2} \cdot ((1 - S^B_{12} - S^B_{11})^2 + (1 - S^B_{21} - S^B_{22})^2) \tag{3.17}$$

Where $S^{B,A,C}_{12,21,22}$ are the S-matrices $(S_{12}, S_{12}, S_{11})$ for all components before (A) and after (C) the studied component (B). $P_{in}$ is the power incident on component A (i.e. on the tuning section).

This method allows for calculation of the optical loss and the generated photo-current, without detailed knowledge on the actual absorption mechanism. The carrier-photon interaction, associated with absorption, was shown to impact the carrier-density in formula 3.6. Interband absorption adds carriers to the carrier-density, while intra-band absorption excites carriers out of the tuning layer, reducing the carrier-density. For calculation of the carrier-density the absorption mechanism is relevant. This is calculated as (for

the free-carrier absorption):

$$\frac{dn_{fc}}{dt} = \frac{P^B_{absorbed}}{h\nu} \cdot \frac{\alpha_{fc}}{\alpha_{total}} \tag{3.18}$$

Where $\alpha_{total}$ is the sum of all absorption mechanisms (minus the gain). The generated carriers for the other absorption mechanisms are found in a similar manner.

The impact of the absorbed power on the carrier-density is calculated by distributing the absorbed photons over the different absorption mechanisms, proportional to their absorption coefficient. Note that even material gain can be treated with this approach, by subtracting it from the total absorption.

### 3.4.3 Simplifications and limitations

The presented model provides a tool, which includes the most important parameters for device design. Inherently, this model makes simplifications:

**1** Reflectivity of all coatings is assumed constant over the tuning range. This is practically achievable for most reflection values. For very low values of reflection ($\ll 1\%$)and very high values of reflection ($> 90\%$) this approximation is not valid anymore.

**2** The contribution of spontaneous emission to the optical mode in tuning sections is not considered. This is in general a good assumption, since spontaneous emission adds 'white' noise to the optical modes. Only if this white noise intensity is significant compared to the power in the mode it can affect the gain margin and SMSR.

**3** Amplification of light in the tuning sections is neglected. This assumption is not correct at high values of current injection, where optical gain saturates the dependence of refractive index on injection current. Also, optical gain in a tuning section can support a laser cavity between front and back facet, impeding or hindering lasing at the grating wavelength.

**4** Spatial and spectral hole burning, especially relevant in the gain section, are neglected.

**5** Wavelength dependence of the gain in the gain section is neglected.

### 3.4.4 Device simulation procedure

A device simulation is performed through the following steps:

**1. Define the simulation parameters** Basic parameters, such as the wavelength range and resolution, are set.

**2. Define the material parameters** The lattice-matched material used in the device is defined by its As-composition $y$. Typically, only two materials are used, one for the gain and one for the tuning section. The parameters that have no explicit dependence on temperature (assuming 300 K operation) and carrier-density are calculated (these parameters are $A$, $B$, $E_g(300K)$, $\Delta_0$, $\epsilon_\infty$, $\epsilon_s$, $\frac{dE_g}{dT}$, $m_c$, $m_{hh}$, $m_{lh}$, $m_{so}$, $C$, $C_{hh}$, $C_{lh}$, $\mu_{hh}$, $\mu_{lh}$).

3. **Define the device structure** The device is sub-divided into sections that are described by S-matrices. For each section the parameters needed to construct the S-matrix are defined (section-length, material type and e.g. grating strength and mirror reflectivity). For each section the optical overlap between tuning-layer and optical field is calculated with mode-solver software and the result is used in this simulation. The effective index for the fundamental mode is calculated from the refractive index of the tuning layer and of InP. It is assumed that the portion of the field that does not overlap with the tuning layer does overlap with the surrounding InP. Each section is connected to its current source. The tuning section component on which the optical power is incident is selected. Typically this is the first component of the tuning section.

4. **Set the external stimuli** The ambient temperature, value of current sources and incident optical power on the tuning sections are set.

5. **Calculate state of each section** Current injection is distributed over the sections, assuring that sections connected to the same current source receive the same current density. The photo-current in each section is calculated. Only with a high incident power ($> 10\ mW$) the carrier-density is significantly altered. For each section the resultant carrier-density is calculated. This enables the calculation of the change in refractive index, due to bandgap shrinkage and bandfilling. The difference in absorption with the zero current density case is used in the Kramers-Krönig relation, where the energy-range is limited to be between the bandgap energy and 200 meV above this value. The impact of changes at higher energies rapidly decreases. With this information the parameters that depend on temperature and carrier-density are calculated ($E_g(T)$, $N_c$ and $N_v$, $F_c$ and $F_v$). This calculation is repeated for every change in device settings, such as injection current, temperature and incident optical power.

6. **Calculate the round-trip loss spectrum** The S-matrix for each optical components in the device is now calculated at any given wavelength. Round-trip loss and phase is calculated over a chosen wavelength range (with a chosen wavelength resolution). This is illustrated in figure 3.4a. For each wavelength the refractive index of each section is calculated separately.

7. **Find the optical modes** In figure 3.4 it is illustrated how by using the round-trip phase information the optical modes in the laser cavity are found (i.e. the wavelengths at which the round-trip phase equals an integer times $2\pi$).

8. **Find the lasing mode and the strongest side-mode** The round-trip loss/gain for these optical modes is compared and the mode with lowest round-trip loss is selected, as well as the second-lowest-loss peak. The former mode is at the lasing wavelength and optical gain required for lasing equals the round-trip loss. The latter mode round-trip loss is used to calculate the round-trip loss difference with the lasing mode, a measure from which the SMSR is calculated.

9. **Output the simulation results** The simulation outputs the lasing wavelength, required gain, round-trip loss difference and mode spacing.

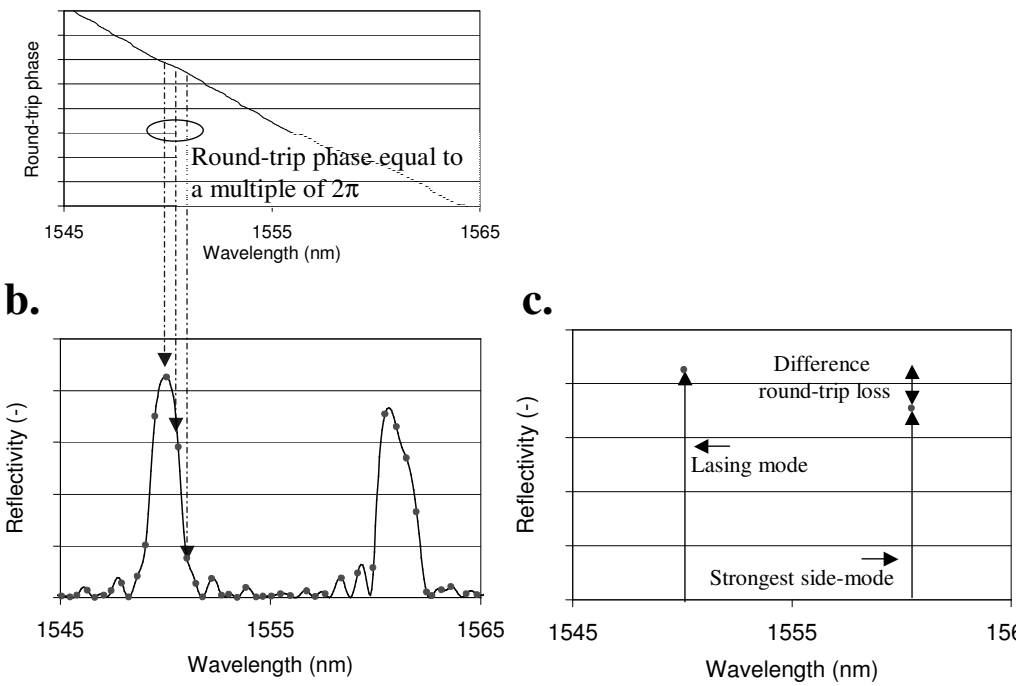


*Figure 3.4: Simulation procedure for a laser; a) The round-trip phase is calculated over a wavelength range. b) At the wavelengths where the phase equals a multiple of $2\pi$ a cavity mode is found and the reflectivity of the tuning section is calculated; c) The cavity mode with highest reflectivity of the tuning section is the lasing mode, while the difference in reflectivity with the strongest side-mode is determined to calculate the SMSR.*

10. **calculate the device setting** Using the optical gain, the front facet reflectivity and the tuning section reflectivity, the laser threshold current, external slope efficiency and SMSR is calculated, through the formulas in section 3.1.

By sweeping the external stimuli (e.g. drive currents or output power) and repeating step 5 to 10, the device performance for different operating conditions is obtained.

# Chapter 4

# Cascaded Sampled Grating Laser

The following two chapters introduce two novel widely tunable laser concepts. The first one is the Cascaded Sampled Grating (CSG) laser. The concept is introduced in section 4.1. Section 4.2 treats design aspects of the device, and in section 4.3 simulation and experimental results are presented. Finally, in section 4.4 a summary is provided.

## 4.1 Device concept

### 4.1.1 Introduction

Section 2.2.2 introduced the sampled grating. It was shown that the cascade of a number of short grating and propagation sections gives a reflection spectrum with multiple resonances. The position of the center resonance is determined by the Bragg wavelength of the grating, the resonance spacing depends on the optical length of each period (=grating-burst + propagation section length) and the reflectivity is controlled by the combined length of the grating-burst sections and the grating strength.

Combining two sampled gratings with regularly, but differently, spaced resonances a tunable laser is made using the Vernier effect (see section 2.2.4). If at a wavelength the reflection spectrum of both sampled gratings is resonant, that wavelength is selected for the laser to operate at. No two other resonances overlap, thanks to the difference in spacing, between resonances, for the two sampled gratings. Wavelength tuning of the selected resonance is achieved by shifting (independent of the tuning mechanism) both reflection spectra simultaneously. By shifting only one reflection spectrum, a different combination of sampled grating resonances overlaps and lasing occurs at the wavelength of those resonances. The above procedure allows for selecting a resonance in the sampled grating spectrum over a wide wavelength tuning range (as shown in figure 2.7). The selectivity of that sampled grating resonance allows for selection of a cavity mode.

The (S)SG-DBR laser [54] is an example of how a combination of two sampled gratings (with different periodicity) is used to obtain Vernier-type tuning. The laser cavity is

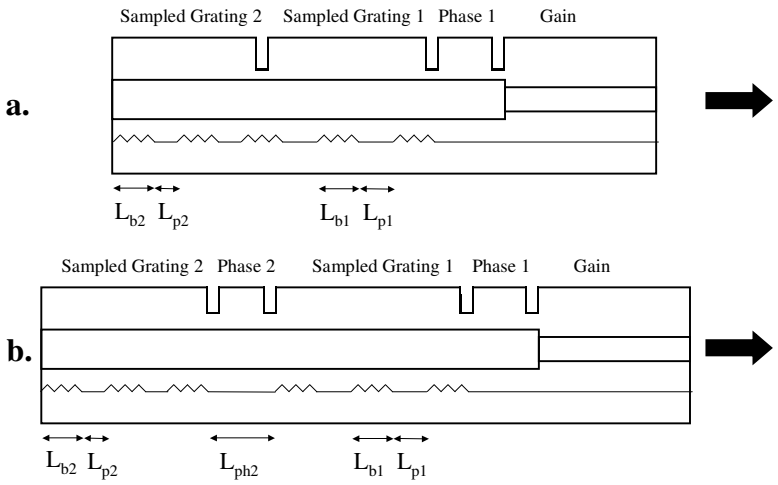


*Figure 4.1: Schematics of a CSG laser: a) 4-section CSG laser and b) 5-section CSG laser. On the left side the sampled grating sections are shown. Together with the phase sections these provide optical feedback into the gain section (on the right). The light exits the laser-cavity at the front facet on the right. The indents between the different sections (indicated by a different thickness of the waveguiding layer) indicate an electrical separation channel.*

formed by a gain and phase section, in between two sampled gratings. This approach has the advantage that two reflection coefficients are multiplied, which theoretically improves selectivity. However light has to pass through the sampled grating at the front facet-side, before escaping the laser cavity. This section tends to introduce free-carrier absorption with increased tuning current. As a result, output power varies significantly with tuning current [38]. Together with the requirement for a front section reflectivity of 10-30%, optimization of the output power implies that the length of the front mirror section has to be short. Thus, the wavelength selectivity of the front facet tuning section is much smaller than that of the back facet side reflector. Hence, the advantage of spectrum multiplication is lost. Also, a wide-band low reflectivity coating has to be applied on the front facet to avoid feedback at undesired wavelengths. In short, the SG-DBR laser has a low output power that is dependent on tuning current. The front facet reflector does not significantly contribute to the cavity mode selectivity (e.g. SMSR) of the laser.

An improved concept, the Cascaded Sampled Grating (CSG) laser introduced in this chapter, overcomes these limitations. By cascading two sampled grating sections at the back-facet-side of the device, the Vernier effect is still used. The resultant reflection spectrum of the two sampled gratings is single peaked over the tuning range and there is no (absorbing) tuning section at the front-facet. The reflectivity of the front facet is selected after manufacturing, by applying a dielectric coating. With a suitable choice for material composition, the variation of output power with tuning current is compensated for by material gain at higher values of current injection in the tuning sections, as demonstrated for tunable DBR lasers [96].

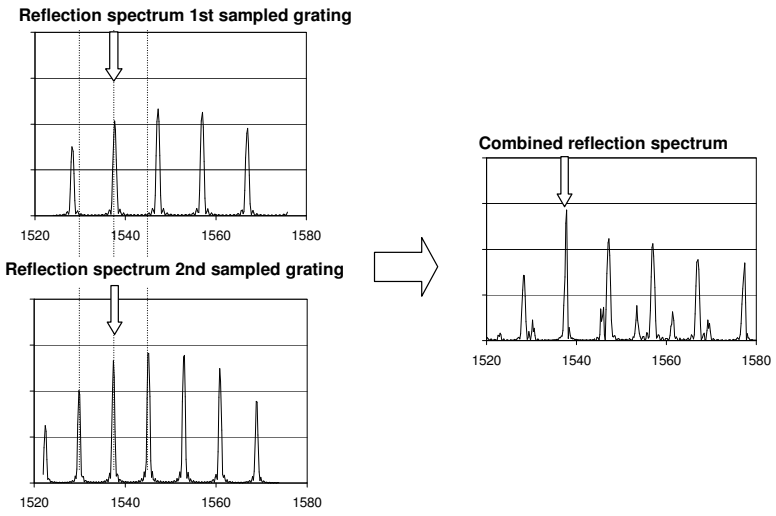


*Figure 4.2: Reflection of a Cascaded Sampled Grating. The reflection spectrum of the two sampled gratings in the CSG are given on the left hand side. The resultant reflection spectrum of the CSG is shown on the right hand side*

### 4.1.2 Device description

In figure 4.1a a 4-section CSG laser is shown. The design consists of a gain section, a phase section and a CSG, formed by two sampled gratings.

In this configuration the gain section generates and amplifies the optical field within the laser cavity. The CSG provides mode selectivity. The first sampled grating provides a multi-peaked reflection spectrum. The reflection spectrum from the second sampled grating is added, such that one dominant sampled grating resonance remains for laser operation (see figure 4.2). The phase section provides tuning of the optical length of the laser-cavity, to control the spectral position of the laser mode.

To control each section separately, sections need to be electrically isolated from one another, while maintaining an optical connection. Independent of the technical implementation (e.g. removal of the highly doped toplayer or proton implantation) there is always a finite distance between the two sampled gratings in which current injection is not possible. As a result, the current injection is not uniform over the full length of the sampled grating, and especially the period(s) close to the isolated region has a different optical length. This influences the optical properties of the CSG and prevents smooth tuning performance.

To overcome this limitation, a 5-section design is proposed (figure 4.1b). An extra phase section is inserted between the two sampled grating sections, such that the current injection in the first and second sampled grating section is uniform over the complete length. To accomplish this the electrical isolation at both interfaces with the second phase section is located completely in this section. This second phase section is made phase-transparent by tuning the refractive index of that section. It does present an extra complexity for tuning of this component.

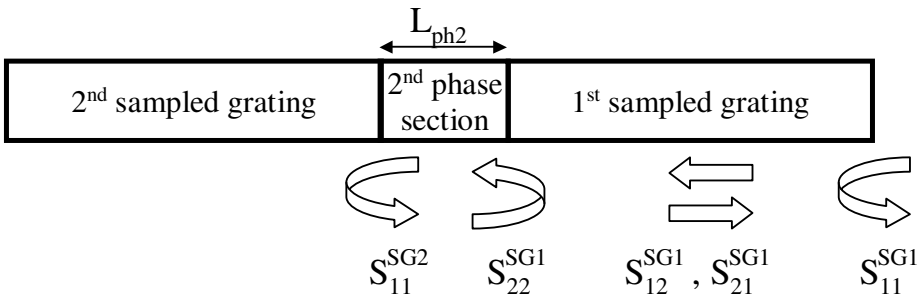


*Figure 4.3: Definition of terms in formula 4.1.*

### 4.1.3 Theoretical background

The reflection spectra of the sampled gratings, with multiple resonances, add to give the single resonance reflection spectrum of a CSG. This is illustrated in figure 4.2. The selectivity of the CSG spectrum is enhanced by the reflectivity-phase of the two sampled gratings. Only if both reflection-terms are in phase (ideally, this only occurs at the wavelength where two sampled grating resonances overlap) full coherent addition is achieved.

Reflectivity from the (5 section) CSG section, as defined in figure 4.3, is expressed through the amplitude-based addition of (multiple) reflections on these sections:

$$\begin{aligned} r_{CSG} &= S_{11}^{SG1} + S_{12}^{SG1} \cdot S_{11}^{SG2} \cdot S_{21}^{SG1} \cdot \exp(i \cdot 2\pi \cdot \frac{2 \cdot \mu_{ph2} \cdot L_{ph2}}{\lambda}) + \\ &\quad S_{12}^{SG1} \cdot (S_{11}^{SG2} \cdot S_{22}^{SG1}) \cdot S_{11}^{SG2} \cdot S_{21}^{SG1} \cdot \exp(i \cdot 2\pi \cdot \frac{4 \cdot \mu_{ph2} \cdot L_{ph2}}{\lambda}) + \ldots \\ R_{CSG} &= \left| S_{11}^{SG1} + \frac{S_{12}^{SG1} \cdot S_{21}^{SG1} \cdot S_{11}^{SG2} \exp(i \cdot 2\pi \cdot \frac{2 \cdot \mu_{ph2} \cdot L_{ph2}}{\lambda})}{1 - (S_{22}^{SG1} \cdot S_{11}^{SG2}) \cdot \exp(i \cdot 2\pi \cdot \frac{2 \cdot \mu_{ph2} \cdot L_{ph2}}{\lambda})} \right|^2 \\ &\quad with \;\; 2 \cdot \mu_{ph2} \cdot L_{ph2} = integer \cdot \lambda \\ &= \left| S_{11}^{SG1} + S_{11}^{SG2} \cdot \frac{S_{12}^{SG1} \cdot S_{21}^{SG2}}{1 - S_{22}^{SG1} \cdot S_{11}^{SG2}} \right|^2 \end{aligned} \tag{4.1}$$

In this equation $S_{21}^{SG1}$ denotes the (amplitude-based) transmission through the first sampled grating (SG1, SG2 for the second sampled grating) from front-facet-side (=1) to back-facet-side (=2). Similarly, $S_{11}^{SG1}$ denotes the reflection coefficient at the front-facet side of the first sampled grating. $L_{ph2}$ and $\mu_{ph2}$ are the length and effective index of the second phase section and $\lambda$ represents the lasing wavelength.

By replacing the $L_{ph2}$ term by the length of a propagation section of the first sampled grating this formula describes a 4-section CSG laser, as well. It follows that the response of a 4-section CSG laser is essentially equal (disregarding the absorption in the second phase section) to that of a 5-section CSG laser, if the optical length difference between the second phase section and a propagation section in the first sampled grating is a multiple of $\frac{1}{2}\lambda$.

From above equation, the relation between CSG reflection properties and sampled grating reflectivity is less straightforward than for an SG-DBR laser, where the combined response is based on multiplication. For the CSG section the resultant spectrum is a combination of two sampled grating spectra. The part of the second sampled grating reflection that is added to the spectrum of the first sampled grating is a function of reflection and transmission of both sampled gratings.

Maximum reflectivity of the CSG is obtained if the reflection terms of both sampled gratings are in phase at the begin of the tuning section. The phase upon reflection of a sampled grating is given as $-\frac{\pi}{2} + k \cdot \pi \cdot \frac{L_b}{L_p+L_b}$ [54] (equation 2.12) for a sampled grating resonance of order k. The length of the first sampled grating is a multiple of its resonance wavelengths, and hence the first sampled grating is phase transparent, at resonance. Therefore it follows that the reflection terms from the first and second sampled grating add constructively for sampled grating resonances of the same order, when the ratio of burst section length to sampled grating period is identical. For resonances of different order the reflection terms have a different phase and resonances need to be detuned from one-another. This widens the resonance and reduces selectivity. However, the reflectivity is comparable, since sampled grating reflectivity is insensitive to wavelength variation close to the resonance wavelength.

## 4.2 Design

The design optimization of the CSG laser addresses two objectives. Firstly, to meet the main requirements as specified in section 1.3, optical output power and side mode suppression ratio. And secondly, to reduce the variation in operating current in the gain section over a tuning range of 40 nm.

In the following sections the trade-offs in the design of the CSG laser are discussed and design choices are motivated. Realistic assumptions are made for the properties of the layerstack. Design of the layerstack is deferred to section 4.2.4.

### 4.2.1 Laser design

High power, single-mode operation of the tunable laser requires a high external efficiency, a low threshold current and a low value for $\delta\alpha_m$, at which the SMSR requirement is met. To limit the variation in operating current in the gain section over the tuning range, the sensitivity of the output power to a change in the tuning section properties has to be minimized.

In figure 4.4 a schematic drawing is shown of a laser cavity of length $L_{cav}$. The feedback into the cavity is from the front- and back-facet reflection, $R_B$ and $R_F$. The optical gain is the product of the overlap $\Gamma$ of the optical mode with the gain generating material and the material gain $g$.

Using the expressions 2.5 and 2.6 in chapter 2, the dependence of threshold current and ex-facet power on facet-reflectivity is calculated. In this calculation the roll-over of the output power (due to heating and material non-linearity) is neglected. This means that the output power is over-estimated, certainly at higher levels of current injection. In figure 4.5 the simulated optical power at 50 mA and 150 mA operating current is

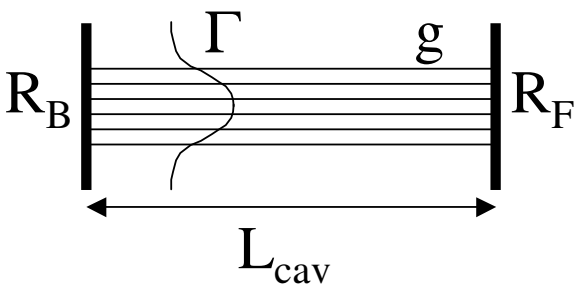


*Figure 4.4: Schematic drawing of a laser cavity. A 6-quantum well gain generating medium is shown between two reflectors ($R_F$ and $R_B$ at a spacing $L_{cav}$). The optical gain is the product of the material gain g and the overlap of the optical mode with the quantum wells* $\Gamma$.

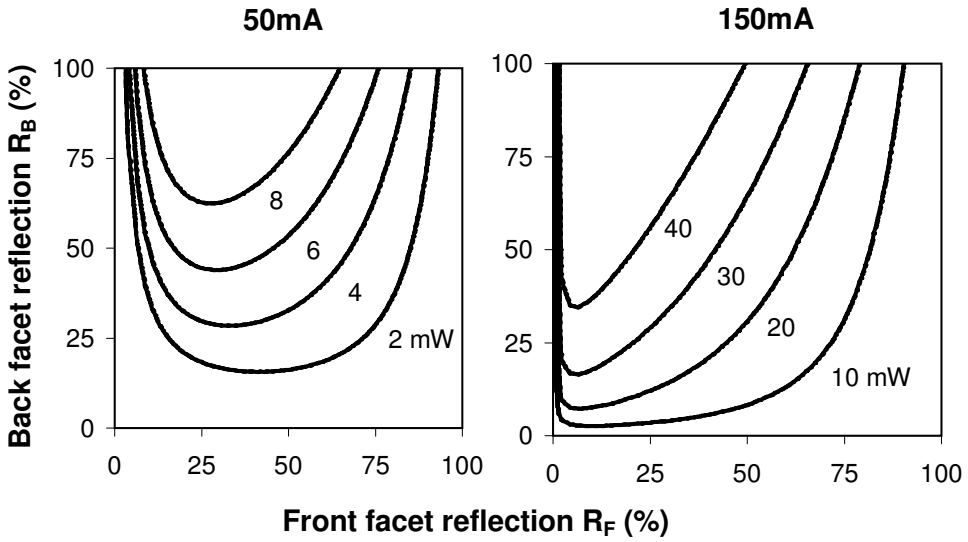


*Figure 4.5: Laser output power, versus front and back facet reflectivity, for 50 and 150 mA operating current. The output power is calculated from formulas 2.6 and 2.5. For the calculation the following assumptions were made:* $l_{cav} = 400\ \mu m$, $\lambda = 1550$ *nm,* $\eta_i = 80\%$ *and* $\Gamma = 3\%$.

shown for a laser-cavity of 400 $\mu m$ length, versus the reflectivity at the front and back facet-side of the gain section.

For a fixed injection current, there is an optimal value for the front facet reflectivity, limited at the lower end by an increase in threshold current. For low operating current, this increase in threshold current has a relatively large impact on the output power. Hence, the front facet reflectivity for maximum output power shifts towards lower values at a higher operating current. An increase in the back-facet reflection improves both the external efficiency and the threshold current. For high power operation of the laser this reflection term needs to be maximized.

The distance between the contour-lines in the figure is a measure for sensitivity of

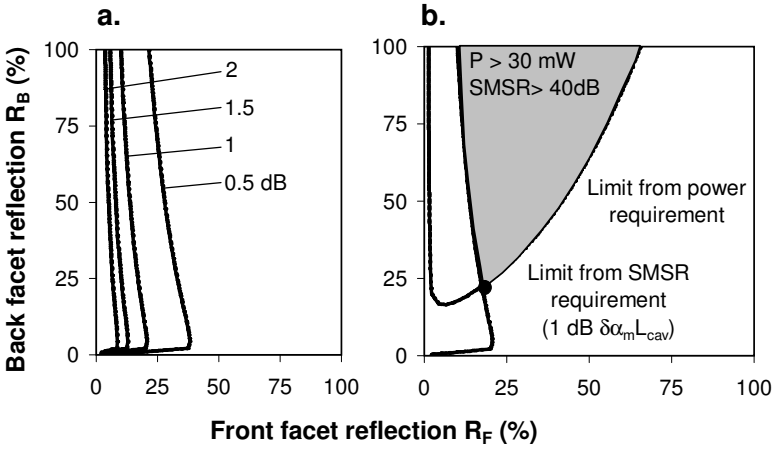


*Figure 4.6: a) required difference in round-trip loss $\alpha_m \cdot L_{cav}$ to ensure 40 dB SMSR; b) derivation of operation points at 150 mA where both the output power requirement of 30 mW and the SMSR requirement of 40 dB is met. The design-point where the back-facet reflectivity is minimized is indicated by the dot. For the calculation the following assumptions were made: $l_{cav} = 400$ $\mu m$, $\lambda = 1550$ nm, $\eta_i = 80\%$ and $\Gamma = 3\%$.*

the output power to changes in reflectivity at the back-facet(a larger distance indicates a lower sensitivity). Hence, in order to reduce the variation in operating current over the tuning range, the front-facet reflectivity is, ideally, larger than its optimal value for maximum output power, because at that set-point also the sensitivity to front-facet reflectivity is reduced.

For low values of threshold current the differential gain $\frac{\delta g}{\delta n}$ is high. However, for higher values the differential gain reduces. As a consequence, the threshold current is sensitive to variation in the loss in the laser cavity, especially when the threshold current is high. To reduce this sensitivity the laser needs to operate at a low threshold carrier-density. This is addressed, in more detail, in the design of the layerstack (section 4.2.4).

In order to ensure single-mode operation over the full tuning range the selectivity for sampled grating resonance and cavity-mode needs to be sufficiently high, as defined by formula 2.8. In figure 4.6a the required $\delta\alpha_m \dot{L}_{cav}$ for 40 dB SMSR at 30 mW operation is plotted, versus front- and back-facet reflectivity (earlier this figures was shown in chapter 2). From the figure it follows that the required gain-difference has minimal dependence on the back-facet reflectivity. For low front-facet reflection, the required $\delta\alpha_m \cdot L_{cav}$ increases rapidly (as seen from the increasing density of lines in figure 4.6). For values higher then about 1 dB, the required $\delta\alpha_m \cdot L_{cav}$ becomes very sensitive to front-facet reflectivity. Therefore, in this treatment the parameter $\delta\alpha_m \cdot L_{cav}$ needs to remain below 1 dB.

To obtain a target output power of 30 mW with an SMSR of at least 40 dB, the curves in the two figures are combined to define the allowed range of front- and back-facet reflectivity. In figure 4.6b a graph is plotted for a 400 $\mu m$ long gain section. A minimum value of front facet reflectivity is defined by the contour-line of 1 dB $\delta\alpha_m \cdot L_{cav}$.

A minimum value of back-facet reflectivity is defined by the contour-line for 30 mW output power. In the figure the area that meets both power and SMSR requirement is shaded. A minimum back-facet reflectivity is required, as indicated by the dot. This is a significant parameter, since the design trade-offs for the CSG section design become more difficult when the reflectivity requirement over the tuning range is higher.

In the analysis of output power and SMSR of a laser cavity the device length and the optical confinement are the main variables. Optimization of these variables will be done in the following paragraphs. For other parameters, such as the device internal loss, the injection efficiency and the relation between material gain and carrier-density typical values from literature were used.

Only the threshold current is dependent on the optical confinement. For sufficiently high values of the modal gain (the product of confinement and material gain $\Gamma \cdot g$) lasing operation is supported at a low carrier-density, making the threshold current less sensitive to variations in the back-facet reflection. Hence, good confinement of the optical mode in the gain section quantum wells is required to achieve a low carrier-density at threshold condition. For higher values of optical confinement, the effect on threshold current is small (minor decrease in carrier-density) or negative (if the active volume increases).

The device length has an impact on both the optical power at a given current and the SMSR. Again, once the product of optical gain and device length ($\Gamma \cdot g \cdot L_{cav}$) compensates for mirror loss and internal loss at a low value of carrier-density, an increase in device length has a minimal impact on the efficiency. However, the increase in length does increase the threshold current by an increase in active volume and the cavity modespacing will decrease, placing a tougher requirement on the selectivity of the tuning section. Best device performance is obtained at a minimum value of device length, for which the gain requirement is met at a low value of the carrier-density.

Performing the calculation for figure 4.6 with different values of device length, gives that for gain section lengths between 400 and 600 $\mu m$ the minimum required reflectivity at the back-facet (or at the tuning sections) is between 22 and 23%. Given the low variation over this range of device lengths, the shortest possible cavity length is preferred.

### 4.2.2 Tuning element design

The tuning element in a CSG laser is a cascade of two sampled gratings (figure 4.7), positioned at the back-facet side of the gain section. The first sampled grating generates a reflection spectrum, with resonances that are sufficiently narrow to select a single cavity mode. With the reflection spectrum of the second sampled grating one of the resonances in the first sampled grating is favored (see figure 4.2). For the CSG design, first the properties of a sampled grating are discussed, to be used in the design of the full CSG.

In figure 4.7 the design parameters for a CSG are illustrated. For each sampled grating section these are the number of periods $N$, the length of propagation sections $L_p$, the length of grating-burst sections $L_b$, the grating strength $\kappa$ and the overlap $\Gamma$ of the optical field with the tuning layer.

#### Sampled grating

In section 2.2.2 the reflection spectrum of a sampled grating was introduced. For the

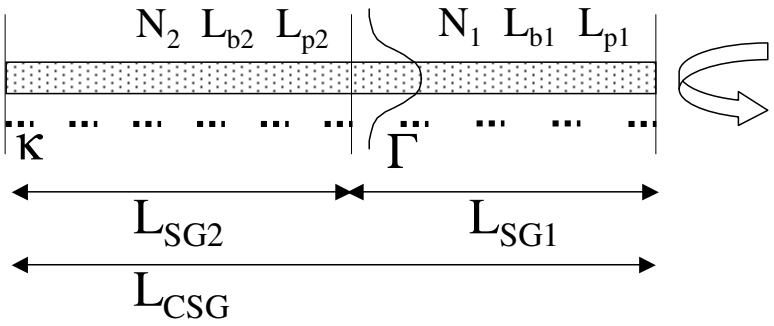


*Figure 4.7: Schematic drawing of a Cascaded Sampled Grating. The CSG consists out of two sampled grating sections, both with a number of short grating bursts. The periodicity of these bursts is different for both sampled gratings. Further design parameters are the grating strength and the confinement of the optical field with the tuning layer. The shown CSG has 5 periods ($N_1$) in the first sampled grating and 4 periods ($N_2$) in the second sampled grating.*

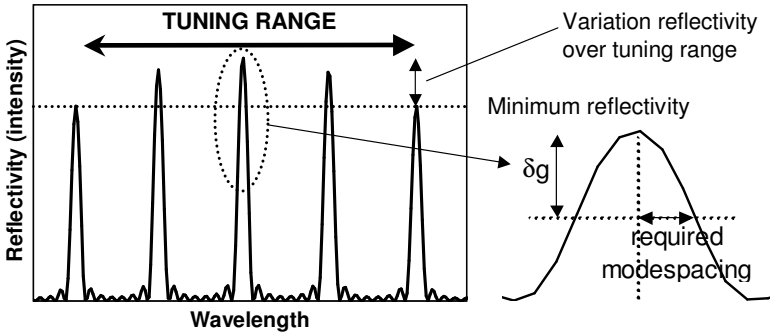


*Figure 4.8: Parameters for optimization of the sampled grating response: 1) the minimum reflection of any resonance in the tuning range, indicated by the horizontal dotted line. 2) the difference in reflection from the resonances over the tuning range, indicated by the vertical arrow. 3) the minimum modespacing for a mode-selectivity of $\delta g$ (see the insert).*

purpose of use in a tunable laser, this element needs to be optimized over the tuning range (here taken to be 40 nm). First, the minimum reflection of the sampled grating resonances over the tuning range (i.e. 20 nm away from the center resonance) defines the maximum threshold gain (and current) for the laser. Secondly, the variation in reflection from sampled grating resonances, over the tuning range, determines the ability of the CSG laser to select a particular mirror resonance. Finally, the spectral width of the sampled grating resonances defines the ability of the CSG laser to select a particular cavity mode with sufficient suppression for other cavity modes. In figure 4.8 these parameters are illustrated.

The relation between the minimum reflectivity and the variation in reflectivity is plotted in figure 4.9 (for a spacing between sampled grating resonances of 10 nm). The reflectivity for a resonance at 20 nm from the central resonance (for a 40 nm tuning

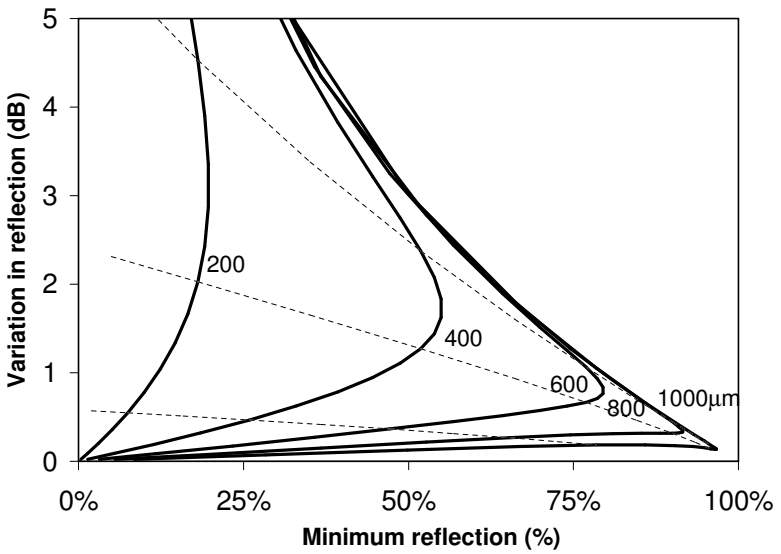


*Figure 4.9: Parametric plot of variation in reflection versus the minimum reflectivity for resonances within a 40 nm tuning range. Curves correspond to different values of sampled grating length. Curves are plotted as function of the grating-burst section length. Increments of 10% of the sampled grating periodicity are indicated by dotted lines. The parameters are explained in figure 4.8.*

range) is plotted on the x-axis. The y-axis gives the difference in reflectivity with the central resonance. Each curve is for a specific total length of the sampled grating (varied from 200 $\mu m$ to 1000 $\mu m$), with a grating burst length increasing from zero. For each increment in grating burst length by 10% of the grating periodicity these curves are intersected by a dotted line.

With an increasing grating-burst section length, the reflectivity of the outer resonance in the tuning range reaches a maximum and decreases. The central resonance however keeps getting stronger, making the variation over the tuning range larger. For a design with a high reflectivity and small variation in reflectivity, a short grating-burst section length is preferred ($< 25\%$ for $\kappa = 15\ mm^{-1}$).

A grating strength of 15 $mm^{-1}$ was used in the calculation. For higher values the reflectivity at the edges of the tuning range increases, while the difference with the central resonance decreases. For more narrowly spaced resonances, the minimum reflectivity decreases (since higher order sampled grating resonances are present within the tuning range), while the central resonance is not affected. Hence, the variation in reflectivity over the tuning range increases for a lower value of resonance spacing.

The third dimension in the sampled grating design is shown in figure 4.10: the required modespacing for a 1 dB suppression of other cavity modes. On the y-axis, the spectral distance between the center of the resonance and where the reflectivity is down by 1db is given (based on the gain difference requirement proposed in the laser design section). On the x-axis the minimum reflectivity of the resonances in the tuning range

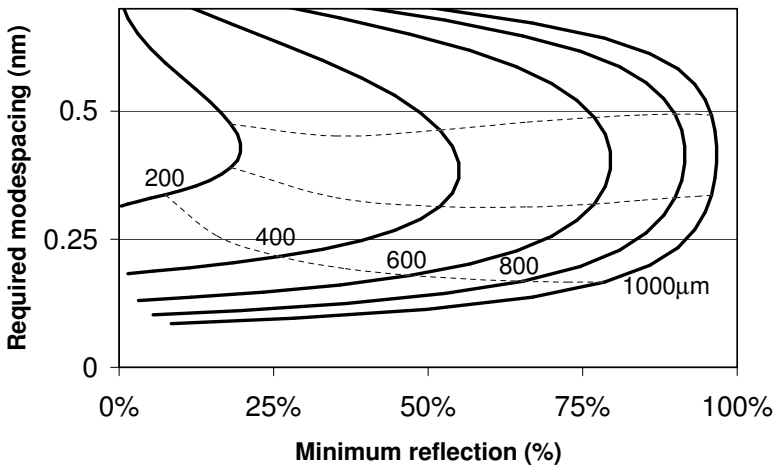


*Figure 4.10: Parametric plot of the difference in resonance-reflectivity over a 40 nm tuning range versus 1-dB width of main sampled grating resonance. Different curves correspond to different values of sampled grating length Curves are plotted as function of the grating-burst section length. Increments in the grating-burst section length by 10% of the sampled grating periodicity are indicated by dotted lines. The parameters are explained in figure 4.8.*

is given.

In equation 2.13 an expression for the spectral width of a resonance in the sampled grating spectrum was given. This spectral width has a floor given by $\frac{\lambda^2}{2 \cdot L_{sg} \cdot \mu_g}$. For sufficiently long sampled gratings the width is proportional to the product $\kappa \cdot \frac{L_b}{L_b + L_p}$. With an increasing effective grating strength the spectral width increases. Again, the curves are intersected by dotted lines at each increment of the grating burst length by 10% of the sampled grating period. Since the highest effective grating strength is realized at the central resonance, any other resonance is more selective for cavity modes.

Resonances in the sampled grating spectrum are spaced by $\frac{\lambda^2}{2 \cdot \mu_g \cdot (L_p + L_b)}$ ($\mu_g$ being the group-index). To allow a tunable laser to address all wavelengths in the tuning range, this spacing needs to be less than the wavelength range over which the Bragg wavelength of the grating can be tuned. For the quaternary tuning layer used here, a tuning range of up to 16 nm has been demonstrated [37]. In our design, a conservative tuning range of 12 nm is used. Such a resonance spacing corresponds to a sampled grating periodicity of at least 30 $\mu m$ and 3-4 resonances within the 40 nm tuning range.

Associated with a large resonance spacing is a high carrier-density to shift the Bragg wavelength to an intermediate wavelength. The free-carrier absorption associated with a high carrier-densities is significant, but is reduced by spacing the resonances more closely (i.e. using a higher periodicity). In figure 4.11, the reflectivity of the central sampled grating resonance is shown versus the absorption coefficient of the tuning layer material, for a 400 $\mu m$ long sampled grating and different values for the resonance spacing. Even though configurations with more closely spaced sampled grating resonances have a lower reflectivity at no absorption, they require a lower level of current injection to address all

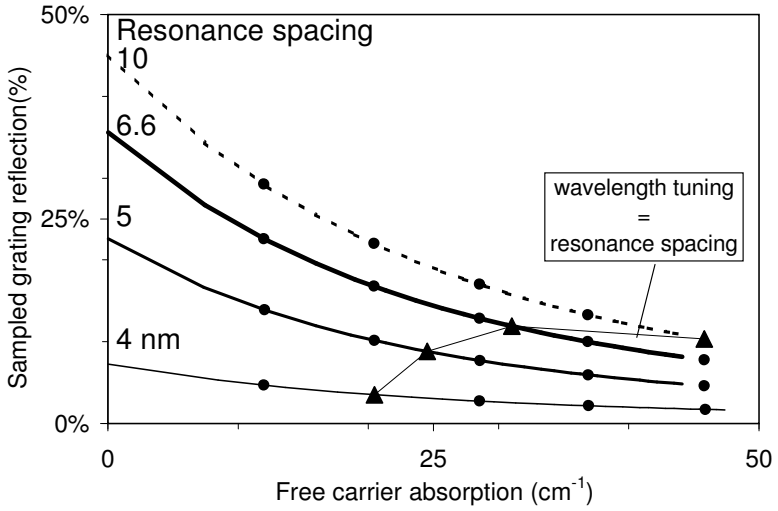


*Figure 4.11: Sampled grating reflection versus material absorption for a 400 $\mu m$ long sampled grating and different values of resonance spacing. Assumptions made for the calculation: $L_b/L_p = 15\%$. $\kappa_0$ =15 $mm^{-1}$, $L_{SG}$ = 400 $\mu m$ and $\lambda_B$ = 1550 nm.*

wavelengths between sampled grating resonances. For each curve the set-point where the Bragg wavelength has been detuned by the resonance spacing is indicated by a triangle. Clearly, even though the free-carrier absorption over the tuning range is lower for the more narrow resonance spacing, the minimum reflectivity is not. The optimal reflectivity over the tuning range is obtained for an 8-10 nm spacing between resonances, with a minor decrease for higher values of resonance-spacing. A large spacing is clearly the preferred design.

In this analysis a particular sampled grating configuration was chosen. This analysis was repeated over a relevant range of grating burst lengths, resonance spacing and sampled grating lengths, which showed that the above conclusion holds true. From this analysis a reduction in reflectivity with current injection of a factor three is taken as the worst-case situation.

### Cascaded sampled grating

The reflection spectrum of a CSG needs to have one dominant resonance, with sufficient selectivity for the laser cavity modes (for an SMSR of 40 dB). Through current injection, in both sampled gratings, the full tuning range should be accessible with a value of reflectivity, which enables 30 mW operation of the CSG laser.

The relationship between the CSG reflectivity and the reflectivity of the constituting sampled gratings is given in figure 4.12, under an assumption of positive interference (which is valid for resonances of the same order). The addition of the two reflection terms is fully symmetric. Intuitively, this is understood by considering two sampled gratings of equal periodicity, but different length (and hence different reflectivity). For

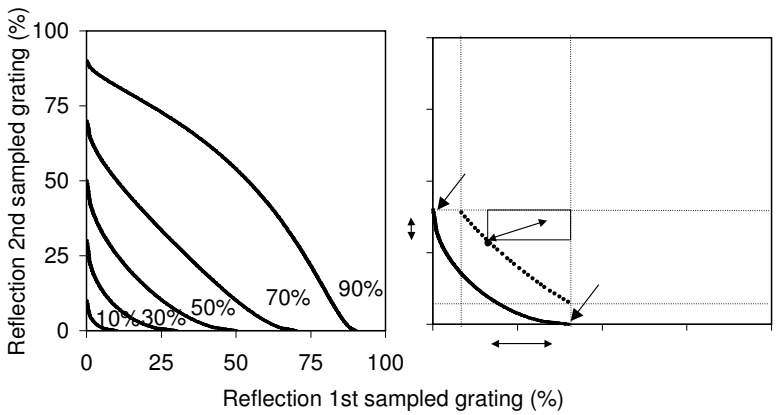


*Figure 4.12: a) CSG reflectivity versus the reflectivity of the first and second sampled grating. The contributions of the two sampled gratings are added constructively; b) Illustration of CSG operation. Arrows on the axis represent the resonance reflectivity for the separate sampled gratings. The cascade of these two sampled gratings results in a reflectivity range indicated by the diagonal arrow. In order to achieve a 1 dB suppression of all other resonances than the selected resonance the maximum reflectivity of each sampled grating needs to be lower than the value indicated by the arrows.*

the combined reflectivity the order of these two sampled gratings does not matter.

Figure 4.12 serves as the basis for the CSG design. This is illustrated on the right hand side of the figure. When the Bragg wavelength of both sampled gratings is detuned, such that the dominant CSG resonance is at the edge of the tuning range, the minimum CSG reflectivity is obtained (here we neglect absorption). As an example, such a set-point is indicated by the dot in the figure, though an equal reflectivity is obtained for all combinations of sampled grating reflectivity on the dotted line. To suppress competing resonances in both sampled gratings, these should be suppressed by at least 1 dB in the CSG spectrum (indicated by the bold line). This means that for wavelengths, different from the resonance wavelength, the combination of sampled grating reflectivity needs to be below and to the left of the bold line. The intersection of this bold line with the axes gives the maximum allowed reflectivity of the central sampled grating resonance, for which still 1 dB suppression is obtained. Since this is the maximum sampled grating reflectivity over the tuning range, the reflectivity of the dotted line can only be obtained with a minimum value for the reflection of the other sampled grating. The guidelines give the limitations on sampled grating reflectivity.

A design point with equal reflectivity for both sampled gratings has for both sampled gratings an equal allowed variation in reflectivity over the tuning range (i.e. between the design-point reflectivity and the maximum reflectivity). By lowering the reflectivity of one sampled grating, that sampled grating is allowed to have a larger variation in reflection over the tuning range. However, the margin for the second sampled grating is then reduced. For the design point in the figure, the rectangular box indicates within which range the resonance reflectivity of both sampled gratings is allowed to vary. Clearly the margin for the second sampled grating is reduced by the choice of this design-point.

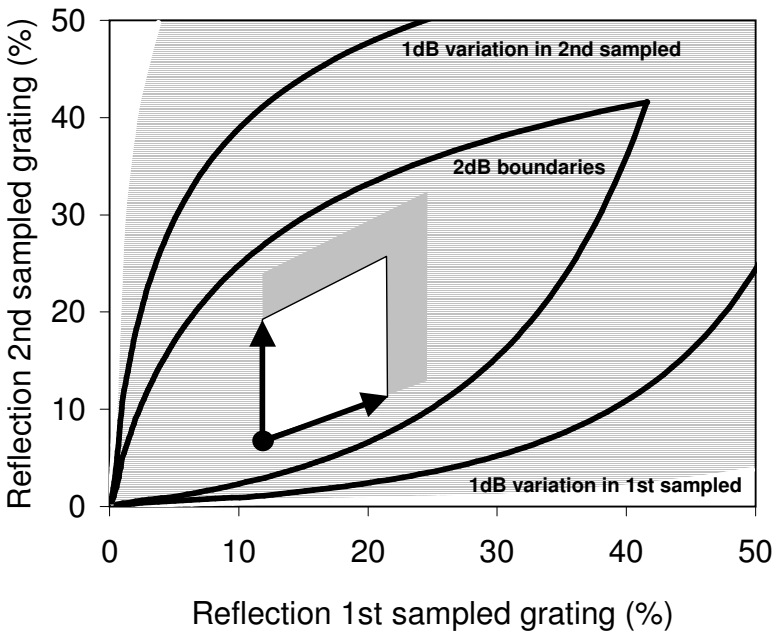


*Figure 4.13: Illustration of range of operation points over tuning range for CSG laser, when free-carrier absorption is considered. The dot represents the set-point where reflectivity of both sampled grating resonances is lowest (edge of the tuning range with maximum sampled grating currents). The reflectivity of the sampled grating resonance at this outer set-point increases within the white area with a decrease in sampled grating currents. The vertical arrow corresponds to a decrease in current in the second sampled grating. The diagonal arrow corresponds to a decrease in current in the first sampled grating. Due to the variation in sampled grating reflectivity over the tuning range the CSG set-point varies within the white plus grey area over the tuning range.*

The arrow indicates the variation in CSG reflectivity, for a specific design that meets these constraints.

It can be argued that the reflectivity of the other sampled grating is not necessarily zero at a resonance wavelengths for one of the sampled gratings and that a stricter limit on the maximum reflectivity is needed. On the other hand, the figure assumes positive interference of the two reflection terms. This is not necessarily met at wavelengths other than the CSG resonance wavelength. Here, it is assumed that these nuances on the analysis offset one-another.

Figure 4.13 shows a limited parameter space for the sampled grating reflectivity values. From the above discussion, for a given CSG reflectivity, only a limited range of set-points can offer 1 dB of suppression of other resonances (in figure 4.12 this range was indicated by the dotted line for one value of CSG reflectivity). These set-points all lie within the shaded area. In addition, over the tuning range, each sampled grating has a variation in reflectivity of its resonances. This requires an additional margin from the edges of this shaded area. In the figure the boundaries are given for a 1 dB and 2 dB

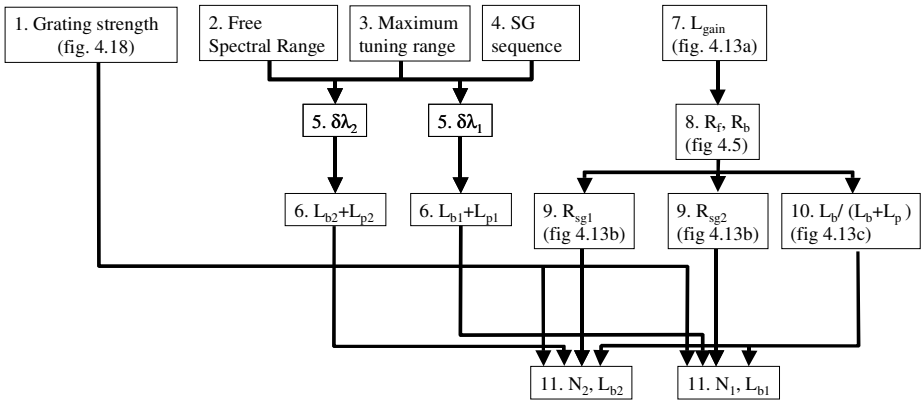


*Figure 4.14: Illustration of sequence used for design choices and interdependence of these choices.*

allowed variation in resonance reflectivity over the tuning range.

The above analysis was all based on a loss-less structure. Free-carrier absorption is inherent to the current-injection based tuning in the CSG. Starting from a design point with maximum absorption in both sampled gratings (i.e. lowest reflectivity), the reflectivity of each sampled grating is increased, by lowering the tuning current. For the situation where only the current in the second sampled grating is reduced the shift in design point is indicated by the vertical arrow. With a reduced current in the first sampled grating not only the reflectivity of the first sampled grating increases, also the transmission of the first sampled grating increases. This increases the effective contribution of the second sampled grating. This is indicated in the figure by the diagonal arrow. The CSG-design-points (defined at the edge of the tuning range) available to a particular CSG design, over a range of free-carrier absorption is indicated in the figure by the white region. In addition, the reflectivity of the sampled grating resonances varies over the tuning range. The grey region is used to account for this. The combined area of white and gray region needs to be within the indicated boundaries.

### 4.2.3 Design choice for the CSG laser

In the previous sections the different aspects in the design of a CSG laser (laser, sampled grating and CSG) were discussed. Now, it is the time to combine these design insights and choose a specific design. In support of the considerations provided below, figure 4.14 shows a flow-schedule on the sequence in which the design decisions are made. In figures 4.15 to 4.17 key figures are reproduced to guide the design considerations.

1. **Grating strength** $\kappa$ A maximum grating strength $\kappa_0$ of 15 $mm^{-1}$ is assumed. In the design of the layerstack (section 4.2.4) and figure 4.22 this is shown to be realistic.

2. **Free spectral range** The spacing of sampled grating resonances are chosen such that, within the tuning range, the sampled gratings are both in resonance at only

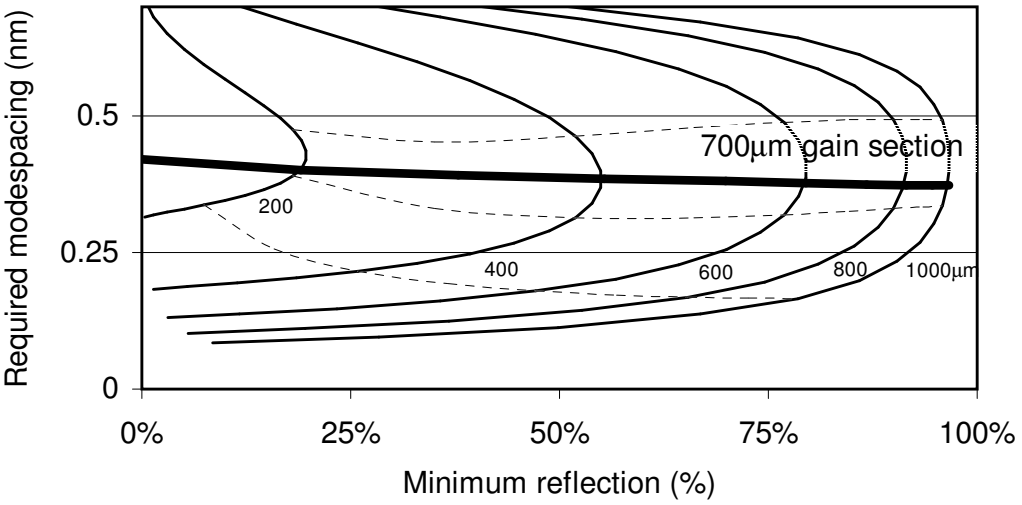


*Figure 4.15: Reproduction of figure 4.10. The thick line draws the requirement for cavity mode-spacing for a 700 µm long gain section. The thin lines are parametric plots of the allowed cavity mode-spacing to provide 1 dB suppression of other cavity modes versus sampled grating reflectivity. The lines are drawn for increasing values of grating burst length and each line corresponds to a different sampled grating length. The dotted lines indicate a burst section length of 10, 20 and 30% of sampled grating periodicity. The parameters are explained in figure 4.8.*

one wavelength. The distance between overlapping resonances needs to be wider than the intended tuning range, to avoid mode or resonance competition at the edges of the tuning range. For this purpose a Free Spectral Range (FSR) of 60 nm is chosen (1.5 times the tuning range).

3. **Bragg wavelength tunability** The tunability of the Bragg wavelength is practically limited to 12 nm (higher values - up to 16 nm - can be realized, but reproducibility is not ensured).

4. **Sequence of sampled gratings** Free-carrier absorption in the first sampled grating reduces the effective reflectivity of the second sampled grating (through a reduced transmission coefficient). To avoid this increased sensitivity to the tuning current in the first sampled grating, the length of the first sampled grating needs to be reduced. By choosing the highest resonance spacing for the first sampled grating, its length (and sensitivity to its tuning current) is reduced for a given reflectivity.

5. **Sampled grating resonance spacing** $\delta\lambda_1$ *and* $\delta\lambda_2$ The resonance spacing for the first sampled grating is equal to the maximum tunability of the Bragg wavelength (12 nm). The resonance spacing for the other sampled grating is chosen to have one extra resonance within the Free Spectral Range. Therefore the spacing is $(\frac{60nm}{1+60nm/12nm} =)$ 10 nm.

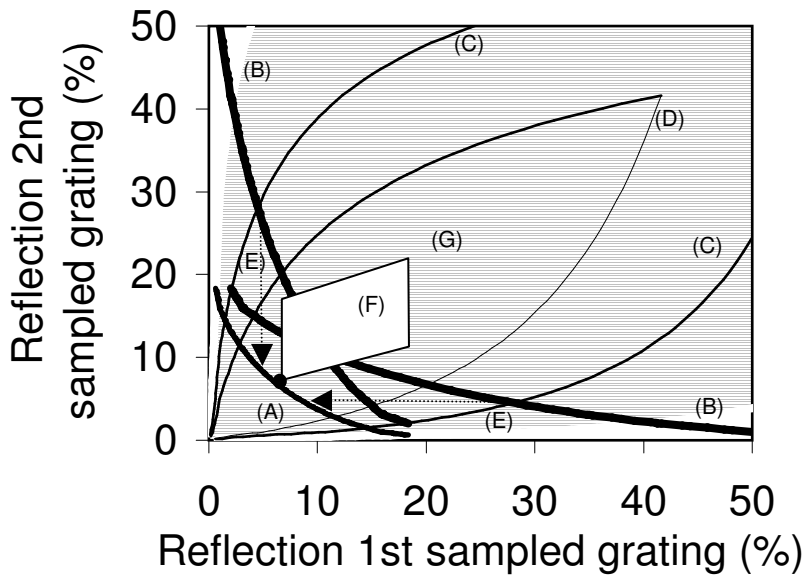


(A) Contourline for 23% CSG reflectivity, the minimum requirement over the tuning range
(B) 5dB increase in reflectivity of sampled gratings, due to less free carrier absorption
(C) Limits on sampled grating reflectivity for a maximum of 1dB variation in reflection over tuning range
(D) Limits on sampled grating reflectivity for a maximum of 2dB variation in reflection over tuning range
(E) Minimum limits for sampled grating reflectivity to allow 1dB variation in reflection over tuning range
(F) Area of set-points for the CSG laser over the tuning range for different values of free carrier absorption
(G) Maximum CSG reflectivity over tuning range is 52%

*Figure 4.16: Reproduction of figure 4.12 to explain the design choice for the CSG section.*

6. **Sampled grating periodicity** $(L_{b1} + L_{p1})$ *and* $(L_{b2} + L_{p2})$ The chosen resonance spacings translate into a periodicity of 32 $\mu m$ $(= \frac{\lambda^2}{2 \cdot n_g \cdot 12nm})$ for the first sampled grating and 40 $\mu m$ for the second sampled grating.

7. **Gain section length** $L_{gain}$ Figure 4.10 is reproduced in figure 4.15. Again the minimum mode-spacing for a 1 dB suppression of cavity modes is plotted versus the reflectivity of the sampled grating for different lengths of sampled grating. Added to this figure is the mode-spacing for a 700 $\mu m$ long gain section, in combination with a 100 $\mu m$ long phase section and a sampled grating. The mode-spacing in the laser-cavity needs to be larger than the minimum mode-spacing for which the sampled grating can provide 1 dB cavity mode-selectivity. Therefore, the design-point needs to lie below the thick line. Even for such a long gain section it is observed that the gain section length is not a limiting parameter for the cavity modespacing of the CSG laser, since the maximum in reflection is obtained with a more narrow mode-spacing. From the laser-section design (section 4.2.1) the requirements on the reflectivity of the CSG for 30 mW operation at 150 mA is between 22% and 23% for gain section lengths between 400 and 600 $\mu m$. The gain

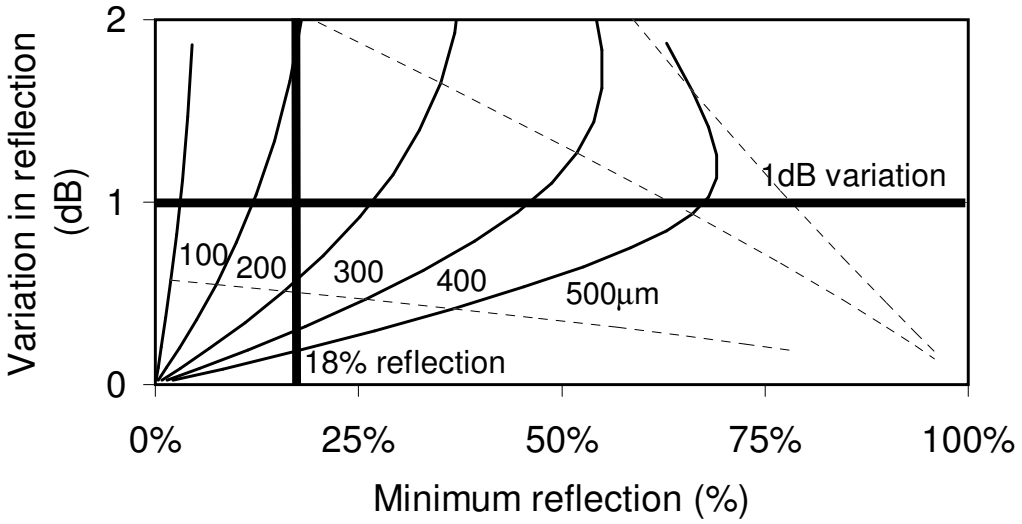


*Figure 4.17: Reproduction of figure 4.10. The thin lines are parametric plots of the variation in resonance reflection over the tuning range versus the sampled grating reflectivity. The lines are drawn for increasing values of grating burst length and each line corresponds to a different sampled grating length. The dotted lines indicate a burst section length of 10, 20 and 30% of sampled grating periodicity. The bold lines show the design requirements of an 18% sampled grating reflectivity and a maximum variation in sampled grating reflectivity over the tuning range. The parameters are explained in figure 4.8.*

section length is reduced to increase mode-selectivity of the CSG and a 400 $\mu m$ long gain section is the design choice.

8. **Facet reflection** $R_f$ *and* $R_b$ For a 400 $\mu m$ long gain section a minimum in required back facet reflection is obtained at 17% front-facet reflectivity. For this set-point a minimum back-facet reflectivity of 23% is required (e.g. see figure 4.6). This reflection value has to be realized even with maximum free-carrier absorption in both sampled gratings.

9. **Sampled grating reflection** $R_{sg1}$ *and* $R_{sg2}$ In figure 4.16 the parameter-space for sampled grating reflectivity is reproduced. The line where the minimum 23% CSG reflectivity is obtained is shown (indicated as A). The CSG design-point with maximum current in both sampled gratings (i.e. highest free-carrier absorption) is located on or above this line. The sampled grating reflectivity changes with free-carrier absorption. It has been verified through simulations that a maximum variation of 5 dB in sampled grating reflectivity is expected (over the range of likely sampled grating designs). This increase in reflectivity of both sampled gratings is indicated by the two additional lines (B). On both the line of 23% CSG reflectivity and these lines of increased sampled grating reflection, viable set-points need to be available (i.e. within the shaded region). In addition, a variation of sampled grating reflectivity needs to be supported over the tuning range. In the figure the

limits for a 1 dB and 2 dB allowed variation are given (respectively C and D). Only for the 1 dB variation viable set-points are available. The lines E indicate the limits this puts on the reflectivity of the separate sampled gratings. For the 23% CSG reflectivity both sampled gratings need to provide a reflectivity of 6% at high values of current injection. By completing the area of operation (the area F) a minimum sampled grating reflectivity is found of 18% over the tuning range without current injection. The variation of resonance reflectivity over the tuning range needs to be less than 1 dB. At the setpoint of maximum reflectivity for both sampled gratings the CSG-reflectivity is 52% (G).

10. **Burst section length** $L_b/(L_b + L_p)$ In figure 4.17 the variation in resonance reflectivity over the tuning range is plotted versus the minimum reflectivity. To obtain a sampled grating with at least 18% reflectivity and a variation over the tuning range of less than 1 dB, a grating burst length of at most 15% of the grating periodicity is allowed. Since the highest possible value also allows for minimization of the total CSG length, this value is chosen.

11. **Sampled grating configuration** $N_1,\ L_{b1}\ and\ N_2,\ L_{b2}$ The final design for the first sampled gratings is a grating burst length of 4.8 $\mu m (L_{p1} = 27.2\ \mu m)$. For the second sampled grating it is 6 $\mu m (L_{p2} = 34\ \mu m)$. With these settings the first sampled grating requires 11 periods to provide the 18% reflectivity, while the second sampled grating requires 12 periods (since the resonance spacing is lower). This implies lengths of 352 and 480 $\mu m$ for the first and second sampled grating respectively. The total CSG length is 832 $\mu m$.

### 4.2.4 Optical layerstack

Cross-sectional views of the layerstack in the CSG laser are provided in figure 4.18. The buried waveguide in the gain section is formed by a multi-quantum well (QW) with quaternary confinement layers (to provide optical confinement and waveguiding). In the tuning sections a bulk quaternary tuning layer is used. An Fe-doped current blocking layer is grown next to the waveguide. Below and above the waveguiding layers, the InP material is n- and p-doped, respectively.

A grating layer remains in the grating-burst sections below the tuning layer and is removed in all other parts of the device. The integration of the two layer-stacks in the device is achieved through a buttjoint regrowth.

A more detailed processing sequence is provided in appendix A.

#### Gain section layerstack

The purpose of the gain section is to provide optical gain and enable lasing operation over the full wavelength tuning range, with a low threshold current and minimal variation in the operation current. Only the fundamental transverse mode is allowed to propagate in the gain section to reduce the risk for low SMSR. The buttjoint connection between gain and tuning section is to be optimized to reduce reflectivity and loss within the laser-cavity.

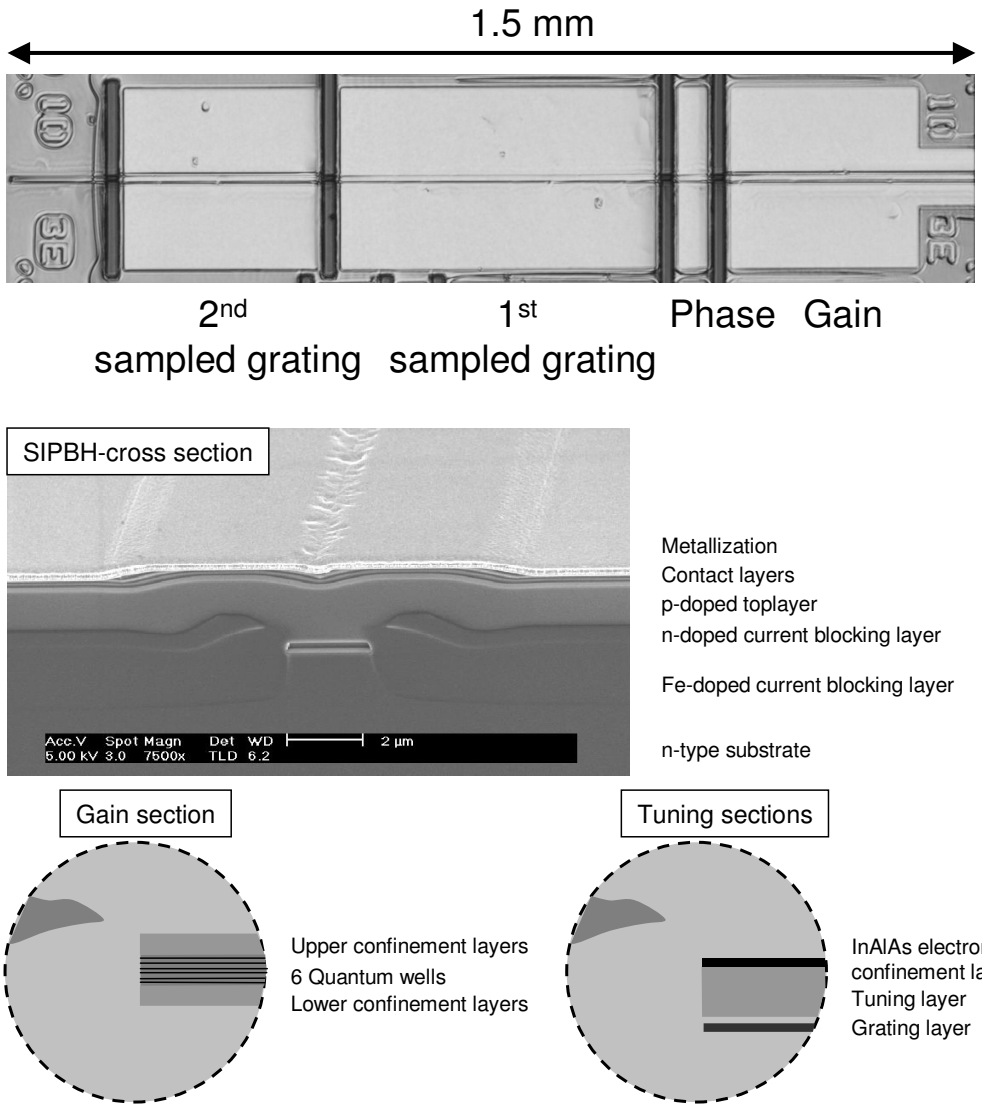


*Figure 4.18: Top-view and cross-section of a CSG laser. The optical microscopy picture shows a 4-section CSG laser. The SEM-images shows the cross-section through the SIPBH-structure (an etchant has been used to accentuate doping and material contrast). The cross-section is similar in each section. The insets detail the layers in both gain and tuning sections*

The gain section layerstack, used here, is based on prior work on other laser-products (such as DFB lasers and DBR lasers). In this existing design, 4 InGaAs quantum wells are surrounded by a 3-layer confinement structure (see figure 4.18), to facilitate carrier transport to the well and avoid carrier escape. The bandgap profile of these confinement layers is stepwise and matches a parabolic profile versus the distance from the quantum well. The bandgap increases from 1.03eV (for Q1.20 barrier material) to 1.35eV (for InP). The threshold gain ($\alpha_i + \alpha_m$) for 500 $\mu m$ long lasers with this 4 QW gain section design is in the range of 30 to 40 $cm^{-1}$, with a threshold current below 20 mA. This is derived from calculations on DFB lasers and comparison to fabricated lasers. For this design the optical confinement is 1.75% (a gain of about 20 $cm^{-1}\%^{-1}$). DFB lasers with this structure operate in the linear regime of the gain versus current-density curve and a change in mirror-loss has a minor impact on the threshold current and operation current. This is apparent from the limited variation in average threshold current between production DFB wafers.

To build upon the design optimization already performed for this layerstack, and the proven reliability, here the profile of the confinement layer and the type of quantum wells is fixed. Only the number of quantum wells and the total thickness of the confinement layer is varied for design optimization. The CSG design provided in the previous section gives an estimate for the mirror-loss (with $R_B = 23\%$ and $R_F = 17\%$) of $\alpha_m = 41\ \ cm^{-1}$ and hence the required gain is $g_{th} = \alpha_m + \alpha_i \approx 55\ \ cm^{-1}$. To provide margin against design-variations and to provide the flexibility to reduce the gain-section length the design target is set to a gain of more than 60 $cm^{-1}$. Hence, a quantum well confinement higher than 3% is required. As stated in section 4.2.1 this minimum gain is required to start lasing at a sufficiently low current density. Higher values of confinement are only beneficial to lasing operation if the active volume of the gain material does not increase (i.e. when the number of quantum wells is fixed).

In figure 4.19 the optical confinement in the quantum wells is plotted versus the thickness of the confinement layers (i.e. the thickness of the 3-layer confinement structure at one side of the quantum well) for several numbers of quantum wells. For a 6QW layerstack the plot is made for a range of values for waveguide-width. The minimum requirement for the optical confinement is also indicated in the figure. Only the 6QW layerstack fulfills the gain requirement and provides a wide design range for both waveguide width and confinement layer thickness. It is preferred not to use more quantum wells, since this increases the threshold current density and increases the risk of problems with carrier transport to the quantum wells. For the same reason a narrow waveguide width is preferred.

For single mode operation, higher-order modes are required to be cut-off (i.e. not guided by the laser-section). Therefore in figure 4.19 only design-points are plotted where higher order modes are not supported by the waveguide. From the figure a 6QW, 1.8 $\mu m$ wide waveguide with a thick confinement layer results in a high value of confinement, without exciting higher order modes. Such a value of waveguide width also ensures that the resistance of the layerstack is acceptable.

As expressed in formula 3.12 the laser-gain is not uniform over the full tuning range. This results in an additional gain-difference between resonances over the wavelength range. Design of a laser-structure that minimizes this difference is outside of the scope

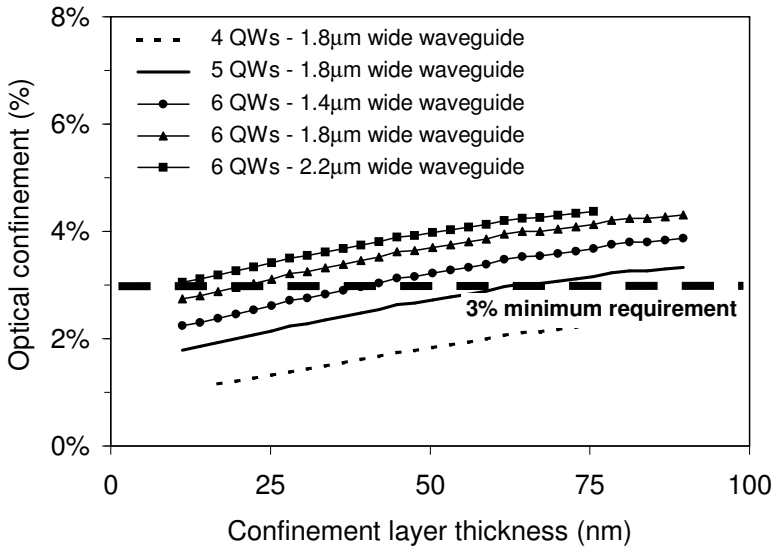


*Figure 4.19: Quantum-well optical confinement versus confinement layer thickness for a different number of quantum wells. The dotted line indicates the confinement requirement for the gain section. Only combinations where the first order mode is suppressed are drawn. The calculations have been performed with the FIMMWAVE package.*

of this work. This is however an area, where the performance can be improved. Several methods exist to manufacture an inherent wider gain versus wavelength characteristic, such as n-doping of the barriers in the quantum well [19] and chirping of the quantum well [82]. Here it is assumed that the layerstack already provides a sufficiently wide gain-peak. A short gain section helps in reducing the gain variation over the tuning range.

The composition of the material needs to be chosen such that the gainpeak overlaps with the Bragg wavelength. Alternatively, a gainpeak at a lower wavelength than the Bragg peak can be used to compensate for material absorption. It also compensates for higher operating temperatures (through device heating).

The gain section design is fixed to a 6-QW laser design. The waveguide width is set to 1.8 $\mu m$. Hence, the confinement layer thickness needs to be larger than 25 nm, to obtain sufficient confinement. The choice for this thickness is not made here, but is rather based on the maximization of the optical overlap with the mode in the tuning section, at the butt-joint.

### Tuning section layerstack

The purpose of the tuning section layerstack is to provide a high wavelength tuning range and tuning efficiency (change in wavelength per mA current injection). Furthermore the grating strength is to be maximized (for improved sampled grating performance) and the higher order modes are ideally cut-off (both in the lateral and transverse direction).

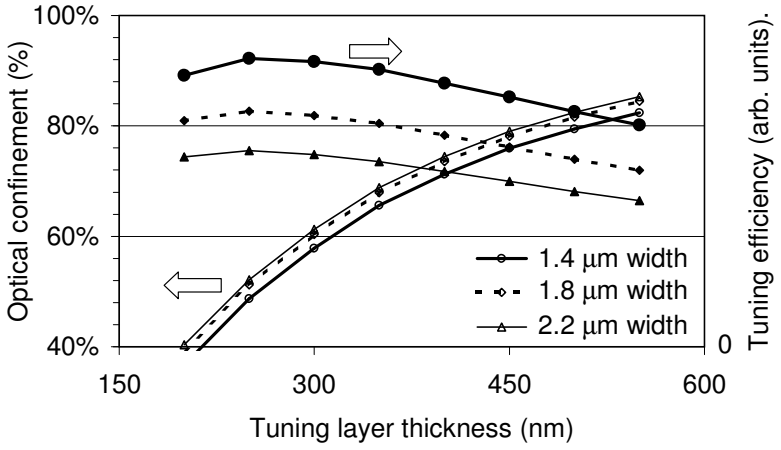


*Figure 4.20: Overlap of the fundamental mode with the tuning layer versus tuning layer thickness. Also the tuning-efficiency is included.*

The wavelength tuning range is given as $\Delta\lambda = \frac{\Delta\mu_{mat,max}}{\mu_{eff}} \cdot \Gamma \cdot \lambda$, where $\Delta\mu_{mat,max}$ is the maximal achievable change in material refractive index and $\Gamma$ is the overlap of the optical mode with the tuning layer. $\Delta\mu_{mat,max}$ is both dependent on the material composition and the maximum achievable carrier-density in the tuning layer. The tuning efficiency is a measure of the amount of injection current needed, to achieve a given change in Bragg wavelength. This parameter depends on the applied current, but scales with $\frac{\Gamma}{V_a}$.

The design parameters for the tuning sections are the thickness of the tuninglayer and the width of the waveguide. In figure 4.20 the confinement of the optical field in the tuning layer and the tuning efficiency are plotted versus the tuning layer thickness. An increase in tuning layer thickness improves the overlap of the optical field with the tuning layer (and the wavelength tuning range), but reduces the tuning efficiency (since the increase in confinement is sub-linear with the active volume). At 400 nm thickness a sufficient optical confinement is obtained without sacrificing the tuning efficiency.

The optical confinement has minimal dependence on the waveguide-width. In the range of interest (1.4 - 2.2 $\mu m$) the choice for a narrow waveguide allows for a high tuning-efficiency. Limitations of the contact-lithography process (especially reproducibility) motivate a choice for waveguide-width of 1.5 $\mu m$. With this choice of waveguide-width, the second order transverse mode is cut-off and cannot propagate in the tuning section. The first order mode is also cut-off, but is of lesser concern, since coupling between the symmetric fundamental mode in the gain section and the asymmetric first order mode in the tuning section is negligible. For connection to the wider waveguide in the gain section and to reduce the coupling loss at the butt-joint a lateral taper is used.

With the geometry of the tuning section layerstack defined, the tuning layer material needs to be chosen. In figure 4.21a material absorption at a wavelength of 1550 nm is plotted versus the tuning material bandgap wavelength, at different levels of carrier-density. The material absorption increases for a bandgap wavelength close to the evaluation wavelength. The increase in free-carrier absorption, with increasing carrier-density,

is insignificant, when the bandgap wavelength is close to the evaluation wavelength. For a bandgap wavelength up to about Q1.45, the maximum absorption over the carrier-density range is constant. Therefore a design choice close to this bandgap wavelength is most suitable to reduce the variation in operating current in the gain section. This increases the absorption (and reduces reflectivity) at low tuning current, but it should be realized that the goal is to obtain a small power variation over the tuning range. Since the target tuning-range for the tunable laser is from 1525-1565 nm, a Q1.425 tuning layer material is chosen. A higher quaternary composition leads to increased absorption, while a lower quaternary composition results in a lower resonance tuning range and more variation in output power over the tuning range.

To verify that this material can provide sufficient wavelength tuning range figure 4.21b plots the relation between the change in refractive index and material absorption. Again the bold curves correspond to different values of carrier-density level in the tuning layer and are drawn for a range of quaternary compositions, starting from Q1.3 (on the left side of the curve) to Q1.5. For a bandgap wavelength, too close to the lasing wavelength, the absorption increases rapidly, without a significant benefit to the tuning range. A refractive index tuning range of approximately 0.036 is needed (with 70% confinement). In the figure a thin dotted line indicates the relation between refractive index change and absorption for the material composition of choice (Q1.425). The curve is drawn for increasing values of carrier-density in the tuning layer. This confirms the choice for Q1.425 material, which achieves the 10 nm tuning range at a carrier-density of $2.5 \cdot 10^{18}\ cm^{-3}$).

To increase the achievable carrier-density of the tuning layer, an $InAl_{0.40}Ga_{0.07}As$ layer is added on the p-side of the tuninglayer. This material has a conduction band offset that is larger than for quaternary material. This means that after alignment of the Fermi-energy a step in the conduction band energy is created, while the valence band energy remains continuous. As a consequence, electrons are blocked from escaping the tuning layer, while holes face no extra barrier for injection into the tuning layer. Since the carrier-density is partly limited by the escape of electrons from the tuning layer into the p-type region an increased carrier-density and tuning range can be realized [112]. For a tunable DBR laser an increase in tuning range of about 10% was achieved [1].

From the CSG design it follows that maximization of the grating strength is preferred (section 4.2.2). The grating strength is improved by increasing the grating layer thickness and decreasing the distance between tuning layer and grating layer. The manufacturing method limits the grating-layer thickness to about 100 nm (thicker layers can not be etched within the used technology) and the active layer regrowth technology requires a minimum spacer layer thickness of about 25 nm to ensure planar regrowth [31].

In figure 4.22 the dependence of grating strength on spacer thickness and tuning layer thickness is shown. The dependence of grating strength on waveguide width is minimal. Grating strengths up to 20 $mm^{-1}$ are achieved for a thin tuning layer. However, optimization of the tuning section required a tuning layer of 400 nm. Therefore the grating strength is limited to about 15 $mm^{-1}$ with a 25 nm spacer-layer and a 80 nm thick grating layer. It was verified that the pull of the grating-layer on the optical mode resulted in less than 3% variation in optical confinement for the tuning layer. A slight further increase of the grating strength is possible by an increase in the bandgap

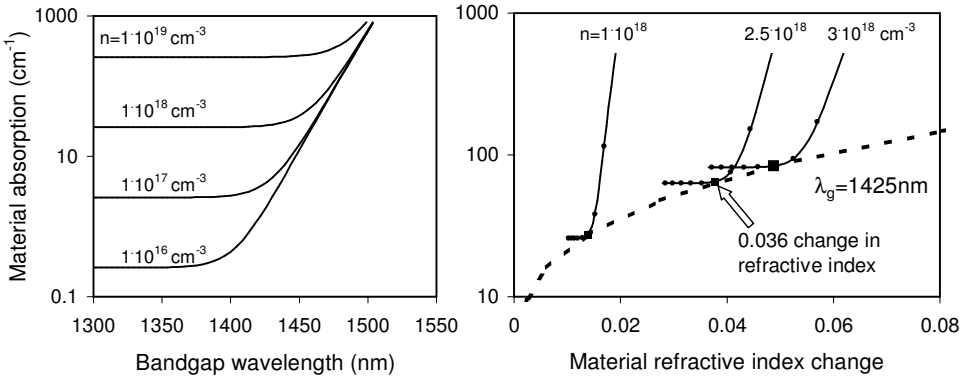


*Figure 4.21: Calculations at 1550 nm; a) material absorption as function of bandgap wavelength and carrier-density; b) relation between refractive index change and material absorption for different levels of carrier concentration. Each line corresponds to different values of bandgap wavelength. Dots are indicated where the bandgap wavelength is a multiple of 25 nm, starting at 1300 nm.*

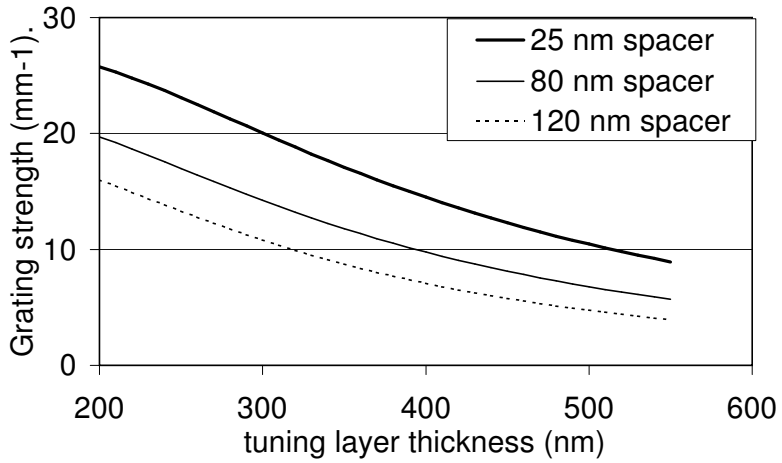


*Figure 4.22: Optical overlap with tuning section versus tuning-layer thickness, for different values of spacer-layer thickness. Grating layer thickness is set to 80 nm.*

wavelength of the grating layer. This will however also lead to an increase in absorption.

### Overlap at buttjoint

The connection between gain and first phase section is of major importance to avoid unwanted feedback (resulting in wavelength dependent interference terms) and loss (reducing the device output power).

From a technology stand-point this is achieved by a high quality auto-aligned interface, which is implemented in the growth sequence.

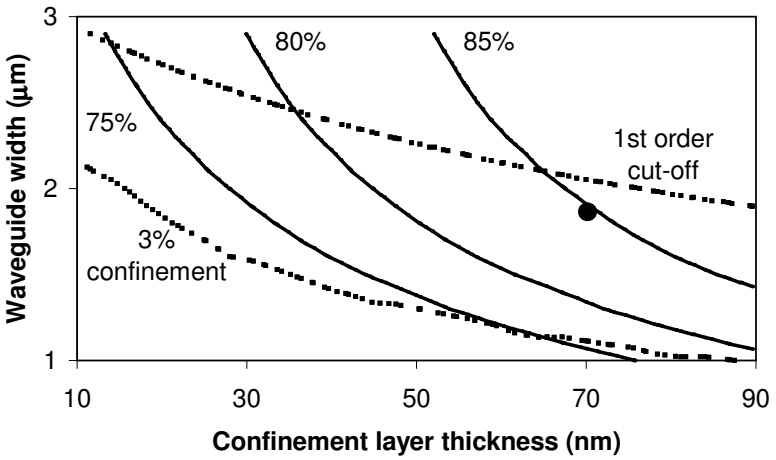


*Figure 4.23: Buttjoint transmission and reflectivity between 0th order modes. Contour lines increase from 75% to 85% transmission (left to right). The lower thick line indicates the gain section requirement of 3% confinement. The upper thick line indicates the combination of parameters at which the first order mode is cut-off.*

From a design stand-point the optical overlap of the fundamental optical mode in both layerstacks is maximized. This needs to be done within the constraints set by the design for gain and tuning section, leaving the waveguide width and gain section confinement layer thickness as variables for optimization (the tuning section is considered most important and hence the tuninglayer thickness is fixed). Both due to alignment of mask and the methods used for the waveguide etch, the width of the waveguides at the buttjoint interface is the same, but by tapering the width in both tuning and gain section can be different.

Using the eigenmode expansion algorithm in section 3.2.2 the coupling of the optical modes in the gain section to modes in the tuning section is calculated. In figure 4.23 the optical loss at the buttjoint is plotted as a function of waveguide width and confinement layer thickness (in the gain section). In the figure the design constraints are also shown (at least 3% optical confinement in the gain section and a maximum width to cut-off higher order modes in the gain section). The optical loss is caused by forward coupling of the optical mode into radiating modes or backward coupling in either the fundamental mode or radiating modes. The backward coupling into the fundamental mode (reflectivity) is less than 0.1%, for all considered values.

The waveguide width in the gain section and at the buttjoint is designed to be 1.8 $\mu m$, with a confinement layer thickness of 80 nm. This ensures a buttjoint coupling loss of -0.7 dB per pass.

### Design summary

In table 4.1 (second column), the design choices for the CSG are listed.

| **Parameter** | Design and simulation value | Experiment value |
|---|---|---|
| Gain section length | 400 $\mu m$ | 400 $\mu m$ |
| Front facet reflectivity | 17% | 27% |
| Gain section waveguide width | 1.8 $\mu m$ | 1.8 $\mu m$ |
| Gain section confinement thickness | 80 nm | 89 nm |
| Propagation length sampled grating 1 | 27.2 $\mu m$ | 37.2 $\mu m$ |
| Grating burst length sampled grating 1 | 4.8 $\mu m$ | 4.2 $\mu m$ |
| Number of sections sampled grating 1 | 11 | 7 |
| Propagation length sampled grating 2 | 34.0 $\mu m$ | 24.1 $\mu m$ |
| Grating burst length sampled grating 2 | 6.0 $\mu m$ | 8.9 $\mu m$ |
| Number of sections sampled grating 2 | 12 | 3 |
| Grating strength | 15 $mm^{-1}$ | 15 $mm^{-1}$ |
| Tuning section composition | Q1.425 | Q1.43 |

*Table 4.1: Summary of design parameters for CSG laser. The first column lists the final design parameters, as used in the simulation. The second column lists the design of the presented experimental laser. Significant deviations exist since some wafers were processed before all design insights were complete.*

## 4.3 CSG operation

The previous section was devoted to the design of a CSG laser. In this section the operation of such a CSG laser is demonstrated. For this purpose first the optimal design is modeled to demonstrate the tuning mechanism of the CSG laser. Then the experimental results on a processed device are presented. A more extensive analysis is performed on a larger sample population to improve correlation between experiment and simulation. Finally, two potential causes for the deviations between presented simulation and experimental results are presented.

### 4.3.1 Device performance

#### Device simulation

The optimized design, in the middle column of table 4.1 is simulated using the tool from section 3.4. For this simulation interaction between the optical field and the carrier-density is neglected (in the simulation this is achieved by setting the incident power to the tuning section to zero). The phase-shift, introduced by the phase section, is adjusted to align the cavity modes with the resonance in the CSG reflection spectrum. Also, in other resonances, it is assumed that cavity modes are aligned to this resonance. This means that an underestimate is made for the device SMSR.

The wavelength of the laser is plotted versus the tuning current, in the first sampled grating, in figure 4.24a. Hops between sampled grating resonances, towards higher wavelength, are observed with increasing tuning current, consistent with tuning of the section with largest resonance spacing. However, the curves are not continuously rising and hops towards lower wavelength are observed. Mostly, this is caused by a low selectivity between sampled grating resonances at the transition points, where cavity modes in other sampled grating resonances can be activated. This is visible on several transitions. In the stable regime between the transition points the selected wavelength behave regularly and all intermediate wavelengths can be accessed.

A total accessible tuning range of 40 nm (1530-1570 nm) is predicted. The required round-trip gain varies between 3800 and $5600m^{-1}$ (a CSG reflectivity of 18 to 84%, with a 17% front facet reflectivity) and the model predicts a range for the operating current in the gain section between 120 mA and 180 mA (for 30 mW ex-facet operation). At these current levels the assumption of no roll-over is not valid anymore. Therefore, these calculations provide an underestimate of the actual required gain section current. The threshold current is calculated to vary between 30 and 50 mA.

A feature to notice in the figure is that at 0 mA tuning currents the wavelength is equal to the Bragg wavelength. This is a consequence of the continuous applied grating pattern over the tuning section. At the zero current setting the length of all propagation sections is exactly equal to a multiple of the grating pitch and the propagation sections have no net phase effect. The CSG then operates similarly to a DBR laser.

The ex-facet output power at 150 mA is plotted in figure 4.24b. The effect of free-carrier absorption is clearly visible, but the decrease in output power is limited to 2.5 dB over the tuning range. In a real device the increase in free-carrier absorption is partly compensated by an increase in material gain (see section 4.3.4). For Q1.425 tuning

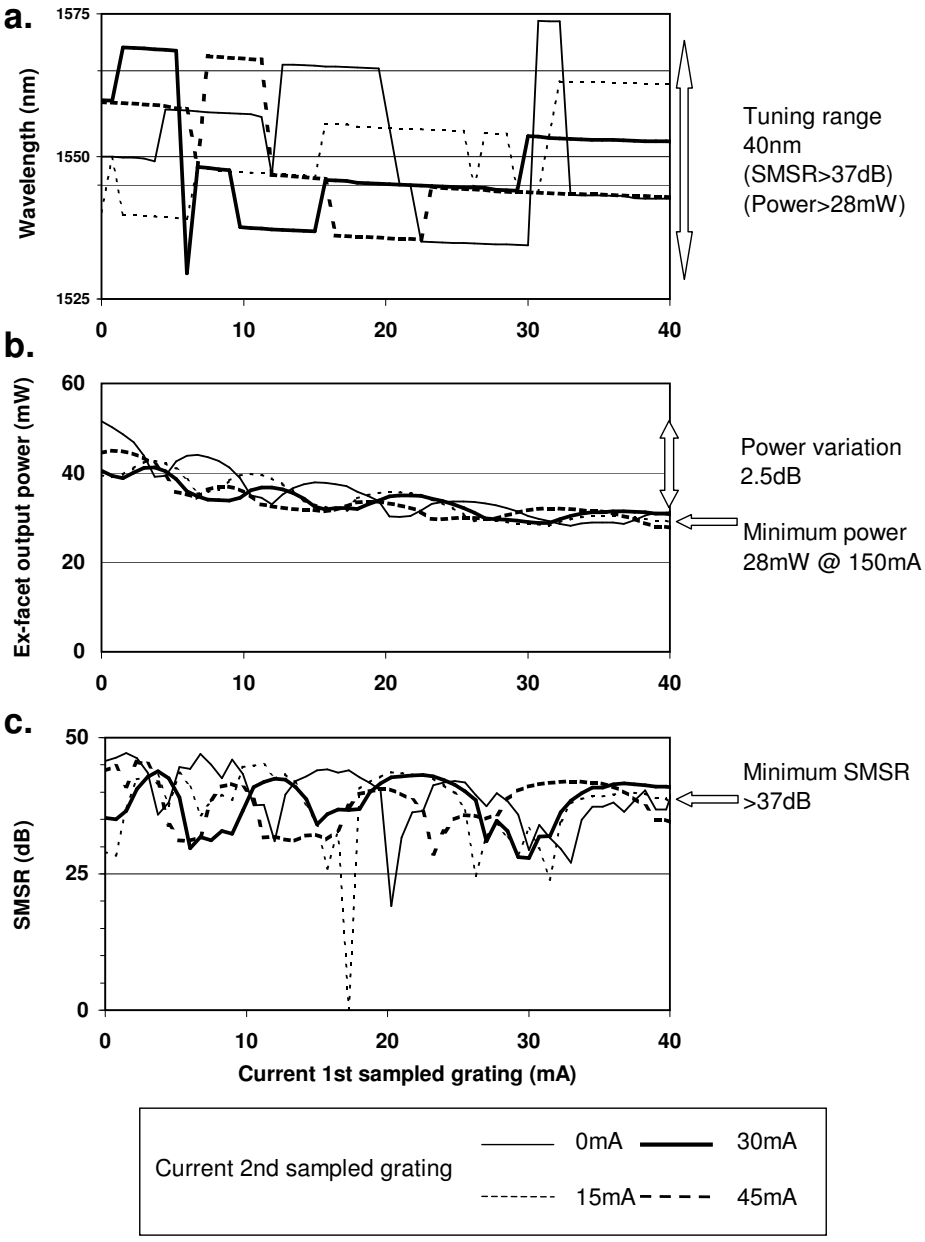


*Figure 4.24: Simulated tuning behavior of a 4 section CSG laser. Current injection is uniform over the complete sampled grating sections. The top-graph (a) plots the wavelength, the middle graph (b) plots the ex-facet output power versus the current in the first sampled grating, for several current levels in the second sampled grating. The bottom graph (c) plots the SMSR.*

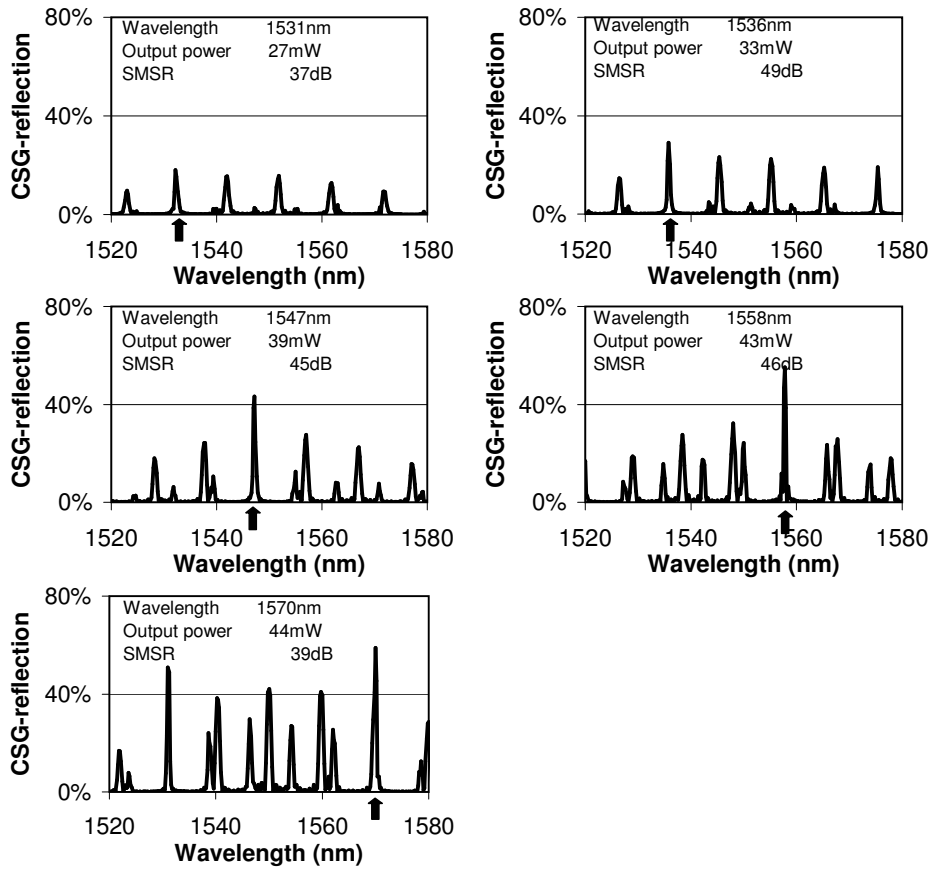


*Figure 4.25: Calculated CSG reflection spectra over the tuning range of 53 nm.*

material, this reduces the power decrease over the tuning range.

The Side-Mode Suppression Ratio, for this device configuration, is shown in figure 4.24c. Over a 40 nm tuning range it is better than 37 dB when the cavity mode is aligned with the sampled grating resonance (each local maximum in the tuning curve). The SMSR is fairly independent of the tuning current and shows a decrease of up to 8 dB over the current range. This variation of SMSR over the tuning range is explained by the variation in output power and increase in mirror-loss (see formula 2.8). The gain difference, between modes, is only marginally affected by the increased absorption.

In figure 4.25 the CSG reflection spectrum is plotted at several points in the modemap. The tuning range of 40 nm is visible, though the CSG reflectivity reduces significantly towards lower wavelength, due to material absorption. A maximum reflectivity is obtained around 1550 nm. Each spectrum provides a gain-difference for cavity modes of at least 0.7 dB, resulting in a minimum SMSR of 37 dB.

The presented results, thus far, were based on the assumption that the phase section current was optimized to align the selected cavity mode with the CSG resonance. This is

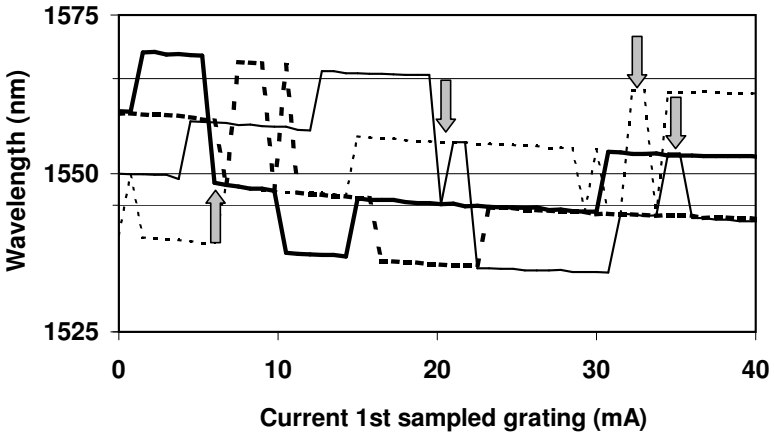


*Figure 4.26: Wavelength versus tuning current, without alignment of cavity modes with the main CSG resonance. This figure demonstrates that in the measurement on the actual device irregular modehops (as indicated by the arrows) can occur.*

not easily achieved during device characterization, due to the time it takes to optimize the phase section current. Therefore, during a typical measurement this current is fixed and alignment of the cavity modes with the CSG resonance is not assured. As a consequence, competition with better-aligned cavity modes in a lower reflectivity CSG resonance, can force the laser to select a secondary CSG resonance. In the wavelength tuning chart this shows up as a seemingly irregular change in wavelength, larger than the cavity modespacing. In figure 4.26 the wavelength tuning is plotted versus the tuning current with a fixed phase section current. Comparing this with the original plot (figure 4.24a), it is observed that more irregular wavelength jumps between resonances occur, in some of the mode-plateaus (indicated by arrows). This is caused by a mode in a side-mode that is higher than any of the modes in the main resonance. The result is that characterization of a real device becomes more complex.

It is verified that even though the tuning seems irregular, this irregularity only occurs at points in-between set-points, where the selectivity is low. For the device, the available tuning range with an SMSR better than 37 dB is still 40 nm, since the cavity modes are aligned to the CSG feedback by optimizing the phase section current.

These simulations show that the CSG conceptually can deliver the requirements of 30 mW output power over the tuning range (at a slightly higher current than 150 mA), with an SMSR better than 35 dB. In the effort to design a high output power device, the selectivity of the CSG section was sacrificed (through the choice of a high resonance spacing and large burst section length). This results in low mode selectivity at wavelength jumps between resonances, resulting in irregularity of the tuning curve. For a device, operating at a lower output power, a design can be chosen with more selectivity in the CSG response. This increases tuning regularity and tuning range.

In this analysis the direct interaction between optical field and carrier-density was not taken into account. For higher values of output power this can result in saturation and non-linearity. Also optical gain at higher values of tuning current was not considered.

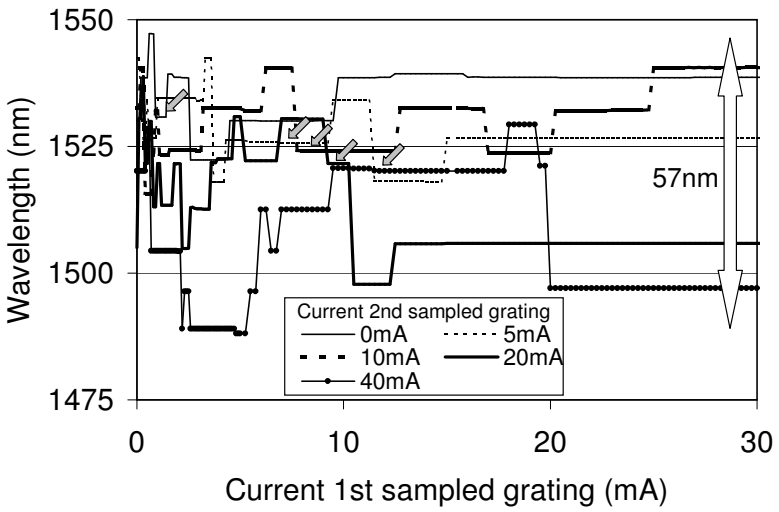


*Figure 4.27: Wavelength of experimental CSG laser versus first sampled grating tuning current for several tuning currents in the second sampled grating. Tuning is irregular with an available tuning range of 57 nm (1489-1546 nm).*

This enables a higher power device (or lower tuning currents).

**Experimental device performance**

An experimental record of the wavelength tuning of a CSG laser from wafer B (see appendix B for details on the experimental material) is shown in figure 4.27. The device design is given in the third column in table 4.1. The major deviation from the simulated device is the number of sections in the second sampled grating, since full device wafers were processed before all design insights were complete. Also no coating was applied to the front-facet. A simulation on the design of the experimental devices showed a wavelength tuning range of 31 nm with an SMSR larger than 35 dB and a gain section operating current between 130 and 220 mA. This compares to a wavelength range of 40 nm and an operating current range between 120 and 180 mA for the optimal design.

This device shows a tuning range of 57 nm (1489-1546 nm) and SMSR is measured to be better than 30 dB over a continuous range of 34 nm (consistent with the simulation for this design). The output power from this device at 100 mA varies between 5 and 10 mW, compared to a simulated power between 8 and 20 mW at 100 mA. This device does not generate the desired 30 mW ex-facet power, partly because of the uncoated front-facet (the simulation tool predicts at 10 mW penalty, compared to the 17% coating) and partly because of a strong roll-over of the LI-curve, possibly due to a poor gain section material.

The wavelength tuning, even compared to the simulations, is irregular. In the figure it is observed that the mode-plateaus are shifting with applied current through the second sampled grating (see the arrows), as expected from a regularly tuning device. The large number of hops between resonances indicates a poor selectivity between CSG resonances.

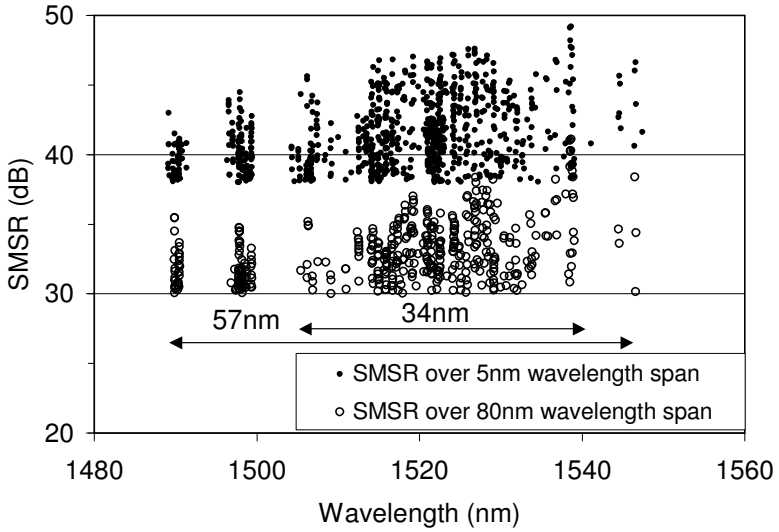


*Figure 4.28: SMSR of experimental CSG laser versus operating wavelength. A distinction is made between SMSR within 5 nm (i.e. between cavity modes within the same CSG resonance) and within 80 nm (i.e. including the modes within secondary CSG resonances) around the lasing wavelength.*

Due to the irregular tuning, not all wavelengths within the 57 nm range are addressable with a sufficient value for SMSR.

In figure 4.28 the SMSR is plotted versus the wavelength. A distinction is made between the SMSR over a range of 5 nm around the lasing wavelength (i.e. the suppression of cavity modes by the selected CSG resonance) and 80 nm around the lasing wavelength (i.e. including mode competition with modes in other CSG resonances). Clearly the SMSR-limitation for this device is due to mode-competition with modes in secondary CSG resonances. An SMSR of more than 30 dB is maintained over a tuning range of 57 nm. For a tuning range of 34 nm all intermediate wavelengths are addressed.

These experimental and simulation results confirm the operating principle of the CSG laser. Even thought the experimental data only has scant comparison to the simulation data, full tunability has been demonstrated over a 34 nm wavelength range (and over 57 nm with SMSR lower than 30 dB). The remainder of this chapter is devoted to understanding the difference between the performance of this experimental device and the simulations.

### 4.3.2 Simulation tool verification

#### Sampled grating reflectivity

In the previous section a comparison was presented between an experimental device and a simulation. Although a good qualitative agreement was established, quantitative agreement was limited. Therefore, first the modeling tool needs to be experimentally

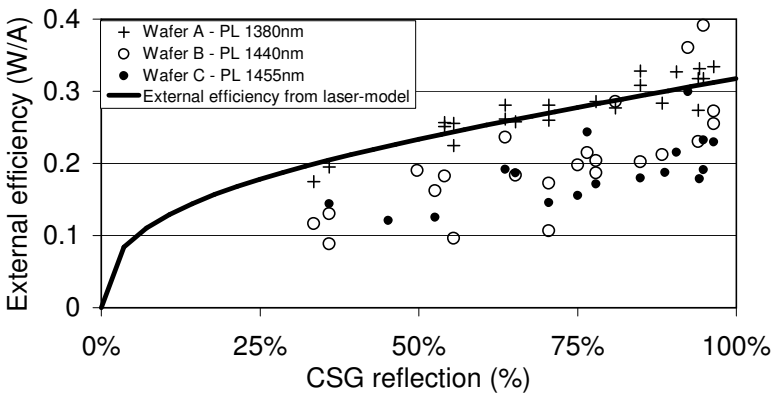


*Figure 4.29: Relationship between the measured external efficiency for the three fabricated CSG wafers with the calculated CSG reflectivity. The solid line gives the relationship for loss-less tuning layer, comparable to a PL wavelength less than 1400 nm.*

verified.

A larger sample population of about 90 CSG laser, including several design variants (variants in sampled grating periodicity, burst section length and number of sampled grating sections) is used for this verification. For each device the output power versus gain section current is measured at 0 mA tuning currents. From this measurement the external efficiency is determined. For each device, the CSG reflectivity is calculated based on the device configuration. The correlation between external efficiency and CSG reflectivity is studied, since a wide range of values for external efficiencies have been measured (due to a range of CSG configurations on the wafers) and in the calculation of the external efficiency only a limited number of assumptions have to be made (see formula 2.6).

In figure 4.29 the measured external efficiency is plotted versus the calculated CSG reflectivity. Also, the calculated relationship, for a loss-less tuning layer material is shown. Firstly, the external efficiency decreases with a decrease in CSG reflectivity, since the amount of power leaving the cavity at the back-facet side increases. Secondly, the external efficiency is higher for tuning-material with a lower bandgap wavelength. Clearly, the effect of material absorption on the output power of the device is seen. For the wafer with Q1.35 tuning layer material (low material absorption) the distribution of data points closely follows the predicted curve.

The wafers B and C clearly have a lower external efficiency over the full range of CSG reflectivity. However, for higher values of reflectivity the difference becomes smaller. This is explained by realizing that the lower the reflection value, the deeper the optical field penetrates into the tuning section (i.e. the effective length increases). As a result a larger fraction of the light is absorbed.

In conclusion, this section has demonstrated the impact of tuning section composition on the external efficiency of a tunable laser. For material with low absorption, close correlation was found between theoretical prediction and experimental data. This shows that the simulation model provides an accurate description of the reflection values of a

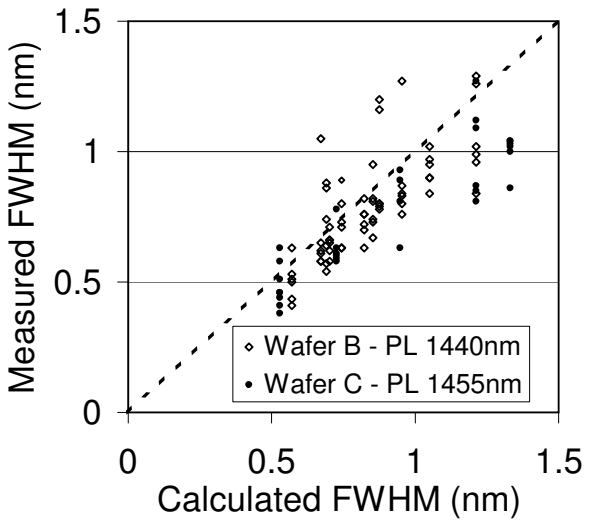


*Figure 4.30: Relationship between calculated and measured width of the main CSG resonance for two of the fabricated CSG wafers.*

CSG section. In addition, it was argued that the reduction of external efficiency with an increasing tuning layer bandgap wavelength, is minimized at high values of CSG reflectivity.

**Sampled grating selectivity**

The measured external efficiency is a measure for the reflectivity of the tuning section and has a large impact on the achievable output power. The side-mode suppression is determined by the resonance selectivity of the CSG section.

The method described in appendix C was used to measure the reflection spectra of CSG lasers, from which the FWHM (Full Width Half Max) of the resonances is determined. In figure 4.30, the measured CSG resonance FWHM is plotted versus the calculated FWHM for the CSG sections.

Again, close correlation is found between the theoretical predictions and the experimental results. Material absorption is not expected to significantly affect the spectral width of the resonance, as confirmed by the data (the overlap of data-points from two different wafers, with different tuning layer bandgap wavelength). This leads to the conclusion that the simulation tool provides a good description of the CSG properties.

### 4.3.3 Isolation channel between sampled gratings

The previous section showed that the simulation model provides a good description for both the reflectivity and the spectral selectivity of a CSG reflection spectrum. The correspondence between simulated and experimental data, at a device level is, however, poor thus far. The deviation between simulation and experiment, therefore, seems to be

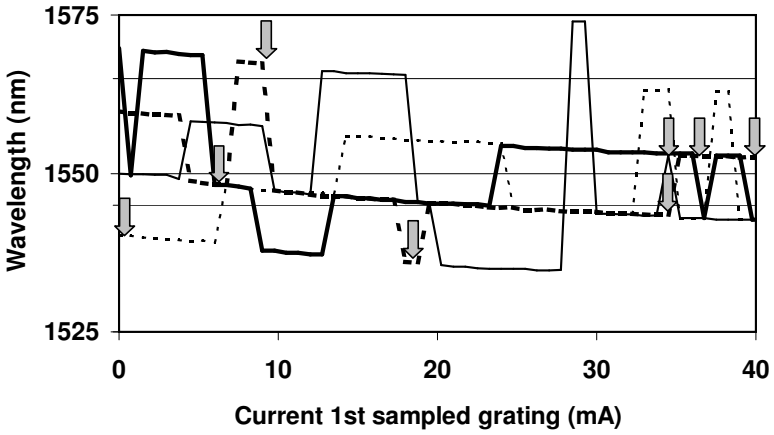


*Figure 4.31: Simulated tuning behaviour of CSG laser. Current injection in the region of the isolation channel, between both sampled gratings, is set to zero. Arrows indicate where the wavelength tuning deviates from the simulation, where the isolation channel was neglected.*

in the description of the experimental devices.

In practical devices, an isolation channel is present between the first sampled grating and the second sampled grating, to prevent current leakage and electrical cross-talk (see figure 4.1). As a result, a small region exists, in both sampled gratings, without current injection (the last period of the first sampled grating and the first period of the second sampled grating). These sampled gratings are therefore not completely pumped and the current density, along the length, is not uniform. This results in an anomalous phase-change near the isolation channel and reduced selectivity of the CSG.

The effect on the laser wavelength of such an isolation channel of 20 $\mu m$ is demonstrated in figure 4.31. For this simulation it was assumed that the isolation channel was centered over the last grating-burst section of the first sampled grating. The isolation channel thus extends 8.9 $\mu m$ into the propagation regions of both sampled gratings. The refractive index below the isolation channel is taken to be independent of the tuning currents.

Clearly, the wavelength tuning behavior becomes less regular, with additional hops between resonances (indicated by the arrows, compare to figure 4.24). From the simulation it follows that the output power over the tuning range is not affected, but these intermediate hops reduce the SMSR. This reduces the tuning range to 26 nm (1534-1560 nm), with a wavelength region between 1560 nm and 1567 nm, where no wavelength is addressed.

Because of the isolation channel between the two sampled grating sections full wavelength accessibility is threatened. A solution to this problem is the 5 section CSG (figure 4.1). This device configuration requires two isolation channels in a second phase section making the current injection in the sampled gratings uniform. However, a second phase section is introduced to control the phase between the two sampled gratings (in order to restore the positive interference of the reflection terms). The added complexity of this design, both in characterization and control, makes the 5 section CSG laser less favorable

to existing widely tunable laser types with four or less contacts.

As suggested the isolation channel in the design is a possible cause for the irregular tuning in the experimental device. The simulations have proven this to be a reasonable assumption, though they are not conclusive. In addition, in the measurement of the experimental device the phase section current is not adapted to align the cavity modes with the CSG resonance, resulting in lower mode-selectivity. At the very least, these effects make the design more susceptible to other effects that affect the selectivity of the CSG section. Examples are the flatness of the gain curve of the gain section material, the increase of temperature with tuning currents and spatial and spectral hole burning. Finally, it has to be noted that the experimental device deviated from the optimum design.

### 4.3.4 Electro-optical interaction in CSG

Free-carrier absorption in the tuning section reduces the CSG reflectivity over the tuning range. In addition to this, the optical power incident on the CSG is absorbed and generates a position dependent photo-current in the tuning sections. Also, with sufficiently high carrier-density, gain is generated in the tuning layer. In the following section the effect of absorption in the CSG on the mode-pattern is demonstrated, and it is shown that this can be a cause for the irregular tuning that was observed. In the following section an experimental demonstration is presented of the effect of gain in the tuning section with increasing current injection.

#### Saturation effects in the CSG laser

Following the methodology described in section 3.4 the reflection spectrum of a CSG section at different levels of incident power is calculated with a stepwise increase in the incident power on the tuning section. After each calculation the photo-current is recalculated. This approach is needed to achieve a self-consistent solution. With this approach it is not tried to calculate a complete mode-map of the tunable laser, since this cannot be un-ambiguously defined. At any given output power and current setting, multiple set-points can exist with a specific combination of power incident on the CSG section and CSG reflectivity. This hysteresis effect reduces the usefulness of a calculation of wavelength tuning versus current.

In figure 4.32 reflection spectra from a CSG section are shown at different levels of incident power. A combination of tuning currents was chosen, where the sampled grating sections are aligned with regard to one-another and both power and SMSR is high. A tuning layer material composition is used of Q1.425 and Q1.325. Since the absorption of the Q1.325 material is lower, the photocurrent and sensitivity to incident power is lower. In the spectra for the Q1.425 material it is seen that for incident power of 20 mW and higher the reflection spectrum has significantly changed from the spectrum with no incident power. The spectrum for the Q1.325 material also changes with increased incident power. However, thanks to the lower absorption the impact of the photo-current is lower and the Q1.325 material still selects the same resonance at 30 mW incident power as at 0 mW power.

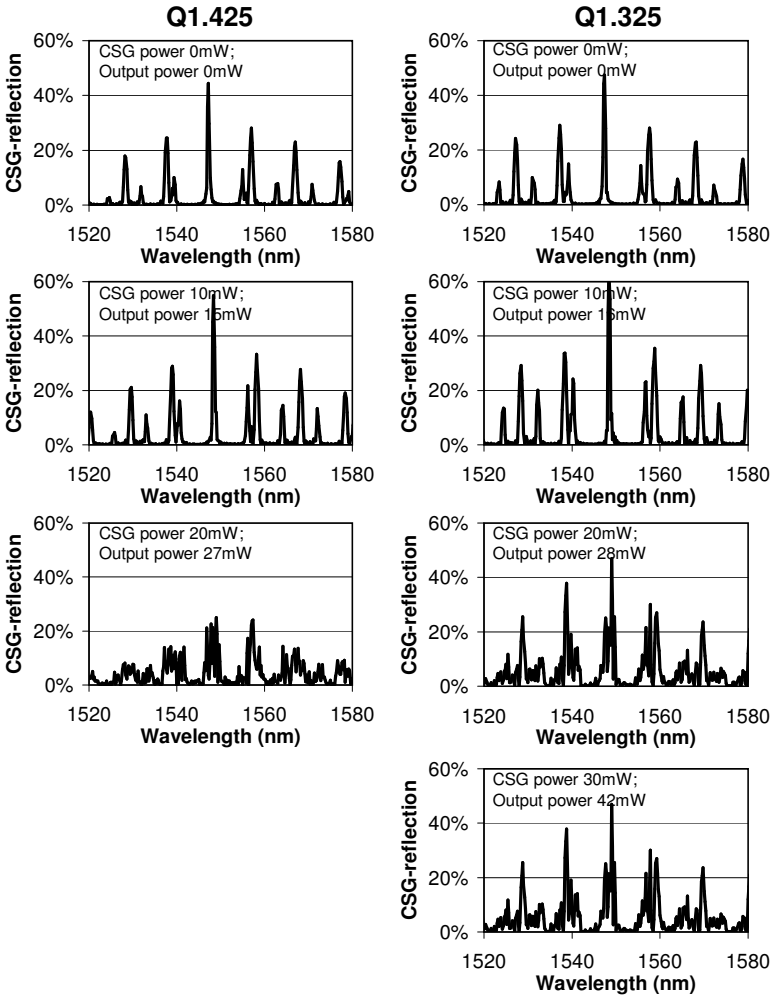


*Figure 4.32: Calculated spectra of CSG section with increasing values of incident power. For a Q1.425 material the spectrum is shown for 0, 10 and 20 mW incident power. The 20 mW spectrum is distinctly different from the 0 mW spectrum. For a Q1.325 material the spectrum is shown for 0, 10, 20 and 30 mW incident power. Even though the spectrum becomes more noise, high reflectivity and selectivity is still obtained.*

This figure clearly demonstrates that a design with a too high bandgap wavelength for the tuning layer is highly dependent on the incident power on the tuning section. Even if the design supports 30 mW operation, based on the spectrum at low power, the change in spectrum at higher power levels makes single mode operation impossible.

For the tested experimental device output powers up to 10 mW were measured. At these power levels the simulations predict no significant impact on the CSG reflection spectrum. Therefore, the experimental data are not likely affected by this phenomenon.

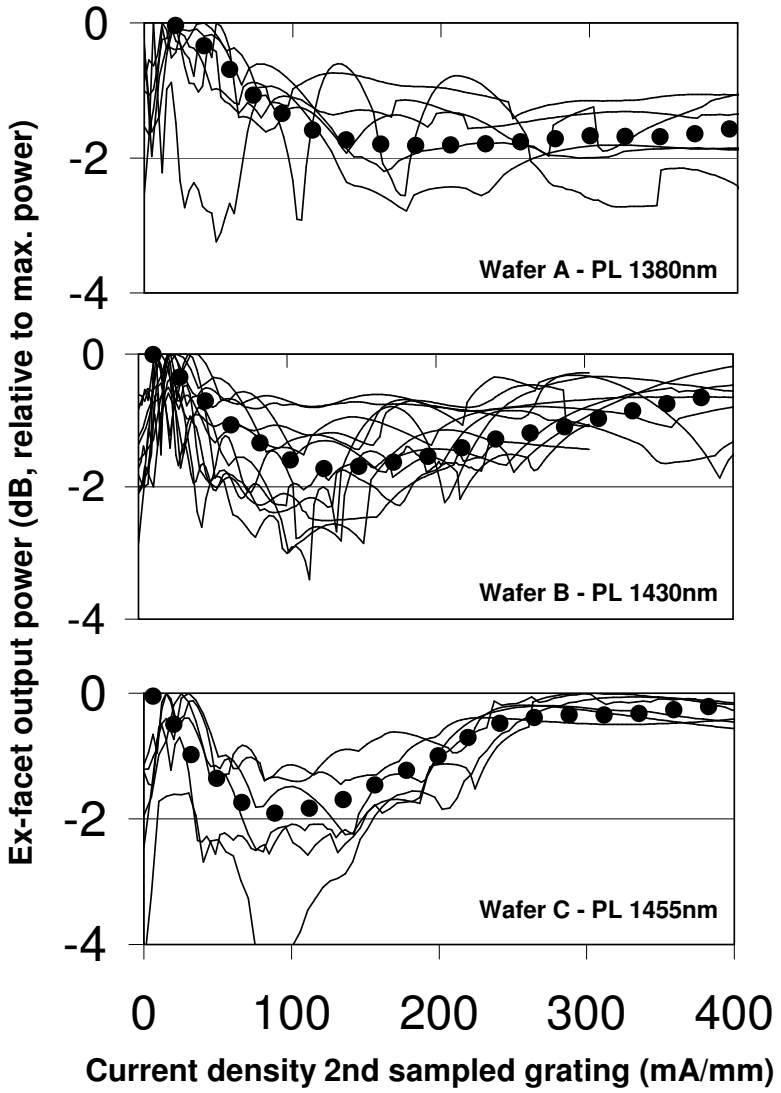


*Figure 4.33: Dependence of output power on current through the first sampled grating. Output power is relative to the maximum output power. For each graph up to 10 different devices are plotted. The thick dotted line provides a guide for the eye.*

### Tuning layer composition

The choice of tuning layer composition is important in reducing the variation of operating current in the gain section over the tuning range. In the design and simulation sections it was argued that a material bandgap close to the operating wavelength reduces this variation over the tuning range, by allowing the material absorption at no current

injection to be comparable to the maximum free-carrier absorption. A second effect that occurs with a bandgap wavelength close to the laser wavelength is a larger amount of stimulated emission (i.e. gain). Through this effect, an increase in tuning current and free-carrier absorption can be partly compensated for by the increase in gain coefficient.

In the process of free-carrier absorption, an electronic carrier is excited from the conduction band, towards a higher energy level. The probability for this process is proportional to the product of available carriers in the original state and the number of free states at the final energy. Since the higher energy levels are fully depleted, the free-carrier absorption is proportional to the carrier-density in the conduction band.

The process of stimulated emission involves the stimulation by a photon of a carrier in the conduction-band to decay towards the valence band, while emitting a photon. The product of the available carriers and free states again gives the probability for this process. Since the valence band is typically occupied by carriers, the number of free states in the valence band is limited to the number of carriers that have been excited to the conduction band (in charge equilibrium). Hence, the process of stimulated emission is proportional to the square of the carrier-density. For higher levels of current density the gain can therefore compensate for the free-carrier absorption.

In figure 4.33 the dependence of optical output power on tuning current density is shown for lasers from the three CSG wafers. These curves were measured with a constant current into the gain, phase and first sampled grating section. Different CSG configurations (with differences in sampled grating periodicity, grating burst length and number of sections per sampled grating) are displayed together, explaining the spread in behavior.

In figure 4.33 guides to the eye are drawn, to highlight the difference in behavior of devices from the different wafers. For the low bandgap wavelength material a decrease in absorption is seen, with stabilization at higher values of current density. For increasing bandgap wavelength, a recovery of the output power is observed. For the tuning layer material with a Photo-Luminescence (PL) wavelength at 1455 nm the output power fully recovers for high values of current density. The minimum in output power is observed at lower current density values.

The expectations was that an increased stimulated emission in material with higher quaternary composition reduces the output power variation. However, the power variation over the tuning range is not reduced by this gain effect. For unknown reasons, the decrease in output power is higher for the material with higher bandgap wavelength. This is not expected to be due solely to free-carrier absorption (which is proportional to the carrier-density and hence current density, at low current). Possibly, it is due to an increased carrierdensity from photo-current. Additionally, for DBR lasers, it was observed that the tuning range was reduced from 11 to 9 and 8 nm for wafer A, B and C respectively.

These results demonstrate gain at high carrier-density in widely tunable lasers, which depends on the tuning material composition, for a wide range of material composition (tuning layer PL wavelength range of 100 nm). Though not well understood, these results indicate that a lower value of bandgap wavelength can improve both output power and output power variation over the tuning range.

## 4.4 Summary

In summary, the operation of a CSG laser was simulated and experimentally demonstrated. The simulation showed that, by design, a CSG laser can generate an output power of more than 30 mW over a tuning range of 40 nm with an SMSR better than 37 dB, for gain section current lower than 180 mA. The experimental device (different from the optimum design) was tunable over a total tuning range of 57 nm, though only over a range of 34 nm all wavelengths were accessible, with an SMSR better than 30 dB. Output power varied between 5 and 10 mW at 100 mA gain section current. In comparison between simulation and experiment, the wavelength tuning of the experimental device is highly irregular.

It was verified that the simulation tool provides an excellent description of the reflection spectrum of a CSG laser. Therefore, the irregular tuning behavior of the CSG laser is attributed to a reduced CSG resonance selectivity, due to a non-optimal design, the presence of an isolation channel between sampled grating sections and the absence of alignment between resonance and cavity modes during measurement.

It was demonstrated that the interaction between optical field and carrier-density in the tuning sections can significantly influence the performance of the tunable laser. For a bandgap wavelength of Q1.425 it was shown that 30 mW output power cannot be obtained, due to a decreased selectivity and reflectivity of the CSG at high (>20 mW) power-levels. In addition it was shown that gain in the tuning-section counter-acts the increase in free-carrier absorption with tuning current. This effect was strongest for the material with a higher bandgap wavelength, but devices in this material did also show the largest variation in output power over the tuning range. Therefore, it is advised to reduce the bandgap wavelength of the tuning layer material further than the Q1.425 used in the presented design.

# APPENDIX A: Fabrication

The fabrication process for the CSG laser is similar to that of a tunable DBR laser (refer to [104]). The device structure is known as Semi-Insulating Planarly Buried Hetero (SIPBH) . Though a detailed description is out of the scope of this thesis, a cursory overview of the fabrication of the CSG laser is given below:

**Epitaxy grating layer** The quaternary grating layer with InP cap layer is grown on an n-doped InP substrate.

**Sampled grating definition** The grating is defined on the full wafer by a holographic process. With a masking step the resist in the gain, phase and propagation sections is exposed, after the holographic exposure. After photo-resist development, $SiO_2$ etching and wet chemical grating etch the grating only remains in the grating-burst sections.

**Epitaxy gain layer** The spacer-layer and gain layerstack is regrown on the grating surface.

**Buttjoint definition** The gain section is protected by a $SiO_2$ mask and wet chemical etching is used to remove the gain section layerstack outside of this mask.

**Epitaxy tuning layer** The tuning layerstack is regrown selectively in the etched away regions. Device operation is sensitive to the connection between gain and tuning section layerstack, since residual reflections may occur here. A process was developed to ensure a high-quality auto-aligned butt-joint connection.

**Epitaxy cladding layer** After removal of the $SiO_2$ mask an InP cladding layer is regrown on top of the gain and tuning sections.

**Waveguide definition and etch** The waveguide is defined in a $SiO_2$ mask and the material outside the waveguide is removed by a combination of dry and wet chemical etching.

**Epitaxy blocking layer** The iron-doped blocking layer is regrown.

**Isolation channels** To ensure electrical isolation between sections an isolation channel is defined in $SiO_2$ between all sections. In this channel of 20 $\mu m$ length the InP-thickness on top of the waveguide is 700 nm. This ensures a high electrical resistance ($\approx 10k\Omega$) and a negligible overlap with the optical field.

**Epitaxy top layer** The highly doped toplayer and contact layer is grown. Since $SiO_2$ remains in the separation channels, no regrowth occurs in the isolation channels.

**P-metalization and lift-off** Since this device consists of several sections it is mounted EPI-up . Consequently the metalization is defined through a lift-off process, which allows to separate the sections electrically and allows for the inclusion of fiducials on the chip. A sputtering process is used for the deposition of metal and an acetone-based lift-off process is used to remove the metal deposited on photo-resist.

**Thinning** The wafer is thinned down to 150 $\mu m$ to reduce thermal impedance

**N-metalization** N-metal is sputtered on the back-side of the thinned substrate.

**Bar cleave and coating** The wafer is cleaved into bars. Coating is performed in a sputtering system both for the back-facet AR coating and the font facet 5 - 30 % coating.

# APPENDIX B: Processed material

CSG lasers were fabricated from three wafers with different tuning layer composition. In table 4.2 the various parameters for these wafers are collected. Variants in grating burst section length, propagation section length and number of periods for both sampled gratings were included on each wafer.

During the growth of the gain section layerstack part of the confinement layer was omitted, due to a mistake in the growth-recipe. This resulted in an asymmetric layerstack. For a good buttjoint coupling the thickness of the tuning layer was reduced to 330 nm, reducing the tuning efficiency. From calculations this resulted in a decrease in confinement to 55 % from 65%. Tunable DBR lasers fabricated on these wafers had a tuning range between 8 and 11 nm, as compared to a typical 13 nm. Therefore the reduced tuning range can not solely be attributed to the thinner tuning layer, but also to a reduced material performance or process control.

| | Wafer A | Wafer B | Wafer C |
|---|---|---|---|
| Wafer ID | 15908 | 15910 | 15911 |
| PL gain section (nm) | 1546.9 | 1546.9 | 1544.5 |
| Standard deviation over wafer (nm) | 5.7 | 5.4 | 5.3 |
| PL passive section (nm) | 1381 | 1438 | 1453 |
| Standard deviation over wafer (nm) | 4.1 | 3.8 | 3.5 |
| Bragg wavelength (nm) | 1530 | 1530 | 1530 |

*Table 4.2: Overview of process parameters for wafers with CSG lasers*

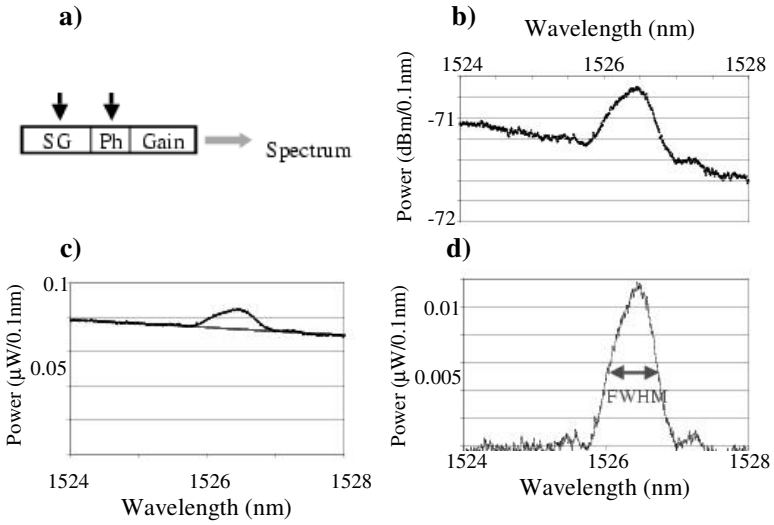


*Figure 4.34: Method for determining the resonance width of the grating section.*

# APPENDIX C: Measurement of grating properties

The standard tunable laser configuration considered here is a sequence of gain section, phase section and tuning section(s). Figure 4.34a illustrates how current injection into the phase section, allows us to derive the tuning section reflection spectrum. The spontaneous radiation, emitted from the phase section, couples partly to the waveguide and propagates in both directions. The emitted light, at the gain section facet, consists out of light that propagated directly through the gain section and light that was reflected on the tuning section and propagated through the phase and gain section. This light is collected into a fiber. Since photons are generated by spontaneous emission, and no cavity effects are supported by the highly absorbing gain section, no interference effects are present at combination of the two beams. With zero injection current in the gain section any cavity effects between front facet and tuning section are effectively suppressed. A small amount of current injection is used to decrease the absorption in the gain section and increase detection sensitivity.

In 4.34 a spectrum reflected from a DBR grating is shown. In this case only 13 % of the detected light, did reflect on the grating (the resonance is at -70.7 dBm as compared to a -71.3 dBm background level). The background level is removed from the spectrum as indicated in 4.34c, after which the resultant DBR reflection spectrum is found (figure 4.34d).

This resonance is fit to formula 2.12 and with the known grating length of 400 $\mu m$ the grating strength is determined. It should be noted that the detected resonance is the resonance of the TM mode, since the absorption in the multi-quantum well gain section is considerably smaller for a TM mode than for a TE mode. With a proper mode solver program both the TE and TM mode are easily calculated to correlate the TE and TM properties.

# Chapter 5

# Tunable MMI Laser

This chapter focuses on the other novel concept for a widely tunable laser: the Tunable Multi-Mode Interference section (T-MMI) Laser [25]. The concept is introduced in section 5.1. In section 5.2 the design of the device is detailed. Section 5.3 presents computed and experimental verification of the performance. In section 5.4 a summary is provided of the performance of this widely tunable laser concept.

## 5.1 Device concept

The CSG device presented in the previous chapter is based on a Vernier-type tuning scheme. With the two sampled gratings, both controlling the cavity mode selection, accurate control over both tuning currents is required and device control is complicated. In contrast, with tuning sections in which the selection of cavity mode and sampled grating resonance is separated, a tight control over only one tuning current is needed. In section 1.2, the GCSR was described as a prime example. The device introduced in this chapter, the Tunable MMI (T-MMI) laser, builds upon the same principle.

In figure 5.1 a schematical topview of the T-MMI laser is shown. Starting from the emitting facet on the right, the device consists of four sections. The gain section provides amplification. The phase section fine-tunes the position of the cavity modes. The sampled grating provides a reflection spectrum with multiple resonances. And the tunable MMI section selects one of the multiple sampled grating resonances of the sampled grating. A different cavity mode is selected by tuning the sampled grating reflection spectrum and a different sampled grating resonance is selected by shifting the narrow tunable MMI section transmission spectrum.

The basis of this device is the selectivity of the transmission of an MMI and the tunability of the wavelength of maximum transmission of the T-MMI coupler. The MMI-transmission curve is sharper than for two-mode interference devices, due to the higher order modes that propagate in the MMI. The tunability is achieved through localized current injection into the T-MMI laser. The associated localized refractive index change results in a shift in the wavelength of maximum transmission.

Building on the work presented in previous chapters, this section focuses on the

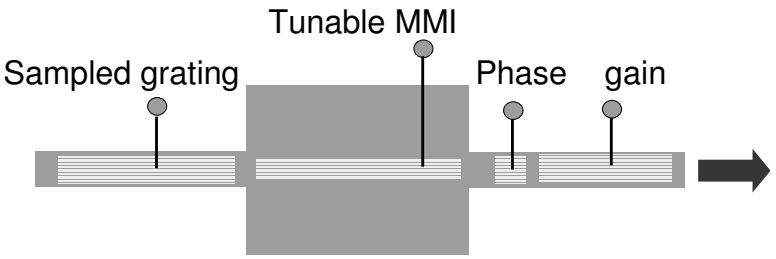


*Figure 5.1: Schematical top-view of Tunable MMI laser: the contour of the device (dark area) is shown with the electrical contacts for current injection (gray areas with pointer)*

operation of the tunable MMI coupler. First the component basics are presented, followed by an analysis on tapering and tuning of the T-MMI coupler.

### 5.1.1 Multi-Mode Interference section

#### Basics

A Y by Z MMI coupler is a wide waveguide, in which several optical modes can propagate. The input field is generated by Y (typically single-mode) input waveguides and the output field is collected at Z output waveguides. In figure 5.2 a 1 by 1 MMI coupler is shown for reference.

At the position where the input waveguide connects to the wide waveguide region the optical field in the input waveguide is decomposed into the optical modes that propagate in the MMI coupler. At this interface the overlap is nearly complete (i.e. coupling to radiation modes is negligible) [70]. These modes each have a different effective index and thus experience a different phase-shift upon propagation. As a result, the field intensity profile changes, along the MMI coupler length, due to interference. In an MMI coupler the optical modes image the original input field, at each multiple of the MMI coupler periodicity ($L_{MMI}$). At intermediate points, a distance $\pm\frac{L_{MMI}}{N}$ from the image, an N-fold copy of the input-field is imaged. In figure 5.2 the field in an MMI coupler is shown for the wavelength of maximum transmission. At the output waveguide the exciting input mode is imaged. A 2-fold image is projected at $\frac{1}{2}$ of the length, a 3-fold image at $\frac{1}{3}$ and at $\frac{2}{3}$ of the length, and-so-forth.

The propagation constant $\beta_j$ for mode j is expressed as [21]:

$$\beta_j = k - \frac{(j+1)^2\pi}{4\mu_r W_{MMI}^2}\lambda \quad \rightarrow \quad \mu_j = \mu_r - \frac{(j+1)^2\lambda^2}{8\mu_r W_{MMI}^2} \tag{5.1}$$

In this equation $\beta_j$ and $\mu_j$ are the propagation constant and effective index for mode j (0, 1, etc.), k (= $k_0\mu_r$) is the wavenumber, $\mu_r$ is the slab-index in the MMI coupler region, $W_{MMI}$ is the MMI coupler width and $\lambda$ is the free-space wavelength. This equation shows that the difference between the mode-indices is a multiple of $\frac{\lambda^2}{8\mu_r W_{MMI}^2}$ and, hence, that after a propagation length $\frac{8\mu_r W_{MMI}^2}{\lambda}$ all modes in the MMI coupler have

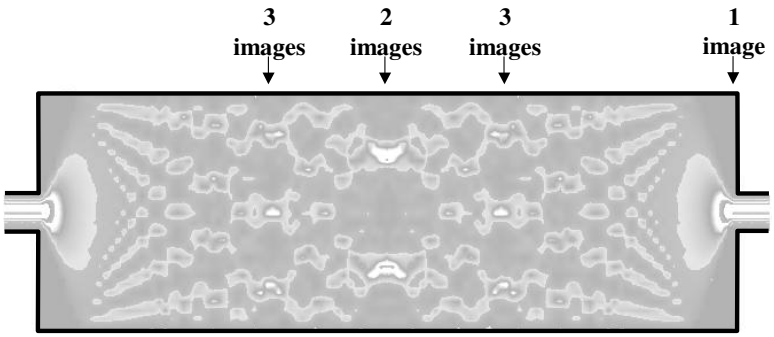


*Figure 5.2: Distribution of optical power in 1 x 1 MMI coupler, when excited by a single mode input field. The mode is injected through the left waveguide and at the right-hand side of the MMI coupler the field images and is coupled into the single-mode output waveguide. At intermediate positions, multiple images of the input field are projected.*

an $integer \cdot 2\pi$ phase difference with one another. At this position the original image is imaged, through the interference of the separate modes.

MMI coupler geometries exist in which only specific modes are excited. In the restricted interference design, the input field is at $\pm\frac{W_{MMI}}{6}$ from the center and only the mode pairs 0-1, 3-4, 6-7 are excited. Alternatively, the symmetric design requires an input field, symmetrical along the center of the MMI coupler, such that only even modes are excited. For these geometries the image length is reduced by a factor 3 and 4, respectively [21].

From formula 5.1 it follows that the MMI coupler length at which imaging occurs is given by [21]:

$$L_{MMI} = \frac{M}{N}\frac{4 \cdot \mu_r \cdot W_{MMI}^2}{a \cdot \lambda} \tag{5.2}$$

Where N is the number of images, M is an integer (without a common divider with N) that defines the number of positions along the MMI coupler, where an N-fold image appears, and a is a geometry specific number. Its value is 1, 3 or 4 for the general, restricted and symmetric design, respectively [21].

At the wavelength of maximum transmission the original field is imaged at the output waveguide, but at other wavelengths (with an offset $\Delta\lambda$ from the wavelength of maximum transmission) the image point is positioned before or after the output waveguide. The shift in the image point is given by $\Delta L_{MMI} = \frac{-M}{N}\frac{4\mu_r W_{MMI}^2}{\lambda^2}\Delta\lambda$. The coupling of this image to the output waveguide can be calculated through a Gaussian expansion and an optical overlap calculation [21]. From this the spectral width of the MMI coupler transmission curve follows [21] (see e.g. figure 5.5):

$$\delta\lambda(\alpha) = \frac{\pi}{L_{MMI}} \cdot \mu_r d_0^2 \cdot Z(\alpha) = \frac{N}{M} \cdot \frac{a\pi}{4\mu_r} \cdot \frac{d_0^2}{W_{MMI}^2} \cdot Z(\alpha) \cdot \lambda \tag{5.3}$$

The spectral width $\delta\lambda(\alpha)$ is defined as the wavelength range over which the wavelength dependent transmission loss is less than $\alpha$ dB. $d_0$ is the Gaussian waist of the

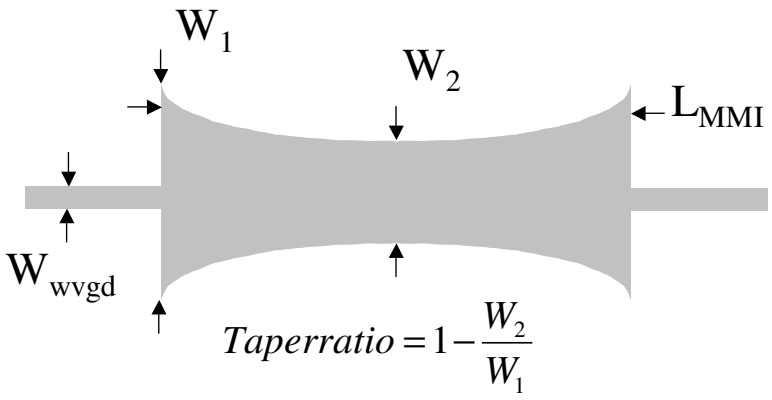


*Figure 5.3: Schematical representation of tapered MMI coupler. The taper ratio is the percentage change in MMI coupler width.*

input field and $Z(\alpha)$ is an approximate function following from the mentioned overlap calculation (see appendix in [21]).

In this thesis only symmetric 1 by 1 MMI couplers are considered, reducing the above equations to ($N = 1; a = 4$):

$$\begin{aligned} L_{MMI} &= M \cdot \frac{\mu_r W_{MMI}^2}{\lambda} \\ \delta\lambda(\alpha) &= \frac{\pi}{2L_{MMI}} \cdot \mu_r d_0^2 \cdot Z(\alpha) = \frac{1}{M} \cdot \frac{\pi}{2\mu_r} \cdot \frac{d_0^2}{W_{MMI}^2} \cdot Z(\alpha) \cdot \lambda \end{aligned} \tag{5.4}$$

These formulas reveal a number of interesting aspects of MMI couplers. Firstly, the spectral width and hence wavelength selectivity is inversely proportional to the length of the device. For any choice of width the same length is required to obtain a given wavelength selectivity. Secondly, the main parameters influencing the MMI coupler bandwidth are the device length and the width of the input field. Thirdly, the MMI coupler wavelength of maximum transmission scales with $L^{-1}$, $\mu_r$ and $W_{MMI}^2$ of which only the last parameter is hard to control: a control over the MMI coupler center wavelength of 10 nm (0.6% at 1550 nm) requires a width control better than 0.3% of design width (0.06 $\mu m$ for a 20 $\mu m$ wide MMI coupler). For this reason wide MMI couplers offer better control over the MMI coupler transmission wavelength during manufacturing.

The above analysis is fully based on the paraxial approximation, leading to formula 5.1. This requires that the optical field guided within the MMI coupler, such that the modes resemble plane waves. When this assumption breaks-down the modes do not build up a multiple of $2\pi$ phase difference among one another, at the same position, and full imaging is no longer achieved. This results in lower transmission and increased spectral width (see section 5.2.3 for more details).

### MMI coupler tapering

The previous section introduced the basic MMI coupler properties, including wavelength

selectivity. The inclusion of a long sufficiently selective MMI coupler in a laser cavity makes the laser cavity modespacing unacceptably narrow. A shorter MMI coupler is required for single mode laser operation.

This can be effectively achieved by tapering the MMI coupler [70]. In figure 5.3 the basic layout of a tapered MMI coupler is shown. At its input the MMI coupler has its maximum width $W_1$ and the input field is decomposed into the available modes. Over the length of the MMI coupler these modes are adiabatically tapered to width $W_2$, such that the distribution of optical power over the modes is retained and the difference in propagation constant between modes increases (see formula 5.1). Near the output the MMI coupler is again tapered to maximum width and the original field is imaged. Since the difference in propagation constant between modes is larger in narrow MMI couplers, the MMI coupler length, needed to build up the multiple of $2\pi$ phase difference between modes, is shorter. Since the position of the image point depends on the shift in phase-difference near the output waveguide of the MMI coupler, the tapering does (ideally) not influence the spectral width of the MMI coupler transmission.

The requirement of adiabatic tapering restricts the maximum length reduction that can be achieved. When the taper-ratio is too high, cross-talk between different modes occurs and full recovery of the image is not possible anymore, resulting in an increased insertion loss and degrading selectivity. Higher order modes, to which some optical power is coupled at the input waveguide, become cut-off and radiate power to radiation modes and lower order modes, such that both insertion loss and selectivity are affected (refer to section 5.2.3).

MMI coupler tapering is studied in a paper by D.S. Levy et al. [70]. The study shows that for a highly confined MMI coupler structure (20 $\mu m$ wide, with an effective index contrast of 2.3 and a 4 by 4 MMI coupler configuration) the length reduction achieved by tapering is linear with the taper-ratio and a reduction by 60% is shown for a 50% taper-ratio. For this taper-ratio the decrease in transmission is less than 1 dB. For devices with a lower port-count (in this case a 1 by 1 configuration) the dependence of transmission on taper-ratio decreases. Although, not treated in [70], the MMI coupler bandwidth is also affected by tapering.

At high taper-ratio the transitions in the MMI region are not fully adiabatic anymore, resulting in a loss of power in each mode. In addition, some of the modes that are supported in the wide MMI region become cut-off in the narrow region. Power in these modes is radiated or coupled into the other supported modes. As a consequence, both the power and phase of these modes is altered and the longitudinal position where the condition of an $integer \cdot 2\pi$ phase difference is reached different for each combination of modes.

In figure 5.4 simulation of tapering on a 20 $\mu m$ wide MMI coupler with an index contrast of 2.3 is shown. A Beam Propagation Model (BPM) tool was used for this calculation. The (1,1) order Padé approximation is used to improve the results at high taper ratio. The results presented here on length reduction are in line with calculations from D.S. Levy et al. [70]. The transmission calculated in that publication is however less sensitive to tapering. These differences are most likely due to the handling of radiation modes in the algorithm and the accuracy of the algorithm at high index-contrasts.

Different taper shapes are possible (e.g. parabolic tapers, linear tapers or tapers

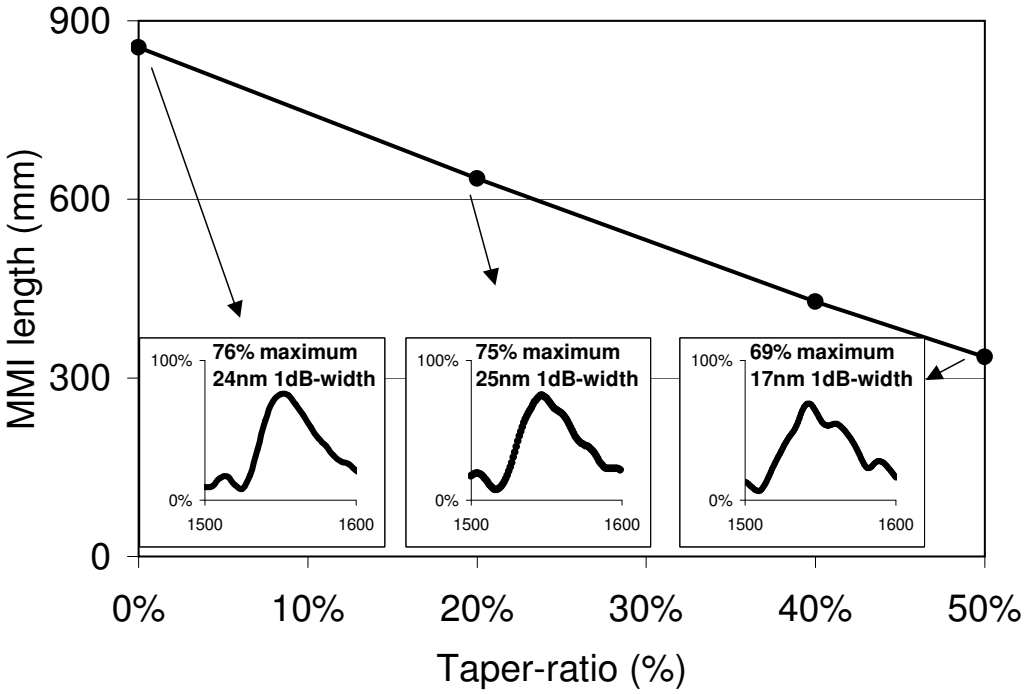


*Figure 5.4: MMI coupler length versus taper-ratio for 20 $\mu m$ wide MMI coupler. In the insets the calculated transmission by BPM at 0, 20 and 50% taper-ratio is shown.*

that scale with the effective index of the waveguide). It is however established [74] [70] that parabolic tapers give a better performance than linear tapers in terms of length reduction and selectivity [74].

A last consideration for MMI coupler properties is the insertion loss. Since typically these devices are fully passive and the optical mode has limited overlap with any etched sidewall, the loss is low. Imperfections, which affect the phase-difference at the output waveguide, and material absorption, dominate the insertion loss. With a material loss of 10 $cm^{-1}$ (for Q1.45) and a transverse optical confinement of 70%, the optical loss in a 1mm long MMI coupler is 3 dB. A reduction in MMI coupler length, through tapering, can lead to a net decrease in insertion loss.

### MMI coupler tuning

The wavelength of maximum transmission of an MMI coupler is determined by the effective index difference between the lateral modes ($n_0 - n_2$, $n_0 - n_4$, $n_2 - n_4$ and so on). Control over this effective index difference enables tuning of the wavelength of maximum transmission for the MMI coupler. Since optical modes are distributed differently over the width of the MMI coupler, a localized change in refractive index has affects the effective index of each mode differently. A local change in the refractive index can be accomplished by current injection. Dependent on the position of the current injection

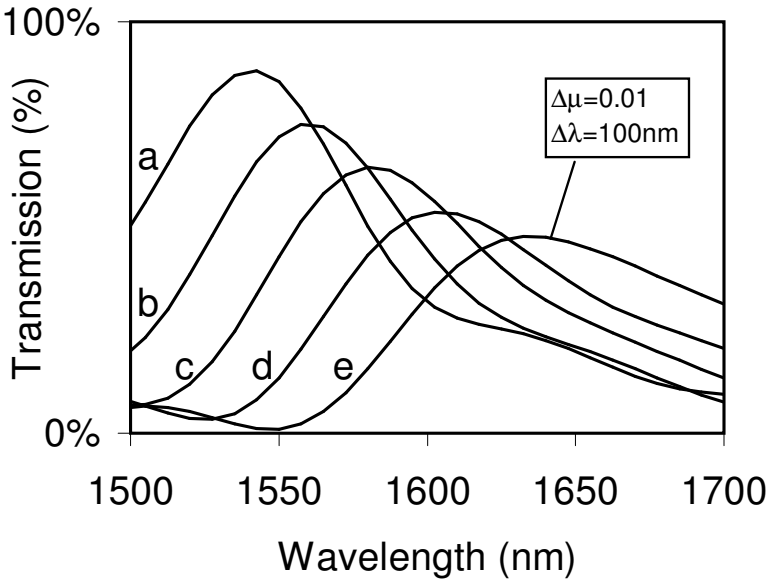


*Figure 5.5: Transmission versus wavelength for a tunable, 20 μm wide, 1x1 T-MMI coupler. The area of current injection is 3 μm wide. Upon tuning, the spectral selectivity and optical transmission degrade; Transmission spectra are shown for a) no current injection; b) 0.0025; c) 0.005; d) 0.0075; e) 0.01 lower effective index in center of MMI coupler. For a change in effective index, below the contact, of 0.01 a 100 nm wavelength tuning is obtained.*

either a reduction (i.e. tuning to higher wavelength) or increase in the effective index difference (i.e. tuning to lower wavelength) is obtained.

For the symmetric tunable MMI coupler presented here localized current injection is achieved through electrode(s) along the length of the MMI coupler. An electrode in the middle of the MMI coupler enables a positive wavelength shift (since the refractive index difference between modes is reduced), while two electrodes at the outside of the MMI coupler enable a shift towards negative wavelength. In figure 5.5 the tuning-performance for the configuration with a centered contact is simulated with a BPM tool (see section 3.2). A wavelength shift of more than 100 nm is achieved by a change in effective index of less than 0.01 (an effective index change of more than 0.03 is achievable).

In figure 5.5 it is observed that the transmission loss and spectral width increase with current injection. This is caused by the breakdown of the relation in formula 5.1, where the effective index difference between modes scales with $(j+1)^2$ (j is the mode-number). After propagation over the MMI coupler length, the phase difference between different modes is not a multiple of $2\pi$ anymore at the same position along the MMI coupler. The image of the original field is therefore not complete anymore and extra insertion loss and widening of the transmission curve is observed. This can also be concluded from the asymmetry in the transmission spectrum, between the higher and lower wavelength side of the wavelength of maximum transmission. The wavelength of maximum transmission is mainly determined by the index-difference between the fundamental and second order

mode (since these two modes contain most of the optical energy). For higher order modes the change in effective index is smaller than for the second-order mode and thus the position where these modes are in phase with the fundamental mode occurs at a larger wavelength. Consequently, the spectrum widens towards the larger wavelength side. At the shorter wavelength side the transmission curve becomes sharper, since the optical intensity of higher order modes does not add constructively at this side of the transmission curve.

## 5.2 Design

The T-MMI laser is processed as a ridge type laser. Therefore, re-optimization of the layerstack (both for laser and tuning section) is required, compared to the CSG design. This is addressed after the conceptual design.

### 5.2.1 Laser design

The conceptual design of the laser section is similar as for the CSG laser (section 4.2.1). Therefore, the design-choice from chapter 4 for a gain section length of 400 $\mu m$ is equally valid for the T-MMI laser. This choice again reduces the requirement on the back-facet reflectivity and increases the cavity modespacing. Both a shorter ($< 400\ \mu m$) and longer ($> 600\ \mu m$) gain section length requires a higher reflectivity from the sampled grating section. For a gain-section length up to 600 $\mu m$ the requirement on back-facet reflection is constant, but spacing between cavity modes decreases.

From the analysis in section 4.2.1, this design requires a front facet reflectivity of 17% and a back-facet reflectivity of at least 23%, to enable 30 mW output power at 150 mA. A 1 dB selectivity between modes is required to ensure 40 dB SMSR.

### 5.2.2 Tuning elements design

In this tunable laser concept, the T- MMI coupler provides the selection of a resonance in the sampled grating reflection spectrum. Therefore, the design target for the MMI coupler is to provide good sampled grating resonance selectivity and a low transmission loss over its tuning range. The design goal for the sampled grating is high reflectivity, cavity mode selectivity and a sufficiently large sampled grating resonance spacing, to support selectivity of the T-MMI coupler.

#### Sampled grating

For the T-MMI laser the achievable grating strength is assumed to be 15 $mm^{-1}$. The validity of this assumption is proven in the design section for the layerstack. As for the CSG laser, inherently in this ridge-type structure a 12 nm tuning range can be achieved. However, since the design of the T-MMI coupler places a limitation on the material composition, here a reduced tuning range of 10 nm is used. This corresponds to a 40 $\mu m$ periodicity in the sampled grating.

Similarly as in the design section from chapter 4 the choice for the sampled grating design is based on the figures 4.9 and 4.10. Here these figures are reproduced. In figure

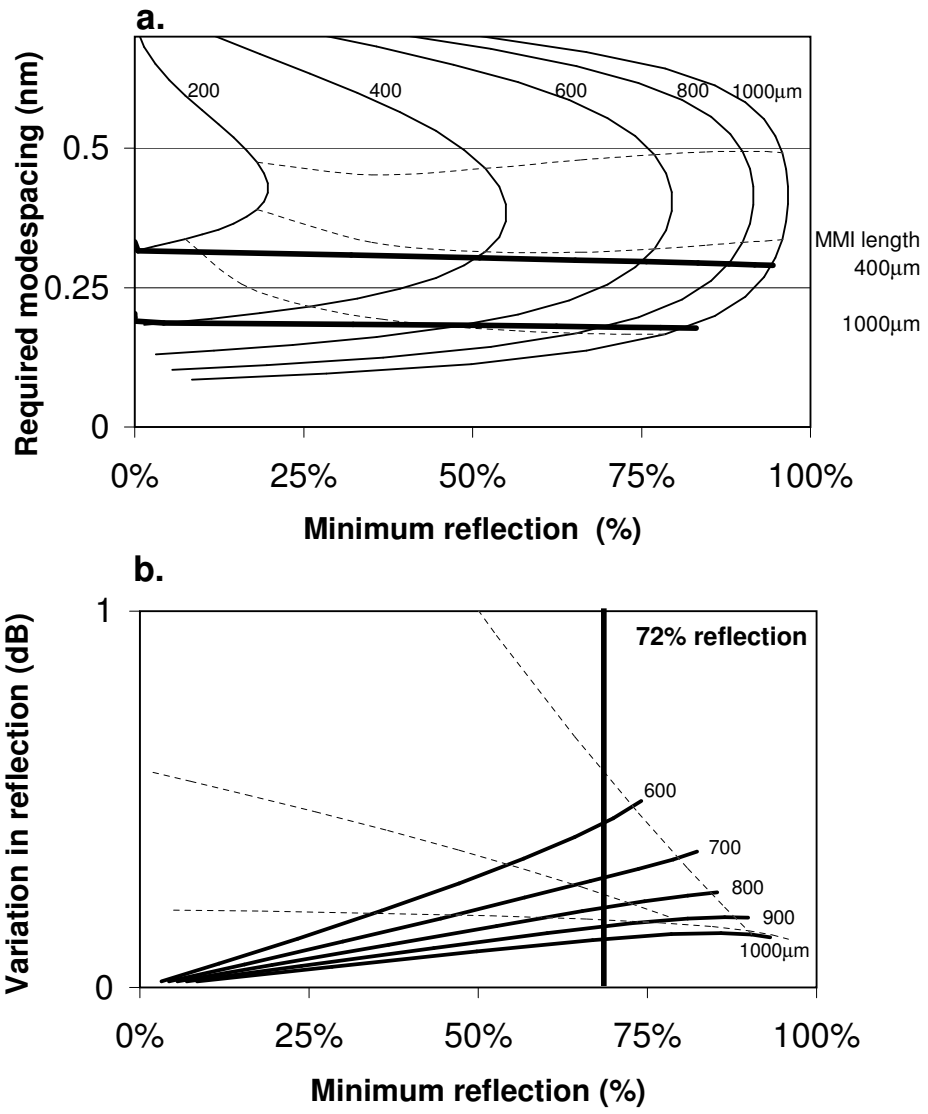


*Figure 5.6: Parametric plot for sampled grating properties. a) required cavity modespacing versus minimum sampled grating reflectivity over the tuning range. The solid curves, for different values of sampled grating length, are plotted for increasing values of burst section length, with increments by 10% indicated by the dotted lines. Included are the modespacing for a cavity formed by the sampled grating, a 400 µm gain section, a 100 µm phase section and a 400 or 1000 µm long MMI section. b) variation in reflection between two sampled grating resonances versus the sampled grating minimum reflectivity over the tuning range. The solid curves, for different values of sampled grating length, are plotted for increasing values of burst section length, with dotted lines indicating a burst section length of 6, 10 and 14% of sampled grating periodicity. Only settings for which the sampled grating cavity mode selectivity supports a laser cavity with a 400 µm long MMI section are included.*

5.6a the modespacing for a 400 $\mu m$ long gain section, a 100 $\mu m$ phase section, a 400 or 1000 $\mu m$ long MMI coupler and a sampled grating are included. Clearly, modespacing in the T-MMI laser is a limiting condition, for both the burst-section length and the sampled grating length. MMI coupler tapering is essential in reducing the cavity length.

Different from the CSG laser, sampled grating resonance competition is only between neighboring resonances, since the MMI coupler transmission is monotonously decreasing over the full tuning range and therefore provides an excellent suppression of resonances, further away from the MMI coupler transmission wavelength. At the edge of the tuning range the difference between neighboring resonances is largest. In figure 5.6b the difference between the two outer-most resonances within a tuning range of 40 nm is displayed versus the minimum sampled grating reflectivity over the tuning range. The curves are only drawn for the set-points that provide a sufficient mode-selectivity with an MMI coupler length of 300 $\mu m$.

The sampled grating needs to provide at least 23% reflectivity to support 30 mW operating. Taking into account the change in sampled grating reflectivity with current injection of a factor 2.5 (as found from calculations for a 10nm tuning range on a wide range of sampled grating configurations), a 58% reflectivity is required. To support a T-MMI coupler insertion loss of 0.5 dB, the total reflectivity should be more than 72%. This requirement is included in figure 5.6b. In this figure it is seen that for a burst-section length larger than 14% of the sampled grating periodicity, the cavity modespacing becomes too large for the SMSR requirements. To add some margin we choose a burst section length of 12% of the sampled grating periodicity (i.e. 4.8 $\mu m$). The total length of the sampled grating is chosen to be 720 $\mu m$ (i.e. 18 periods) to meet the reflectivity requirement with a low variation in peak-reflection.

The chosen design requires the MMI coupler to provide a selectivity of at least 1.4 dB between cavity modes in neighboring resonances (0.4 dB for suppression of the neighboring resonance plus an additional 1 dB to ensure sufficiently high SMSR). This selectivity is obtained in two passes through the MMI coupler.

**Tunable MMI coupler**

The design approach, for the T-MMI coupler, is to design first an untapered MMI coupler for the desired transmission properties. As a next step, the length of the MMI coupler is reduced by tapering. Since bandwidth and transmission are affected by tapering, a factor 2 margin is included in the design for the selectivity. The advantage of this approach is that optimization is done on basis of conceptual understanding and simple analytical formulas.

The main design criterion for the MMI coupler is wavelength selectivity. The optical bandwidth is given by formula 5.4 for an untapered MMI coupler. An independent input to this formula is $d_0$, the Gaussian waist (width of the mode, where the amplitude is $e^{-1}$ of its maximum) of the input and output field. In figure 5.7 the Gaussian waist of a fundamental mode is plotted versus the waveguide width. Since the in- and output waveguides to the MMI coupler do not need an electrode on top, the width is only limited by the capabilities of the lithography. For a straight waveguide widths down to 0.7 $\mu m$ can be realized with contact-lithography. However, the reproducibility is limited and since these waveguides have to connect to the wide MMI coupler region the definition

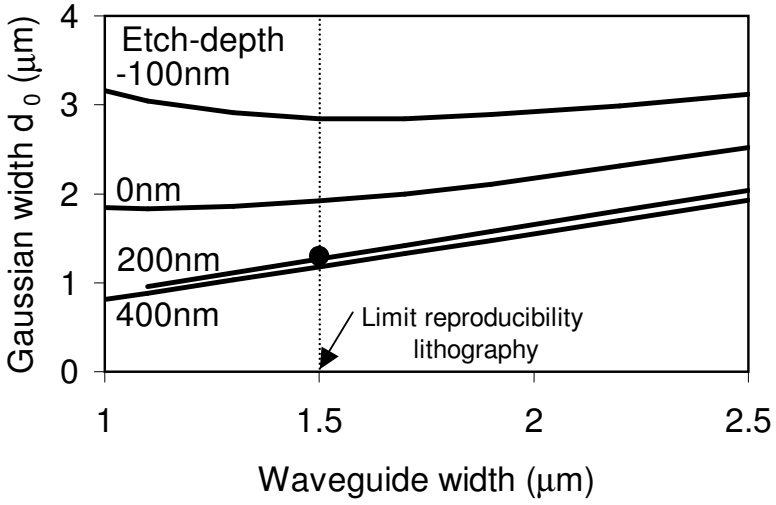


*Figure 5.7: Gaussian waist of fundamental mode in input waveguide to T-MMI coupler. The waist $d_0$ is plotted versus the waveguide width for several values of etch-depth around the waveguide. For a negative etch depth, the cladding layer, on top of the tuning layer, is not completely removed.*

of the waveguide near the MMI coupler is more difficult. A minimum waveguide width of 1.5 $\mu m$ is used to ensure reproducibility. From the figure it follows that a minimum Gaussian waist is obtained by etching at least 200 nm into the tuning layer around the waveguide. A waist of down to 1.2 $\mu m$ can be obtained.

To obtain a 1.4 dB resonance selectivity, the MMI coupler wavelength dependent transmission needs to provide 0.7 dB suppression (since the optical mode will pass twice through the MMI coupler on a round-trip) at 10 nm from the transmission wavelength. To address the previously mentioned margin of a factor 2 to compensate for reduction in MMI coupler selectivity upon tapering a target single pass suppression of 1.4 dB is used. With typical MMI coupler parameters ($\mu_r = 3.4$, $d_0 = 1.2\mu m$ and $Z(1.4\ dB) = 1.0$) the relation between MMI coupler length and bandwidth is given as: $\delta\lambda(1.4\ dB) = \frac{14.4\mu m^2}{L_{MMI}} < 20\ nm$. This implies a minimum MMI coupler length of 770 $\mu m$.

MMI couplers of these lengths are unpractical in a device application, since the long laser-cavity results in narrowly spaced laser-modes (more narrow than the allowed 0.27 nm) and material loss results in a high insertion loss. Different tapering structures are available. Here, we choose to make use of parabolic tapering, since extensive work is available on this type of tapers [74] and because both linear tapers and tapers, as defined in [70], result in longer devices for the same taper-ratio (though the optical insertion loss is less for adiabatic tapering, according to [74]).

Following the work in [70], taper-ratio's up to 50% result in optical insertion loss lower than 1 dB. This does not take the reduction in material loss into account, leading to a smaller actual increase in insertion loss. With such taper ratio a length reduction of up to 60% can be obtained.

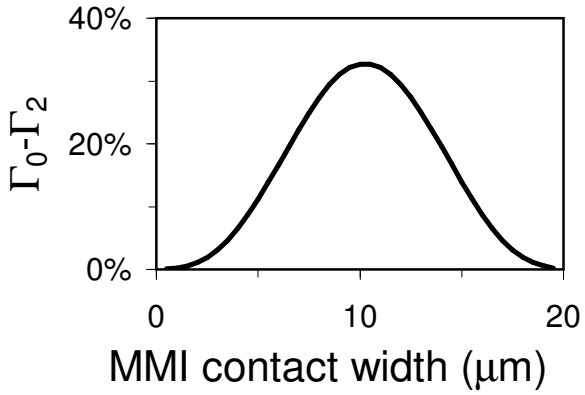


*Figure 5.8: Difference in optical confinement below contact, for fundamental and second order mode, versus the width of the centered contact.*

With these considerations the design for the T-MMI laser with a 10 nm minimum sampled grating resonance spacing is a 310 $\mu m$ long MMI coupler with 50% tapering. The maximum width of the MMI coupler is 18 $\mu m$ (consistent with the length). The in- and output waveguides to the MMI coupler have a width of 1.5 $\mu m$. The wider MMI coupler design makes the MMI coupler transmission wavelength less sensitive to processing variation. A 0.2 $\mu m$ change in MMI coupler width results in a 34 nm shift in MMI coupler transmission wavelength. To control the transmission wavelength of a processed device an accurate linewidth control is required and/or a process to correct for deviations from the target width. Alternatively, the MMI design needs to support a wide tuning range, allowing for a large tolerance of MMI coupler transmission wavelength.

Tuning of the MMI coupler transmission wavelength is achieved by control over the effective index for the different modes. This is done by a local change in the refractive index. The different modes are affected differently by this, corresponding to their optical overlap with that region.

$$\Delta\mu_{eff,k} = \Gamma_k \cdot \Delta\mu_{mat} \tag{5.5}$$

With $\Gamma_k$ the optical confinement of mode k (0,1,2 etc.) in the region with material index change $\Delta\mu_{mat}$.

The MMI coupler wavelength of maximum transmission is mainly determined by the difference in effective index for modes 0 and 2 (since a symmetric MMI coupler is used, mode 1 is not excited): $\lambda_{MMI} = (\mu_{eff,0} - \mu_{eff,2}) \cdot L_{MMI}$. Hence, the wavelength shift is given at $\Delta\lambda_{MMI} = (\Gamma_0 - \Gamma_2) \cdot \Delta\mu_{mat} \cdot L_{MMI}$.

The dimension of the contact on the MMI coupler determines the portion of the MMI coupler cross-section, over which a change in refractive index is induced by current injection. In figure 5.8 the absolute difference in optical confinement between the fundamental and second order mode is given versus the dimensions of the centered contact. A maximum difference in optical confinement is obtained for a contact that covers half of the MMI coupler. For this configuration a difference in confinement of 32% is obtained. A change in wavelength of 60 nm would then only require a change in material refractive

index of 0.0002 (< 1% of the physically achievable change). Therefore, there is a wide design margin for the width of the tuning contact, as well as for the material tunability.

However, current injection in the MMI coupler and the subsequent change in modal-indices changes the effective index difference between modes, widening the MMI coupler response and increasing the insertion loss. Therefore the T-MMI laser tuning range is limited by the breakdown in performance of the MMI coupler at higher current injection, rather than by the tunability of the refractive index.

The use of electrodes at the outside of the MMI section allows for tuning towards lower wavelength. However, since the MMI coupler is deeply etched, surface recombination can occur, reducing the tuning efficiency. Most importantly, the use of these electrodes can give flexibility in device design and allows for compensation of fabrication tolerances. A device can be envisioned with both contacts in the middle and outside of the MMI coupler to fully compensate for the MMI coupler center wavelength fabrication tolerance.

Since current injected into the MMI coupler is not confined to the region below the contact, the region over which the MMI coupler material refractive index is changed is wider than the contact. Since there is a wide design margin on contact width, a contact design of 25% of the MMI coupler width (i.e. 4.5 $\mu m$) is chosen.

### 5.2.3 Optical layerstack

In contrast to the CSG-laser the T-MMI laser cannot easily be fabricated in a SIPBH structure. The large angles in the MMI coupler design make blocking layer regrowth impossible [55]. Therefore a ridge structure is chosen for implementation of this device.

In figure 5.9 the cross-section of the device is shown at several positions along its length. The T-MMI laser has two distinct layerstacks: one for the gain section and one for the tuning sections. In the gain section, a multi-quantum well is sandwiched between quaternary confinement layers (for waveguiding and carrier transport) and InP. In the tuning sections, the bulk tuning layer is positioned between InP layers. The top InP-layer is p-doped, while the lower InP layer is n-doped. In the grating burst regions a grating layer is present below the tuning layer. The waveguide is defined by etching away the toplayer of InP in the layerstack. Both in sampled grating and gain section, a cladding layer is left and the etch does not extend into the gain or tuning layer, to avoid carrier recombination at the etched surface. In the MMI coupler region the etch preferably extends into the tuning layer to improve the selectivity performance of the MMI coupler.

To avoid loss in the metallisation pattern, it is separated from the optical mode. In the ridge this is achieved by using a 2000 nm toplayer. In the region around the waveguide a 350 nm SiON layer is used to create a separation between metal and the optical mode.

The choice for a ridge structure puts constraints on the dimension of the waveguide. Since an electrode has to be aligned on top of the waveguide a minimum width of 2 $\mu m$ is required.

#### gain section

As for the CSG laser, the objective in the design of the gain section layerstack is to

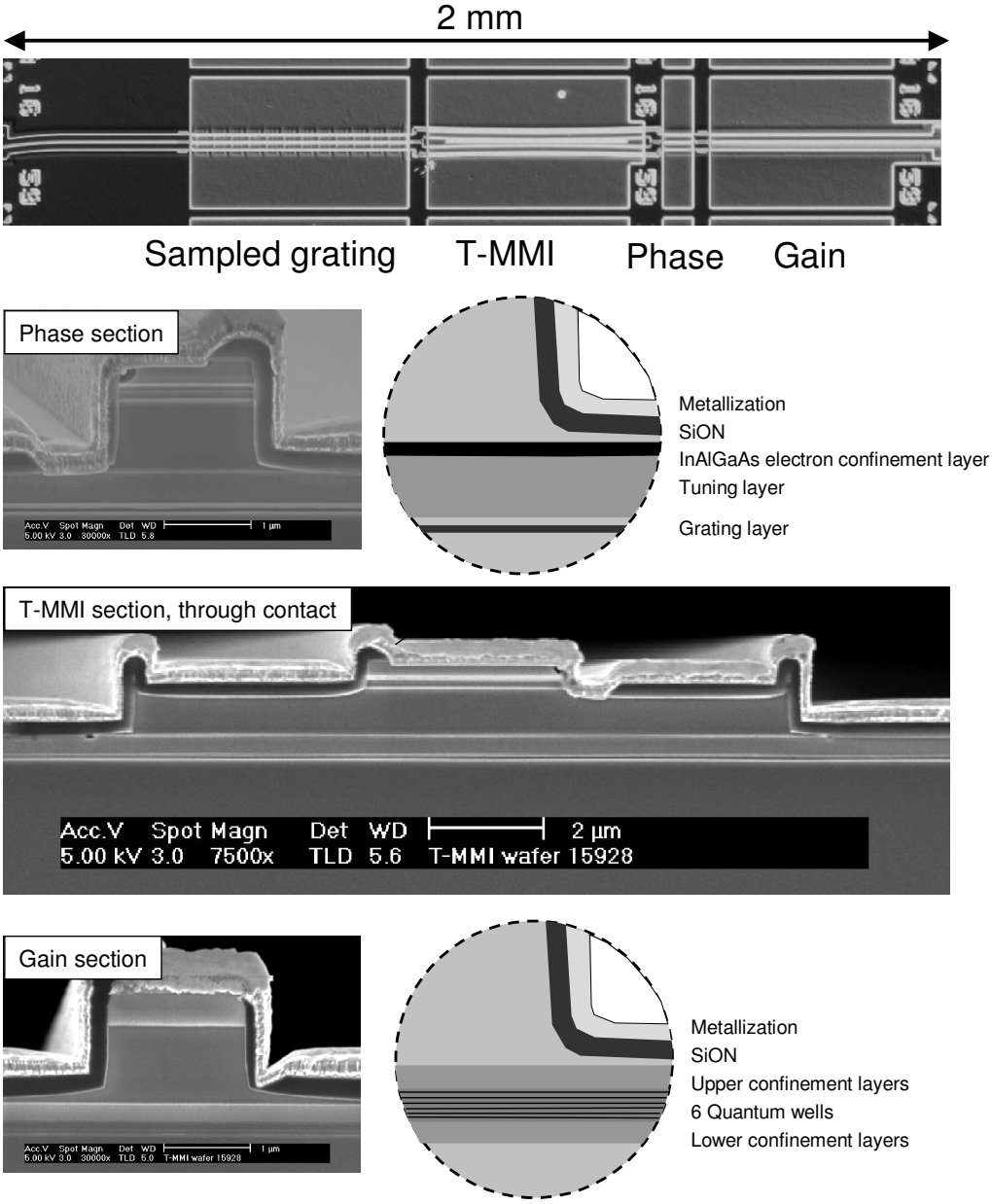


*Figure 5.9: T-MMI laser topview and SEM cross-section at different positions in the T-MMI laser. The cross-section samples have been etched to accentuate doping and material contrast. The layers in the phase and T-MMI section are detailed in the top-inset. The lower inset provides the layers in the gain section. In the SEM-pictures it can be seen that the opening in the SION is mis-aligned. Also, at the edge of the MMI the layer-stack is not etched. This is only the case on the wafers D and E.*

provide sufficient optical gain for laser operation, at a low carrier-density. Since the device is fabricated in a ridge structure, the optimization for the optical confinement and the overlap at the buttjoint has to be re-calculated.

The gain to be provided by the gain section is high to compensate for reduced feedback at high tuning currents, due to degradation of the MMI coupler transmission and/or free-carrier absorption in the sampled grating section. As for the CSG laser, the proven DFB design with the 3-layer confinement structure is used as building-block for the gain section. It is assumed that a similar gain can be obtained in a ridge structure (about 20 $cm^{-1}$ per % confinement). To overcome an estimated loss of about 42 $cm^{-1}$ ($R_f = 17\%; R_b = 23\%$), internal loss $\alpha_i = 12.5\ cm^{-1}$ and 1 dB MMI coupler insertion loss over a 400 $\mu m$ long gain section the number of quantum wells is increased to 6. A confinement of about 3% is required to overcome all loss terms. The device is expected to still operate in the linear regime of the quantum well gain versus carrier-density. Mirror loss variations can then be compensated for by a relatively small change in current.

To avoid loss, due to surface recombination the ridge cannot be etched into the quantum well and confinement layers. Furthermore, the chosen fabrication technique, Reactive Ion Etching (RIE), shows significant depth variation over a 2-inch wafer. Therefore, a minimum cladding thickness of 100 nm is maintained to provide margin against this etch-depth variation.

The thickness of the InP cladding layer is to remain as small as possible, to increase the confinement of the optical mode below the waveguide. A thick cladding layer results in a lateral diffusion of the electrical carriers and a broadening of the optical mode-profile, reducing the injection-efficiency of the laser. Similar arguments are applicable to the tuning sections. Also, when the optical mode is not well confined below the waveguide, its dimensions will increase and a first order mode is more likely to be supported. Therefore, the cladding layer is set to 100 nm.

**tuning sections**

As for the CSG laser, the tuning section in the T-MMI laser is to provide a sufficiently high optical confinement with a high tuning efficiency. The confinement in the MMI coupler region is of lesser importance, given the calculated tuning efficiency in section 5.2.2. The grating strength in the grating burst sections needs to be maximized for sampled grating efficiency.

The etch in the sampled grating and phase sections is not allowed to extend into the tuning layer, since this creates recombination centers in the high carrier-density region of the device. Similarly as for the gain section layerstack a minimum InP cladding layer thickness of 100 nm is required.

The product of optical confinement and material tuning range determines the total available tuning range in the tuning sections. In figure 5.10 the optical confinement and tuning efficiency of the tuning layer is plotted versus the tuning layer thickness. As a reference, the curve for the CSG laser is also included. The confinement is only marginally dependent on etch-depth and waveguide width (a 0.4 $\mu m$ reduction in mesa width results in a 2% decrease in confinement; a 100 nm thicker cladding-layer gives 1% higher confinement). For improved tuning efficiency a narrow waveguide is preferred, but the lithographic process (for definition of a contact) requires the width to be at least

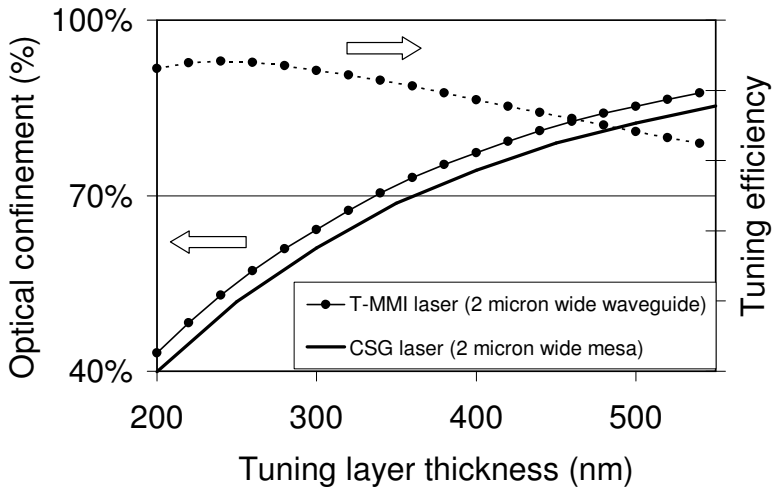


*Figure 5.10: Overlap of optical mode with tuning layer versus waveguide thickness. A 1.8 $\mu$m wide waveguide is used, though dependence on waveguide width is minimal. Also shown the tuning efficiency and the curve for the CSG-laser.*

2 $\mu m$.

In comparison to the CSG laser the T-MMI coupler structure allows for a more effective tuning and a wider tuning range, given by a higher confinement of about 4%. This is mainly caused by broadening of the optical mode, to the region at the side of the waveguide. The tuning efficiency is underestimated, since in the ridge design the current spreads out from under the waveguide and the effective active volume is larger. Based on this figure, a tuning layer thickness of 350 nm is preferred as compromise between tuning efficiency and tuning range.

To increase the carrier-density in the tuning layer at high injection currents a thin electron-blocking $InAl_{0.40}Ga_{0.07}As$ layer is added at the p-side of the tuning layer. As in the CSG laser, this avoids leakage of electrons out of the bulk layer by increasing electrical confinement and hence improves the tuning range [112]. Since this Al-containing layer is not exposed to air, no reliability impact is expected.

From calculations with the mode-solver software in section 3.2.1, the first order mode in the tuning section is guided for all practical waveguide widths. Therefore, coupling of light into this mode needs to be avoided at the buttjoint. Since the waveguide becomes more cut-off at lower InP cladding thickness, the etch-depth is set to 100 nm. Calculations with the eigenmode expansion algorithm (section 3.2.2) show that power coupling to this transmitted mode is less than $10^{-7}$ for all considered design-points.

For gain, phase and sampled grating section, etching into the tuning layer results in surface recombination. For the T-MMI coupler however, the carriers are concentrated in the center of the device and etching into the tuning layer around the MMI coupler does not lead to surface recombination. In figure 5.11 it is shown that this etching is beneficial to the T-MMI coupler performance. With an increased etch-depth (i.e. when comparing a T-MMI with a 100nm cladding-layer and one etched into the tuning layer)

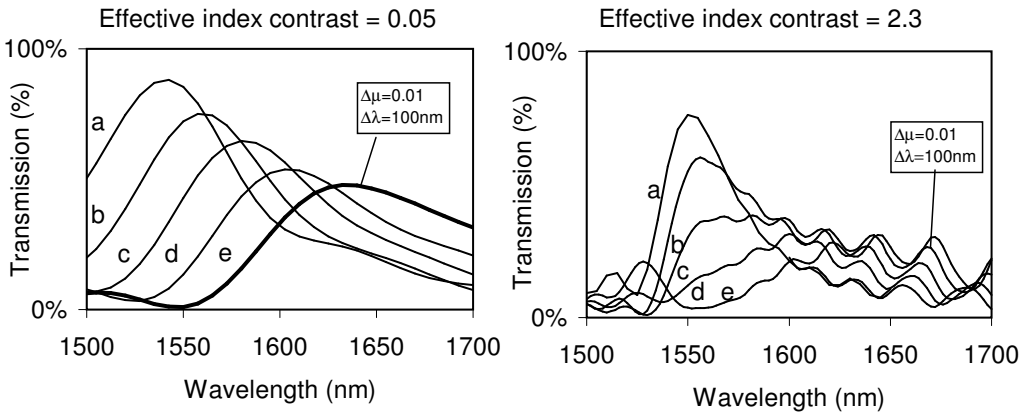


*Figure 5.11: Tuning of T-MMI coupler transmission spectrum. Curves are for an effective index contrast of 0.05 and 2.3 (higher contrast is achieved by etching into the tuning layer around the T-MMI coupler). At a higher contrast the BPM simulations show a larger insertion loss and a more selective transmission spectrum. With increased tuning the decrease in transmission is higher for the T-MMI coupler with a high index contrast. Curves correspond to a) 0, b) 0.0025, c) 0.005, d) 0.0075 and e) 0.01 change in effective index in the center 3 $\mu m$ of the T-MMI coupler.*

the selectivity of the T-MMI coupler improves, due to a higher effective index contrast. The BPM-simulation shows a reduced transmission and a noisy tuning curve at higher tuning current. This is however not expected from a theoretical stand-point and it is assumed that the limitation of the BPM algorithm to handle high contrast structures, with divergent fields, is the cause of this decrease.

For a wavelength selective MMI coupler the position, where positive interference occurs between the different modes, should overlap. When the condition in formula 5.1 is fulfilled (i.e. the paraxial approximation is correct) this is achieved. In figure 5.12 the deviation of the modal-index for modes 4, 6 and 8 from equation 5.1 is shown for a given value of etch-depth. An etch-depth of 0 indicates that the etch stops on the tuninglayer, an etch-depth of 350 means that the etch removes all tuning-layer material next to the MMI coupler. When the etch does not extend into the tuning-layer a variation of the wavelength where modes image can be up to 50 nm. From the figure, the etch next to the MMI coupler, should extend into the tuning layer. The actual depth is not critical. At this interface, no current is injected, hence no surface recombination occurs here.

In figure 5.13 the impact of the cladding layer thickness on the modal effective index is shown. With a decreasing cladding-layer thickness, the contact provides index guiding for the optical modes in the MMI coupler. This results in a break-down of the modal relation in formula 5.1. To avoid this break-down a cladding layer thickness of at least 600 nm is preferred. This will ensure that the image length is similar for each mode-pair.

The design of the grating layer is similar for the T-MMI laser as for the CSG laser. With a grating layer of 70 nm and a spacer layer of 40 nm a grating strength of 15 $mm^{-1}$ is realized.

Material selection for the tuning layer material is a compromise between the optical

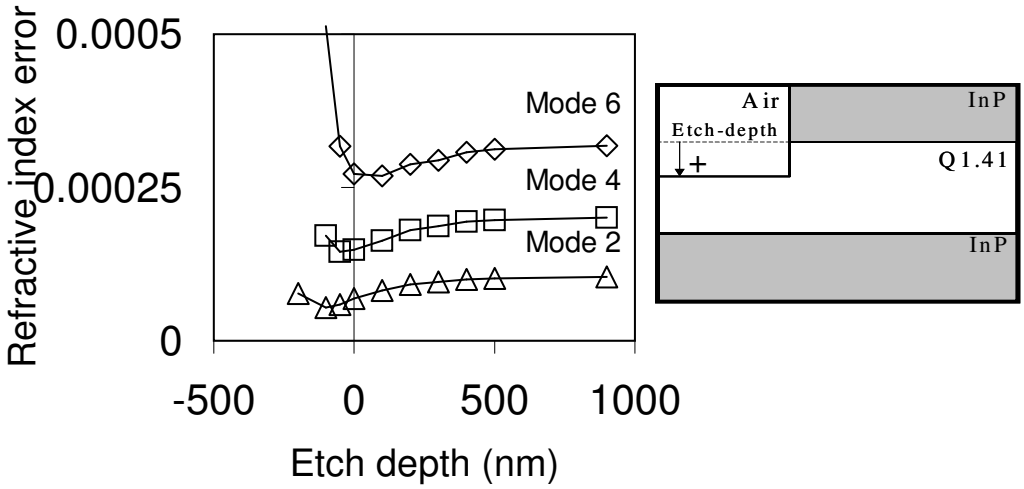


*Figure 5.12: Deviation in modal index from formula 5.1 versus etch depth in MMI coupler region. Etch depth is defined in reference to the top of the tuninglayer. Only even modes in a 20 $\mu m$ wide MMI coupler are considered.*

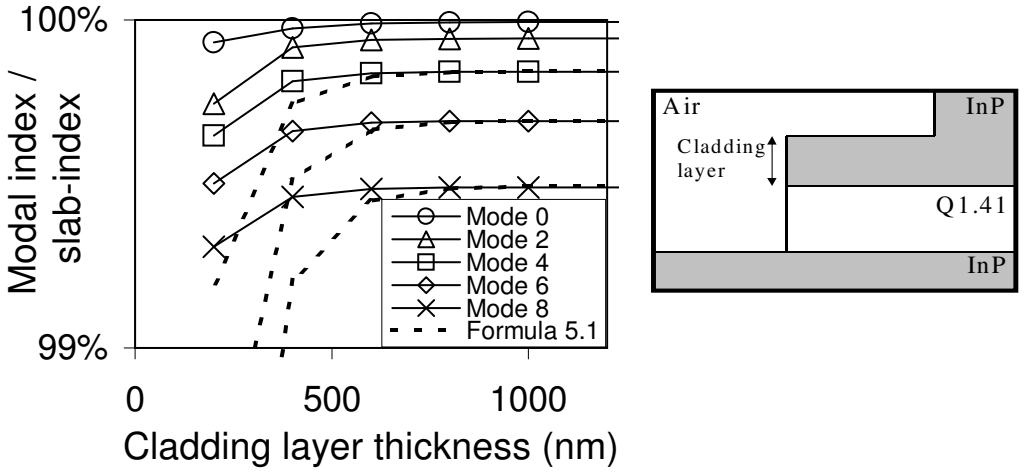


*Figure 5.13: Modal index as percentage of slab-index versus the InP cladding layer thickness. Etch-depth is 0.4 $\mu m$ on a 20 $\mu m$ wide MMI coupler with a 4 $\mu m$ wide contact.*

absorption, free electron absorption and available tuning range. The material choice for the CSG laser was based on a trade-off between tunability and absorption. This was achieved by choosing a material with a bandgap relatively close to the laser-wavelength. The T-MMI coupler, however, behaves mostly as a passive component. Only the intrinsic material loss is significant for this component, since the device has considerable length and only requires a low level of carrier-density over a small part of its cross-section for

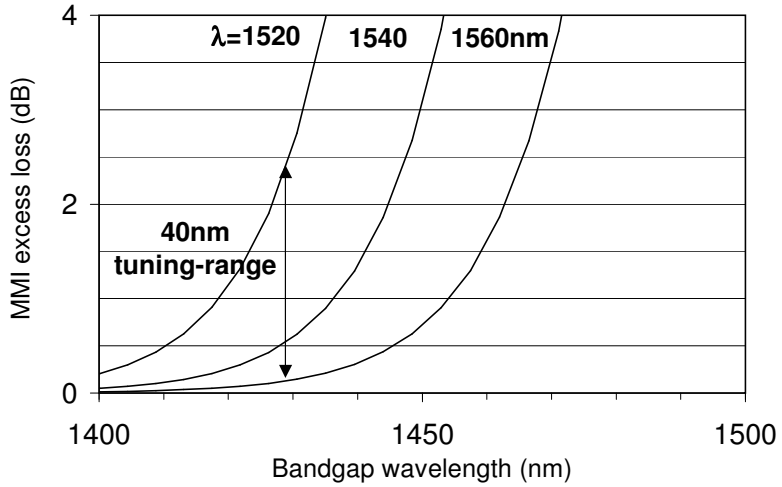


*Figure 5.14: Excess insertion-loss for T-MMI coupler due to material absorption, over a 40 nm tuning-range, plotted versus the tuning material bandgap wavelength. A 400 $\mu m$ long MMI coupler is assumed, with 70% overlap of the optical mode with the tuning material.*

tuning.

In figure 5.14 the excess insertion-loss of a 400 $\mu m$ long MMI coupler, with a 70% overlap of the optical mode with the tuning layer, is plotted versus the material bandgap wavelength. The three curves correspond with the lowest, center and highest wavelength in the tuning range. A low insertion loss over the full tuning range requires a bandgap wavelength below 1410 nm (0.5 dB loss). For larger values of bandgap wavelength the insertion loss rapidly increases.

Comparing this result with figure 4.21 it is seen that free-carrier absorption quickly dominates material absorption at this bandgap wavelength. In the T-MMI coupler the modal overlap with the region of current-injection is however low and the expected tuning-efficiency of the MMI coupler is high (resulting in a low carrier-density in the T-MMI coupler). Therefore, the free-carrier absorption is neglected in the T-MMI coupler.

Referring back to the figure 4.21, this choice of material results in a lower available index-change (or higher required carrier-density) for the sampled grating section. The reduction in index-change is about 20%, reducing the available sampled grating tuning range from 12 nm to about 10 nm, motivating the earlier choice for sampled grating resonance-spacing.

### Buttjoint coupling

High quality coupling, between gain and tuning section, requires a match of the optical modes at the buttjoint. For this purpose waveguide width and cladding layer thickness are optimized with the eigenmode expansion algorithm (section 3.2.2). The reflection at the interface is to be reduced, to avoid a secondary cavity within the laser cavity. However, non-transmitted power is not necessarily coupled into the reflected mode. Power

also couples to substrate modes. Calculations on the buttjoint coupling shows that the reflection coefficient back into the fundamental mode is below 0.03% over the complete parameter space. The transmission from the fundamental mode in the gain section to the first order mode in the tuning section is lower than $10^{-7}$ over the range of interest. A confinement layer thickness (the thickness of the quaternary layers around the gain section QWs) of 60 nm and a waveguide width of 2 $\mu m$ is selected to provide 87% of coupling at the buttjoint.

### 5.2.4 Design summary

The optimized design of the tunable MMI laser is summarized in the first column in table 5.1.

| **Parameter** | Design and simulation value | Experiment value |
|---|---|---|
| Gain section length | 400 $\mu m$ | 400 $\mu m$ |
| Front facet reflectivity | 17% | 27% |
| Gain section waveguide width | 2 $\mu m$ | 1.7 $\mu m$ |
| Gain section confinement thickness | 60 nm | 89 nm |
| Gain section cladding layer thickness | 100 nm | 100 nn |
| MMI width | 18 $\mu m$ | 20 $\mu m$ |
| MMI length | 310 $\mu m$ | 442 $\mu m$ |
| MMI taper-ratio | 50% | 40% |
| MMI etch depth | >200 nm | -100 nm |
| MMI cladding layer thickness | 700 nm | 700 nm |
| Propagation section length | 35.2 $\mu m$ | 31.2 $\mu m$ |
| Grating burst length | 4.8 $\mu m$ | 5.8 $\mu m$ |
| Number of sections sampled grating | 18 | 12 |
| Tuning section waveguide width | 2 $\mu m$ | 1.7 $\mu m$ |
| Tuning layer thickness | 350 nm | 400 nm |
| Tuning section composition | Q1.4 | Q1.43 |
| Grating strength | 15 $mm^{-1}$ | 15 $mm^{-1}$ |

*Table 5.1: Summary of design parameters for T-MMI laser. The first column lists the final design parameters, as used in the simulation. The second column lists the design of the presented experimental T-MMI. Deviations between the two designs are explained by the elapsed time between design finalization and processing of first wafers.*

## 5.3 Device optimization and realization

With the design considerations from the previous section, simulation and experimental realization is needed to demonstrate the device performance and to further optimize the design. The simulation tool from chapter 3 allows for the calculation of the T-MMI laser

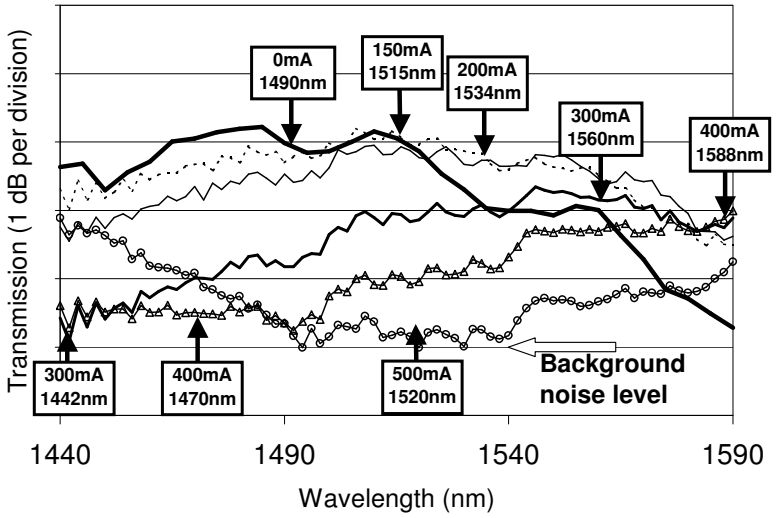


*Figure 5.15: Transmission spectrum for 20 $\mu m$ wide MMI coupler. Different curves correspond with different values for injection current. The arrows indicate the position of the maximum (or minimum) in the transmission curve, demonstrating a shift in MMI coupler wavelength with injection current. The open arrow indicates the background noise level in the measurement.*

performance. Experimentally, several wafers have been processed to demonstrate the T-MMI laser operation (see appendix B for details on the experimental wafers).

In this section, first the performance of a separate T-MMI coupler is demonstrated. Then, the design is verified with the aid of the device-simulation tool. Finally, experimental data are presented of operating T-MMI lasers and the performance is compared to expectations.

### 5.3.1 Tunable MMI operation

The tunability of the T-MMI coupler is the basis of the T-MMI laser. To characterize this tunability, samples (untapered, 20 $\mu m$ wide MMI couplers) were prepared for transmission measurements by cleaving T-MMI sections from the wafer material. These samples include the full T-MMI coupler plus approximately 50 $\mu m$ long in- and output waveguides. An AR coating was applied on both facets and after device separation, T-MMI couplers were mounted and bonded. The T-MMI coupler transmission loss over the wavelength tuning range was characterized for a range of injection currents. The set-up and the experimental approach are described in appendix C. The samples used in this experiment were collected from wafers that did not yield operating T-MMI lasers. This is attributed to a high internal loss in the gain section layerstack (see appendix B) and not expected to impact the performance of the tuning layerstack.

In figure 5.15, transmission curves are shown for one T-MMI coupler. Despite noisy curves, due to the low optical power levels in this measurement setup, it is observed that the wavelength of maximum transmission shift over a range of more than 110 nm.

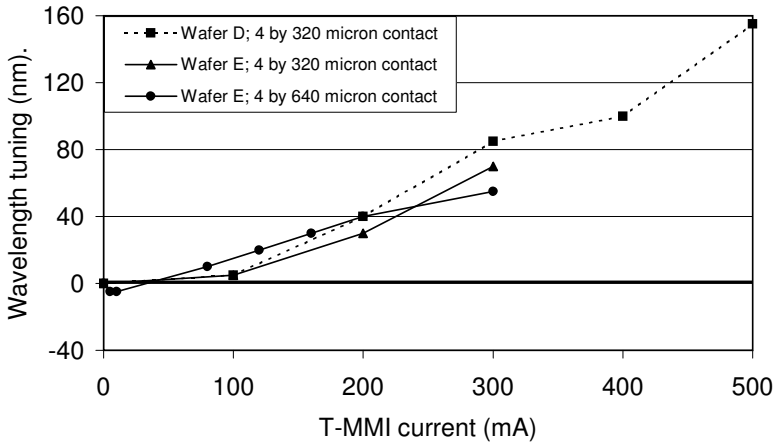


*Figure 5.16: Shift in wavelength of maximum transmission versus injection current for untapered T-MMI couplers.*

Following the minimum in transmission (for curves that have no maximum in the wavelength range of the testing laser) it can be observed that the shift is even larger, by at least 40 nm.

Several samples have been characterized in this manner. The wavelength of maximum transmission is determined with a fit to a quadratic function. For injection current settings, where the MMI coupler wavelength was outside of the tuning range of the testing laser, the minimum in the fitted curve was used to determine the shift in wavelength. In figure 5.16 the wavelength shift is plotted versus the injection current. The tuning performance is shown to be consistent for two different wafers. A tuning-range of 150 nm for an injection current up to 500 mA is demonstrated.

In figure 5.16 the wavelength shift is towards lower wavelengths for the first 20 mA. This effect is attributed to current-spreading over the full MMI coupler width for low levels of current injection. Apparently, this results in a reduction of the modal index of the second order mode. In the following sections, this effect is reproduced on an actual T-MMI laser.

As discussed in appendix C, there are multiple paths between in- and output fiber in the experimental set-up. Hence, a significant part of the transmitted power is not passing through the T-MMI coupler. In figure 5.15 the level of this wavelength independent component to the transmission curve is indicated. An estimate for the T-MMI coupler selectivity is obtained by correcting the measured curves for this background level. From this, the wavelength dependent transmission loss is less than 1 dB over a wavelength range of 62 nm without injection current. This width increases to more than 100 nm for an injection current of 200 mA. This is to be compared to a calculated value of 10 nm for untapered, 20 $\mu m$ wide MMI couplers.

In contrast to the optimal design, these T-MMI couplers were not etched into the tuning layer. As a consequence the effective index of each mode in the MMI deviates from the value given by formula 5.1. In figure 5.11 it is illustrated that this results in

wider transmission curves. For the calculated example (a 0.05 effective index contrast) a width of 48 nm without injection current was found, widening to 65 nm at 40 nm tuning range. In addition, the cladding layer in the experimental device has a thickness of 400 nm. This results in a further deviation of the modal relationship from the formula 5.1 (see figure 5.13). A lower selectivity of the MMI coupler transmission curves is also expected from this effect. An increase in etch-depth and effective index contrast can greatly improve selectivity.

The remaining discrepancy between the selectivity determined from the experiment and the calculated value may be due to a wavelength dependent component of the stray-light (e.g. light that is coupled to the input waveguide and passes through the MMI coupler, but is not coupled into the output waveguide).

The change in peak transmission over the tuning range is limited to 1 dB. This is inconsistent with the BPM-simulations and suggests that part of the reduced transmission in the BPM calculations is due to the limitation of this method, especially for calculation of devices with a high index contrast.

Here, the operation of a tunable MMI coupler has been demonstrated, with a tuning range of up to 150 nm. The spectral width of the T-MMI coupler deviates from the calculated value. This is partly attributed to the low etch-depth and thin cladding layer in the MMI coupler region. In addition, the measurement set-up did not allow for an optimized coupling to the waveguides and T-MMI coupler, resulting in alternative optical paths (see appendix C) between lens objectives and a low transmitted intensity. The spectral width can be improved by resolving these issues (i.e. by etching into the tuning layer material around the T-MMI coupler and using a thicker cladding layer). Also it is shown that the change in T-MMI coupler transmission over the tuning range is limited to 1 dB, suggesting that the BPM simulations provide a worst case estimate.

### 5.3.2 Tunable MMI laser simulation

Having demonstrated the tunability of a T-MMI coupler, this section simulates the use of a tunable MMI coupler in a widely tunable laser. For this purpose the device performance is calculated with the transfer-matrix based tool, described in chapter 3. In this model, the real part of the MMI coupler transmission is described using formula 5.3 (see the transfer-matrix 3.16E). The imaginary part is described as a waveguide, such that the phase and material absorption effects are included in the model. Free-carrier absorption in the T-MMI coupler is not taken into account, since the optical overlap of the modes with the region where current is injected is small, as is the current density (and hence carrier-density) in the T-MMI coupler. For the simulations the optical field is assumed to be weak to limit the interaction between carrier-density and photon density.

In figure 5.17 the simulated wavelength tuning of a T-MMI laser, defined in table 5.1, is shown versus the MMI coupler wavelength of maximum transmission. The phase section current is adjusted to align the lasing wavelength with the sampled grating resonance. Also the output power and SMSR are shown for a gain section current of 150 mA (roll-over is not included). The MMI coupler transmission wavelength shift towards higher wavelength with increasing current, selecting the sampled grating resonance with which it is best aligned. A large tuning range is available since in the calculation the MMI coupler transmission is monotonously decreasing away from the MMI coupler wave-

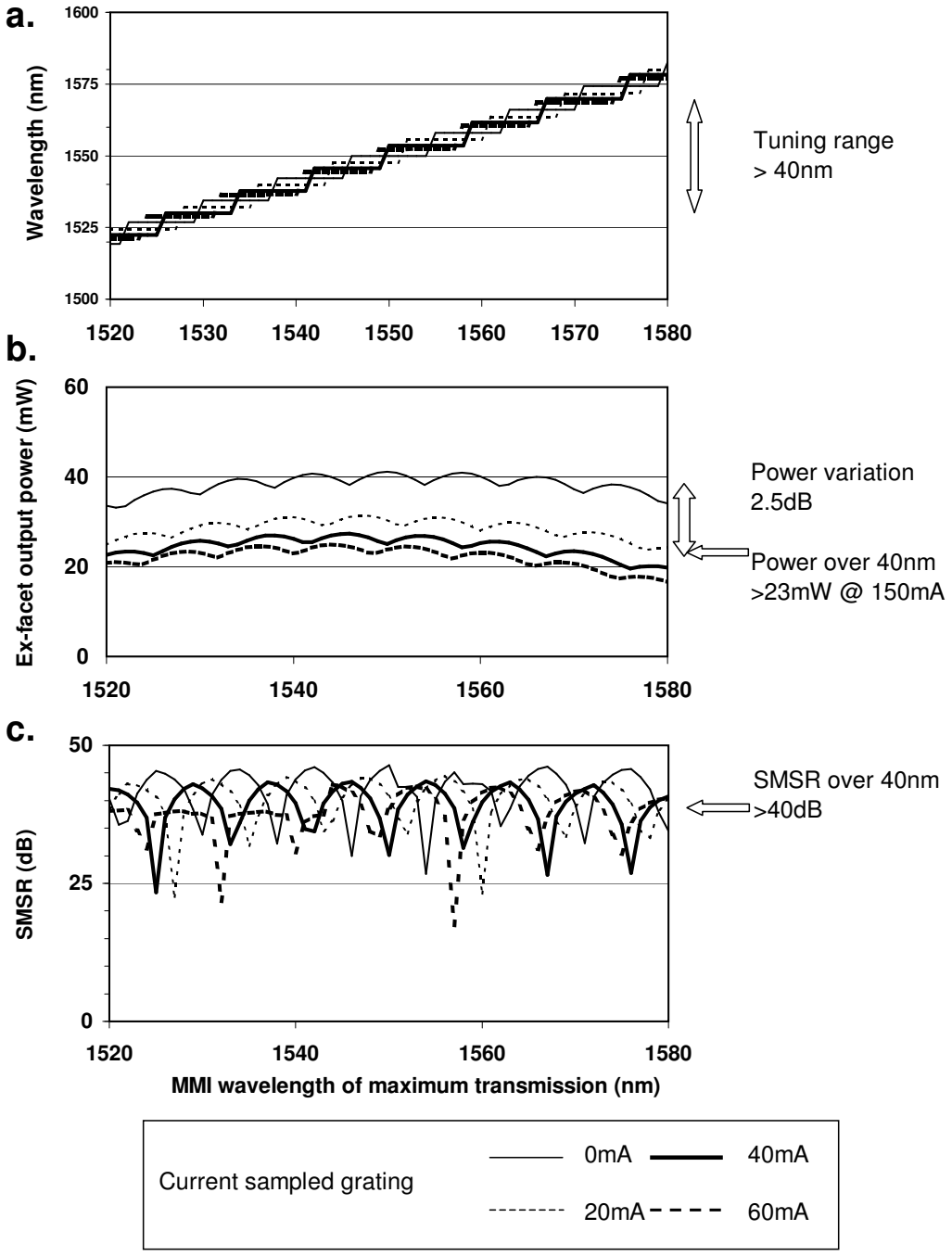


*Figure 5.17: Operating wavelength, ex-facet output power and SMSR for simulated T-MMI laser at 150 mA gain section current.*

length. In practice MMI couplers do not provide infinite suppression and transmission resonances are available of from the main MMI coupler transmission wavelength. Since the sampled grating resonances become weaker, further away from the Bragg wavelength, the effective reflectivity of the main MMI transmission resonance and the sampled grating resonance at some point becomes weaker than the effective reflectivity of the center sampled grating resonance with a secondary weak T-MMI transmission peak.

In the graph for the ex-facet output power, the tuning between sampled grating resonances is visible as small ripples on an envelope, that follows the reflectivity of the sampled grating. At increased sampled grating current the output power decreases, because of free-carrier absorption in the sampled grating. A power-variation of 2.5 dB over the 40 nm tuning range is observed.

From the third graph it is seen that SMSR is better than 40 dB over the 40 nm tuning range. The peaks in SMSR are slightly asymmetric, since the resonance-competition is more favorable when the distance between the T-MMI coupler transmission wavelength and the high-reflection sampled grating resonance (closer to the Bragg wavelength) is slightly wider than the spacing between resonances.

In the application for this device, the gain section current is changed to stabilize the output power to 30 mW. A power variation of 2.5 dB needs to be compensated for. This requires a gain section operating current between 160 and 220 mA over a 40 nm tuning range. The threshold current is between 35 and 60 mA. This simulation assumed similar wavelength dependence of the MMI coupler transmission, upon tuning. Also, the interaction between material absorption and optical power was not taken into account (for the low bandgap material used, this is a reasonable assumption). A 1 dB insertion loss for the MMI coupler was assumed.

The selectivity of the MMI coupler is crucial for device selectivity. Simulations have been performed, with an 18 $\mu m$, 13 $\mu m$ and 9 $\mu m$ wide MMI coupler. This corresponds to MMI couplers with an 1-dB width of the transmission peak of 5, 10 and 20nm, respectively. The change in optical bandwidth does not affect the drive-current range for 30 mW operation. However, the competition between resonances prevents lasing operation at higher order sampled grating resonances and reduces the SMSR. The achievable SMSR at 18, 13 and 9 $\mu m$ MMI coupler width (length 310, 155 and 78 $\mu m$, respectively) is 37, 32 and 30 dB, respectively. The tuning range for the 9 $\mu m$ wide T-MMI coupler is reduced to 25 nm. This demonstrates the importance of a highly selective MMI coupler over the full tuning range.

In this section the feasibility of using a T-MMI coupler to make a tunable laser was shown. 30 mW power and 40 dB SMSR was predicted over a tuning range of 40 nm, with a gain section operating current up to 220 mA. This performance is based on the assumption of 1 dB insertion loss of the T-MMI coupler. At low tuning current this is an overestimate (with typical experimental values of down to 0.5 dB), while the BPM-simulations suggest that this is an underestimate at higher tuning currents (though the accuracy of these BPM simulations is in doubt).

### 5.3.3 Experimental verification

From the wafers (see appendix A for the list of processes) with operating T-MMI couplers a device is chosen with a parabolic tapered MMI coupler (from 20 to 12 $\mu m$, with a total

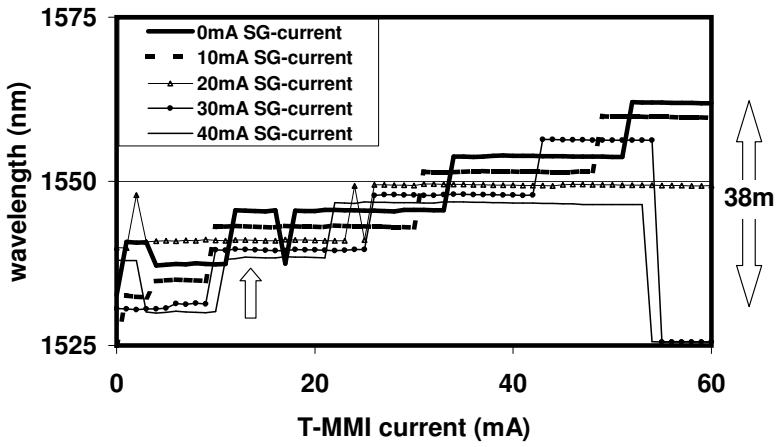


*Figure 5.18: Wavelength tuning performance at 100 mA gain current, of experimental T-MMI laser, versus MMI coupler tuning current for several values of sampled grating tuning current. A tuning range of 38 nm is observed. At the arrow a shift of the sampled grating resonance wavelength is clearly observed with increasing sampled grating current.*

length of 442 $\mu m$) and a sampled grating of 10 nm periodicity (12 periods of 37 $\mu m$ with grating burst sections of 5.8 $\mu m$). The tuning characteristic is shown in figure 5.18.

In the figure a tuning range of 38 nm is visible for an MMI coupler tuning current up to 60 mA. For increasing current, the MMI coupler selects the consecutive sampled grating resonances. By current injection into the sampled grating section, the wavelength is tuned within the MMI coupler transmission spectrum. This is most clearly visible near the arrow in the figure. Irregular mode-hops are observed, where the cavity modes in two different resonances compete (mainly when the device is close to a hop). This is a similar phenomenon as observed for the CSG laser. The tuning efficiency of the T-MMI coupler is higher than for the untapered MMI couplers, due to a higher current density (with the length reduction by 40% tapering) and a larger difference between effective indices for the optical modes in the MMI coupler.

In figure 5.19 the optical spectrum of an T-MMI laser is plotted over the tuning range. A tuning range of 38 nm is visible with an SMSR better than 25 dB. The SMSR improves for a lasing wavelength close to the Bragg wavelength. The envelope for power and SMSR is symmetric around the sampled grating Bragg wavelength. This indicates that over the range of T-MMI coupler tuning currents, the insertion loss of the MMI coupler does not significantly increase. Again, this experimental observation challenges the results of the BPM calculation which showed a strong dependence of T-MMI coupler insertion loss on tuning range (figure 5.11).

Over the tuning range the output power varies between -2 and 8 dBm. The output power versus MMI coupler current is plotted in figure 5.20. This decrease in output power is mainly associated with the sampled grating current (4 dB over 40 mA), as expected from the free-carrier absorption. As was observed on the measured spectra, the output power is not dependent on the T-MMI coupler tuning current. This justifies neglecting

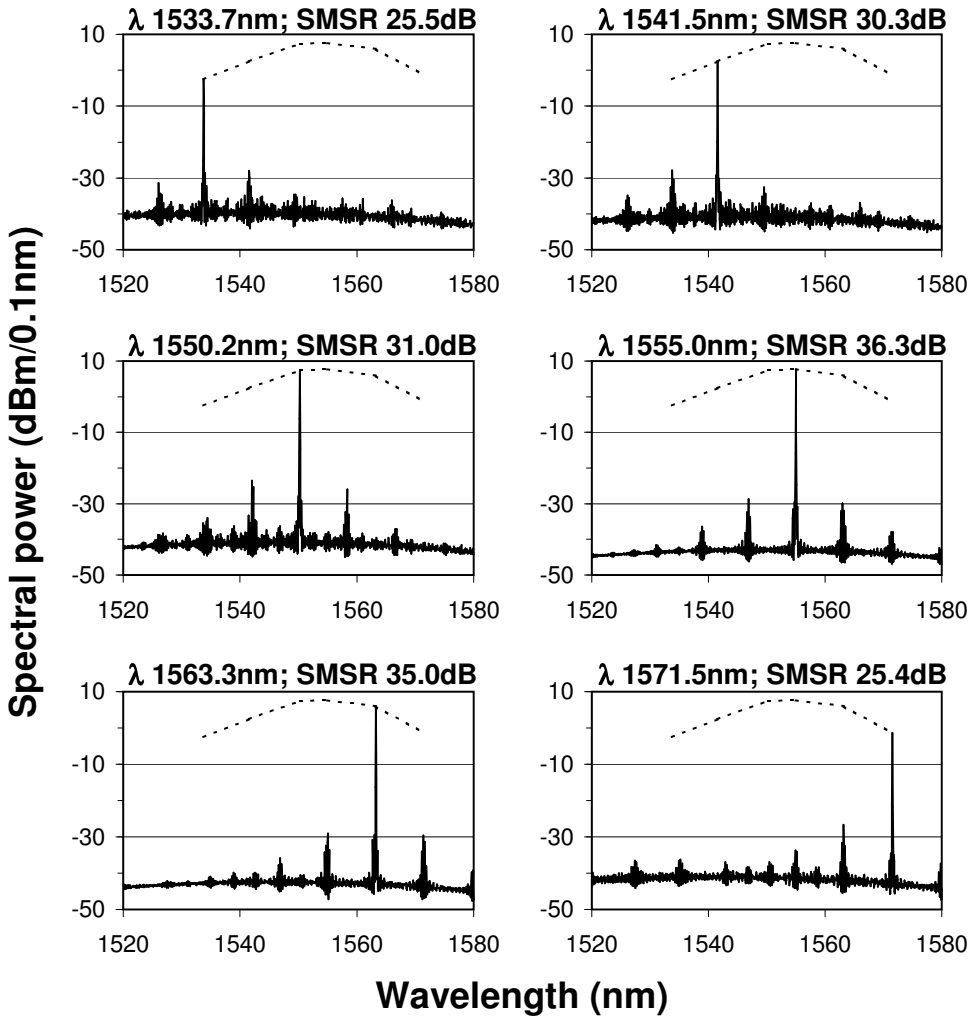


*Figure 5.19: Optical spectrum at 100 mA gain current, of experimental T-MMI laser, over the full accessible tuning range of 38 nm. Side-Mode Suppression Ratio is better than 25 dB for each spectrum. The dotted line in each figure shows the envelope of the peak optical power over the tuning range.*

free-carrier-absorption in the modeling of the MMI coupler and using a fixed insertion loss. This again points to a limitation on the accuracy of the power-transmission in the BPM tool.

Based on the laser-model from chapter 2, a threshold gain of 60 $cm^{-1}$ is calculated when the MMI coupler is aligned with the center sampled grating resonance. Using the internal loss measured for this wafer and the calculated sampled grating reflectivity, an MMI coupler transmission loss is found of 4-5 dB, much higher than demonstrated on

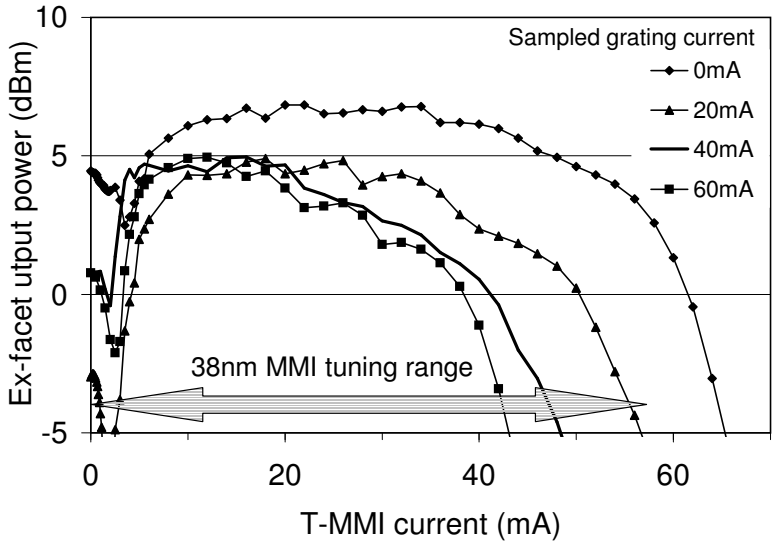


*Figure 5.20: Optical power from experimental T-MMI laser versus the T-MMI coupler current at 100 mA gain current. The arrow indicates over which current range the 38 nm tuning range is achieved.*

these types of MMI couplers [21]. Comparing this to the value for quaternary material in figure 5.14, this is consistent with a detuning between lasing wavelength and tuning layer bandgap wavelength of 90 nm. The PL wavelength for this wafer of 1430 nm indicates a detuning lower than 110 nm. Given the strong dependence of the insertion loss at that value of material detuning, a small variation in the detuning over the wafer and/or a minor inaccuracy in the PL measurement can explain this high insertion loss. Also the loss due to scattering at the MMI coupler sidewalls, the thickness of the cladding-layer and the limited etch-depth around the MMI coupler adds to the total MMI coupler loss. The result indicates that a tuning layer composition was used with too low bandgap energy.

The MMI coupler power (figure 5.20) shows a dependence on the MMI coupler tuning current at low values. The power decreases before it starts to increase. This is consistent with the previous transmission measurements, where a decrease in MMI coupler wavelength was observed for low values of tuning current. This was attributed to spreading of the injected current over the full MMI width for low values of current injection.

These results demonstrate the single mode T-MMI laser. However, they also demonstrate its deficits. Threshold current is in the range of 50 to 80 mA and output power is low (0.63 to 6.3 mW ex-facet). This is attributed, for a major part, to the choice for the tuning material bandgap energy. Reduction of the tuning layer PL wavelength by 50 nm should improve the maximum output power at 150 mA by a factor 3. The SMSR over the 40 nm tuning range always better than 25 dB. Improvement in the etch-depth of the MMI coupler is required to make the MMI coupler more selective.

### 5.3.4 Threshold current and wavelength

In the previous section the best performing device with regards to wavelength tuning and tuning range was shown. Other devices were tested with similar tuning range or higher output power (up to 10 mW ex-facet over a tuning range of 23 nm). A complete presentation of all devices details is impossible in the context of this work. However, measurements on more than 50 devices with different designs (variation in sampled grating period, burst-length and periods, and variation in T-MMI length) allow for a quantitative analysis of the tunable MMI coupler behavior.

Fabricated devices varied in their design of the T-MMI coupler. Both linear and parabolic tapered MMI couplers of various taper ratio were used (and hence different length). Intentionally, the length of the MMI coupler was varied around the design-length by 3 and 6 % in either direction, to account for the sensitivity of the MMI coupler transmission wavelength to the MMI coupler width (see formula 5.4).

In figure 5.21 the wavelength and threshold current without current injection is shown versus the MMI coupler length for devices from 2 different wafers (with a different offset in MMI coupler width from the design). For these wafers a negative offset in width from the design was found of 0.5 and 0.7 $\mu m$(from SEM cross-section analysis). The data without current injection is used, since at this setting free-carrier injection does not play a role and the MMI coupler wavelength is only dependent on fabrication.

Data for 3 different values of taper ratio (30, 45 and 60%) and two different taper types (linear and parabolic) are available. The threshold current has a minimum at a device length that is 97% and approximately 93% of the design length, respectively. These values correlate reasonably well with the measured offset of the T-MMI coupler width (0.5 $\mu m$ corresponds to 95%, and 0.7 $\mu m$ corresponds to 93%). The lowest threshold current is achieved when the MMI coupler transmission wavelength overlaps with the main sampled grating resonance. In the figure it is indicated by arrows that at minimum threshold current the wavelength is approximately 1550 nm, the designed Bragg wavelength. A higher threshold current corresponds to the selection of a sampled grating resonance of higher order, with a lower reflectivity.

From the wavelength plot versus the device length it can be observed that the MMI coupler transmission wavelength shifts towards lower wavelength. This shift is approximately 2.2 nm per % length change, which is much lower than the expected 15 nm per % (based on $\frac{\delta L}{L} = \frac{\delta \lambda}{\lambda}$). Thus the resonance of the sampled grating resonance that is overlapping with the peak in the MMI transmission is not selected. Instead either the main-resonance or a close side-resonance is selected (depending on the alignment of the cavity modes). The change in threshold current is therefore a good measure of the change in MMI coupler transmission at the selected wavelength.

In the figure there is no discernible difference in the threshold current and wavelength of the different types of MMI couplers and the different taper-ratio. This means that either tapering of the T-MMI does not add significant insertion loss to the MMI coupler or that any increase in insertion loss is compensated for by a decrease in material loss. From these results it can be concluded that for the used material composition a high taper ratio (and MMI coupler length reduction) can be used, without sacrificing T-MMI coupler transmission performance. With a change in material composition, the effect of taper ratio and type might become observable. The overlap of the curves shows that the

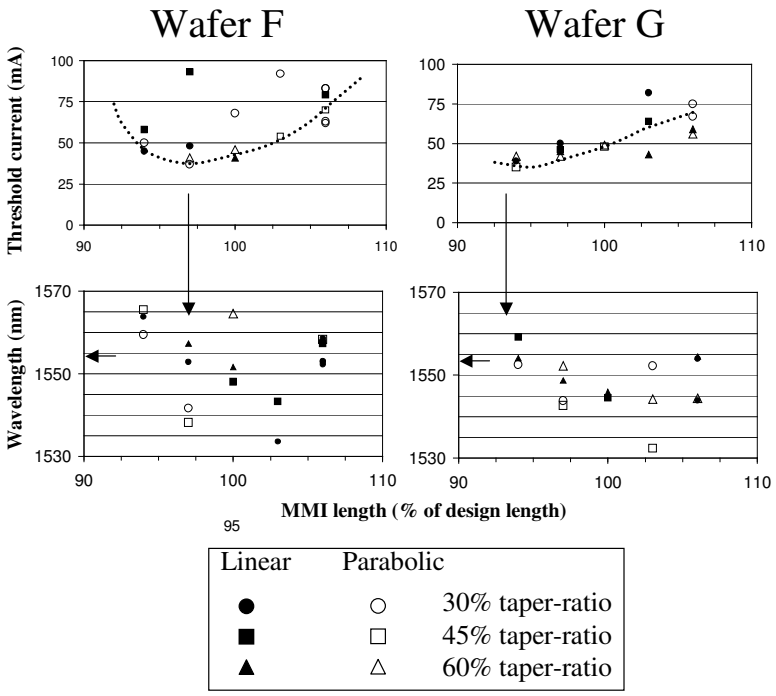


*Figure 5.21: Threshold current and wavelength, with no tuning current, versus the MMI coupler length. Different taper-types and taper-ratio are shown. Data for two different wafers is shown (left side wafer F and right side wafer G). Each dot corresponds to a different T-MMI laser. Minimum in threshold current is at 97 and 94% of the MMI coupler design-length. For that set-point the laser operates close to its Bragg wavelength.*

model, used to calculate the design length for the different taper-types, is sufficiently accurate.

In this section it was demonstrated that, within the investigated range of 30-60% taper ratio, the performance of the T-MMI laser is independent of the tapering geometry, i.e. the taper ratio and type. An offset in MMI coupler length, where the MMI coupler is aligned with the sampled grating Bragg wavelength, is found to be roughly consistent with measured MMI coupler dimensions.

### 5.3.5 Current spreading

The performance of the T-MMI coupler depends on a local variation in the carrier-density in the MMI coupler. The dimension of the contact sets the window for current injection in the MMI coupler, but no structure is present to reduce the current spreading over the width of the MMI coupler. In section 3.3 a model was introduced to calculate the current injection profile, through a resistive diode model.

In figure 5.22 a simulation of current spreading is shown for a 20 $\mu m$ wide and 500 micron long MMI coupler with a 3 $\mu m$ wide contact in the center of the MMI coupler. It

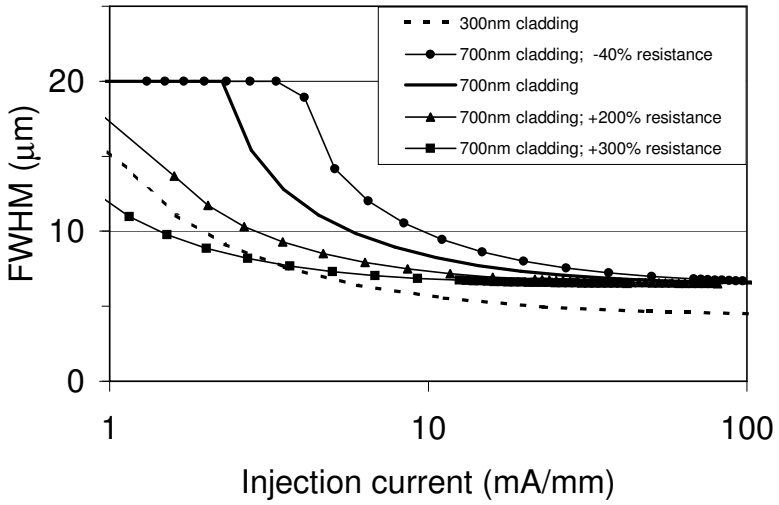


*Figure 5.22: Current spreading calculation for a 20 $\mu m$ wide MMI coupler with a 3 $\mu m$ wide contact. Curves for a cladding layer of 700 nm and 300 nm are included, as well as several curves at different values of material resistance.*

can be seen that at low values of current injection the current spreads towards the MMI coupler edges. However, for current values higher than 20 mA the current is confined to a region within 5 micron from the contact. As stated in section 5.2.2 the MMI coupler tuning is most efficient for a carrier-density confined to the middle 50% of the MMI coupler width.

The simulated current spectrum is insensitive to the choice for the diode parameters. Therefore, only the value of the InP resistance is varied. It can be seen that for a material with higher resistance, less current spreading is observed at low values of injection current. At higher values of injection current the voltage over each diode is clamped and the FWHM is independent of this resistance. Obviously the thinner the cladding layer, the better the carrier confinement, but given the values of current spreading no design trade-off is needed to minimize the impact of current spreading.

In all the calculations the carrier diffusion current is calculated and it is verified that the diffusion current is at most 0.23% of the total current into each region.

Current spreading is experimentally verified by cleaving 500 $\mu m$ long samples through untapered 20 $\mu m$ wide MMI couplers. An AR coating was applied on both facets to avoid internal reflection of spontaneous generated and amplified light. The samples had a 4 $\mu m$ wide contact for current injection. Two different types of MMI couplers were prepared, with an InP cladding thickness of 720 and 450 nm.

Upon current injection the charges distribute over the MMI region and a carrier-density builds up locally. Proportional to this carrier-density spontaneous emission (SE) is generated. At the front facet of the sample the optical power density along the MMI coupler is measured with an infra-red camera.

The following measurements are all presented with courtesy to J.A. de Poorter.

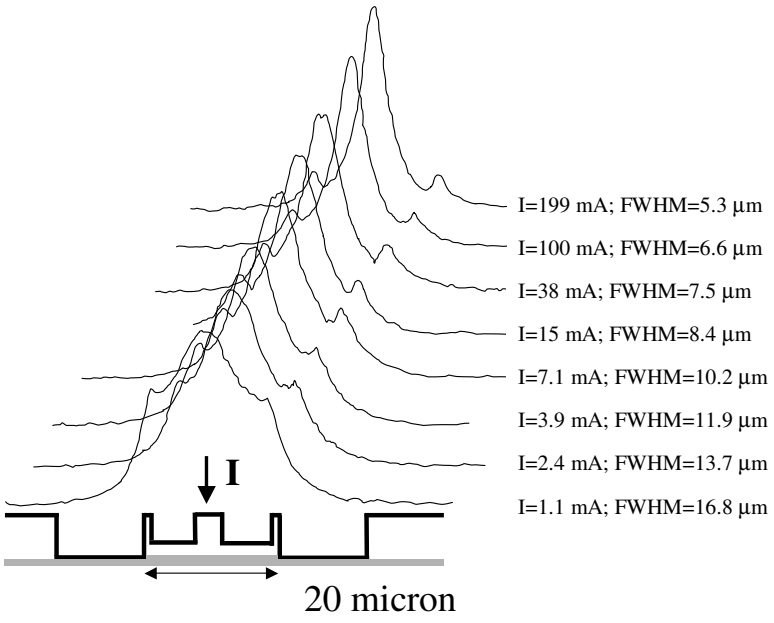


*Figure 5.23: T-MMI coupler spontaneous emission for 20 µm wide MMI coupler samples, with 4 µm wide contact region. Traces are for different value of T-MMI coupler current. On the foreground the sample cross-section is drawn. Due to specifics of the processing, the material at the edge of the T-MMI coupler was not removed, resulting in narrow ridges that guide some of the light.*

In figure 5.23 the emission from an MMI coupler with a 720 nm thick cladding layer is shown. Emission curves for different values of injection current demonstrate current spreading at low currents and a narrowing of the FWHM for increased current injection. Since this MMI coupler has extra (technology related) ridges at the side of the MMI coupler also guided light is observed at the edge of the MMI coupler.

The measured full-width-half-max (FWHM), neglecting the features at the edge of the MMI coupler, of two samples from both wafers is plotted versus injection current in figure 5.24. Also included in this figure is the simulated width for a 700 nm cladding layer.

Though the simulation predicts the experimental trend, a significant quantitative discrepancy is observed. This is most likely due to the detection of spontaneous emission from within the sample. This radiation propagates towards the front-facet, while it expands as a Gaussian beam. Hence, the detected distribution of optical power at the front facet is wider, than the distribution generated in a cross-section. This is also supported by the detection of guided light below the side-structures of this MMI coupler. Furthermore the simulation assumes a resistance value of 0.05 $\Omega cm^{-1}$. With a lower value, a wider FWHM is calculated. However the fast decrease in FWHM with current is not observed in the experiment. The value of FWHM for higher values of current injection shows consistency between experiment and simulation.

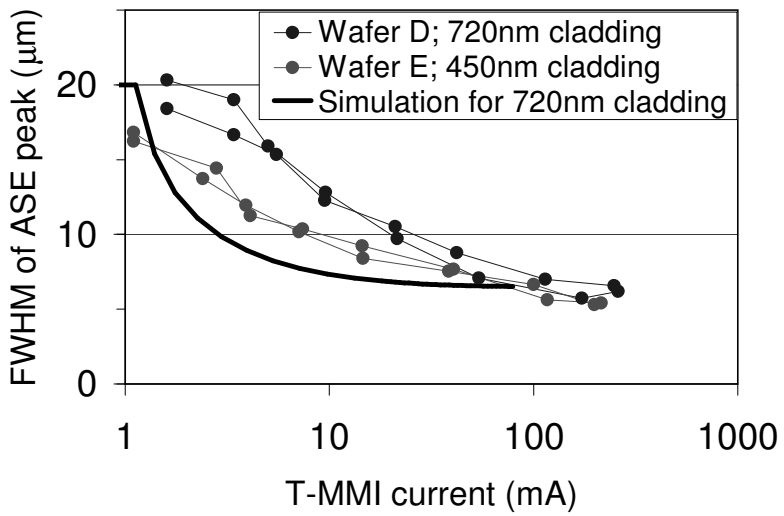


*Figure 5.24: FWHM of current spreading profile for T-MMI coupler sections from wafers D and E. The InP cladding thickness was 720 and 450 nm, respectively. Also included the calculated FWHM for wafer D.*

In this section it has been demonstrated, both by experiment and simulation, that current spreading is not considered a risk for device operation and that it is not sensitive to the device configuration. A limited overlap between experiment and simulation was observed.

## 5.4 Summary

In this chapter the operation principle of a tunable MMI coupler and its application in a T-MMI laser has been introduced. The design requirements and design optimization were given. Both from theoretical and experimental perspective the feasibility of this design is shown and several experimental aspects of the operation were analyzed.

The operation of a T-MMI laser was simulated and demonstrated with experimental devices (which were not of the optimal design). The simulation showed that a T-MMI laser can generate an output power of more than 30 mW over a tuning range of more than 40 nm with an SMSR better than 40 dB, for gain section current lower than 220 mA. The experimental device accessed a total tuning range of 38 nm, with an SMSR better than 25 dB. Output power varied between 0.7 and 7 mW at 100 mA gain section current. Individual T-MMI couplers were shown to have a wavelength tuning range of up to 150 nm.

Based on the experimental data and the comparison to the calculations the bandgap wavelength of the tuning material needs to be reduced by at least 40 nm (to 1400 nm), to reduce the insertion loss of the MMI coupler. Furthermore the area around the MMI coupler needs to be etched into the tuning layer, to improve the selectivity of the MMI coupler.

# APPENDIX A: Fabrication

In contrast to the CSG laser the T-MMI laser is fabricated in a ridge structure. The main reason for this is the incompatibility of the blocking layer (selective) regrowth process with the 90° angles in the MMI coupler.

The requirement of localized current injection in the MMI coupler region requires a two-level ridge-etch process, with the area outside the MMI coupler etched into the tuning layer and the MMI coupler-area outside the contact etched down to a couple of 100 nm above the tuning layer. The isolation channels are also defined at this depth. A total of 4 epitaxial growth steps are required.

Fabrication of the T-MMI laser consists of the following steps.

**Grating growth** The grating layer with InP cap-layer is grown in the first epitaxial growth.

**Grating fabrication** A grating is defined over the complete wafer by holographic exposure. A masking step is used to overexpose the areas where no grating is to remain. The grating teeth are defined by a wet chemical etching process.

**Active layer growth** The spacer-layer plus gain section layerstack is grown.

**Gainblock etching** Gainblocks are defined in the active layer with a $SiO_2$ mask and etched by a wet chemical process.

**Tuning layer growth** Selective regrowth is performed to grow the tuning layerstack around the gain-blocks. The selective regrowth technique ensures a high quality buttjoint with low residual reflections.

**Toplayer growth** After removal of the gain-block masking the remainder of the layerstack is grown, including contactlayers.

**Two-step ridge etching** A Reactive Ion Etch (RIE)-process is used to etch the waveguide. First the complete MMI coupler and waveguides are defined in $SiO_2$ and the material outside this region is removed up to a given depth. In a following step the masking of the isolation channels and of the part of the MMI coupler without current injection is removed. The RIE-etching is then continued down to the required depth.

**P-metallisation and lift-off** $SiO_2$ is deposited on the wafer and removed on top of the contacts. A lift-off process is employed to define the metallisation pattern on the p-side.

**Wafer-thinning and n-metallisation** The wafer is thinned to the desired thickness and n-metallisation is sputtered.

**Coating and back-end process** Bars are cleaved and coated, after which chips are separated, mounted and bonded for testing.

# APPENDIX B: Processed material

For demonstration of the T-MMI laser several wafers were fabricated. On these wafers device variants were included with different MMI coupler width, MMI coupler taper ratio and sampled grating design, as well as common DBR lasers. To compensate for fabrication tolerances in the MMI coupler width, devices with MMI coupler length of $\pm 3\%$ and $\pm 6\%$ around the design length were included. Between wafers, there was intentional variation in cladding layer thickness and tuning material composition.

The gain section internal loss of each of these wafers has been determined by a length-series of Fabry-Perot lasers [111]. In table 5.2 the data for different wafers is given. Wafers D, E and F show a high internal loss (typical values are 10-15 $cm^{-1}$). Therefore, no operational T-MMI lasers were obtained from these wafers. Possible reasons for the high loss are surface recombination due to etching into the active layer or low-quality regrowth onto a thin spacer layer (required for a high grating strength). Both hypotheses could not be verified conclusively. The high internal loss is not inherently related to the tunable MMI coupler concept, since gain-sections operated as ridge lasers performed equally poor.

The etch depth in the MMI region is the same as in the phase and sampled grating sections. As a consequence the confinement in the MMI coupler is sub-optimal. Estimated MMI coupler index-contrast is between 0.05 and 0.10.

| Wafer ID | Wafer D 15830 | Wafer E 15847 | Wafer F 15906 | Wafer G 15907 | Wafer H 15972 |
|---|---|---|---|---|---|
| Internal loss ($cm^{-1}$) | 25 | 36 | 34 | 12.4 | 15.4 |
| Injection efficiency (%) | 81 | 69 | 48 | 98 | 76 |
| Ridge width ($\mu m$) | 2.9 | 2.9 | 1.5 | 1.8 | |
| MMI cladding (nm) | 724 | 451 | 400 | 400 | 400 |
| MMI width deviation ($\mu m$) | -0.7 | -0.5 | NA | NA | NA |
| $\lambda_B$(nm, from DBR) | 1546 | 1548 | $\sim 1550$ | $\sim 1550$ | $\sim 1550$ |

*Table 5.2: Overview of fabricated wafers with T-MMI lasers*

# APPENDIX C: T-MMI coupler transmission measurement

Transmission of MMI couplers is measured [80] [48] with a setup as shown in figure 5.25. Two fiber-lens assemblies are used to couple an optical signal from the measurement setup to and from a sample. This sample is a cleaved untapered MMI coupler with short input and output waveguides (about 50 $\mu m$ long). Both facets are AR-coated to avoid cavity resonances.

A signal of a tunable extended-cavity laser is coupled into the input waveguide of the MMI coupler. A polarization controller controls the polarization of the input light. Both the input and output power is measured to determine the optical loss in the sample. Transmission loss is measured at three polarization settings, from which the transmission in both TE and TM mode polarization is derived [6].

The coupling efficiency of the signal, to input and output waveguides, is optimized through the generation of spontaneous emission below the MMI coupler contact by current injection.

The acquired transmission spectrum depends on the quality of the coupling between measurement setup and sample. Ideally only light that propagates through the waveguides and MMI coupler is collected at the output fiber-lens assembly. But several other optical paths exist:

Light that is not coupled from MMI coupler to output waveguide is partly collected by the fiber-lens assembly, due to the short output waveguide from the MMI coupler.

Light that is not coupled to the input waveguide can propagate into the MMI coupler and be collected at the output waveguide, due to the short input waveguide to the MMI coupler.

Light that is not coupled to the sample can directly couple into the output fiber-lens assembly, due to the short sample length.

These sources of stray-light introduce a significant amount of noise in the measurement and cause the measured MMI coupler response to be less selective than the actual spectrum.

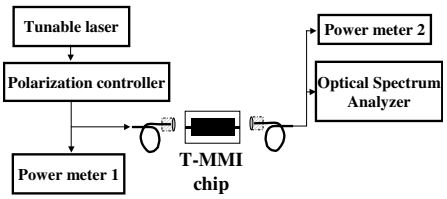


*Figure 5.25: Measurement set-up for MMI coupler transmission measurements. The probe signal, generated by a tunable laser, is coupled to the MMI coupler sample, through a polarization controller and fiber-lens assembly (at the left side). The right side lens-fiber assembly collects the signal into a power-meter and optical spectrum analyzer.*

# Chapter 6

# Discussion

The analysis of the two widely tunable laser concepts is conpleted in this chapter with a comparison to other integrated widely tunable lasers. This chapter is concluded with a summary of the presented work and its relevance to the field of widely tunable lasers.

## 6.1 Evaluation of the CSG and T-MMI laser

The experimental realization of the two new concepts has left a mixed impression of the performance of these tunable lasers. On one hand, the tuning concepts have been demonstrated and requirements were shown to be within reach for both tuning range (40 nm) and output power(30 mW). On the other hand, the demonstrated devices were irregular in the tuning performance and the target of 30 mW output power is not achieved.

One reason is that the wafers were processed before all design insights were obtained. Therefore, processed devices were not fine-tuned according to the optimum design, as presented in this thesis. For the T-MMI laser, the high quaternary composition of the tuning layer and the etch-depth around the MMI are examples of this. For the CSG laser, the length of the sampled gratings was not optimal. Also, processing complications introduced problems. For the CSG laser, an error in the growth of the gain section layerstack forced the use of a thin tuning layer and for the T-MMI laser, several of the wafers had a high internal loss in the gain region, along with a not well controlled etch-depth in the RIE-process. Experimental devices, when processed with the optimal design, are expected to show an improvement on the already achieved experimental results.

In the following sections the experimental result, as well as the simulations, are analyzed. The main target is to derive the inherent capabilities of each concept and to compare those to existing concepts. Also the capability to reach the required specifications is discussed. The most important criteria for a widely tunable laser, output power and SMSR, are the main criteria to judge both new laser concepts. But also considerations for practical use, such as manufacturability, testability and controllability will be considered.

In the evaluation, only the comparison to other integrated semiconductor-based tun-

able lasers is discussed. The choice is made to focus on this category, based on the discussion in section 2.3. ECL type lasers are expected to be superior in performance, but less favorable in terms of cost, compared to integrated designs. VCSEL's inherently generate low output power and only compete for a niche market segment. Array concepts present a high level of complexity and are therefore not preferred, when alternatives are available. They also require additional components, such as an optical amplifier or a MEMS mirror.

The evaluation of the different integrated semiconductor-based concept is based on the same areas of operation as in section 2.3. In addition the available tuning range needs to be considered. The tuning range of both CSG and T-MMI laser was shown to meet the required 40 nm, both from simulation and experimental verification. The simulations predict accessibility of all intermediate wavelengths, though the irregular tuning of mainly the CSG lasers resulted in intermediate wavelengths that could not be accessed on processed devices.

### A. optical output power

From simulations, CSG and T-MMI operation at 30 mW can be obtained with the optimized designs. Devices were demonstrated for the CSG laser with an output power between 5 and 10 mW over 40 nm. For the T-MMI the power varied between 0.7 and 7 mW over a 38 nm tuning range. These power-values were achieved at 100 mA gain section current. For other devices, with a lower tuning range, a higher output power was realized.

The discrepancy between experiment and simulation is for the CSG lasers attributed to a non-optimal design choice for the CSG and processing errors, such as the growth of an asymmetric confinement layer structure. For the T-MMI lasers, the low power is attributed to excessive loss in the MMI section, as confirmed in calculations. In addition it was found that several wafers grown in the period of these experiments showed a high internal loss. Solution of these problems can result in a significantly better performance that approaches the simulation results. Further material improvements are needed for the laser section to provide a higher gain at a lower current. Quantum well improvements and/or the inclusion of Al-based material to reduce electron leakage are considered promising.

Free carrier absorption presents a limitation for semiconductor current-injection based tuning schemes. To achieve an output power of 30 mW, with a sufficient side-mode suppression and a gain section current in the range of 150 mA, the reflectivity of the back-facet needs to be higher than 23% over the full tuning range. To achieve this long sampled gratings are needed, with a high value of grating strength (and for the T-MMI laser a low loss MMI). Other technology platforms exist, such as used for the SG-DBR [54], that can generate up to $30mm^{-1}$ grating strength. A CSG or T-MMI within that platform can be designed with shorter sampled grating sections and hence a lower penalty for free carrier absorption.

An output power of up to 5 mW for the GCSR and SG-DBR over the 40 nm tuning range is demonstrated [38]. The SG-DBR laser does not have the potential to reach high output power without amplification, but for the GCSR a 25 mW power was demonstrated over 25 nm [44]. For the modulated grating Y-branch laser a device has been demon-

strated with more than 13 dB of output power over the tuning range[116]. With the optimal design of both CSG and T-MMI, simulations show that 30 mW of output power can be realized (with gain section currents up to 220 mA). Devices without a tuning section at the front facet are very similar in their potential to reach high output power. Optimization of design choices and processing technology is needed to demonstrate this.

### B. single mode operation

Simulations on the CSG and T-MMI show that an SMSR larger than 37 dB can be realized over a 40 nm tuning range. Experimentally, the SMSR values were lower, partly due to relatively short (compared to the optimal design) sampled grating sections. It was shown that the T-MMI selectivity can be improved by an increase in the etch-depth around the T-MMI. Also a different technology platform with a higher grating strength can reduce the sampled grating length and improve the mode-spacing.

For the CSG laser SMSR values better than 30 dB have been demonstrated, while the T-MMI laser delivered better than 25 dB SMSR. This compares to demonstrated values of 30 dB with the GCSR design and better than 40 dB with the SG-DBR and modulated grating Y-branch laser [15] [44] [116].

Conceptually, the achievable SMSR is higher than 35 dB for all concepts and the actual realized value is not an important differentiator for use of these lasers in telecommunication networks.

### C. variation of power and SMSR over the tuning range

The CSG laser has demonstrated an output power variation of 3 dB over the tuning range and an SMSR variation of 8 dB. The T-MMI laser showed a 10 dB variation over the tuning range and a SMSR variation $> 10\ dB$ (consistent with this large power variation). In the simulations for these devices an output power variation of 2.5 dB was predicted for the CSG and T-MMI laser. If the SMSR target is met over the complete tuning range, the actual variation in SMSR is not relevant.

The variation in power for the other integrated concepts is comparable or larger. 3 dB variation was demonstrated for the GCSR laser [38] and more than 5 dB for the SG-DBR laser. For the modulated grating Y-branch laser a variation of less than 1.5 dB over the tuning range is reported [116].

Concepts with only a sampled grating section at the back-facet side offer an inherent advantage in variation in power over the tuning range, compared to a concept with a sampled grating at the front facet. Typically a variation less than 3 dB can be achieved for most concepts.

### D. tuning complexity and stability

Inherent to tunable lasers a change in tuning section properties results in a change in laser wavelength. Though this is a beneficial property, it means that the device is sensitive to external noise.

A change in the tuning section current, results in a change in its transmission and/or reflection spectrum. At the lasing wavelength, the cavity phase changes and the lasing

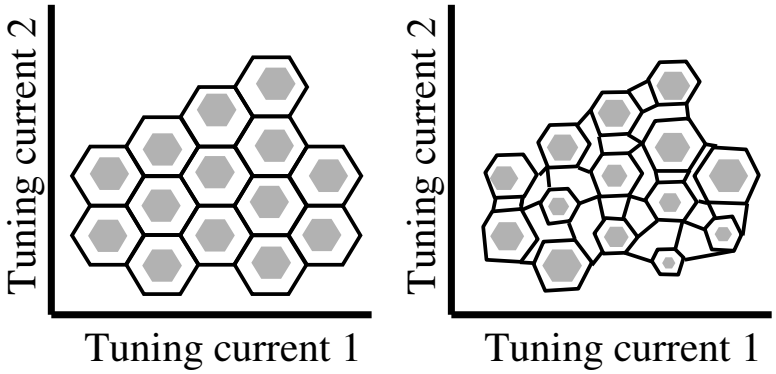


*Figure 6.1: Location of mode-boundaries versus tuning currents. At the interfaces the lasing wavelength changes, from one laser cavity mode to another. The gray areas between modehops are the stability regions where all specifications are met. a) No competition between modes in different tuning section reflection resonances. b) Competition between modes in different tuning section reflection resonances. The mode-boundaries are misformed, when the mode-hop is not towards a neighboring cavity mode. The occurrence of such a mode-hop is dependent on the alignment of modes in the competing reflection resonance and is irregular.*

wavelength has to shift, to fulfill the laser condition. If initially the selected cavity mode was aligned with the tuning section resonance, this might no longer be the case after the shift in lasing wavelength. If the misalignment becomes too large, a different cavity mode, that is better aligned, is selected. This is known as a modehop and if this can occur during normal operation, over the device lifetime, the laser is not sufficiently reliable for most telecommunication applications.

To express the stability of the wavelength to a control signal, it needs to be established by how much the cavity round-trip phase at a given lasing wavelength changes. The lasing wavelength will then shift over the wavelength range $\Delta\lambda$ needed to compensate for that phase change. This wavelength change is $\Delta\lambda = \Delta\lambda_{cav} \cdot \frac{\Delta\phi}{2\cdot\pi}$. With $\Delta\lambda_{cav}$ the cavity modes spacing and $\Delta\phi$ the phase change of the tuning section response at the original lasing wavelength.

In appendix A the sensitivity of the lasing wavelength to changes in the tuning sections is calculated for the different integrated widely tunable lasers discussed here.

A lasing mode can be misaligned by half the cavity modespacing, before competition with a neighboring cavity mode results in a mode-hop. Therefore the size of a stability region (within which the tunable laser operates without modehops) for one control parameter is defined as $\frac{\Delta\lambda_{cav}}{\delta\lambda/\delta z}$, with $\delta z$ the change in that control parameter. Performing this analysis for all control parameters of the tuning sections gives a multi-dimensional stability region. In figure 6.1a this is shown for a two dimensional structure, such as the CSG section. Set-points where modehops occur are indicated by black lines, resulting in islands (stability regions), within which the device is lasing in one cavity mode.

A regular mode-map is obtained when only mode-competition between neighboring cavity modes is considered (i.e. within the same tuning section resonance). Mode competition with modes in other tuning section resonance can change this regularity.

Dependent on the alignment of the cavity modes within other resonances, a mode in that resonance can take over lasing before a modehop between neighboring cavity modes occurs. This modehop reduces the size of the stability region and makes the tuning performance irregular.

The effect on the tuning map is illustrated in figure 6.1b. A mode-pattern is shown, where modes in different resonances compete for lasing operation. The boundaries, where the modehops occur, have an irregularly shape and the stability regions decrease in size. This competition with modes in other tuning section resonances is uncontrollable in nature.

To avoid this reduction in stability area and increase in irregular tuning performance the design has to suppress the cavity modes with overlap with a non-selected sampled grating resonances. In this manner any mode-hop will occur within the selected resonance. This can be accomplished in two ways: either an over-design of the tuning section to suppress all non-selected sampled grating resonances or by a reduction in the selectivity of the sampled grating resonances to increase the selection of cavity modes in the same sampled grating resonance over other cavity modes. The latter method does reduce the SMSR.

The combination of sensitivity of the lasing wavelength, on tuning section currents, and the irregularity of the tuning behavior have impact on at least three areas:

**reliability** To meet optical communication reliability standards the operating current and device wavelength need to be controlled within tight specifications over the device lifetime. This requires inherent stability of the material system and an insensitivity of the tunable laser to changes in the tuning section. Changes in a semiconductor laser properties are due to physical changes in the material, or due to external feedback (of any kind). The physical changes that can occur in a device are correlated with the technology chosen for manufacturing. However the impact of these physical changes on device properties is determined by the device concept.

**Testing and control** The ability to quickly distinguish good and bad devices, and to fully characterize a device within minutes is essential for manufacturing widely tunable lasers. For most widely tunable lasers, with typically 3 or 4 contacts, a full characterization is not a good approach. Even a small number of points per dimension (say 50), leads to a huge number of characterization points (e.g. 0.125 and 6.25 million for 3 and 4 dimensions, respectively) that need to be measured and analyzed.

For each specific laser-type an optimized algorithm is required to intelligently look for the operation points. This algorithm needs to make full use of each type of measurement, with its own characteristic evaluation time (e.g. electrical measurements can be done faster than a ms, optical power can be measured typically within a few ms, a wavelength measurement takes about 100ms and an optical spectrum requires at least 500ms). Several intelligent ways have been proposed to screen devices and find the mode boundaries, by only measuring the electrical characteristics. Examples are the measurement of the gain section voltage [68] and the measurement of generated photocurrent in the phase section (not reported).

The characterization of a tunable laser is facilitated by a predictable tuning section response, regularly positioned modehops and a dependence of properties on a minimal number of external sources.

**linewidth** In [14] the excess linewidth for a TTG laser (modeled as a Fabry-Perot cavity) and a 3-section DBR is analyzed. A full extension of this analysis to other widely tunable laser types shows that the linewidth is proportional to the change in wavelength with tuning current, as expressed in equation 2.9.

From this analysis if follows that the excess-linewidth is proportional to the change of wavelength with tuning current, as expressed in table 6.3.

Considering the above, tuning complexity is inversely proportional to the size of the stability region, and device concepts with an inherent larger stability region, provide a more stable set-point that can be determined with less complexity.

For each integrated widely tunable laser considered here, the sensitivity of the wavelength to changes in the tuning sections is calculated from the formulas in table 6.3. The results are summarized in table 6.1. For this numerical calculation the following representative values are used:

$$\begin{aligned} cavity-mode\ spacing &\quad \Delta\lambda_{cav} &\quad 0.4\ nm \\ Length\ phase\ section &\quad L_{phase} &\quad 100\ \mu m \\ Effective\ index\ gain\ and\ tuning\ sections &\quad \mu &\quad 3.5 \\ Effective\ length\ laser\ cavity &\quad L_{cav} &\quad 700\ \mu m \\ Effective\ length\ sampled\ grating &\quad L_{eff} &\quad 300\ \mu m \\ Reflection\ sampled\ grating &\quad r_{SG1}\ r_{SG2} &\quad 40\% \end{aligned} \tag{6.1}$$

| Design | Section | Wavelength sensitivity |
|---|---|---|
| All concepts | Phase section | $\delta\lambda/\delta\mu = 0.0016\ nm$ |
| CSG | 1st Sampled grating section | $\delta\lambda/\delta\lambda_B = 0.08\ nm/nm$ |
| | 2nd Sampled grating section | $\delta\lambda/\delta\lambda_B = 0.08\ nm/nm$ |
| T-MMI | Sampled grating section | $\delta\lambda/\delta\lambda_B = 0.17\ nm/nm$ |
| | T-MMI section | $\delta\lambda/\delta\lambda_{MMI} = 6 \cdot 10^{-6}\ nm/nm$ |
| SG-DBR | Sampled grating sections | $\delta\lambda/\delta\lambda_B = 0.17\ nm/nm$ |
| GCSR | Sampled grating section | $\delta\lambda/\delta\lambda_B = 0.17\ nm/nm$ |
| MG-Y | 1st Sampled grating section | $\delta\lambda/\delta\lambda_B = 0.08\ nm/nm$ |
| | 2nd Sampled grating section | $\delta\lambda/\delta\lambda_B = 0.08\ nm/nm$ |

*Table 6.1: Numerical values for operating wavelength sensitivity to tuning section properties.*

It is understood that for each particular device design the number can vary significantly (up to about a factor 4). Even so, the comparison between different widely tunable laser concepts remains valid, since most errors in the assumption are equally valid for all concepts.

In this comparison, the GCSR and T-MMI lasers, based on the selection of a sampled grating resonance with a coarse filter, provide the largest stability region. The

wavelength is almost independent on the current setting in the coarse filter element and only the sampled grating current needs to be controlled accurately to provide the control over the lasing wavelength. The larger stability region is a real benefit for device operation, because it requires a less complex stabilization algorithm and reduces the tuning complexity by one dimension (since the wavelength is not dependent on the coarse tuning element the wavelength can also not be controlled by it).

In addition, the coarse filter elements in the GCSR and T-MMI, provide increased selectivity further away from the lasing wavelength (assuming that the transmission curve is monotonous decreasing). Therefore irregular tuning, to other resonances over the complete tuning range, is suppressed.

Furthermore, the wavelength can only change by $\Delta\lambda_{cav}$ within a stability region. By providing a large laser cavity (as is needed for T-MMI and GCSR) further stabilization of the wavelength is achieved. The size of the stability region is however not affected.

Concepts based on the Vernier effect - like SG-DBR, modulated grating Y-branch laser and CSG - have a much smaller stability region, since wavelength is sensitive to both sampled grating currents.

In the comparison between SG-DBR and both CSG and modulated grating Y-branch laser the former is more sensitive to changes in tuning section current. In the formulas it can be seen that changes in tuning current in sampled grating have an impact proportional to their contribution to the total phase of the CSG or modulated grating Y-branch. For the SG-DBR the change in phase of a sampled grating is equal to the change in cavity phase. As a result the stability region is smaller for an SG-DBR.

In conclusion, both T-MMI and GCSR provide a stability region, which size is only limited by the sampled grating section. A CSG and modulated grating Y-branch laser control the lasing wavelength through two control signals, though the phase change of the separate sampled grating sections is reduced by the addition of the two reflection terms of both sampled gratings. The SG-DBR has the most narrow stability regions, since any phase change of its sampled gratings reflection changes the cavity phase by the same amount.

### E. wavelength tuning time

The ability to tune the wavelength of a tunable laser from any setting to a given set-point is independent of the device design and mainly dependent on the tuning principle. For devices with tuning based on current injection (as opposed to thermal or mechanical tuning) wavelength tuning times in the order of 10s of ns are achievable. The different devices do not offer significant differentiation.

### F. device size

The device size of all widely tunable laser concepts is large, in comparison to the source lasers they intend to replace (typically 500 $\mu m$ length or less). For the use in the network, this is not a relevant consideration, since the dimensions of any package is considerably larger than the widely tunable laser chips. It does however increase the cost, through the number of devices per processed wafer.

The typical length of a widely tunable laser is in the range of 1 - 2mm, formed by a gain section, a phase section and tuning sections. The MG-Y design has a conceptual advantage by using parallel tuning sections (total length about 1mm). The CSG design and SG-DBR design are conceptually equal in length (about 1.2mm). The GCSR is a long device, since the vertical coupling filter has a long beat length (about 2mm). The T-MMI length is also longer than the CSG or SG-DBR design, due to the MMI section. It's length could however be reduced by tapering (about 1.6mm).

#### G. technological complexity

Device concepts such as the CSG, the SG-DBR and the GCSR do not pose a restriction on the technology platform for realization. These concepts can be fabricated equally well in a ridge, SIPBH or buried structures. The T-MMI and sampled grating Y-branch laser cannot be realized in a SIPBH structure, since Y-junctions and MMI's are incompatible with the blocking layer regrowth process. In addition, since the current injection in the T-MMI needs to be localized, the T-MMI can also not be made in a buried ridge platform.

The technology used in this thesis for the fabrication of a CSG laser is equal to the established SIPBH technology for DFB lasers. Also, the buttjoint regrowth and the grating definition is a well-established technique used for EML [22] and tunable DBR devices [96]. The most relevant deviation from established processing technology is the growth of a thin spacer-layer, before the gain section layers are grown. Even though planarization of the growth surface can be achieved within 25 nm of growth [31], it has not been proven that this has no impact on the quality of the gain section (and, indeed, it might be the reason for a high internal loss and low tuning efficiency of some of the processed wafers). Alternatively, a grating can be defined on top of the tuning section material.

The technology used for the fabrication of the T-MMI laser is more novel, even though ridge laser processing is a well established process. The ridge and the MMI need to be defined with an RIE etch, since this is not easily achieved with a wet chemical etch. The required different etch depths in the gain section and the two depths in the MMI section make this a complex process that is not readily available. An advantage of the process is that it involves a reduction in the number of steps of epitaxial growth and a significant reduction in the complexity of the regrowth processes involved, compared to the SIPBH platform.

In summary, the T-MMI and sampled grating Y-branch laser concepts constrain the freedom to choose any processing platform. In addition the T-MMI laser requires a non-standard etching process. In contrast, the other concepts are closer to standard manufacturing technology and can be realized in most technology platforms.

### 6.1.1 Overall judgment

The CSG and T-MMI are very similar in performance on the three main requirements (output power, tuning range and SMSR) to the other integrated semi-conductor based concepts and only the SG-DBR is not suitable to generate 30 mW output power. The T-MMI laser needs a higher gain section current to achieve this output power, but this

performance disadvantage comes with an inherent stability of the concept and regularity of the tuning performance.

Comparison of the experimental devices from CSG and T-MMI lasers to the available data on other concepts, shows that the current realization of the two new concepts does not yet meet the performance of the competitive concepts. Implementation of the design optimization presented in this thesis is expected to improve the performance of both concepts. Given that the other concepts have been developed over a long time and that these new concepts are in their infancy, it is believed that with realistic improvements, both CSG and T-MMI are capable on delivering state-of-the-art devices with similar or better performance as other semiconductor integrated concepts. The T-MMI provides a significant simplification in the area of device control, characterization and manufacturability, which makes it preferred over the other concepts.

| Type | Output power | Single-mode operation | Low variation over tuning-range | Low complexity/High stability | Fast tuning speed | Small device size | Simplicity of technology |
|---|---|---|---|---|---|---|---|
| SG-DBR | - | 0 | 0 | - | 0 | 0 | + |
| GCSR | + | 0 | 0 | + | 0 | - | - |
| Syntune | + | 0 | 0 | - | 0 | + | - |
| CSG | + | 0 | 0 | - | 0 | 0 | + |
| T-MMI | + | 0 | 0 | + | 0 | - | - |
| Source laser | + | + | X | + | X | + | + |

*Table 6.2: Rating of different concepts; + designates an excellent performance of the device, compared to the other concepts and - denotes a disadvantage compared to the other concepts. The 0 denotes that the concept provides neither and advantage nor disadvantage for that item. The X designates the unavailability of tuning performance in a regular source laser.*

## 6.2 Improvements to be realized

The evaluation of the CSG and T-MMI concept and the comparison to other devices has demonstrated that these concepts can provide an as good if not better integrated semiconductor tunable laser than presently available. To demonstrate this, the performance of the CSG and MMI laser has to be improved, over the presented experimental data.

Several aspects of the experimental wafers were not as designed. This is one of the reasons for the lower than expected performance of the widely tunable lasers. Based on the experiment evaluation and the simulation on these devices, recommendations are presented that should further improve the device performance.

### 6.2.1 CSG laser

The CSG laser is inherently limited by the use of an isolation channel between the two sampled gratings. Though this can be remedied by the use of a 5-section design, this is not a realistic solution (due to the anticipated extra effort needed for characterization). By improving the CSG selectivity and reducing the size of the isolation channel a good 4-section CSG can be achieved. The following improvements are proposed:

**Use optimized design** The presented devices were different from the optimum design. Device performance will improve if this design optimization is implemented.

**Increase grating strength** In the presented design the grating layer is located below the tuning layer, limiting the grating strength to approximately 15 $mm^{-1}$ (see section 4.2.4). In a different technology platform a higher value of grating strength can be realized [54]. This allows for the design of shorter, more selective sampled gratings, with more design margin for optimization of the sampled grating selectivity.

**Reduce size of isolation channel** To avoid the impact of the isolation channels on the performance of the CSG section the channels need to be reduced in size. This can be accomplished by proton implantation, instead of an isolation channel. With this technique a reduction of the isolation channel width to 5 $\mu m$ is possible [8].

**Decrease tuning material bandgap wavelength** Experimental data suggest that a reduction in the tuning material bandgap wavelength allows for a lower power-variation over the tuning range and a higher overall power. In addition, the interaction between optical field and carrier-density is reduced, giving a more regular tuning performance. Also, simulations, on the dependence of the CSG reflection spectrum on incident optical power, suggest that 30 mW operation is not possible due to saturation, at too high a material bandgap wavelength. The analysis in section 4.3.4 suggest a choice for tuning layer PL wavelength down to 1350 nm.

**Improve material quality** Improvement of material quality and laser properties provides more margin for the optical output power. This allows to make changes to the design that improve selectivity and/or reduce tuning irregularities. This is particularly achievable, since the wafer-material grown for the experimental devices showed an internal loss that was relatively high.

### 6.2.2 T-MMI laser

For the MMI laser the following improvements are proposed:

**Tuning material bandgap wavelength** The presented devices had MMI's with a large material absorption. To reduce this the tuning material bandgap wavelength needs to be reduced to 1400 nm or lower. Results on the CSG laser suggest that a further reduction allows for a higher reflectivity of the sampled grating over the tuning range. One probably wants to keep the bandgap wavelength larger than about 1350 nm, since lower values reduce the achievable tuning range and provide no advantage in reduced absorption.

**MMI-tapering** The measured threshold current for devices with different taper ratio demonstrate that in the range of up to 60% tapering, no difference in threshold current is observed (see section 5.3.4). Consequently a high taper-ratio of 60% can be used to increase the MMI width and selectivity.

**MMI etch depth** In order to improve the MMI selectivity, the different modes that propagate in the T-MMI coupler needs to experience a $2\pi$ phase-difference between one-another at the same location. This can be achieved by etching into the tuning layer around the T-MMI. An etch depth of 200 nm, around the T-MMI and the in- and output waveguides, is sufficient.

**Cladding layer thickness** An increase in cladding layer thickness to 600 nm will further improve the bandwidth of the device. Current spreading simulations and measurements have shown that this does not pose a problem for device operation.

## 6.3 Recent developments

The experimental work presented in this thesis dates from the years 2002 and 2003. Since then the field of widely tunable lasers has seen continued development with improved performance for the existing concepts, introduction of new concepts and a gradual change in performance requirements.

Several manufacturers of widely tunable lasers have ceased to exist in the economical down-turn. Only a couple of companies remain operational: Agility (SG-DBR, acquired by JDSU), Bookham (Digital Supermode DBR), Iolon (ECL based on a Littman-Metcalf cavity), Intel (ECL based on thermal tunable etalons), Santur (actively coupled DFB array) and Beam-express (electrically pumped tunable VCSEL). These companies have made improvements to the performance of their respective concepts.

In addition, a small number of companies has entered the widely tunable laser market. Syntune, as already described in this thesis, manufactures a Modulated Grating Y-Branch Laser [115]. Two-chip Photonics makes an electrically pumped VCSEL by hybrid integration of a silicon MEMS chip and a chip with bottom DBR mirror and gain-generating layers [89]. The reduction of the number of players in the field is partly a sign of consolidation and maturity, but it also reflects the difficulty to meet evolving performance requirements.

Initially, tunable lasers were designed to replace fixed-wavelength CW lasers in the long-haul network. Early on it became clear that only an offering with a full band tuning range (C or L band) provides a significant cost-advantage for network operators. In addition, these lasers need to provide comparable power as the single-wavelength devices

they are replacing. As argued in this thesis, this is a hard target to achieve with any integrated tunable laser concept. Therefore tunable lasers were monolithically integrated with a Semiconductor Optical Amplifier (SOA) [113]. This has the two benefits that the output power of the device becomes independent of the actual power from the tunable laser and that the output power can be blocked (for example during switching).

Due to the economical downturn and the ensuing focus on lower-cost network operation (as opposed to higher functionality) 2.5Gbps Direct Modulated Lasers (DMLs) emerged as the main telecommunications market. To be compatible with this changed market-demand tunable lasers are required to also provide the modulation functionality. Since direct modulation is most often not possible for these tunable laser concepts (due to the potential for modehopping [28]), it is required to integrate a modulator behind the SOA. First demonstrations have been achieved with an Electro-absorption Modulator [108] [9]. An alternative is a Mach-Zehner modulator, allowing a higher frequency operation and less dependence on lasing wavelength [16]. In addition, fast switching between wavelengths is becoming more important [58][94].

The latest development in telecommunications is the transition to small form factor hot-pluggable packages with low power dissipation [23]. The large foot-print and high power consumption of widely tunable lasers makes the transition into this direction challenging.

Not only the requirements for widely tunable lasers are evolving. Also the required integration level has changed. Whereas with tunable DBR lasers the device control was relatively straightforward, more complex concepts require a look-up table to find the correct wavelength and to control that set-point over the lifetime of the device. In addition, these set-points are dependent on the calibration of the used current sources. Therefore, a tunable laser needs to be recalibrated in the customer's application. Since system integrators typically do not want to deal with this complication the tunable laser manufacturer has to deliver his product at a higher level of integration (including all electronics and software). For the customer the exact operation of the device becomes invisible and irrelevant. The establishment of an MSA for such a module was critical [51].

In addition to the described efforts to deliver a tunable laser that can address customer needs, also more fundamental work has been going on to, similar to the work in this thesis, demonstrate alternative concepts for tunable lasers. Several new extended cavity laser concepts have been introduced, such as a laser cavity with a liquid crystal based tunable mirror [89] and an extended cavity laser with an electronic tuning element integrated in the gain chip [66]. Another concept uses an AWG, of which the optical length of the arms can be separately controlled. A tunable laser is formed by placing this element in a cavity with an optical amplifier [42]. For monolithic integration, ring resonators have been demonstrated to provide sufficient selectivity for a tunable laser [102][32].

The increase of the change in index that can be achieved in the tuning layer has been pursued by the use of type-II bandgap material. Such a configuration separates electrons and holes and reduce the recombination rate in the tuning material [90]. Photonic crystals have been demonstrated to reduce the size of tunable lasers and improve selectivity [75]. Finally, an interesting application of tunable lasers is as component in a wavelength converter [77][101].

# APPENDIX A: Operating wavelength sensitivity to tuning sections

When the laser-mode is aligned with a resonance in the reflection spectrum, a shift in Bragg wavelength results in a misalignment of the cavity mode. Neglecting the modes in other resonances, the mode-competition with the neighboring cavity modes becomes more competitive. With an increasing offset in Bragg wavelength, this neighboring mode takes over lasing-operation. This is a mode-hop. Ideally, mode-hops are regularly spaced (in tuning current) and there is a large stability region between mode-hops where the requirements on output power, SMSR and other specifications are met.

The effective length ($L_{eff}$) of a sampled grating is given by [54],

$$L_{eff} = \frac{\phi_{SG} \cdot \lambda}{4\pi \cdot \mu_{SG}} = \frac{1}{2|\kappa_k|} \cdot tanh(|\kappa_k| \cdot L_{SG}) \tag{6.2}$$

In the CSG section, the two sampled gratings only differentiate in the periodicity (grating strength and reflection phase are similar). Furthermore, we only consider alignment of same-order reflection resonances. Therefore, the effective length of the CSG is the same as for a sampled grating (formula 6.2).

With a change in Bragg wavelength of the sampled grating ($\Delta\lambda_B$), the phase at the original resonance-wavelength shifts by $\Delta\phi_{SG} = -\Delta\lambda_B \cdot 4\pi \cdot L_{eff} \cdot \mu_{SG}/\lambda^2$. To compensate for this phase-change the mode within the laser cavity (of length $L_{cav}$ and effective index $\mu_{cav}$ ) needs to re-align by $\Delta\lambda = \Delta\lambda_B \cdot (L_{eff} \cdot \mu_{SG})/(L_{cav} \cdot \mu_{cav})$.

For the CSG section the change in phase with current is more complicated and expressed through the vector addition in figure 6.2. The reflection terms of the first and second sampled grating, $r_{SG1}$ and $r_{SG2}$, add coherently. Since resonances of the same order are aligned, the phase of these two terms is equal. With a change in phase of the second sampled grating, expressed through the effective length of the individual sampled grating, the total phase changes, as expressed in the figure. The sensitivity of the CSG phase is given by: $\Delta\phi_{CSG} = atan((r_{SG2}/(r_{SG1} + r_{SG2})) \cdot tan(\Delta\phi_{SG2})) \approx (r_{SG2}/(r_{SG1} + r_{SG2}))\Delta\phi_{SG2}$. For a change in the first sampled grating, the expression is similar (with $r_{SG1}$ and $r_{SG2}$ interchanged). This shows that the phase-shift for a CSG is always smaller than the phase-shift of the constituting sampled gratings. Translating this to an expression for the cavity mode shift, we obtain: $\Delta\lambda = -\Delta\phi_{CSG} \cdot \lambda^2/(2\pi \cdot L_{cav}\mu_{cav}) \approx -(r_2/(r_1 + r_2)) \cdot \Delta\lambda_B \cdot (L_{eff} \cdot \mu_{SG})/(L_{cav} \cdot \mu_{cav})$.

This derivation is completely similar for the modulated grating Y-branch laser.

For the CSG a secondary effect is that the reflection phase of the second sampled grating changes with a change in Bragg wavelength of the first sampled grating. In the above derivation the reflection phase of the other sampled grating was assumed constant. However, changes in the first sampled grating affect the transmission phase of this section and hence the combined reflection phase. A lower Bragg wavelength reduces the reflection phase of the second sampled grating and this reduces the change in cavity mode with Bragg wavelength. This further makes the CSG less sensitive to changes in tuning current.

For a T-MMI the change in MMI wavelength is given by: $\Delta\lambda_{MMI} = (\Gamma_0 - \Gamma_2) \cdot \Delta\mu_{contact} \cdot L_{MMI}$, where $\Delta\mu_{contact}$ is the change in material index below the contact in

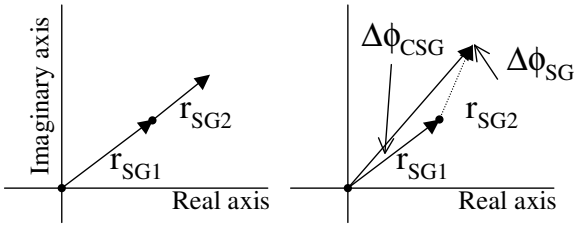


*Figure 6.2: The reflection terms of both sampled gratings add in phase to give the combined reflectivity of a resonance in the CSG reflection spectrum. For small changes in the reflection phase of one of the sampled gratings, the simplified drawing is used to calculate the resultant change in CSG reflection phase.*

| Design | Section | Wavelength sensitivity |
|---|---|---|
| All concepts | Phase section | $\frac{\delta\lambda}{\delta\mu} = \Delta\lambda_{cav} \cdot \frac{L_{phase}}{\mu \cdot L_{cav}}$ |
| CSG | 1st Sampled grating section | $\frac{\delta\lambda}{\delta\lambda_B} = -\frac{r_{SG1}}{r_{SG1}+r_{SG2}} \cdot \frac{L_{eff} \cdot \Delta\lambda_{cav}}{L_{cav}}$ |
| | 2nd Sampled grating section | $\frac{\delta\lambda}{\delta\lambda_B} = -\frac{r_{SG2}}{r_{SG1}+r_{SG2}} \cdot \frac{L_{eff} \cdot \Delta\lambda_{cav}}{L_{cav}}$ |
| T-MMI | Sampled grating section | $\frac{\delta\lambda}{\delta\lambda_B} = \frac{L_{eff} \cdot \Delta\lambda_{cav}}{L_{cav}}$ |
| | T-MMI section | $\frac{\delta\lambda}{\delta\lambda_{MMI}} = \frac{\Gamma_0}{\Gamma_0 - \Gamma_2} \cdot \frac{\lambda}{\mu \cdot L_{cav}}$ |
| SG-DBR | Sampled grating sections | $\frac{\delta\lambda}{\delta\lambda_B} = \frac{L_{eff} \cdot \Delta\lambda_{cav}}{L_{cav}}$ |
| GCSR | Sampled grating section | $\frac{\delta\lambda}{\delta\lambda_B} = \frac{L_{eff} \cdot \Delta\lambda_{cav}}{L_{cav}}$ |
| MG-Y | 1st Sampled grating section | $\frac{\delta\lambda}{\delta\lambda_B} = -\frac{r_{SG1}}{r_{SG1}+r_{SG2}} \cdot \frac{L_{eff} \cdot \Delta\lambda_{cav}}{L_{cav}}$ |
| | 2nd Sampled grating section | $\frac{\delta\lambda}{\delta\lambda_B} = -\frac{r_{SG2}}{r_{SG1}+r_{SG2}} \cdot \frac{L_{eff} \cdot \Delta\lambda_{cav}}{L_{cav}}$ |

*Table 6.3: Sensitivity of operating wavelength to tuning section properties.*

the MMI and $\Gamma_0$ and $\Gamma_2$ are the overlap factors, of the fundamental and second order mode, with the area below the contact. The change in transmission phase of the MMI is given by $(2\pi \cdot L_{MMI} \cdot \Gamma_0 \cdot \Delta\mu_{contact})/\lambda$, since it is determined by the optical length for the fundamental mode. Combining these two expressions to express the change in cavity modespacing as a function of change in MMI wavelength gives: $\Delta\lambda_{cav} = \Delta\lambda_{MMI} \cdot (\Gamma_0 \cdot \lambda)/((\Gamma_0 - \Gamma_2) \cdot \mu_{cav} \cdot L_{cav})$. A factor 2 is added to the analysis to reflect the double-pass through the T-MMI in a round-trip. Given the magnitude of the different parameters, the shift of cavity modes with MMI wavelength is negligible.

For the GCSR the analysis is similar as for the T-MMI, where the shift in cavity modes by the coarse filter is only dependent on the change in optical length of the coarse tuning element.

Table 6.3 summarizes the dependence for several device concepts.

# Summary

Widely tunable lasers can significantly reduce the costs and increase the functionality of optical networks. So far, the performance of integrated semiconductor based tunable lasers lagged behind the performance of the fixed wavelength sources they need to replace. The objective of this thesis is to investigate new widely tunable laser concepts and compare their performance with the alternatives. In this work two new concepts for widely tunable lasers are introduced: the Cascaded Sampled Grating (CSG) laser and the T-MMI (Tunable Multi-Mode Interference section) laser.

The tuning element in the Cascaded Sampled Grating (CSG) consists of two sampled grating sections. The reflection spectra of these elements add to give a CSG-reflection spectrum with one dominant reflection resonance. The design of this element is detailed and simulations are presented.

Experimental devices were processed and characterized. In these devices an output power of up to 10 mW was achieved with an SMSR of at least 30 dB over a tuning range of 57 nm. Simulations, based on the experimental results, predict a capability to generate $>$ 30 mW output power and an SMSR $>$ 37 dB over a 40 nm tuning range.

The tuning element in the T-MMI consists of a sampled grating and a novel tuning element, the T-MMI section. The transmission curve of this element can be shifted over a wide wavelength range by current injection in the center of the MMI section. By shifting the transmission curve of the T-MMI section, subsequent sampled grating resonances are selected. The design of this laser is detailed and simulations on the final design are presented.

Experimental devices were demonstrated with up to 7 mW output power. The SMSR was more than 25 dB over a tuning range of 38 nm. Over this tuning range a 10 dB variation in output power was observed. Simulations based on these experimental results predict a capability to generate 30 mW output power and an SMSR of 40 dB over a tuning range of 40 nm (for a maximum gain section current of 220 mA) for an optimized design.

An aspect of tunable lasers that has not been given sufficient attention in the past is the role of absorption of optical power in the tuning sections. In this thesis it was demonstrated that for 30 mW operation the composition of the material in the tuning layer is critical. For a tuning layer with bandgap wavelength close to the laser wavelength, the reflection spectrum of the tuning elements saturates before 30 mW output power is achieved.

In the comparison between the CSG and T-MMI with other concepts for widely tunable lasers, it follows that both CSG and T-MMI are similar or better than other concepts in the area of output power and SMSR. An important differentiation for the T-MMI is achieved in its simplicity of operation.

# Samenvatting

'Widely tunable lasers' hebben de potentie om de kosten van optische netwerken te verlagen en de functionaliteit te verbeteren. Tot nu toe zijn de prestaties van geïntegreerde verstembare lasers, gebaseerd op halfgeleider materiaal, achtergebleven bij die van de conventionele lasers, die ze moeten vervangen. Het doel van dit proefschrift is om nieuwe concepten voor 'widely tunable lasers' te onderzoeken en de prestaties hiervan te vergelijken met alternatieven. In dit werk worden twee nieuwe concepten geïntroduceerd: de 'Cascaded Sampled Grating' (CSG) laser en de 'Tunable Multi-Mode Interference' (T-MMI) laser.

Het verstemmings-element in de CSG bestaat uit twee 'sampled grating' secties. De reflecties van deze twee secties worden bij elkaar opgeteld om een CSG reflectie spectrum te produceren met één dominante reflectie-piek. Het ontwerp van dit element en de resultaten van simulaties worden in detail gepresenteerd.

In het kader van dit onderzoek is een serie experimentele CSG lasers gerealiseerd en gekarakteriseerd. Met deze lasers is een optisch vermogen tot 10 mW en een SMSR van tenminste 30 dB gedemonstreerd over een verstemmings-bereik van 57 nm. Simulaties, gebaseerd op de experimentele resultaten, voorspellen meer dan 30 mW vermogen met een SMSR beter dan 37 dB over een verstemmings-bereik van 40 nm.

Het verstemmings-element in de T-MMI bestaat uit een 'sampled grating' in combinatie met een nieuw element, de T-MMI sectie. De transmissie karakteristiek van dit element kan worden verschoven over een groot golflengtebereik door stroom-injectie in het centrum van de MMI sectie. Met het verschuiven van het maximum in de transmissie van het T-MMI element kunnen de verschillende 'sampled grating' resonanties worden geselecteerd. Het ontwerp van deze laser en een aantal simulatie-resultaten zijn in detail beschreven.

Experimentele T-MMI lasers tonen een optisch vermogen van 7 mW. De SMSR was tenminste 25 dB over een bereik van 38 nm. Over dit bereik is een vermogensvariatie van 10 dB gemeten. Simulaties gebaseerd op de experimentele resultaten voorspellen 30 mW optisch vermogen en 40 dB SMSR over een afstemmingsbereik van 40 nm (voor een stroom injectie van maximaal 220 mA) voor een geoptimaliseerd ontwerp.

Een onderbelicht aspect van verstembare lasers is de absorptie van optisch vermogen in de verstemmingselementen. In dit proefschrift wordt gedemonstreerd dat voor het bereiken van 30 mW uitgangsvermogen de materiaal compositie van de laser cruciaal is. Voor een halfgeleider met een bandgap golflengte dicht bij de laser golflengte degradeert het reflectie-spectrum voordat de 30 mW vermogen bereikt is.

Bij het vergelijken van CSG en T-MMI lasers met reeds gerealiseerde 'widely tunable lasers' blijken beiden gelijkwaardig of beter te zijn op het gebied van vermogen en SMSR. De T-MMI laser onderscheidt zich voorts door de eenvoud van de verstemmingsprocedure.

# Dankwoord

Nu het laatste woord geschreven is en dit proefschrift naar de printer kan is er wat tijd om terug te kijken. En dan blijkt dat het werk dat in dit proefschrift gepresenteerd is enkel en alleen mogelijk was dankzij de hulp en steun van een groot aantal mensen. Het afronden van dit proefschrift is meer dankzij de inspanningen van hen dan die van mij.

Laat me beginnen met de sponsor van dit onderzoek, JDS Uniphase Eindhoven (ofwel UNL), die dit werk heeft ondersteund en toestemming heeft verleend voor dit proefschrift. Binnen de organisatie wil ik het management en met name Bart Verbeek en Frank Wijnands bedanken voor hun steun voor dit project.

Binnen UNL heeft bijna iedereen wel zijn steentje bijgedragen aan dit werk. Een volgorde aanbrengen is dus altijd arbitrair en geen reflectie van de geleverde bijdrage.

Ik wil graag beginnen met de naaste medewerkers binnen de R&D groep. Hans de Vrieze en Remco Strijbos hebben een grote bijdrage geleverd aan dit project door respectievelijk hun uitstekende practische en theoretische inzicht. Hans Binsma heeft de technologische uitdaging van dit project op zich genomen en samen met Kitty Sander-Jochem, Ad Valster, Mark van Geemert en Toine Husken zorg gedragen voor de processing. En dankzij Henri Fledderus konden de devices probleemloos gemeten worden. Discussies met Piet Kuindersma zijn met name erg nuttig geweest voor het begrip van de devices. Verder wil ik binnen de R&D groep Hans Naus, Peter Maat, Peter Mols, Erik Hummel, Bruno van Dooren en Sandor van Kollenburg bedanken voor een prettige samenwerking.

De lasers in dit proefschrift werden niet met een volledig standaard proces gemaakt. Daarom heb ik uitgebreid kunnen samenwerken met de proces engineers binnen UNL. Dankzij hun ontwikkelwerk hebben we de gepresenteerde experimentele resultaten kunnen boeken. Ik wil daarvoor de volgende personen bedanken: Henry van Bakel, Ger Dinghs, Geert van der Hofstad, Hans Maes, Jos Rutten, Teus van Dongen, Thierry de Smet, Frank Otten, Wim van den Einden, Huub Ambrosius, Kees-Jan Niemantsverdriet, Peter Knapen, Arie Corbijn, Bianca van der Veer, Esther Steding, Peter Thijs, Ron Vriezema, Alex Jonkers en Jan de Poorter.

Ik realizeer me dat de afsluiting van het hoofdstuk UNL geen goede herineringen achterlaat bij sommigen. Toch kijk ik terug op een plezierige 2 en een half jaar bij UNL en ik wil daarvoor alle ex-medewerkers bedanken.

In het voorjaar van 2002, toen ik voor het eerst contact met Meint opnam om dit werk aan widely tunable laser om te zetten in een proefschrift, verwachte ik na één of twee jaar een afgerond proefschrift te kunnen verdedigen. Echter, reorganisaties bij UNL, mijn verhuizing naar de VS en het uitwerken van de resultaten heeft er aan bijgedragen dat het meer dan 3 jaar geduurd heeft. De reden dat ik dit uiteindelijk heb kunnen afronden is dankzij de aanmoedigingen en steun van mijn promotor Meint Smit, co-promotor Erwin Bente, mijn managers Pierre en Bruno en de steun van mijn vriendin Yanyan.

De eerste ervaring met wetenschappelijk werk heb ik opgedaan binnen de vakgroep Opto-Electronic Devices in Delft. Ik wil daarom de oud-collega's daar bedanken hiervoor, evenals voor de prettige herinneringen aan die tijd.

Verder zijn mijn vrienden en familie uiteraard een continue en onvoorwaardelijke bron van steun gebleken over de afgelopen jaren.

Iedereen bedankt: zonder jullie was dit werk niet mogelijk geweest !

# Bibliography


[1] Based on internal work on DBR lasers.

[2] (2003, March) L192-type OC-192/STM-64 1310 nm uncooled DFB laser with integrated driver. [Online]. Available: http://www.triquint.com/company/divisions/telecom_datacom/docs/L192/L192.pdf

[3] Abelès, *Optical properties of solids*, 1972.

[4] Ackerman, *et al.*, "A practical approach to wavelength selectable DWDM sources," in *Conference on Lasers and Electro-Optics*, vol. 1, November 2001, pp. 171–172.

[5] Adachi, "Material parameters of $In_{1-x}Ga_xAs_yP_{1-y}$ and related binaries," *J. Appl. Phys.*, vol. 53, no. 12, pp. 8775–8792, December 1982.

[6] *PDL measurements using the 8169A polarization controller product note*, Agilent, 2002.

[7] Agrawal and Dutta, *Long-wavelength semiconductor lasers*. CRC Press, 2001.

[8] Ahmed, Too, Sealy, and Gwilliam, "Proton implantation for effective electrical isolation of InP, InGaAs and GaAs: role of variable doses and implant temperature," in *Conference on Indium-Phosphide and Related Materials*, vol. 14th, May 2002, pp. 225–228.

[9] Akulova, *et al.* (2005, April) Monolithic integrated tunable transmitters. [Online]. Available: http://www.agility.com/intervals/files/69.pdf

[10] Amann, *DFB lasers*, 1998.

[11] Amann and Buus, *Tunable Laser Diodes*, 1998.

[12] Amann, Illek, Schanen, and Thulke, "Tunable twin-guide laser: a novel laser diode with improved tuning performance," *Appl. Phys. Lett.*, vol. 54, pp. 2532–2533, 1989.

[13] Amann, Illek, Schanen, and Thulke, "Tuning range and threshold current of the tunable twin-guide (TTG) laser," *IEEE Photon. Technol. Lett.*, vol. 1, no. 9, pp. 253–255, September 1989.

[14] Amann and Schimpe, "Excess linewidth broadening in wavelength-tunable laser diodes," *Electron. Lett.*, vol. 26, no. 5, pp. 279–280, March 1990.

[15] Anthon, *et al.*, "External cavity diode lasers tuned with silicon MEMS," in *Conference on Optical Fiber Communications*, 2002, pp. 97–98.

[16] Barton, Skogen, Mašanović, Denbaars, and Coldren, "A widely tunable high-speed transmitter using an integrated SG-DBR laser-semiconductor optical amplifier and MachZehnder modulator," *IEEE J. Select. Topics Quantum Electron.*, vol. 9, no. 5, pp. 1113–1117, October/November 2003.

[17] Barut, *The theory of the scattering matrix for the interactions of fundamental particles*. Maxmillan, 1967.

[18] Beaudoin, DeVries, Johnson, Laman, and Tiedje, "Optical absorption edge of semi-insulating GaAs and InP at high temperatures," *Appl. Phys. Lett.*, vol. 70, no. 26, pp. 3540–3542, June 1997.

[19] Belenky, Reynolds, Shterengas, Hybertsen, Donetsky, Shtengel, and Luryi, "Effect of p-doping on the temperature dependence of differential gain in FP and DFB 1.3-$\mu m$ InGaAsPInP multiple-quantum-well lasers," *IEEE Photon. Technol. Lett.*, vol. 12, no. 8, pp. 969–971, August 2000.

[20] Bennett, Soref, and Amano, "Carrier-induced change in refractive index of InP, GaAs, and InGaAsP," *IEEE J. Quantum Electron.*, vol. 26, no. 1, pp. 113–122, January 1990.

[21] Besse, Bachmann, Melchior, Soldano, and Smit, "Optical bandwidth and fabrication tolerances of multimode interference couplers," *J. Lightwave. Technol.*, vol. 12, no. 6, pp. 1004–1009, June 1994.

[22] Binsma, Kuindersma, Gestel, Cuypers, Peeters, Dongen, and Thijs, "DFB lasers with integrated electroabsorption modulator," in *Conference on Indium-Phosphide and Related Materials*, 1995, pp. 709–712.

[23] Bond, Wolf, Stackhouse, Sipics, Jiaming, and Jambunathan, "Challenges in opto-electronic component packaging for next generation pluggable modules," in *Conference on Lasers and Electro-Optics*, October 2005, pp. 706–707.

[24] Borchert, Illek, Wolf, Rieger, and Amann, "Vertically integrated Mach-Zehnder interferometer (VMZ) widely tunable laser diode with improved wavelength access," *Electron. Lett.*, vol. 30, no. 24, pp. 2047–2049, November 1994.

[25] Bukkems, "Widely tunable laser," Patent 6 687 267, February 3, 2004.

[26] Burkhard, Dinges, and Kuphal, "Optical properties of $In_{1-x}Ga_xAs_yP_{1-y}$, InP, GaAs and GaP determined by ellipsometry," *J. Appl. Phys.*, vol. 53, no. 1, pp. 655–662, January 1982.

[27] Casey, Sell, and Wecht, "Concentration dependence of the absorption coefficient for n- and p-type GaAs between 1.3 and 1.6 eV," *J. Appl. Phys.*, vol. 46, pp. 250–257, 1975.

[28] Chacinski, Isaksson, and Schatz, "High-speed direct modulation of widely tunable MG-Y laser," *IEEE Photon. Technol. Lett.*, vol. 17, no. 6, pp. 1157–1159, June 2005.

[29] Chandra, Coldren, and Strege, "Refractive index from $In_{1-x}Ga_xAs_yP_{1-y}$ films," *Electron. Lett.*, vol. 17, pp. 6–7, 1981.

[30] Chang-Hasnain, "Tunable VCSEL," *IEEE J. Select. Topics Quantum Electron.*, vol. 6, no. 6, pp. 978–987, November/December 2000.

[31] Chu, Tanbun-Ek, Logan, Vandenbarg, Sciortino, Wisk, and Pernell, "Grating overgrowth and defect structures in Distributed-Feedback-Buried Heterostructure laser diodes," *IEEE J. Select. Topics Quantum Electron.*, vol. 3, no. 3, pp. 862–873, June 1997.

[32] Chung, Kim, and Dagli, "Widely tunable coupled-ring reflector laser diode," *IEEE Photon. Technol. Lett.*, vol. 17, no. 9, pp. 1773–1775, September 2005.

[33] Cohen, Skogen, Nolde, and Coldren, "A monolithic chemical sensor using tandem heterodyned sampled grating DBR lasers," in *Conference on Lasers and Electro-Optics*, vol. 1, November 2001, pp. 238–239.

[34] *PIC3D User's manual*, CrossLight Software Inc., 2002.2.

[35] Day, "External-cavity tunable diode lasers for network deployment," in *Conference on Optical Fiber Communications*, vol. TuJ4, 2001, pp. 1–2.

[36] Merlier, Morthier, and Baets, "The influence of lateral carrier diffusion and surface recombination on the behavior of semiconductor optical amplifier (SOA)-based MMIs," *IEEE J. Quantum Electron.*, vol. 39, no. 7, pp. 880–885, July 2003.

[37] Debrégeas-Sillard, *et al.*, "DBR module with 20-mW constant coupled output power, over 16 nm (40x 50-GHz spaced channels)," *IEEE Photon. Technol. Lett.*, vol. 13, no. 1, pp. 4–6, January 2001.

[38] Delorme, Alibert, Ougier, Slempkes, and Nakajima, "Sampled-grating DBR lasers with 101 wavelengths over 44 nm and optimised power variation for WDM applications," *Electron. Lett.*, vol. 34, no. 3, pp. 279–281, February 1998.

[39] Delorme, Grosmaire, Alibert, Rose, and Ougazzaden, "4-wavelength DBR laser array fabricated with a single holographic exposure technique," in *Conference on Optical Fiber Communications*, 1996, pp. 300–301.

[40] Besten, "Integration of multi-wavelength lasers with fast electro-optical modulators," Ph.D. dissertation, Technical University Eindhoven, Eindhoven.

[41] Doerr, Joyner, and Stulz, "40-wavelength rapidly digitally tunable laser," *IEEE Photon. Technol. Lett.*, vol. 11, no. 11, pp. 1348–1350, November 1999.

[42] Doerr, Stulz, Pafchek, Dreyer, and Zhang, "Potentially low-cost widely tunable laser consisting of a semiconductor optical amplifier connected directly to a silica waveguide grating router," *IEEE Photon. Technol. Lett.*, vol. 15, no. 10, pp. 1446–1448, October 2003.

[43] Fujiwara, Kakitsuka, Ishikawa, Kano, Okamoto, Kawaguchi, Kondo, Yoshikuni, and Tohmori, "Inherently mode-hop-free Distributed Bragg Reflector (DBR) laser array," *IEEE J. Select. Topics Quantum Electron.*, vol. 9, no. 5, pp. 1132–1137, september/october 2003.

[44] Gustafsson, *et al.*, "Record output power (25mW) across C-band from widely tunable GCSR lasers without additional SOA," *Electron. Lett.*, vol. 39, no. 3, pp. 292–293, February 2003.

[45] Hadley, "Multistep method for wide-angle beam propagation," *Opt. Lett.*, vol. 17, no. 24, pp. 1743–1745, December 1992.

[46] Hadley, "Transparent boundary condition for the beam propagation method," *IEEE J. Quantum Electron.*, vol. 28, no. 1, pp. 363–370, January 1992.

[47] Hatakeyama, Kudo, Yokoyama, and Sasaki, "Wavelength-selectable microarray light source for wide-band DWDM applications," *IEEE J. Select. Topics Quantum Electron.*, vol. 8, no. 6, pp. 1341–1348, November/December 2002.

[48] Heffner, "Deterministic, analytically complete measurement of polarization-dependent transmission through optical devices," *IEEE Photon. Technol. Lett.*, vol. 4, pp. 451–454, 1992.

[49] Henry, "Theory of the phase noise and power spectrum of a single mode injection laser," *IEEE J. Quantum Electron.*, vol. 19, no. 9, pp. 1391–1397, September 1983.

[50] Henry, "Theory of the linewidth of semiconductor lasers," *IEEE J. Quantum Electron.*, vol. QE-18, no. 2, pp. 259–264, February 1982.

[51] Hutchins, Kubicky, Batra, Simmons, Hayes, and Affolter. (2003, July) The OIF compliant tunable laser MSA. [Online]. Available: http://www.tunablelasermsa.com/msa.php

[52] Ishii, Tohmori, Yoshikuni, Tamamura, and Kondo, "Multiple-phase-shift super structure grating DBR laser for broad wavelength tuning," *IEEE Photon. Technol. Lett.*, vol. 5, no. 6, pp. 613–615, June 1993.

[53] Jackson, *Classical Electrodynamics*. Wiley, 1998.

[54] Jayaraman, Chuang, and Coldren, "Theory, design and performance of extended tuning range semiconductor lasers with sampled gratings," *IEEE J. Quantum Electron.*, vol. 29, no. 6, pp. 1824–1834, June 1993.

[55] Jowett, Moule, Wright, and Briggs, "The growth of MQW planar buried heterostructure lasers with semi-insulating blocking layers by OMVPE," in *Conference on Indium-Phosphide and Related Materials*, vol. 3th, April 1991, pp. 208–211.

[56] Jänich, *Analysis für Physiker und Ingenieure*. Springer-Verlag, 1990.

[57] Katz, *Indium Phosphide and Related Materals: Processing, Technology and Devices*, 1992.

[58] Kauer, Girault, Leutholt, Honthaas, Pellegri, Goullancourt, and Zirngibl, "16-channel digitally tunable external-cavity laser with nanosecond switching time," *IEEE Photon. Technol. Lett.*, vol. 15, no. 3, pp. 371–373, March 2003.

[59] Kingston, "Electroabsorption in InGaAsP," *Appl. Phys. Lett.*, vol. 34, no. 11, pp. 744–746, June 1979.

[60] Kner, Sun, Boucart, Floyd, Nabiev, Davis, Yuen, Jansen, and Chang-Hasnain, "VCSELS...go the distance," *Optics and Photonics News*, pp. 44–47, March 2002.

[61] Knopp, *et al.*, "High power MEMS-tunable vertical-cavity surface-emitting lasers," *Summer LEOS topical meeting 2001.*

[62] Knopp, *et al.*, "High power MEMS-tunable vertical-cavity surface-emitting lasers," in *LEOS Summer Topical Meetings*, 2001, pp. 31–32.

[63] Kobayashi and Mito, "Single frequency and tunable laser diodes," *J. Lightwave. Technol.*, vol. 6, pp. 1623–1633, 1988.

[64] Koch and Koren, "Semiconductor lasers for coherent optical fiber communications," *J. Lightwave. Technol.*, vol. 8, pp. 274–293, 1990.

[65] Kotaki and Ishikawa, "Wavelength tunable DFB and DBR lasers for coherent optical fibre communications," *IEE Proceedings J*, vol. 138, no. 2, pp. 171–177, April 1991.

[66] Kwon, Kim, Sim, Yun, Kim, Kim, and Oh, "Proposal of electrically tunable external-cavity laser diode," *IEEE Photon. Technol. Lett.*, vol. 16, no. 8, pp. 1804–1806, August 2004.

[67] Larson, *et al.*, "High performance widely-tunable SG-DBR lasers," in *Proc. of SPIE*, vol. 4995, 2003, pp. 13–14.

[68] Larson, Bai, Bingo, Ramdas, Penniman, Fish, and Coldren, "Mode control of widely-tunable SG-DBR lasers," in *European Conference on Optical Communications*, vol. P2, 2002, pp. 4–.

[69] Lee and Shin, "On the validity of the effective-index method for rectangular dielectric waveguides," *J. Lightwave. Technol.*, vol. 11, no. 8, pp. 1320–1324, August 1993.

[70] Levy, Scarmozzino, and Osgood, "Length reduction of tapered NxN MMI devices," *IEEE Photon. Technol. Lett.*, vol. 10, no. 6, pp. 830–832, June 1998.

[71] Li, Nabiev, Yuen, Jansen, Davis, and Chang-Hasnain, "Electrically-pumped directly-modulated tunable VCSEL for metro DWDM applications," in *Conference on Optical Fiber Communications*, 2001, pp. 220–221.

[72] Liu and Littman, "Novel geometry for single-mode scanning of tunable lasers," *Opt. Lett.*, vol. 6, no. 3, pp. 117–118, March 1981.

[73] Lohmeyer, "Wave-matching method for mode analysis of dielectric waveguides," *Optical and Quantum Electronics*, vol. 29, no. 9, pp. 907–922, January 1997.

[74] Love, "Application of low-loss criterion to optical waveguides and devices," *IEE Proceedings J*, vol. 136, no. 4, pp. 225–228, August 1989.

[75] Mahnkopf, Arlt, Kamp, Colson, Duan, and Forchel, "Two-channel tunable laser diode based on photonic crystals," *IEEE Photon. Technol. Lett.*, vol. 16, no. 2, pp. 353–355, February 2004.

[76] Manasreh, *InP and Related Compounds: Materials, Applications and Devices (Optoelectronic Properties of Semiconductors and Superlattices).*

[77] Mašanović, Skogen, Barton, Lal, Blumenthal, and Coldren, "Demonstration of monolithically-integrated InP widely-tunable laser and SOA-MZI wavelength converter," in *Conference on Indium-Phosphide and Related Materials*, vol. WB2.2, May 2003, pp. 289–291.

[78] Morthier, Moeyersoon, and Baets, "A $\lambda/4$-shifted sampled or superstructure grating widely tunable twin-guide laser," *IEEE Photon. Technol. Lett.*, vol. 13, no. 10, pp. 1052–1054, October 2001.

[79] Nilsson, "Empirical approximations for the Fermi energy in a semiconductor with parabolic bands," *Appl. Phys. Lett.*, vol. 33, pp. 653–654, 1978.

[80] Nyman, "Automated system for measuring polarization-dependent loss," in *Conference on Optical Fiber Communications*, vol. ThK-6, 1994, pp. 230–.

[81] Oohashi, Shibata, Ishii, Kawaguchi, Kondo, Yoshikumi, and Tohmori, "46.9-nm wavelength selectable arrayed DFB lasers with integrated MMI coupler and SOA," in *Conference on Indium-Phosphide and Related Materials*, vol. 13th, May 2001, pp. 575–578.

[82] Ortiz, Hains, Lu, Sun, Cheng, and Zolper, "Cryogenic VCSELs with chirped multiple quantum wells for a very wide temperature range of CW operation," *IEEE Photon. Technol. Lett.*, vol. 8, no. 11, pp. 1423–1425, November 1996.

[83] Palmer, "Diffraction grating handbook," 1967. [Online]. Available: http www.optics.arizona.edu\Palmer\OPTI380B\PDFdocs\RGL_Diff_Grat_Hdbk.pdf

[84] Pearsal, *GaInAsP alloy semiconductors.* Wiley,, 1982.

[85] Petermann, *Laser diode modulation and noise*, 1988.

[86] Pezeshki, *et al.*, "20mW widely tunable laser module using DFB array and MEMS selection," in *Conference on Optical Fiber Communications*, 2003, pp. 82–84.

[87] Rahman, Fernandez, and Davies, "Review of finite element methods for microwave and optical waveguides," *Proceedings of the IEEE*, vol. 79, pp. 1442–1448, October 1991.

[88] Reid, *et al.*, "A novel broadband DBR laser for DWDM networks with simplified quasi-digital wavelength selection," in *Conference on Optical Fiber Communications*, 2002, pp. 541–543.

[89] Riemenschneider, Maute, Halbritter, Ortsiefer, Shau, Amann, and Meissner, "A new concept for micro-mechanically tunable long wavelength VCSELs," in *Conference on Lasers and Electro-Optics*, vol. 2, May 2004, pp. 1–2.

[90] Rősel, Jacke, Grau, Meyer, and Amann, "Enhanced tuning efficiency in tunable laser diodes using type-II superlattices," *IEEE Photon. Technol. Lett.*, vol. 16, no. 3, pp. 738–740, March 2004.

[91] Scarmozzina and Jr., "Comparison of finite-difference and Fourier-transform solutions of the parabolic wave equation with emphasis on integrated-optics applications," *J. Opt. Soc. Am. A*, vol. 8, no. 5, pp. 724–731, May 1991.

[92] Schmidt, Illek, Gessner, and Amann, "Design and realization of a buried-heterostructure tunable-twin-guide laser diode with electrical blocking regions," *IEEE J. Quantum Electron.*, vol. 35, no. 5, pp. 794–802, May 1999.

[93] Schubert. (2005, May) Room temperature properties of semiconductors. [Online]. Available: http://www.ecse.rpi.edu/ schubert/Light-Emitting-Diodes-dot-org/MaterialsIII.pdf

[94] Simsarian, Bhardwaj, Gripp, Sherman, Su, Webb, Zhang, and Zirngibl, "Fast switching characteristics of a widely tunable laser transmitter," *IEEE Photon. Technol. Lett.*, vol. 15, no. 8, pp. 1038–1040, August 2003.

[95] Soda, Kotaki, Sudo, Ishikawa, S.Yamkoshi, and Imai, "Stability in single longitudinal mode operation in GaInAsP/InP phase-adjusted DFB lasers," *IEEE J. Quantum Electron.*, vol. 23, no. 6, pp. 804–814, June 1987.

[96] Staring, binsma, Kuindersma, Jansen, Thijs, Dongen, and Depovere, "Wavelength-independent output power from an injection-tunable DBR laser," *IEEE Photon. Technol. Lett.*, vol. 6, no. 2, pp. 147–149, February 1994.

[97] Sudbo, "Film mode matching: a versatile numerical method for vector mode field calculations in dielectric waveguides," *Pure Appl. Opt.*, vol. 2, pp. 211–233, 1993.

[98] Sudbo, "Numerically stable formulation of the transverse resonance method for vector mode field calculations in dielectric waveguides," *IEEE Photon. Technol. Lett.*, vol. 5, pp. 342–345, 1993.

[99] Syrbu, *et al.*, "1.55-$\mu m$ optically pumped wafer-fused tunable VCSELs with 32-nm tuning range," *IEEE Photon. Technol. Lett.*, vol. 16, no. 9, pp. 1991–1993, September 2004.

[100] Syrbu, Kapon, Rudra, Mircea, Mereuta, Lakovlev, Suruceanu, and Berseth, "1mW CW 38 nm tunable 1.5 $\mu m$VCSELs with tuning voltage below 4V," in *European Conference on Optical Communications*, vol. PD3.8, 2002, pp. 1–.

[101] Sysak, Barton, Johansson, Raring, Skogen, Mašanović, Blumenthal, and Coldren, "Single-chip wavelength conversion using a photocurrent-driven EAM integrated with a widely tunable sampled-grating DBR laser," *IEEE Photon. Technol. Lett.*, vol. 16, no. 9, pp. 2093–2095, September 2004.

[102] Takahashi, *et al.*, "A stable widely tunable laser using a silica-waveguide triple-ring resonator," in *Conference on Optical Fiber Communications*, March 2005, pp. 1–3.

[103] *Synchronous Optical Network (SONET) Transport Systems: Common Generic Criteria GR-253*, Telcordia Std.

[104] Thijs, Binsma, Young, and Gils, "High temperature operation of $\lambda$= 1.5 $\mu m$ tensile strained multiple quantum well SIPBH lasers," *Electron. Lett.*, vol. 27, no. 10, pp. 791–793, May 1991.

[105] Thompson, *Physics of Semiconductor Laser Devices*. U.K. Wiley, 1980, vol. Chichester,.

[106] Tohmori, Fujiwara, Kakitsuka, Shibata, Kano, Ishikawa, Kawaguchi, Okamot, Kondo, and Yoshikuni, "Wavelength-selectable DBR laser array inherently free from mode-hopping for high speed switching," in *Conference on Optical Fiber Communications*, 2003, pp. 467–468.

[107] Tohmori, Yoshikuni, Tamamura, Yamamoto, Kondo, and Ishii, "Ultrawide wavelength tuning with single longitudinal mode by super structure grating (SSG) DBR laser," in *Conference on Semiconductor Lasers*, vol. 13th, 1992, pp. 268–269.

[108] Ton, Yoffe, Heanue, Emanuel, Zou, Kubicky, Pezeshki, and Vail, "2.5-Gb/s modulated widely tunable laser using an electroabsorption modulated DFB array and MEMS selection," *IEEE Photon. Technol. Lett.*, vol. 16, no. 6, pp. 1573–1575, June 2003.

[109] Turner, Reese, and Pettit, "Exciton absorption and emission in InP," *Phys. Rev. A*, vol. 136, no. 5, pp. 1467–1470, November 1964.

[110] Vakhshoori, Wang, Azimi, Knopp, and Jiang, "MEMS-tunable vertical-cavity surface-emitting lasers," in *Conference on Optical Fiber Communications*, 2001, pp. TuJ1–1–TuJ1–3.

[111] Tartwijk, "Length series results on gain section of tunable DBR laser, internal report."

[112] Wang, Chua, Zhou, Wang, and Wu, "Buried heterostructure InGaAsP/InP strain-compensated multiple quantum well laser with native-oxidized InAlAs current blocking layer," *Apl. Phys. Lett.*, vol. 73, no. 26, pp. 3803–3805, 1998.

[113] Ward, *et al.*, "Widely tunable DS-DBR laser with monolithically integrated SOA: design and performance," *IEEE J. Select. Topics Quantum Electron.*, vol. 11, no. 1, pp. 149–156, January/February 2005.

[114] Weber, "Optimization of the carrier induced effective index change in InGaAsP waveguides - application to tunable Bragg filters," *IEEE J. Quantum Electron.*, vol. 30, no. 8, pp. 1801–1816, August 1994.

[115] Wesstrom, Hammerfelt, Buus, Siljan, Laroy, and Vries, "Design of a widely tunable modulated grating Y-branch laser using the additive Vernier effect for improved super-mode selection," in *Conference on Semiconductor Lasers*, October 2002, pp. 99–100.

[116] Wesstrom, Sarlet, Hammerfeldt, Lundqvist, Szabo, and Rigole, "State-of-the-art performance of widely tunable modulated grating Y-branch lasers," in *Conference on Optical Fiber Communications*, vol. TuE2, February 2004, pp. 1–3.

[117] Wolff, "Theory of the band structure of very degenerate semiconductors," *Phys. Rev.*, vol. 126, pp. 405–412, 1962.

[118] Woodward, Habbab, Koch, and Koren, "The side-mode-suppresion ratio of a tunable DBR laser," *IEEE Photon. Technol. Lett.*, vol. 2, no. 12, pp. 854–856, December 1990.

[119] Yu and O'Dowd, "Influence of mode competition on the fast wavelength switching of an SG-DBR laser," *J. Lightwave. Technol.*, vol. 20, no. 4, pp. 700–704, April 2002.

[120] Yu and O'Dowd, "Interpretation of wavelength switching effects of widely tunable lasers," *IEEE Photon. Technol. Lett.*, vol. 14, no. 10, pp. 1397–1399, October 2002.